

Reflectance and Fluorescence Spectroscopies in Photodynamic Therapy

by

Jarod C. Finlay

Submitted in Partial Fulfillment
of the
Requirements for the Degree
Doctor of Philosophy

Supervised by
Professor Thomas H. Foster

Department of Physics and Astronomy
The College
Arts and Sciences

University of Rochester
Rochester, New York

2003

To Leah

Curriculum Vitae

The author was born in Bryn Mawr, Pennsylvania, in 1975 and received his early education in the Pennsylvania towns of Phoenixville and Montoursville. During his junior year of high school, Finlay moved to Exeter, Pennsylvania where he enrolled in Exeter Township Senior High School. Here, he was first introduced to physics by his teacher Mr. Arthur Murray, whose encouragement of curiosity and inquisitiveness were more valuable than any lesson on Newton's laws, and to higher mathematics by Mr. Robert Dahl, whose sense of humor made learning integral calculus an enjoyable experience. In his final year of high school, Finlay met Leah Janowsky, the woman he would later marry.

After graduating high school in 1993, Finlay was accepted to Alfred University in Alfred, New York, with a National Merit Scholarship which allowed him the financial freedom to spend the next four years studying physics, mathematics, ceramic arts, and various humanities. His education in physics was supplemented by summer research projects at the Maria Mitchell Observatory and the University of Central Florida, both under the auspices of the National Science Foundation's Research Experience for Undergraduates (REU) program, and by research conducted at Alfred under the tutelage of Professor David DeGraff. Finlay graduated

in the Spring of 1997 and was accepted to the graduate program in Physics at the University of Rochester with a Graduate Assistance in Areas of National Need (GAANN) Fellowship. During the following summer, he and Leah were married and started their life together in Rochester. After the requisite year of teaching assistantships and classes, Finlay took advantage of the opportunity to teach a summer undergraduate physics class, earning a Certificate in College Teaching and learning as much about teaching as his students did about physics. Finlay received his Master of Arts degree in Physics from the University of Rochester in 1999.

Despite early intentions to study astrophysics, Finlay quickly developed an interest in biological physics and in the biomedical optics work being done in the laboratory of Professor Thomas Foster. In the summer of 1998, Finlay joined Foster's research group and spent the next four years studying fluorescence spectroscopy, sensitizer photobleaching and reflectance spectroscopy in the context of photodynamic therapy.

In February of 2003, Finlay took up residence in Philadelphia as an Instructor in Physics in the Radiation Oncology Department at the University of Pennsylvania. This position gave him the opportunity to pursue his interest in photodynamic therapy research while gaining experience in the clinical applications of radiation therapy. The final stages of the writing of this thesis were completed during his initial months in Philadelphia.

Publications

J.C. Finlay and T.H. Foster, Method for the simultaneous recovery of tissue absorption and fluorophore concentration from fluorescence spectroscopy, Manuscript in preparation.

J.C. Finlay and T.H. Foster, Quantitative single source-detector separation diffuse reflectance spectroscopy, Manuscript in preparation.

J.C. Finlay, S. Mitra, and T.H. Foster, Photobleaching kinetics of Photofrin *in vivo* and in multicell tumor spheroids indicate multiple simultaneous bleaching mechanisms, Manuscript in preparation.

J.C. Finlay, S. Mitra, and T.H. Foster, *In vivo* mTHPC photobleaching in normal rat skin exhibits unique irradiance-dependent features, *Photochem. Photobiol.* **75**;3 pp 282-288 (2002)

S. Mitra, J.C. Finlay, D. McNeil, D.L. Conover, and T.H. Foster, Photochemical oxygen consumption, oxygen evolution and spectral changes during UVA irradiation of EMT6 spheroids, *Photochem. Photobiol.* **73**;6 pp 703-708 (2001)

J.C. Finlay, D.L. Conover, E.L. Hull, and T.H. Foster, Porphyrin bleaching and PDT-induced spectral changes are irradiance dependent in ALA-sensitized normal rat skin *in vivo*, *Photochem. Photobiol.* **73**;1 pp 54-63 (2001)

Presentations

J.C. Finlay, S. Mitra and T.H. Foster, Irradiance-dependent photobleaching and photoproduct accumulation during Photofrin-, mTHPC- and ALA-PDT *in vivo*: A comparative study, 30th Annual Meeting, American Society for Photobiology, July 13-17, 2002 Quebec City, Canada, Book of Abstracts, p 92

J.C. Finlay and T.H. Foster, Variance-optimized Monte Carlo routine for fluorescence and reflectance of turbid samples, 29th Annual Meeting, American Society for Photobiology, July 7-12, 2001, Chicago, IL, Book of Abstracts, p 76

S. Mitra, J.C. Finlay, D. McNeil, D.L. Conover and T.H. Foster, Photochemical oxygen consumption, oxygen evolution and spectral changes during UVA irradiation of EMT6 spheroids, 29th Annual Meeting, American Society for Photobiology, July 7-12, 2001, Chicago, IL, Book of Abstracts, p 82

J.C. Finlay and T.H. Foster, Irradiance dependence of the fluorescence spectrum of rat skin following ALA-sensitized PDT *in vivo*, 13th International Congress on Photobiology, July 1-6, 2000, San Francisco, CA, Book of Abstracts, p 55

S. Mitra, J.C. Finlay and T.H. Foster, Photobleaching of mTHPC during photodynamic therapy of multicell tumor spheroids and of normal rat skin, 13th International Congress on Photobiology, July 1-6, 2000, San Francisco, CA, Book of Abstracts, p 59

T.H. Foster, J.C. Finlay, D.L. Conover and E.L Hull, Sensitizer photobleaching and dosimetry, SPIE Bios '99, *Optical Methods for Tumor Treatment and Detection: Mechanisms and Techniques in Photodynamic Therapy VII*, January 23-29, 1999, Book of Abstracts, p 42

J.C. Finlay and T.H. Foster, Fluorescence and reflectance spectroscopy of PpIX-sensitized skin during PDT, 8th Congress, European Society for Photobiology, September 3-8, 1999, Granada, Spain, Book of Abstracts, p 88

Acknowledgments

The thesis you hold in your hands is the product of several years of effort, none of which would have been possible without the help and support of a large number of people in the academic community and outside of it. I wish to thank my advisor, Professor Thomas Foster, for providing guidance on all aspects of my graduate work, from research methods and scientific writing to career direction and professional conduct. During my time in his laboratory, I have been exposed to a wide variety of research problems and experimental methods as well as being encouraged to develop and pursue my own interests. His advice, constructive criticism, and careful proofreading have been invaluable in the development of this thesis.

Many of the experiments which contributed to this thesis would have been difficult or impossible without the technical expertise and inventiveness of David Conover, who built the majority of the experimental equipment described here. His diligence in tracking down and eliminating sources of noise, his frequent assistant with experiments and his meticulous documentation of instrument and experiment design are all greatly appreciated.

I also wish to acknowledge many fruitful discussions, frequent experimental

assistance and occasional coauthorship with my fellow graduate students, Edward Hull, Soumya Mitra, Chad Bigelow and William Cottrell. The photobleaching studies described in chapter 3 benefitted from a great deal of help from Soumya and from Ed, who introduced me to much of the instrumentation and experiment design that formed the basis of my future experiments. Soumya and Chad taught me the fundamentals of cell culture and helped me develop the tumor model used in chapters 4 and 5.

Jim Havens and Scott Gibson have been a great help in teaching me basic animal handling and sensitizer preparation. Scott A. Gerber, Amit Lugade, and James Moran, students in the laboratory of Dr. Edith Lord, were very generous with their time and expertise in helping me to develop the EMT-6 tumors used in the animal experiments described in chapters 4 and 5. Dr. William Herkstroeter in the Chemistry department has been very generous with access to his calibrated fluorimeter, which I used extensively for calibration of my experimental equipment. Dr. Stephen Hahn of the University of Pennsylvania has generously provided the Photofrin[®] used in experiments described in chapter 3. My research at the University of Rochester has been supported by National Institutes of Health grants CA68409 and CA36856 awarded by the National Cancer Institute.

The final stages of thesis writing benefited greatly from the time I spent working on it while employed at the University of Pennsylvania. My employers' willingness to accommodate it was very helpful.

Last but in no way least, I owe a great debt of gratitude to my family and to my wife Leah, whose emotional and financial support have made my completion of this work possible, and whose love and patience has played a major part in maintaining

my sanity and happiness throughout its completion. Leah is a constant source of motivation and inspiration.

Abstract

In vivo fluorescence spectroscopy during photodynamic therapy (PDT) has the potential to provide information on the distribution and degradation of sensitizers, the formation of fluorescent photoproducts and changes in tissue autofluorescence induced by photodynamic treatment. Reflectance spectroscopy allows quantification of light absorption and scattering in tissue. We present the results of several related studies of fluorescence and reflectance spectroscopy and their applications to photodynamic dosimetry.

First, we develop and test an empirical method for the correction of the distortions imposed on fluorescence spectra by absorption and scattering in turbid media. We characterize the irradiance dependence of the *in vivo* photobleaching of three sensitizers, protoporphyrin IX (PpIX), Photofrin and mTHPC, in a rat skin model. The photobleaching and photoproduct formation of PpIX exhibit irradiance dependence consistent with singlet oxygen ($^1\text{O}_2$)-mediated bleaching. The bleaching of mTHPC occurs in two phases, only one of which is consistent with a $^1\text{O}_2$ -mediated mechanism. Photofrin's bleaching is independent of irradiance, although its photoproduct formation is not. This can be explained by a mixed-mechanism bleaching model.

Second, we develop an algorithm for the determination of tissue optical prop-

erties using diffuse reflectance spectra measured at a single source-detector separation and demonstrate the recovery of the hemoglobin oxygen dissociation curve from tissue-simulating phantoms containing human erythrocytes. This method is then used to investigate the heterogeneity of oxygenation response in murine tumors induced by carbogen inhalation. We find that while the response varies among animals and within each tumor, the majority of tumors exhibit an increase in blood oxygenation during carbogen breathing.

We present a forward-adjoint model of fluorescence propagation that uses the optical property information acquired from reflectance spectroscopy to obtain the undistorted fluorescence spectrum over a wide range of optical properties. Finally, we investigate the ability of the forward-adjoint theory to extract undistorted fluorescence and optical property information simultaneously from a single measured fluorescence spectrum. This method can recover the hemoglobin oxygen dissociation curve in tissue-simulating phantoms with an accuracy comparable to that of reflectance-based methods while correcting distortions in the fluorescence over a wide range of absorption and scattering coefficients.

Table of Contents

Curriculum Vitae	iii
Acknowledgements	vii
Abstract	x
Table of Contents	xii
List of Tables	xvii
List of Figures	xix
1 Introduction	1
1.1 Singlet oxygen and the photophysics of PDT	4
1.2 PDT dosimetry	6
1.3 Fluorescence photobleaching	8
1.4 Diffuse reflectance spectroscopy	12
1.5 Forward-adjoint fluorescence spectroscopy	17
References	20
2 Theoretical Background	27
2.1 Forward radiative transport theory	27
2.1.1 The diffusion approximation	30

CONTENTS xiii

2.1.2	The P_3 approximation	33
2.1.3	Boundary conditions	37
2.1.4	Beam representation	39
2.1.5	Detector modelling	43
2.2	Adjoint radiative transport theory	49
2.3	Forward-adjoint fluorescence model	53
2.3.1	Solutions in infinite media	54
2.3.2	Solutions in semi-infinite media	58
2.4	Absorber packaging effects	68
2.5	Spectral analysis and fitting techniques	75
2.5.1	Singular value decomposition fitting	75
2.5.2	Nonlinear fitting algorithms and uncertainty propagation	81
2.6	The multiple-mechanism bleaching model	85
2.6.1	Basic kinetic equations	87
2.6.2	Solutions under conditions of constant oxygen concentration	93
2.6.3	Effect of limited 1O_2 diffusion length	104
2.6.4	Implications for dosimetry	105
	References	107
3	<i>In Vivo</i> Photobleaching	110
3.1	Introduction	110
3.1.1	ALA-induced PpIX	113
3.1.2	mTHPC	115
3.1.3	Photofrin	116

3.2	Experimental methods and data analysis	119
3.2.1	Instrumentation	119
3.2.2	Optical properties correction	123
3.2.3	Construction of basis spectra for fluorescence photobleach- ing analysis	127
3.2.4	Animal preparation for <i>in vivo</i> fluorescence photobleaching measurements	135
3.2.5	Sensitizer administration	138
3.2.6	PDT irradiation conditions	139
3.3	<i>In vivo</i> photobleaching results	141
3.3.1	ALA-induced PpIX	141
3.3.2	PpIX bleaching in human patients	150
3.3.3	mTHPC	154
3.3.4	Photofrin	161
3.4	Discussion	166
3.4.1	Diffuse reflectance	166
3.4.2	ALA-induced PpIX	169
3.4.3	mTHPC	178
3.4.4	Photofrin	181
3.4.5	Conclusions and future directions	190
	References	193
4	Single Source-Detector Reflectance Spectroscopy	201
4.1	Introduction	201

4.2	Methods	206
4.2.1	Spectral data acquisition	206
4.2.2	Nonlinear fitting of spectral data	210
4.2.3	Phantom preparation	219
4.2.4	<i>In vivo</i> tumor model	221
4.3	Validation of the diffuse reflectance fitting algorithm	224
4.3.1	Simulated spectral data	224
4.3.2	Phantoms containing erythrocytes	232
4.4	<i>In vivo</i> diffuse reflectance measurements	239
4.5	Discussion	249
	References	252
5	Forward-adjoint Fluorescence Spectroscopy	256
5.1	Introduction	256
5.2	Methods	262
5.2.1	Definition of intrinsic fluorescence	262
5.2.2	Generation of simulated fluorescence spectra	263
5.2.3	Fluorescence phantom preparation	266
5.2.4	Animal tumor model	266
5.2.5	Spectral data acquisition	267
5.2.6	Correction of fluorescence spectral distortion	268
5.2.7	Fluorescence fitting algorithm	269
5.2.8	Choice of fluorescence basis spectra	273
5.3	Fluorescence correction informed by reflectance fitting	275

5.3.1	Correction of simulated fluorescence in infinite media using the forward-adjoint P_3 model	275
5.3.2	Correction of fluorescence in erythrocyte phantoms using the scaled Monte Carlo forward-adjoint algorithm	281
5.4	Fitting of fluorescence spectra	286
5.4.1	Fitting of simulated fluorescence in infinite media using the forward-adjoint P_3 model	286
5.4.2	Fitting of fluorescence acquired from erythrocyte phantoms using the scaled Monte Carlo forward-adjoint model	295
5.5	Analysis of fluorescence spectra acquired <i>in vivo</i> from tumor-bearing mice	306
5.6	Discussion	313
	References	322
A	Variance-matching Fluorescence Monte Carlo	325
A.1	Introduction	325
A.2	Methods	326
A.3	Results	331
A.3.1	Uncertainty estimation	331
A.3.2	Evaluation of efficiency	333
	References	335
B	Volume Probed by Spectroscopic Measurements	336
B.1	Reflectance spectroscopy	337
B.2	Fluorescence spectroscopy	340

CONTENTS **xvii**

References	343
C Errata (Corrected)	344

List of Tables

Table	Title	Page
2.1	Magnitude, position and moments of source distributions used to represent incident pencil beams.	42
2.2	Definitions and units of variables used in the kinetic analysis of simultaneous triplet- and $^1\text{O}_2$ -mediated bleaching.	90
2.3	Numerical values assigned to variables describing photobleaching kinetics.	97
3.1	Sensitizer dose and drug-light interval for each sensitizer investigated.	139
3.2	Irradiation parameters for <i>in vivo</i> PDT on normal rodent skin. . .	141
3.3	Parameters characterizing the irradiance-dependent features of mTHPC photobleaching <i>in vivo</i>	159
3.4	Hemoglobin absorption relevant to reflectance measured during <i>in vivo</i> photobleaching experiments.	167
3.5	Comparison of the PDT treatment parameters and fluorescence excitation and detection wavelengths utilized in our own and three other published studies of PpIX photobleaching.	171

3.6	Mean depth of origin of fluorescence collected by the detectors used in various PpIX bleaching studies, as determined by Monte Carlo simulation.	174
4.1	Published sources of hemoglobin absorption spectra and the wavelength range over which each was used.	212
4.2	Hill parameters extracted from erythrocyte phantom reflectance. .	238
5.1	Hill parameters extracted from erythrocyte phantom fluorescence.	305
A.1	Relative errors achieved by the variance-matching Monte Carlo routine.	332
A.2	Total simulation times for various optical parameters using Monte Carlo algorithms with and without variance matching capability. .	334

List of Figures

1.1	Jabłoński diagram of the photosensitized formation of singlet oxygen.	5
1.2	Absorption spectra of oxy- and deoxyhemoglobin in solution. . . .	13
Figure	Title	Page
2.1	Positions of the image sources that satisfy the extrapolated boundary conditions.	38
2.2	Comparison of the diffusion, P_3 and hybrid reflectance expressions with Monte Carlo results.	47
2.3	Geometry of the forward-adjoint integral in infinite media.	55
2.4	Comparison of the forward-adjoint fluorescence expressions in the diffusion and P_3 approximations with the results of Monte Carlo simulation.	59
2.5	Division of sample volume into annular bins for the scaled Monte Carlo forward-adjoint calculations.	64
2.6	Geometry of a single spherical absorbing particle.	71
2.7	Value of Q resulting from the packaging of an absorber into a 1.6% suspension of 10 μm diameter spherical particles.	73

2.8	Comparison of the absorption spectra of hemoglobin in solution and suspension.	74
2.9	The L-curve of a typical SVD fitting problem.	79
2.10	Jablonski diagram of photosensitized singlet oxygen formation. . .	87
2.11	Concentrations of ground state sensitizer and photoproduct and the corresponding dose of $^1\text{O}_2$ for the case of $170\ \mu\text{M}$ sensitizer. .	100
2.12	Concentrations of ground state sensitizer and photoproduct and the corresponding dose of $^1\text{O}_2$ for the case of $34\ \mu\text{M}$ sensitizer. .	102
2.13	Concentrations of ground state sensitizer and photoproduct and the corresponding dose of $^1\text{O}_2$ for the case of $17\ \mu\text{M}$ sensitizer. . .	103
3.1	Schematic diagram of the system for performing fluorescence and reflectance spectroscopy during PDT.	119
3.2	Correction of fluorescence for changes in optical properties.	126
3.3	Basis spectra used in PpIX SVD fitting.	132
3.4	Basis spectra used in mTHPC SVD fitting.	133
3.5	Basis spectra used in Photofrin SVD fitting.	136
3.6	Spectrally integrated reflectance in ALA-sensitized skin.	142
3.7	A typical series of fluorescence spectra obtained from ALA-sensitized skin.	143
3.8	SVD analysis of a typical <i>in vivo</i> PpIX fluorescence spectrum. . .	145
3.9	Mean spectral amplitude of PpIX as a function of fluence.	146
3.10	Mean spectral amplitudes of PpIX photoproducts as functions of fluence.	147

3.11	Mean spectral amplitude of Up/Cp as a function of fluence. . . .	149
3.12	SVD analysis of <i>in vivo</i> fluorescence from a human skin tumor. . .	152
3.13	Spectral amplitudes of PpIX and product I in normal human skin.	153
3.14	SVD analysis of a typical mTHPC spectrum.	155
3.15	Typical mTHPC bleaching profiles.	156
3.16	Mean mTHPC bleaching profiles.	158
3.17	Mean diffuse reflectance during mTHPC PDT.	160
3.18	Normalized fluorescence spectra obtained from the normal skin of Photofrin sensitized rats before irradiation and after 9 J cm ⁻² of 514 nm irradiation.	162
3.19	Normalized Photofrin amplitude as a function of fluence.	163
3.20	Normalized amplitude of the Photofrin photoproduct as a function of fluence.	164
3.21	Normalized skin reflectance during Photofrin PDT.	165
3.22	Normalized amplitude of PpIX reported by SVD and by spectrally integrating methods.	172
3.23	Bleaching predicted for spheroids by the mixed-mechanism model and by a model including only ¹ O ₂ -mediated bleaching.	183
3.24	Concentrations of ground state sensitizer and photoproduct pre- dicted for mixed-mechanism bleaching <i>in vivo</i>	186
3.25	Effect on the predicted photobleaching rate of increasing or de- creasing the value of the parameter ($k_{ta}[A]/k_{ot}$).	188
4.1	Image of the face of the diffuse reflectance/fluorescence probe. . .	206

4.2	Diffuse reflectance spectrum from an erythrocyte phantom and the best fit corrected for pigment packaging.	213
4.3	Reduced scattering spectrum of a Liposyn II solution containing 0.9% lipids by volume.	218
4.4	Hemoglobin concentration extracted from simulated reflectance data.	226
4.5	Hemoglobin saturation extracted from simulated reflectance data.	227
4.6	Best fit μ'_s extracted from synthetic data.	228
4.7	Best fit values of μ'_s after correction for changes in scale factor. . .	230
4.8	Effect of changing μ'_s on $[Hb]_t$ and SO_2	231
4.9	Typical normalized diffuse reflectance spectra acquired from an erythrocyte phantom.	232
4.10	Fitted concentrations of oxy- and deoxyhemoglobin.	234
4.11	Fitted value of μ'_s at 630 nm.	235
4.12	Fits of the Hill equation to phantom reflectance data.	237
4.13	Normalized diffuse reflectance spectra acquired <i>in vivo</i> from a murine tumor.	240
4.14	Total hemoglobin concentration obtained <i>in vivo</i>	241
4.15	Hemoglobin oxygen saturation acquired <i>in vivo</i>	242
4.16	Change in SO_2 induced by carbogen as a function of initial SO_2 . .	244
4.17	Change in SO_2 induced by carbogen as a function of the change in $[Hb]_t$	247
5.1	Image of the face of the diffuse reflectance/fluorescence probe. . .	267

5.2	Synthetic intrinsic fluorescence spectrum used in Monte Carlo simulation.	276
5.3	Simulated fluorescence spectra in turbid media.	277
5.4	Simulated fluorescence corrected for absorption and scattering using reflectance-derived optical properties.	279
5.5	Typical normalized fluorescence spectra acquired from an erythrocyte phantom containing NADH.	280
5.6	Normalized fluorescence emission spectra obtained from phantoms, corrected for absorption and scattering using optical properties determined by reflectance fitting.	282
5.7	Fluorescence emission spectra obtained from Monte Carlo simulation, corrected for the effects of absorption and scattering.	284
5.8	Simulated fluorescence spectra distorted by propagation through turbid media and best fits using the forward-adjoint P_3 model.	287
5.9	Simulated fluorescence spectra corrected for absorption and scattering effects.	289
5.10	A typical corrected fluorescence spectrum and the components assigned by the fitting algorithm.	290
5.11	Fluorescence amplitudes recovered from simulated data sets.	291
5.12	Ratio of the best fit amplitudes of background fluorophores to NADH in simulated data.	292
5.13	Best fit values of SO_2 and $[Hb]_t$ extracted from synthetic fluorescence data.	294

5.14	Typical normalized fluorescence spectra acquired from an erythrocyte phantom with best fits using the forward-adjoint model. . . .	296
5.15	Fluorescence spectra acquired from an erythrocyte phantom corrected for absorption and scattering.	297
5.16	Typical erythrocyte phantom fluorescence spectrum and the contributions of components assigned by the fitting algorithm. . . .	298
5.17	Best fit values of the fluorescence amplitudes of NADH and Liposyn in a phantom.	300
5.18	Fitted value of μ'_s at 630 nm extracted from phantom fluorescence.	301
5.19	Fitted concentrations of oxy- and deoxyhemoglobin based on phantom fluorescence spectra.	303
5.20	Fits of the Hill equation to phantom SO_2 determined by fitting fluorescence spectra.	304
5.21	Fluorescence emission spectra obtained <i>in vivo</i> from murine tumors.	307
5.22	Intrinsic fluorescence emission spectra extracted from murine tumors using optical properties determined by reflectance fitting. . .	309
5.23	Intrinsic fluorescence emission spectra extracted from murine tumors using optical properties determined by fluorescence fitting. .	311
A.1	Flowchart of the variance matching fluorescence Monte Carlo routine.	327
B.1	Median depth probed by diffuse reflectance measurement as a function of source-detector separation.	338
B.2	Median depth of origin of detected fluorescence measurement as a function of source-detector separation.	341

Chapter 1

Introduction

This thesis includes the results of several related investigations. They are linked by a common theoretical basis and experimental approach and by a common ultimate goal: to improve the understanding of dosimetry in photodynamic therapy (PDT). This chapter will give a brief overview of the current state of PDT research and introduce each of the areas of investigation to be addressed in the thesis.

Photodynamic therapy is a treatment modality which combines a photosensitizing drug with visible light to achieve the destruction of cancerous tumors and benign lesions. The drugs used in PDT generally have little or no toxicity in the absence of light. They are administered systemically or topically hours or days before treatment. At the time of treatment, the target tissue is irradiated with visible or near-infrared light of a wavelength that is readily absorbed by the sensitizer. The activation of the sensitizer by light results in the production of cytotoxic chemicals and to the destruction of the targeted lesion.

Although PDT has been implemented clinically only within the last several

decades, the study of photodynamic action and its connection with fluorescence research have a long history. The first reports of chemical photosensitization date to the late nineteenth century, when Raab and von Tappeiner observed the killing of paramecia by the combined action of light and acridine orange dye. Von Tappeiner went on to perform the first photodynamic treatment of human skin tumors with the fluorescent sensitizer eosin in 1903 (Ackroyd *et al.*, 2001). Despite the early promise of PDT, the field was largely neglected by the medical research community until 1960, when researchers at the Mayo Clinic demonstrated that injection of hematoporphyrin caused preferential fluorescence of tumors. This observation inspired the development of new sensitizers designed specifically to target cancerous tissue. Among these was a porphyrin mixture known as hematoporphyrin derivative (HPD). HPD was later refined and purified to form Photofrin[®], currently the most widely used sensitizer in clinical PDT (Dougherty *et al.*, 1998). In the late 1970's, the first large scale clinical studies of PDT in humans were performed using HPD to treat bladder and skin tumors. Since then, Photofrin PDT has been used to treat malignancies of the skin, bladder, esophagus, lung and gastrointestinal tract and has been used in conjunction with surgical procedures for treatment of brain and peritoneal cancers (Ackroyd *et al.*, 2001; Dougherty *et al.*, 1998). Photofrin is currently approved in the United States and Europe for treatment of bronchial, esophageal and nonsmall-cell lung cancers and precancerous Barrett's esophagus, and in other countries for cervical and bladder cancer (www.scandipharm.com; Dolmans *et al.*, 2003).

More recently developed photosensitizers have been designed to overcome three limitations of Photofrin and HPD: Both cause prolonged skin photosensitivity,

absorb wavelengths short of the optimal transmission of tissue and are composed of mixtures of many different porphyrins, so variations between batches may be problematic. Second-generation photosensitizers including the pure compounds mTHPC and motexafin lutetium (Lutex) have absorption bands shifted to longer wavelengths where light penetrates tissue more easily. mTHPC has exhibited a greater potency and tumor selectivity than Photofrin (Ackroyd *et al.*, 2001) and is involved in clinical trials for treatment of mesothelioma (Friedberg *et al.*, 2003) and prostate cancer (Nathan *et al.*, 2002). It has been approved in Europe for the treatment of head and neck cancers (www.biolitecpharma.com). Lutex is currently being investigated in clinical trials for the treatment of prostate and recurrent breast cancer (Dimofte *et al.*, 2002) and vascular disease (Chou *et al.*, 2002), among other indications.

Another PDT agent which shows promise in treating a number of conditions is aminolevulinic acid (ALA). ALA itself is not a sensitizer, however it induces the formation of the sensitizer protoporphyrin IX (PpIX) in living cells. ALA-induced PpIX clears from the skin faster than Photofrin, and ALA can be administered topically, further reducing unwanted photosensitivity. Formulations of ALA have gained approval for clinical treatment of basal-cell carcinoma and the precancerous skin condition actinic keratosis (Dolmans *et al.*, 2003). In clinical trials, ALA has been shown effective at treating various skin cancers and benign skin conditions ranging from psoriasis to viral warts (Salva, 2002). A second generation of ALA-based drugs make use of ALA esters, which penetrate and sensitize target tissues more effectively than ALA. ALA hexylester has shown promise in the photodynamic detection of bladder cancers, and is currently undergoing clinical trials

under the tradename Hexvix (www.photocure.com; D'Hallewin *et al.*, 2002). A formulation of ALA methylester known as Metvix is currently approved in Australia and is under clinical trial elsewhere for treatment of actinic keratosis and basal cell carcinoma.

In addition to killing cancer cells directly, some sensitizers have been shown to achieve tumor control by sensitizing blood vessels, eliminating the supply of oxygen and nutrients to the tumor. The ability of these sensitizers to target vasculature selectively has led to their use in the treatment of non-cancerous vascular diseases. The most established of these therapies is the treatment of neovascular age related macular degeneration (AMD), a condition in which the overproliferation of the blood vessels behind the retina leads to a reduction in visual acuity and eventual blindness. AMD is the leading cause of vision loss among the elderly in the western hemisphere. Verteporfin, a sensitizer known to cause vascular damage when followed with irradiation shortly after injection, has been proven effective in curtailing the growth of new vessels and the progress of AMD and is currently FDA-approved for treatment of AMD under the tradename Visudyne (Mittra and Singerman, 2002). PDT drugs designed to target blood vessels have also shown promise in the treatment of atherosclerosis and the prevention of restenosis following angioplasty (Krammer, 2001).

1.1 Singlet oxygen and the photophysics of PDT

The majority of currently used sensitizers share a common mechanism of action. These agents, known as type-II photosensitizers, achieve their cytotoxic effect by

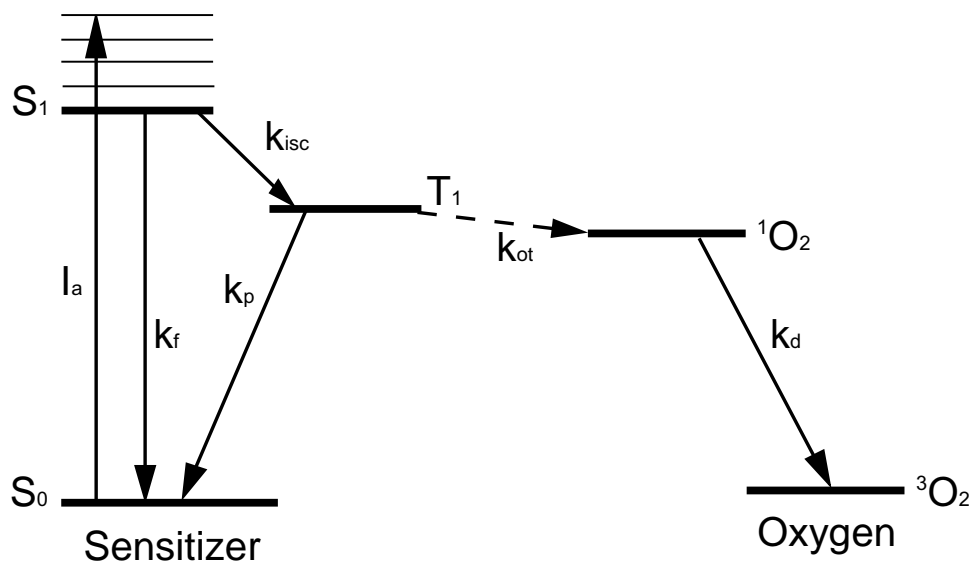


Figure 1.1: Jablonski diagram of the photosensitized formation of singlet oxygen involving a typical type-II photosensitizer.

enabling the generation of singlet oxygen (1O_2) within the target tissue. Singlet oxygen is highly reactive, with a lifetime in the presence of biological substrates of only 0.01 to 0.04 μs (Moan and Berg, 1991). The essential photophysical processes involved in the generation of 1O_2 are illustrated in figure 1.1, which shows the ground and first excited states of a typical photosensitizer and of molecular oxygen. Unlike most molecules, molecular oxygen has a ground state that is a spectroscopic triplet, denoted 3O_2 , and a spectroscopic singlet first excited state. Direct optical excitation of oxygen from the triplet to the singlet state is forbidden by molecular selection rules and does not occur under biologically relevant conditions. An intermediary sensitizer is therefore required for the production of 1O_2 . The photosensitizer's ground state is a spectroscopic singlet, denoted S_0 . The

production of $^1\text{O}_2$ is initiated when a molecule of ground state sensitizer absorbs a photon of light and is promoted to its first excited singlet state S_1 . The excited sensitizer may decay back to its ground state by emission of a fluorescence photon or by non-radiative processes. It may alternatively undergo a transition to its first excited triplet state T_1 , a process known as intersystem crossing. Once in the T_1 state, the sensitizer molecule can transfer energy to a nearby $^3\text{O}_2$ molecule, creating one molecule of $^1\text{O}_2$ and returning the sensitizer to its ground state. Because the sensitizer is not consumed by this process, each sensitizer molecule may be excited many times and produce many $^1\text{O}_2$ molecules. It is the reaction of these $^1\text{O}_2$ molecules with cellular targets that cause photodynamic damage.

In addition to participating in the reactions with cellular substrates that are essential to PDT, $^1\text{O}_2$ may react with sensitizer molecules, resulting in irreversible photobleaching. The photobleaching of the sensitizer reduces the concentration of photochemically active sensitizer molecules and hence the rate of $^1\text{O}_2$ production. Potter *et al.* (1987) recognized that photobleaching could reduce the efficacy of PDT as irradiation progresses. A positive effect of photobleaching, suggested by Boyle and Potter (1987), is that photobleaching could be used to protect normal tissue from photodynamic damage.

1.2 PDT dosimetry

A problem of continuing interest among physicists in the study of PDT is the accurate determination of therapeutic dose and the development of a method of real-time quantitative dosimetry. The *in vivo* generation of $^1\text{O}_2$ by PDT requires

that three primary ingredients be present in the tissue: sensitizer, light of the appropriate wavelength and sufficient molecular oxygen. Many clinical protocols specify the photodynamic dose only in terms of the delivered light fluence and the administered dose of sensitizer (Wilson *et al.*, 1997). In contrast, the research performed in our laboratory over the last 12 years, including the work presented in this thesis, has focused on the effects of tissue oxygenation during PDT. The dynamics of tissue oxygenation are necessarily complex. Oxygen is consumed metabolically by living tissue, and is resupplied by the vascular system. Because $^1\text{O}_2$ reactions are generally irreversible, PDT itself consumes oxygen. The rate of singlet oxygen reactions produced in tissue, and hence the rate of photochemical oxygen consumption, depend on the intensity of the treatment light. If the treatment irradiance is high enough, it is possible that the tissue will become hypoxic, reducing the amount of oxygen available for PDT and the effectiveness of the treatment. A series of animal experiments conducted in the early 1990's at the University of Rochester demonstrated that lowering the treatment irradiance or interrupting treatment to allow tissue oxygenation to recover significantly improved the effectiveness of photodynamic treatment (Feins *et al.*, 1990; Foster *et al.*, 1991; Gibson *et al.*, 1994; 1990). These studies established that a definition of dose that considers only the amount of sensitizer administered and the light fluence applied is insufficient to predict treatment outcome.

While these early animal studies were suggestive of the critical role of oxygenation in determining PDT outcome, the complexity of the *in vivo* environment and the difficulty in making direct measurements of tissue oxygenation limited the ability of the animal results to be modelled from first principles. In order to develop

and verify a quantitative mathematical model of photochemical oxygen consumption effects, a simpler system was needed. Multicell tumor spheroids provide just such a model. Spheroids, like tumors, consist of cells whose distance from the oxygen-supplying medium ranges from zero to tens of microns. Spheroids, however, have the advantages of accessibility to oxygen sensitive probes and a geometry than lends itself to one-dimensional modelling. Foster *et al.* (1993) observed that the rate of cell killing in spheroids was enhanced at reduced irradiance, as expected in cases where a portion of the spheroid was driven hypoxic, protecting it from $^1\text{O}_2$ damage. The model presented in that report used analytic solutions of a simplified oxygen diffusion model to evaluate photochemical oxygen consumption. Successively more sophisticated models incorporated the effect of oxygen concentration on the sensitizer triplet state lifetime (Nichols and Foster, 1994) and the effects of sensitizer photobleaching *via* several different mechanisms (Georgakoudi and Foster, 1998; Georgakoudi *et al.*, 1997). The papers detailing these models included direct measurements of the oxygen concentration in spheroids and in the surrounding medium with sufficient precision that the mechanism by which various sensitizers photobleach could be deduced.

1.3 Fluorescence photobleaching

In the case of photobleaching mediated predominantly by $^1\text{O}_2$, the deposition of photodynamic dose is reported by the bleaching of the photosensitizer (Georgakoudi *et al.*, 1997). The monitoring of sensitizer photobleaching *via* fluorescence measurement can therefore provide a means of real-time ‘implicit’ dosimetry (Wil-

son *et al.*, 1997). Because the photobleaching of the sensitizer is sensitive to the same effects which influence the deposition of photodynamic dose, these effects do not need to be measured explicitly. The direct measurement of *in vivo* fluorescence photobleaching has been undertaken by a number of groups (Mang *et al.*, 1987; Moan, 1986; Rhodes *et al.*, 1997). Forrer *et al.* (1995) studied the photobleaching of the chlorin sensitizer mTHPC, and found its bleaching to be consistent with that predicted by a model that assumed $^1\text{O}_2$ -mediated photobleaching. More recent *in vivo* studies have examined the relationship between photobleaching and treatment irradiance. If photobleaching is to be used as a surrogate measure of damage, the enhanced biological response observed at reduced irradiance should be reflected in more rapid bleaching of the sensitizer. Indeed, irradiance-dependent photobleaching of ALA-induced PpIX has been observed by Robinson *et al.* (1998; 1999) and by Juzenas *et al.* (2002). Other researchers studying the same drug, however, have observed no irradiance dependence (Iinuma *et al.*, 1999; Sørensen *et al.*, 1998).

Chapter 3 of this thesis presents the results of *in vivo* photobleaching studies of three sensitizers: ALA-induced PpIX, mTHPC and Photofrin. This work extends and improves upon previous studies in two important respects. First, it is important to recognize that the fluorescence emission from intact tissue includes contributions from naturally occurring fluorophores in the tissue, known as autofluorescence. The spectral signature of the autofluorescence emission may change as a result of treatment. In addition, many sensitizers produce fluorescent photo-products as a result of their reaction with $^1\text{O}_2$, further complicating the emission spectrum. The complexity of the *in vivo* fluorescence signal motivates the de-

velopment of rigorous spectral analysis techniques. We have adopted a method based on singular value decomposition, outlined in chapter 2, which is capable of separating the contributions of numerous fluorophores, even in the presence of experimental noise and emission from unknown fluorophores. Previous work in our group has demonstrated the ability of a Fourier series added to the SVD basis set to model unknown components in absorption spectra (Hull *et al.*, 1998). Here, the method is extended to the case of fluorescence spectroscopy by weighting the components of the Fourier series for the purpose of fitting fluorescence emission lines and by using the Fourier series to construct basis spectra corresponding to previously unknown emission features. We show that the failure to implement full-spectrum analysis methods can lead to dramatic misinterpretation of *in vivo* fluorescence emission spectra.

The second significant improvement implemented in chapter 3 is an empirically derived correction for the effects of changing optical properties. Fluorescence spectra acquired *in vivo* can be significantly distorted by absorption and scattering of light within the tissue. Several approaches have been taken to correct fluorescence spectra for the distorting effects of absorption and scattering. Gardner *et al.* (1996a) have developed a correction based on a one-dimensional model of photon migration. This algorithm requires knowledge of the penetration depth of light, which can be determined by diffuse reflectance spectroscopy (Gardner *et al.*, 1996b). The validity of this method is limited to measurements in which the illumination of the tissue by the fluorescence excitation light approximates plane wave irradiation. A similar correction scheme based on Kubelka-Monk flux theory has been reported by Durkin *et al.* (1994), however the determination of

the parameters needed for this correction requires a measurement of light transmission through the sample, limiting its applicability to thin tissues or excised samples. Wu *et al.* (1993) have proposed a method recently updated by Müller *et al.* (2001) based on a random-walk model of photon migration which uses measurement of the diffuse reflectance spectrum to correct the fluorescence emission spectrum. Like the previous algorithms, this model requires knowledge of optical properties, however it can be applied to small probes and to measurements made at a single source-detector separation. In chapter 3, an empirical modification of this method has been tested in tissue-simulating phantoms and used to correct fluorescence spectra acquired *in vivo*.

Each of the sensitizers we have studied exhibits irradiance dependent changes in the fluorescence emission spectrum during irradiation, although the details are specific to each sensitizer. The bleaching of ALA-induced PpIX is irradiance-dependent, as is the formation of two fluorescent photoproducts. In addition, we have observed irradiance-dependent changes in autofluorescence which we interpret as direct evidence of mitochondrial damage induced by PDT. The extreme complexity of the emission spectra observed in this case make the implementation of rigorous spectral analysis techniques vital. The fluorescence emission spectrum of skin sensitized with mTHPC is much simpler than that of ALA-sensitized skin, however the bleaching kinetics are more complicated. The photobleaching of mTHPC proceeds in two distinct phases with significantly different bleaching rates, separated by a discontinuity in bleaching rate. In the case of Photofrin, we observe irradiance-independent bleaching in spite of the fact that the accumulation of photoproduct is greater at low irradiance. The photobleaching models

investigated by our group thus far have examined cases where the bleaching of the sensitizer was caused solely by reactions with $^1\text{O}_2$, or solely by reactions between cellular substrates and sensitizer molecules in the S_1 or T_1 state. There is no fundamental reason that a sensitizer cannot participate in more than one type of bleaching reaction simultaneously. The implications of such multiple mechanism bleaching are examined in chapter 2, and it is shown that this mechanism can explain the bleaching and photoproduct kinetics we observe in the case of Photofrin. Parts of chapter 3 and the details of the SVD fitting algorithm described in chapter 2 have been published previously (Finlay *et al.*, 2001; 2002). Co-authorship with Thomas Foster, David Conover, Edward Hull, and Soumya Mitra is gratefully acknowledged.

1.4 Diffuse reflectance spectroscopy

The monitoring of sensitizer photobleaching during PDT gives a measure of the deposition of $^1\text{O}_2$ dose, however it does not provide a direct measurement of tissue oxygenation. Diffuse reflectance spectroscopy provides a non-invasive means of monitoring local oxygen concentration. Throughout the visible wavelengths, the absorption of light by tissue arises primarily from hemoglobin in the red blood cells (Jacques, 1996). The absorption spectrum of hemoglobin changes dramatically when it is bound to oxygen, as shown in figure 1.2. The differences between the spectra of oxy- and deoxyhemoglobin allow the oxygen concentration within the red blood cells to be determined from the absorption spectrum of the tissue being investigated. The absorption spectra of oxy- and deoxyhemoglobin have

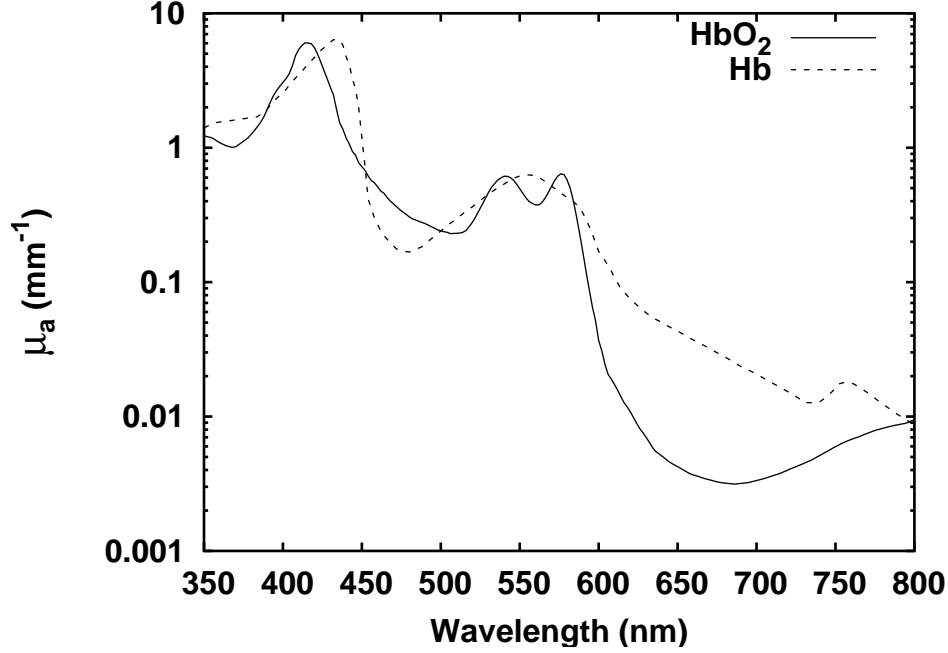


Figure 1.2: Absorption spectra of oxy- and deoxyhemoglobin in solution at a concentration of 50 μM . Data are taken from Prahl (1999).

been measured by several researchers (Joep, 1949; Prahl, 1999; Takatani and Graham, 1987; Van Assendelft, 1970; Wray *et al.*, 1988; Zijlstra *et al.*, 1991). While these measurements are in approximate agreement with one another, none of them take into account the changes in the spectrum induced by the packaging of the hemoglobin into the red blood cells. In chapter 4, we show that this ‘pigment packaging’ effect, first described by Duysens (1956), makes the absorption spectrum of hemoglobin in intact tissue significantly different from that of isolated hemoglobin in solution.

Unlike the absorption spectrum, the scattering spectrum of tissue is generally featureless throughout the visible wavelengths. The scattering coefficient of

tissue is largely determined by the size distribution and refractive indices of its subcellular components and by the arrangement of its connective tissue (Mourant *et al.*, 1998; Saidi *et al.*, 1995). Scattering is insensitive to oxygenation, however it may provide useful information about tissue structure and the status of critical structures such as cell nuclei and mitochondria (Backman *et al.*, 1999; Mourant *et al.*, 2002; Perelman *et al.*, 1999).

Optical oximetry requires a rigorous separation of the effects of absorption and scattering. Several methods have been developed to accomplish this, all of which rely on the fact that photons that traverse different paths through the sample are affected differently by absorption and scattering. In general, photons that take the longest paths through tissue are most sensitive to absorption, while those taking short paths provide the additional information needed to characterize scattering. Time-resolved or frequency-domain measurements of diffuse reflectance effectively sort the collected photons by the time of flight from the source to the detector, a measure equivalent to pathlength (Fishkin *et al.*, 1996; Kienle and Patterson, 1997; Sevick *et al.*, 1991). An alternative approach, which has been adopted in our laboratory's reflectance spectroscopy work, is to make simultaneous steady-state measurements of diffuse reflectance at multiple source-detector separations (Farrell *et al.*, 1992; Hull, 1999; Nichols *et al.*, 1997). In this case, the separation of absorption and scattering is possible because the photons collected at large source detector separations have traversed a greater distance in the tissue than those collected close to the source. The ability of radially resolved steady-state diffuse reflectance measurements to accurately recover the absorption and reduced scattering coefficients has been verified in our laboratory using tissue simulating

phantoms (Hull *et al.*, 1998) and has been applied to the measurement of blood oxygen concentration in rat mammary tumors *in vivo* (Conover *et al.*, 2000; Hull *et al.*, 1999).

Any optical oximetry method requires a quantitative theory describing the propagation of light in tissue. At wavelengths longer than approximately 650 nm, light transport in tissue is dominated by scattering. In this wavelength range, the propagation of light is adequately modelled by photon diffusion theory. The diffusion approximation is based on a series expansion of the more general Boltzmann transport equation, described in chapter 2. Diffusion theory-based algorithms have been used extensively for optical oximetry (Doornbos *et al.*, 1999; Hull *et al.*, 1999; Sevick *et al.*, 1991) and to measure the increase in tissue absorption due to photosensitizers (Patterson *et al.*, 1987; Solonenko *et al.*, 2002). The diffusion approximation, however, is not applicable to shorter wavelengths where tissue is more absorbing, or to measurements made at short source-detector separations.

Several strategies have been used to overcome the limitations of the diffusion theory. The most closely related to diffusion theory is a higher-order approximation to the Boltzmann equation known as the P_3 approximation. Star (1989) and Boas *et al.* (1995) have developed P_3 expressions in a one-dimensional geometry appropriate to plane-wave irradiation of a semi-infinite tissue sample. Dickey *et al.* (1998) have applied this model to the study of the distribution of treatment light during PDT, but have not used it to reconstruct tissue optical properties. A significant effort in our group has led to the extension of the one-dimensional P_3 expression to a two-dimensional model appropriate to fiber-based optical probes (Hull and Foster, 2001; Hull, 1999). This model allows the independent recovery of

absorption and scattering spectra from measurements at smaller source-detector separations and in conditions of higher absorption than possible with the diffusion approximation model. The derivation of the diffusion and P_3 reflectance expressions are reviewed in chapter 2.

In chapter 4, we use the P_3 reflectance expression to analyze the reflectance spectrum acquired at a single source-detector separation. This method does not allow independent determination of the absorption and scattering coefficients at each wavelength, however, by making reasonable assumptions about their spectral shapes, quantitative information about the identity and concentration of absorbers and the characteristics of the scattering spectrum can be extracted. The ability of our algorithm to accurately extract the concentration and oxygen saturation of hemoglobin is demonstrated using simulated data. Diffuse reflectance spectra obtained from tissue simulating phantoms containing intact erythrocytes are fit to extract the hemoglobin oxygen dissociation curve, which is shown to be in agreement with the results of previous studies in our laboratory and with values reported in the literature.

Finally, we analyze reflectance spectra acquired from tumors in mice breathing room air and carbogen using this method, and demonstrate that carbogen breathing is capable of significantly increasing the oxygenation of EMT-6 tumors in mice. This study extends our laboratory's previous work with carbogen in rat tumors (Hull *et al.*, 1999) to a new tumor line and animal model. In addition, the multiple detectors employed in our probe allow different regions of the tumor to be sampled independently, giving an optical characterization of the heterogeneity in blood volume and oxygenation within each tumor.

1.5 Forward-adjoint fluorescence spectroscopy

The observation that absorption and scattering information can be obtained from reflectance measurements leads to the question of whether an analogous method using fluorescence spectroscopy is possible. Investigations of this concept by Vari *et al.* (1993) and Shehada *et al.* (2000) demonstrated that useful absorption information could be recovered from fluorescence measurements, but did not provide a quantitative, theory-based model for extracting this information. We seek a theory capable of modelling fluorescence propagation in tissue from first principles. To this end, we introduce the adjoint radiative transport problem in chapter 2. Instead of modelling the forward propagation of light from its source, this formalism models collected signal *via* the backward propagation of ‘importance’ from a detector (Williams, 1991). The importance is a measure of the probability that a photon at a given point in phase space will eventually be captured by a detector. To model fluorescence, we combine the forward propagation of excitation light and the backward propagation of importance at the emission wavelength, both in the presence of biologically relevant absorption and scattering. Crilly *et al.* (1997) have demonstrated the effectiveness of a Monte Carlo algorithm based on this forward-adjoint principle, however the analytic solution is original to this thesis. We demonstrate the accuracy of a forward-adjoint model that uses the P_3 approximation to radiative transport to evaluate the forward and adjoint distributions in the case of infinite media. In semi-infinite media, we replace the analytic P_3 approximation with a numerical method based on scaling the results of Monte Carlo simulations. This method, suggested by Kienle and Patterson (1996), allows the

1.5. FORWARD-ADJOINT FLUORESCENCE SPECTROSCOPY 18

light distribution in samples with arbitrary optical properties to be calculated from a single Monte Carlo simulation.

In chapter 5, we use the forward-adjoint model to predict the distortion imparted to measured fluorescence spectra by intervening optical properties, and to correct the measured spectra. We show that distortions can be corrected even in the presence of significant absorption and that the forward-adjoint fluorescence model, in combination with the optical property determination methods of chapter 4, is capable of correcting fluorescence for the effects of absorption and scattering with no prior knowledge of optical properties. This method represents a significant improvement over the empirical correction algorithm used in chapter 3; it is valid over a wider range of optical properties and source-detector geometries, and is derived from first principles with no empirical correction factors. Using this method, we recover the intrinsic fluorescence spectra of tissue simulating phantoms containing intact human red blood cells and NADH over the full range of oxygen saturations.

Taking the forward-adjoint approach one step further, we go on to demonstrate that the fitting of measured fluorescence spectra directly can yield intrinsic fluorescence spectra, hemoglobin oxygen saturation, blood volume and information about the reduced scattering spectrum simultaneously. Our fitting algorithms provide accurate recovery of tissue optical properties and intrinsic fluorescence spectra over a wide range of hemoglobin concentrations and saturations in the case of simulated fluorescence in infinite media. To explore the semi-infinite geometry we again use phantoms containing human red blood cells and NADH. We find that the fluorescence fitting algorithm not only recovers the intrinsic fluores-

1.5. FORWARD-ADJOINT FLUORESCENCE SPECTROSCOPY 19

cence, but also determines the oxygen dissociation curve and the corresponding Hill parameters with an accuracy comparable to that of the reflectance fitting described in chapter 4.

As in the case of reflectance, we examine fluorescence spectra acquired *in vivo* from the surface of murine EMT-6 tumors. The preliminary results are encouraging, and demonstrate the potential of single source-detector fluorescence spectroscopy to provide absorption, scattering, and fluorescence information from *in vivo* measurements. We discuss the possibilities and challenges that will accompany these methods into clinical application.

References

- Ackroyd, R., Kelty, C., Brown, N., and Reed, M. (2001). The history of photodetection and photodynamic therapy. *Photochem. Photobiol.* **74**:656–669.
- Backman, V., Gurjar, R., Badizadegan, K., Itzkan, I., Dasari, R. R., Perelman, L. T., and Feld, M. S. (1999). Polarized light scattering spectroscopy for quantitative measurement of epithelial cellular structures *in situ*. *IEEE Journal of Selected Topics in Quantum Electronics.* **5**:1019–1026.
- Boas, D., Lui, H., O’Leary, M., Chance, B., and Yodh, A. (1995). Photon migration within the P_3 approximation. *Proc. SPIE.* **2389**:240–247.
- Boyle, D. G. and Potter, W. R. (1987). Photobleaching of Photofrin II as a means of eliminating skin photosensitivity. *Photochem. Photobiol.* **46**:997–1001.
- Chou, T. M., Woodburn, K. W., Cheong, W. F., Lacy, S. A., Sudhir, K., Adelman, D. C., and Wahr, D. (2002). Photodynamic therapy: Applications in atherosclerotic vascular disease with motexafin lutetium. *Catheter Cardiovasc. Interv.* **57**:387–394.
- Conover, D. L., Fenton, B. M., Foster, T. H., and Hull, E. L. (2000). An evaluation of near infrared spectroscopy and cryospectrophotometry estimates of haemoglobin oxygen saturation in a rodent mammary tumour model. *Phys. Med. Biol.* **45**:2685–2700.
- Crilly, R. J., Cheong, W.-F., Wilson, B. C., and Spears, J. R. (1997). Forward-adjoint fluorescence model: Monte carlo integration and experimental validation. *Appl. Opt.* **36**:6513–6519.
- D’Hallewin, M. A., Bezdetnaya, L., and Guillemin, F. (2002). Fluorescence detection of bladder cancer: A review. *Eur. Urol.* **42**:417–425.
- Dickey, D., Barajas, O., Brown, K., Tulip, J., and Moore, R. B. (1998). Radiance modelling using the P_3 approximation. *Phys. Med. Biol.* **43**:3559–3570.
- Dimofte, A., Zhu, T. C., Hahn, S. M., and Lustig, R. A. (2002). *In vivo* light dosimetry for motexafin lutetium-mediated PDT of recurrent breast cancer. *Lasers Surg. Med.* **31**:305–312.
- Dolmans, D. E. J. G. J., Fukumura, D., and Jain, R. K. (2003). Photodynamic therapy for cancer. *Nat. Rev. Cancer.* **3**:380–387.

- Doornbos, R. M. P., Lang, R., Aalder, M., Cross, F. W., and Sterenborg, H. (1999). The determination of *in vivo* human tissue optical properties and absolute chromophore concentrations using spatially resolved steady-state diffuse reflectance spectroscopy. *Phys. Med. Biol.* **44**:967–981.
- Dougherty, T. J., Gomer, C. J., Henderson, B. W., Jori, G., Kessel, D., Korbek, M., Moan, J., and Peng, Q. (1998). Photodynamic therapy. *J. Natl. Cancer Inst.* **90**:889–905.
- Durkin, A., Jaikumar, S., Ramanujam, N., and Richards-Kortum, R. (1994). Relation between fluorescence spectra of dilute and turbid samples. *Appl. Opt.* **33**:414–23.
- Duysens, L. N. M. (1956). The flattening of the absorption spectrum of suspensions, as compared with that of solutions. *Biochim. Biophys. Acta.* **19**: 1–12.
- Farrell, T. J., Patterson, M. S., and Wilson, B. (1992). A diffusion theory model of spatially resolved, steady-state diffuse reflectance for the noninvasive determination of tissue optical properties *in vivo*. *Med. Phys.* **19**:879–888.
- Feins, R. H., Hilf, R., Ross, H., and Gibson, S. L. (1990). Photodynamic therapy for human mesothelioma in the nude mouse. *J. Surg. Res.* **49**:311–314.
- Finlay, J. C., Conover, D. L., Hull, E. L., and Foster, T. H. (2001). Porphyrin bleaching and PDT-induced spectral changes are irradiance dependent in ALA-sensitized normal rat skin *in vivo*. *Photochem. Photobiol.* **73**:54–63.
- Finlay, J. C., Mitra, S., and Foster, T. H. (2002). *In vivo* mTHPC photobleaching in normal rat skin exhibits unique irradiance-dependent features. *Photochem. Photobiol.* **75**:282–288.
- Fishkin, J. B., Fantini, S., vande Ven, M. J., and Gratton, E. (1996). Gigahertz photon density waves in a turbid medium: Theory and experiments. *Phys. Rev. E.* **53**:2307–2319.
- Forrer, M., Glanzmann, T., Braichotte, D., Wagnières, G., van den Bergh, H., Savary, J. F., and Monnier, P. (1995). *In vivo* measurement of fluorescence bleaching of meso-tetra hydroxy phenyl chlorin (mTHPC) in the esophagus and the oral cavity. *Proc. SPIE.* **2627**:33–39.
- Foster, T. H., Hartley, D. F., Nichols, M. G., and Hilf, R. (1993). Fluence rate effects in photodynamic therapy of multicell tumor spheroids. *Cancer Res.* **53**: 1249–1254.

- Foster, T. H., Murant, R. S., Bryant, R. G., Knox, R. S., Gibson, S. L., and Hilf, R. (1991). Oxygen consumption and diffusion effects in photodynamic therapy. *Rad. Res.* **126**:296–303.
- Friedberg, J. S., Mick, R., Stevenson, J., Metz, J., Zhu, T., Byske, J., Sterman, D. H., Pass, H. I., Glatstein, E., and Hahn, S. M. (2003). A phase I study of Foscan-mediated photodynamic therapy and surgery in patients with mesothelioma. *Ann. Thorac. Surg.* **75**:952–959.
- Gardner, C. M., Jacques, S. L., and Welch, A. J. (1996a). Fluorescence spectroscopy of tissue: Recovery of intrinsic fluorescence from measured fluorescence. *Appl. Opt.* **35**:1780–92.
- Gardner, C. M., Jacques, S. L., and Welch, A. J. (1996b). Light transport in tissue: Accurate expressions for one-dimensional fluence rate and escape function based upon Monte Carlo simulation. *Lasers Surg. Med.* **18**:129–138.
- Georgakoudi, I. and Foster, T. H. (1998). Singlet oxygen- *versus* nonsinglet oxygen-mediated mechanisms of sensitizer photobleaching and their effects on photodynamic dosimetry. *Photochem. Photobiol.* **67**:612–625.
- Georgakoudi, I., Nichols, M. G., and Foster, T. H. (1997). The mechanism of Photofrin photobleaching and its consequences for photodynamic dosimetry. *Photochem. Photobiol.* **65**:135–144.
- Gibson, S. L., Foster, T. H., Feins, R. H., Raubertas, R. F., Fallon, M. A., and Hilf, R. (1994). Effects of photodynamic therapy on xenografts of human mesothelioma and rat mammary carcinoma in nude mice. *Br. J. Cancer.* **69**:473–481.
- Gibson, S. L., VanDerMeid, K. R., Murant, R. S., Raubertas, R. F., and Hilf, R. (1990). Effects of various photoradiation regimens on the antitumor efficacy of photodynamic therapy for R3230AC mammary carcinomas. *Cancer Res.* **50**:7236–7241.
- Hull, E. L., Conover, D. L., and Foster, T. H. (1999). Carbogen-induced changes in rat mammary tumour oxygenation reported by near infrared spectroscopy. *Br. J. Cancer.* **79**:1709–1716.
- Hull, E. L. and Foster, T. H. (2001). Steady-state reflectance spectroscopy in the P_3 approximation. *JOSA A.* **18**:584–599.

- Hull, E. L., Nichols, M. G., and Foster, T. H. (1998). Quantitative broadband near-infrared spectroscopy of tissue-simulating phantoms containing erythrocytes. *Phys. Med. Biol.* **43**:3381–3404.
- Hull, E. L., (1999). *Spectroscopy and characterization of turbid media within the diffusion and P_3 approximations*. PhD thesis, University of Rochester, Rochester, NY.
- Inuma, S., Schomacker, K. T., Wagnières, G., Rajadhyaksha, M., Bamberg, M., Momma, T., and Hasan, T. (1999). *In vivo* fluence rate and fractionation effects on tumor response and photobleaching: Photodynamic therapy with two photosensitizers in an orthotopic rat tumor model. *Cancer Res.* **59**:6164–6170.
- Jacques, S. L. (1996). Origins of optical properties in the UVA, visible, and NIR regions. *OSA Trends in Optics and Photonics on Advances in Optical Imaging and Photon Migration*. **2**:364–371.
- Joep, E. M. (1949), The ultraviolet spectral absorption of haemoglobins inside and outside the red blood cell. In *Haemoglobin*, Roughton, F. J. W. and Kendrew, J. C., editors, pages 205–219. Interscience Publisher, Inc., New York.
- Juzenas, P., Sharfaei, S., Moan, J., and Bissonnette, R. (2002). Protoporphyrin IX fluorescence kinetics in UV-induced tumors and normal skin of hairless mice after topical application of 5-aminolevulinic acid methyl ester. *J. Photochem. Photobiol. B.* **67**:11–17.
- Kienle, A. and Patterson, M. S. (1997). Determination of the optical properties of semi-infinite turbid media from frequency-domain reflectance close to the source. *Phys. Med. Biol.* **42**:1801–1819.
- Kienle, A. and Patterson, M. (1996). Determination of the optical properties of turbid media from a single Monte Carlo simulation. *Phys. Med. Biol.* **41**: 2221–2227.
- Krammer, B. (2001). Vascular effects of photodynamic therapy. *Anticancer Res.* **21**:4271–4278.
- Mang, T. S., Dougherty, T. J., Potter, W. R., Boyle, D. G., Somer, S., and Moan, J. (1987). Photobleaching of porphyrins used in photodynamic therapy and implications for therapy. *Photochem. Photobiol.* **45**:501–506.
- Mittra, R. A. and Singerman, L. J. (2002). Recent advances in the management of age-related macular degeneration. *Optom. Vis. Sci.* **79**:218–224.

- Moan, J. (1986). Effect of bleaching of porphyrin sensitizers during photodynamic therapy. *Cancer Lett.* **33**:45–53.
- Moan, J. and Berg, K. (1991). The photodegradation of porphyrins in cells can be used to estimate the lifetime of singlet oxygen. *Photochem. Photobiol.* **53**: 549–553.
- Mourant, J. R., Johnson, T. M., Carpenter, S., Guerra, A., Aida, T., and Freyer, J. P. (2002). Polarized angular dependent spectroscopy of epithelial cells and epithelial cell nuclei to determine the size scale of scattering structures. *J. Biomed. Opt.* **7**:378–387.
- Mourant, J. R., Freyer, J. P., Hielscher, A. H., Eick, A. A., Shen, D., and Johnson, T. M. (1998). Mechanisms of light scattering from biological cells relevant to noninvasive optical-tissue diagnosis. *Appl. Opt.* **37**:3586–3593.
- Müller, M., Georgakoudi, I., Zhang, Q., Wu, J., and Feld, M. (2001). Intrinsic fluorescence spectroscopy in turbid media: Disentangling effects of scattering and absorption. *Appl. Opt.* **40**:4633–4646.
- Nathan, T. R., Whitelaw, D. E., Chang, S. C., Lees, W. R., Ripley, P. M., Payne, H., Jones, L., Parkinson, M. C., Emberon, M., Gillams, A. R., Mundy, A. R., and Bown, S. G. (2002). Photodynamic therapy for prostate cancer recurrence after radiotherapy: A phase I study. *J. Urol.* **168**:1427–1432.
- Nichols, M. G. and Foster, T. H. (1994). Oxygen diffusion and reaction kinetics in the photodynamic therapy of multicell tumour spheroids. *Phys. Med. Biol.* **39**:2161–81.
- Nichols, M. G., Hull, E. L., and Foster, T. H. (1997). Design and testing of a white-light, steady-state diffuse reflectance spectrometer for determination of optical properties of highly scattering systems. *Appl. Opt.* **36**:93–104.
- Patterson, M. S., Wilson, B. C., Feather, J. W., Burns, D. M., and Pushka, W. (1987). The measurement of dihematoporphyrin ether concentration in tissue by reflectance spectrophotometry. *Photochem. Photobiol.* **46**:337–343.
- Perelman, L. T., Backman, V., Wallace, M., Zonios, G., Manahoran, R., Nusrat, A., Shields, S., Seiler, M., Lima, C., Hamano, T., Itzkan, I., Dam, J. V., Crawford, J. M., and Feld, M. S. (1999). Observation of periodic fine structure in reflectance from biological tissue: A new technique for measuring nuclear size distribution. *Phys. Rev. Lett.* **80**:627–630.

- Potter, W. R., Mang, T. S., and Dougherty, T. J. (1987). The theory of photodynamic therapy dosimetry: Consequences of photo-destruction of sensitizer. *Photochem. Photobiol.* **46**:97–101.
- Prahl, S. A., (1999). Optical properties of hemoglobin. Available from the website omlc.ogi.edu.
- Rhodes, L. E., Tsoukas, M. M., Anderson, R. R., and Kollias, N. (1997). Iontophoretic delivery of ALA provides a quantitative model for ALA pharmacokinetics and PpIX phototoxicity in human skin. *J. Invest. Dermatol.* **108**: 87–91.
- Robinson, D. J., de Bruijn, H. S., van der Veen, N., Stringer, M. R., Brown, S. B., and Star, W. M. (1998). Fluorescence photobleaching of ALA-induced protoporphyrin IX during photodynamic therapy of normal hairless mouse skin: The effect of light dose and irradiance and the resulting biological effect. *Photochem. Photobiol.* **67**:140–149.
- Robinson, D. J., de Bruijn, H. S., van der Veen, N., Stringer, M. R., Brown, S. B., and Star, W. M. (1999). Protoporphyrin IX fluorescence photobleaching during ALA-mediated photodynamic therapy of UVB-induced tumors in hairless mouse skin. *Photochem. Photobiol.* **69**:61–70.
- Saidi, I. S., Jacques, S. L., and Tittle, F. K. (1995). Mie and Rayleigh modeling of visible-light scattering in neonatal skin. *Appl. Opt.* **34**:7410–7418.
- Salva, K. A. (2002). Photodynamic therapy: Unapproved uses, dosages, or indications. *Clin. Derm.* **20**:571–581.
- Sevick, E. M., Chance, B., Leigh, J., Nioka, S., and Maris, M. (1991). Quantitation of time-resolved and frequency-resolved optical spectra for the determination of tissue oxygenation. *Anal. Biochem.* **195**:330–351.
- Shehada, R. E. N., Marmarelis, V. Z., Mansour, H. N., and Grundfest, W. S. (2000). Laser induced fluorescence attenuation spectroscopy: Detection of hypoxia. *IEEE Trans. Biomed. Eng.* **47**:301–312.
- Solonenko, M., Cheung, R., Busch, T. M., Kachur, A., Griffin, G. M., Vulcan, T., Zhu, T., Wang, H.-W., Hahn, S. M., and Yodh, A. G. (2002). *In vivo* reflectance measurements of optical properties, blood oxygenation and motexafin lutetium uptake in canine large bowels, kidneys and prostates. *Phys. Med. Biol.* **47**: 857–873.

- Sørensen, R., Iani, V., and Moan, J. (1998). Kinetics of photobleaching of protoporphyrin IX in the skin of nude mice exposed to different fluence rates of red light. *Photochem. Photobiol.* **68**:835–840.
- Star, W. M. (1989). Comparing the P_3 -approximation with diffusion theory and with Monte Carlo calculations of light propagation in a slab geometry. *SPIE Institute Series*. **IS5**:46–54.
- Takatani, S. and Graham, M. D. (1987). Theoretical analysis of diffuse reflectance from a two-layer tissue model. *IEEE Trans. Biomed. Eng.* **BME-26**:656–664.
- Van Assendelft, O. W. (1970). *Spectrophotometry of Haemoglobin Derivatives*. Charles C. Thomas, Springfield, IL.
- Vari, S. G., Papazoglou, T. G., Pergadia, V. R., Stavridi, M., Snyder, W. J., Papaioannou, T., Duffy, J. T., Weiss, A. B., Thomas, R., and Grundfest, W. S. (1993). Blood perfusion and pH monitoring in organs by laser induced fluorescence spectroscopy. *Proc. SPIE*. **2081**:117–128.
- Williams, M. L. (1991). Generalized contribution response theory. *Nuc. Sci. Eng.* **108**:355–383.
- Wilson, B. C., Patterson, M., and Lilge, L. (1997). Implicit and explicit dosimetry in photodynamic therapy: A new paradigm. *Lasers Med. Sci.* **12**:182–199.
- Wray, S., Cope, M., Delpy, D. T., Wyatt, J. S., and Reynolds, E. O. R. (1988). Characterization of the near-infrared absorption spectra of cytochrome aa_3 and hemoglobin for the noninvasive monitoring of cerebral oxygenation. *Biochim. Biophys. Acta*. **933**:184–192.
- Wu, J., Feld, M. S., and Rava, R. (1993). Analytical model for extracting intrinsic fluorescence in turbid media. *Appl. Opt.* **32**:3583–3595.
- Zijlstra, W. G., Bursma, A., and Meeuwssen-van der Roest, W. P. (1991). Absorption spectra of human fetal and adult oxyhemoglobin, de-oxyhemoglobin, carboxyhemoglobin, and methemoglobin. *Clin. Chem.* **37**:1633–1638.

Chapter 2

Theoretical Background

2.1 Forward radiative transport theory and the P_N approximation

Understanding the physical processes involved in photodynamic therapy and in the noninvasive optical characterization of tissue requires a theoretical description of the propagation and collection of light in scattering and absorbing media. In principle, the distribution of light in tissue could be modelled in terms of electric and magnetic fields and the electromagnetic properties of the medium. In practice, such a model becomes intractably complex for realistic media. An alternative approach is provided by the radiative transport theory. This model was originally developed to study the propagation of light through stellar atmospheres (Schuster, 1905), but its basic assumptions apply to the transport of any neutral particles. Radiative transport theory has been widely utilized in nuclear reactor design to model the propagation of neutrons in reactor cores and has been applied to the

study of light propagation through a variety of turbid media including terrestrial and interstellar clouds, seawater and human and animal tissue.

The fundamental quantity in radiative transport theory is the radiance $L(\mathbf{r}, \hat{s})$, a scalar function equal to the power of radiation per unit area per unit solid angle in direction \hat{s} at position \mathbf{r} . The distribution of radiance within the medium is determined by the medium's optical properties, the distribution of sources within the medium and the characteristics of the medium boundaries. The absorption coefficient μ_a is equal to the probability of absorption per unit distance. Similarly, the scattering coefficient μ_s gives the probability of scattering per unit length. The effects of absorption and scattering on the steady-state distribution of radiance are described by the time-independent Boltzmann equation (Ishimaru, 1997),

$$\nabla \cdot L(\mathbf{r}, \hat{s})\hat{s} = -\mu_t L(\mathbf{r}, \hat{s}) + \mu_s \int_{4\pi} L(\mathbf{r}, \hat{s}') f(\hat{s}, \hat{s}') d\Omega' + S(\mathbf{r}, \hat{s}), \quad (2.1)$$

where the attenuation coefficient μ_t is equal to $(\mu_a + \mu_s)$. Equation 2.1 is a heuristic description of the spatial variation in radiance distribution in the scattering medium. The radiance in direction \hat{s} is decreased by absorption and by scattering away from \hat{s} (first term on RHS) and increased by scattering from all other directions (integral term) and by sources of radiance (final term).

The function $f(\hat{s}, \hat{s}')$, known as the scattering phase function, is defined as the probability that a photon incident in direction \hat{s}' will be scattered into direction \hat{s} . It can generally be assumed that the scattering phase function depends only upon the scattering angle and is independent of spatial location and of the direction of the incident photon. $f(\hat{s}, \hat{s}')$ can then be expressed as a function of $(\hat{s} \cdot \hat{s}')$.

The scattering phase function can be characterized by the scattering anisotropy g , equal to the average of scattering cosine,

$$g = \int_{4\pi} f(\hat{s}, \hat{s}') d\Omega, \quad (2.2)$$

where $d\Omega$ is the differential solid angle, and the integral includes all possible directions of scatter. A large value of g indicates predominantly forward scattering, while isotropic scattering results in a g of 0. A computationally convenient analytic phase function commonly used to model tissue scattering is the Henyey-Greenstein function (Henyey and Greenstein, 1941),

$$f_{HG}(\cos(\theta)) = \left(\frac{1}{4\pi} \right) \frac{1 - g^2}{(1 + g^2 - 2g \cos(\theta))^{\frac{3}{2}}}. \quad (2.3)$$

This equation was originally formulated to approximate Mie theory results for the modelling of scattering in galactic dust clouds, however Jacques *et al.* (1987) have shown that it provides a reasonable match to the scattering phase function observed in tissue. Unless otherwise stated, the derivations and examples in this chapter will use the Henyey-Greenstein phase function.

Exact analytical solutions of equation 2.1 may be obtained for some idealized geometries, however the conditions under which these solutions are valid are too restrictive to make them generally useful in practical applications (Ishimaru, 1997). It is therefore necessary to approximate the Boltzmann equation by an equation or system of equations that yield analytic solutions. A standard method of approximation is to expand the radiance and source terms as series of spheri-

cal harmonics truncated at the N^{th} term, and the scattering phase function as a similarly truncated series of Legendre polynomials,

$$L(\mathbf{r}, \hat{s}) = \sum_{l=0}^N \sum_{m=-l}^l \sqrt{\frac{2l+1}{4\pi}} \phi_{lm} Y_{lm}(\hat{s}) \quad (2.4a)$$

$$S(\mathbf{r}, \hat{s}) = \sum_{l=0}^N \sum_{m=-l}^l \sqrt{\frac{2l+1}{4\pi}} \sigma_{lm} Y_{lm}(\hat{s}) \quad (2.4b)$$

$$f(\hat{s} \cdot \hat{s}') = \sum_{l=0}^N \frac{2l+1}{4\pi} g_l P_l(\hat{s} \cdot \hat{s}'). \quad (2.4c)$$

The substitution of equations 2.4 into equation 2.1 constitutes the P_N approximation to the radiative transport equation.

2.1.1 The diffusion approximation

When the series expansions for the radiance, source distribution and scattering phase function are truncated at $N = 1$, equations 2.4 take the form

$$L(\mathbf{r}, \hat{s}) = \frac{1}{4\pi} \Phi(\mathbf{r}) + \frac{3}{4\pi} \mathbf{j}(\mathbf{r}) \cdot \hat{s} \quad (2.5a)$$

$$S(\mathbf{r}, \hat{s}) = \frac{1}{4\pi} S_0(\mathbf{r}) + \frac{3}{4\pi} \mathbf{S}_1(\mathbf{r}) \cdot \hat{s} \quad (2.5b)$$

$$f(\hat{s}, \hat{s}') = \frac{1}{4\pi} + \frac{3}{4\pi} g(\hat{s} \cdot \hat{s}'). \quad (2.5c)$$

This simplification makes use of the fact that the three ϕ_{1m} can be uniquely represented in linear combination as the components of a single vector \mathbf{j} , and the σ_{1m} as components of the vector \mathbf{S}_1 . The fluence Φ and flux \mathbf{j} are the isotropic and linearly anisotropic components of the radiance, respectively. Truncation of

the series expansions at $N = 1$ implicitly assumes that any anisotropy in the radiance is linear and can be accounted for by \mathbf{j} . Similarly, the source is assumed to have a total strength S_0 and at most a linearly anisotropic component given by \mathbf{S}_1 . Substituting equations 2.5 into equation 2.1 and integrating over all solid angles gives an equation for the divergence of the flux,

$$\nabla \cdot \mathbf{j}(\mathbf{r}) = -\mu_a \Phi(\mathbf{r}) + S_0(\mathbf{r}). \quad (2.6)$$

Multiplying by \hat{s} and integrating over all solid angles gives the corresponding equation for the gradient of the fluence,

$$\frac{1}{3} \nabla \Phi(\mathbf{r}) = -(\mu'_s + \mu_a) \mathbf{j}(\mathbf{r}) + \mathbf{S}_1(\mathbf{r}). \quad (2.7)$$

When only isotropic sources are considered, \mathbf{S}_1 is zero everywhere. In this case equations 2.6 and 2.7 can be combined, yielding the time-independent photon diffusion equation,

$$D \nabla^2 \Phi(\mathbf{r}) - \mu_a \Phi(\mathbf{r}) = S_0(\mathbf{r}). \quad (2.8)$$

The diffusion constant D is equal to $1/3(\mu_a + \mu'_s)$, where μ'_s is the reduced scattering coefficient, equal to $\mu_s(1 - g)$. The flux \mathbf{j} is related to the fluence Φ by an optical version of Fick's law,

$$\mathbf{j}(\mathbf{r}) = -D \nabla \Phi(\mathbf{r}). \quad (2.9)$$

The fact that the diffusion approximation is sensitive only to μ'_s and not to μ_s

and g independently is an example of a first-order similarity relation. The implication of this relation is that an anisotropically scattering medium with scattering coefficient μ_s will generate the same radiance distribution as an isotropically scattering medium with a scattering coefficient of μ'_s . The reduced scattering mean free path, $1/\mu'_s$, is the mean distance a photon must travel in the medium before it is scattered sufficiently many times that its direction is randomized. When considering the relative importance of absorption and scattering to the interaction of light with a given sample, it is useful to define the albedo a and the transport albedo a' , given by

$$a = \frac{\mu_s}{\mu_a + \mu_s} \quad (2.10a)$$

$$a' = \frac{\mu'_s}{\mu_a + \mu'_s}, \quad (2.10b)$$

respectively. Because of the similarity relation described above, a' is a more accurate measure of the relative importance of scattering than a .

In the diffusion approximation, the Green's function for the fluence resulting from an isotropic point source in a homogeneous medium is given by (Case and Zweifel, 1967; Ishimaru, 1997)

$$\Phi(\mathbf{r}) = \frac{1}{4\pi D} \frac{e^{-\mu_{eff}r}}{r}, \quad (2.11)$$

where μ_{eff} is the effective attenuation coefficient, given by $\mu_{eff} = \sqrt{3\mu_a(\mu_a + \mu'_s)}$. The flux can be found by substituting Φ into equation 2.9. The flux and fluence,

when substituted into equation 2.5a, give the complete expression for the radiance in the diffusion approximation.

As noted before, the derivation of the diffusion approximation is based on the assumption that the radiance is only linearly anisotropic. In practice, this means that the diffusion approximation is valid when μ_a is much less than μ'_s and when the distance between the source and the point of interest is greater than one transport mean free path (Fishkin *et al.*, 1996). In typical applications in the field of tissue optics, the requirement of high transport albedo restricts the use of the diffusion approximation to wavelengths in the near infrared, a region of the spectrum referred to as the ‘optical window’. Strong absorption due to hemoglobin at shorter wavelengths and water at longer wavelengths requires that a higher-order approximation to radiative transport be used to obtain accurate results outside of this wavelength range. Even within the optical window, the diffusion approximation breaks down in regions closer than approximately 1 mm from the source. In these regions, the radiance is highly anisotropic because it includes a significant contribution from photons which have not become randomized by multiple scattering.

2.1.2 The P_3 approximation

The approach described above for the diffusion approximation can be generalized to any order of approximation. In the P_3 approximation, the expansions given in equations 2.4a through 2.4c are substituted into equation 2.1. The resulting expression is then multiplied by each Y_{lm} in turn, up to $l = 3$, and integrated over all solid angles, yielding a set of 16 first-order linear differential equations.

Because we seek a Green's function solution for the case of an isotropic point source in a homogeneous medium, a simpler approach is possible. Following the derivation of Hull and Foster (2001), we can make use of the symmetry of the problem to reduce it to the analogous one-dimensional case of an infinite plane source embedded in a homogenous medium. This reduces the number of linear differential equations to four. This set of equations can be solved directly, and the resulting one-dimensional solutions can be transformed to the three-dimensional spherical geometry using relations arising from general transport theory. The expression for the radiance then takes the form of a truncated series of Legendre polynomials in the angle between \mathbf{r} and \hat{s} ,

$$L(\mathbf{r}, \hat{s}) = \sum_{l=0}^3 \frac{2l+1}{4\pi} \Psi_l(r) P_l(\hat{r} \cdot \hat{s}). \quad (2.12)$$

The moments of the radiance are given by

$$\Psi_l(r) = - \left[B^- h_l(-\nu^-) Q_l(-\nu^- r) + B^+ h_l(-\nu^+) Q_l(-\nu^+ r) \right], \quad (2.13)$$

where

$$\nu^\pm = \left(\frac{\beta \pm \sqrt{\beta^2 - \Gamma}}{18} \right)^{\frac{1}{2}}, \quad (2.14a)$$

$$\beta = 27\mu_a\mu_t^{(1)} + 28\mu_a\mu_t^{(3)} + 35\mu_t^{(2)}\mu_t^{(3)}, \quad (2.14b)$$

$$\Gamma = 3780\mu_a\mu_t^{(1)}\mu_t^{(2)}\mu_t^{(3)} \quad (2.14c)$$

and $\mu_t^{(l)} = \mu_a + \mu_s(1 - g_l)$. The components of the radiance corresponding to terms involving ν^+ and ν^- are known as the transient and asymptotic components, respectively. The functions h_l in equation 2.13 are defined as

$$h_0(\nu) = 1 \quad (2.15a)$$

$$h_1(\nu) = -\frac{\mu_a}{\nu} \quad (2.15b)$$

$$h_2(\nu) = \left[-\frac{1}{2} + \frac{3\mu_a\mu_t^{(1)}}{2\nu^2} \right] \quad (2.15c)$$

$$h_3(\nu) = \left[-\frac{9\mu_a\mu_t^{(1)}}{14\mu_t^{(3)}\nu} + \frac{3\nu}{14\mu_t^{(3)}} \right], \quad (2.15d)$$

and the constants B^+ and B^- are given by

$$B^\pm = \frac{(\nu^\pm)^5 \left[3\mu_a\mu_t^{(1)} - (\nu^\mp)^2 \right]}{12\pi\mu_a^2\mu_t^{(1)}[(\nu^\pm)^2 - (\nu^\mp)^2]}, \quad (2.16)$$

corresponding to $(-D')$ and $(-C')$, respectively, in the notation of Hull and Foster (2001). Finally, the radial dependence of the Ψ_l is contained in the functions Q_0 through Q_3 , which are defined by the recursion relation

$$Q_l(x) = Q_{l-2}(x) - \frac{2l-1}{x} Q_{l-1}(x). \quad (2.17a)$$

The first two Q_l are given by

$$Q_0(x) = \frac{e^x}{x}, \quad (2.17b)$$

$$Q_1(x) = \left(1 - \frac{1}{x} \right) \frac{e^x}{x}. \quad (2.17c)$$

Equations 2.15, 2.16 and 2.17 can be substituted into equation 2.13 with $l = 0$ to obtain the expression for the fluence in the P_3 approximation,

$$\Psi_0(r) = B^- \frac{e^{-\nu^- r}}{\nu^- r} + B^+ \frac{e^{-\nu^+ r}}{\nu^+ r}. \quad (2.18)$$

Hull and Foster (2001) have also derived a hybrid diffusion theory- P_3 model, which uses the diffusion theory Green's function with μ_{eff} replaced by ν^- and the diffusion constant D replaced with $\mu_a/(\nu^-)^2$. The resulting fluence expression is

$$\Psi_0(r) = \frac{1}{4\pi(\mu_a/(\nu^-)^2)} \frac{e^{-\nu^- r}}{r}. \quad (2.19)$$

As the albedo approaches unity, ν^- approaches μ_{eff} and the hybrid and P_3 fluence expressions approach the diffusion theory expression.

An approximate similarity relation between the $\mu_t^{(l)}$ can be used to simplify the P_3 and diffusion- P_3 hybrid expressions. As demonstrated by Hull and Foster (2001), $\mu_t^{(2)}$ and $\mu_t^{(3)}$ can be approximated by $(\mu_a + \mu'_s \gamma)$ and $(\mu_a + \mu'_s \delta)$, respectively. For scattering following the Henyey-Greenstein scattering distribution, γ and δ are approximately equal to 1.85 and 2.6, respectively, for a wide range of physiologically relevant values of g (Hull and Foster, 2001). Taking these values of γ and δ allows the P_3 or P_3 -diffusion hybrid expression for diffuse reflectance to be evaluated in terms of μ_a and μ'_s without explicit knowledge of g .

2.1.3 Boundary conditions

In many situations, the tissue can be treated as a semi-infinite slab separated from the ambient nonscattering medium by a planar boundary. The boundary condition in this case requires that no radiance enters the scattering medium from the outside. When the refractive indices of the scattering medium and the surrounding nonscattering medium are identical, this condition requires that $L(\mathbf{r}, \hat{s})$ be zero for all \hat{s} directed inward. When there is an index mismatch at the boundary, the inward-directed radiance is related to the outward directed radiance by the Fresnel reflection coefficient. In either case, the presence of the boundary constrains L for all inward-directed \hat{s} , effectively imposing an infinite number of boundary conditions. In the P_N approximation, only $(N + 1)/2$ of these can be satisfied exactly. Therefore, an approximate set of boundary conditions is required. In the diffusion approximation, a standard method is to satisfy the extrapolated boundary condition (EBC), which requires that the fluence vanish at a distance $z_b = 2AD$ above the physical boundary, where D is the optical diffusion constant and the parameter A depends on the difference in refractive index between the tissue and the surrounding medium (Farrell *et al.*, 1992; Kienle and Patterson, 1997). For a medium illuminated by an isotropic point source at depth z_0 , the EBC can be satisfied by placing an image source of equal and opposite magnitude at $-(z_0 + 2z_b)$.

To rigorously satisfy the boundary conditions in the P_3 approximation, a higher order condition than the extrapolated boundary is required. However, Hull and Foster (2001) have obtained accurate results by assigning the transient

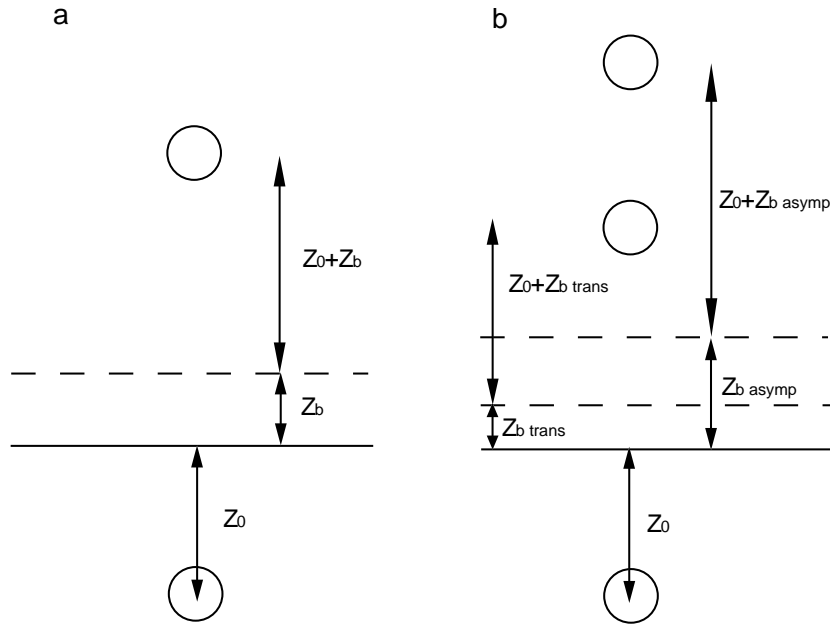


Figure 2.1: Positions of the image sources that satisfy the extrapolated boundary conditions in the (a) diffusion and (b) P_3 approximations to radiative transport for a single isotropic point source at depth z_0

and asymptotic components of the radiance separate image sources, with extrapolation lengths of $z_{b_{tran}} = 2A\mu_a/(\nu^+)^2$ and $z_{b_{asympt}} = 2A\mu_a/(\nu^-)^2$, respectively. The source/image configurations used in the diffusion and P_3 approximations are illustrated in figures 2.1(a) and (b), respectively. It should be noted that other strategies for the formulation of approximate boundary conditions have been proposed. We have adopted the EBC method because of its combination of computational simplicity and accuracy, which has been verified by Haskell *et al.* (1994) and by Hull and Foster (2001) for the diffusion and P_3 approximations, respectively.

2.1.4 Beam representation

In the case of tissue illuminated by a collimated beam or by an optical fiber, the source can be approximated by a pencil beam normal to the surface at the origin. The collimated radiance L_c due to a pencil beam of unit power is given by

$$L_c(\mathbf{r}, \hat{s}) = e^{-\mu'_t z} \delta(x) \delta(y) \delta(\hat{s}, \hat{n}), \quad (2.20)$$

where \hat{n} is the unit vector normal to the surface pointing inward. The delta functions ensure that the collimated irradiance is nonzero only in the direction of propagation of the beam and only at the origin. The radiance of the collimated beam is reduced by scattering and absorption as it passes into tissue. The dependence on the reduced attenuation coefficient μ'_t rather than the attenuation coefficient μ_t is a consequence of the similarity relation discussed in section 2.1.1 and indicates that when scattering is anisotropic, a photon must be scattered multiple times before it effectively leaves the collimated beam.

In the absence of sources within the medium, the source term in equation 2.1 contains only the light scattered out of the collimated beam (Ishimaru, 1997). Again making use of the similarity relation, the effective source term is given by the radiance isotropically scattered from the collimated beam,

$$\begin{aligned}
 S(\mathbf{r}, \hat{s}) &= \mu'_s L_c(\mathbf{r}, \hat{s}') f(\hat{s} \cdot \hat{n}) \\
 &= \frac{1}{4\pi} \mu'_s e^{-\mu'_t z} f(\hat{s} \cdot \hat{n}) \delta(x) \delta(y) \\
 &\approx \mu'_s e^{-\mu'_t z} \left(\frac{1}{4\pi} + \frac{3}{4\pi} g(\hat{s} \cdot \hat{n}') \right) \delta(x) \delta(y),
 \end{aligned} \tag{2.21}$$

where we have used equation 2.5c to approximate the scattering phase function. The source fluence S_0 is found by substituting equation 2.21 into equation 2.5b. Considering only the z -dependence, S_0 is given by

$$S_0(z) = \mu'_s e^{-\mu'_t z}, \tag{2.22}$$

which represents the distribution of isotropic point sources which best model an incident pencil beam, in agreement with the work of Farrell *et al.* (1992). While this model is rigorously correct, its usefulness is limited by the fact that a convolution of a Green's function with an infinite source distribution is required to evaluate it. For computational convenience, it is desirable to find an equivalent model which uses a small number of sources. The finite distribution of isotropic point sources which best matches the distribution given in equation 2.21 can be found by equating the moments of the two distributions with respect to the $z = 0$ plane. A distribution of n point sources can be represented as a sum of delta

functions,

$$S_{finite} = \sum_{k=0}^n s_k \delta(z - z_k), \quad (2.23)$$

where z_k and s_k are the position and magnitude of the k^{th} point source, respectively. The m^{th} moment of this distribution is given by

$$\int_0^\infty z^m \sum_{k=1}^n s_k \delta(z - z_k) dz = \sum_{k=1}^n s_k z_k^m. \quad (2.24)$$

The corresponding moment of the pencil beam distribution is

$$\int_0^\infty z^m \mu'_s e^{-\mu'_t z} dz = \frac{n! \mu'_s}{\mu_t^{n(n+1)}} = \frac{n! a'}{\mu_t^n}. \quad (2.25)$$

Equating equations 2.24 and 2.25 for $m = 0$ leads to the constraint that the total strength of all the isotropic sources must equal a' . If only one isotropic source is used, the first moment requires it to be placed at $z = 1/\mu'_t$ (Farrell *et al.*, 1992). In the P_3 approximation, Hull and Foster (2001) have modelled the pencil beam with two point sources of equal magnitude. The optimal placement of these sources is at $z_1 = 0$ and $z_2 = 2/\mu'_t$. The resulting distribution of sources matches the dipole and quadrupole moments of the pencil beam.

By removing the constraint requiring the sources to have equal magnitude, it is possible to satisfy the octopole moment as well. The distribution satisfying this condition consists of a source of magnitude $(2 - \sqrt{2}) a'/4$ at $z = (2 + \sqrt{2})/\mu'_t$ and a source of magnitude $(2 + \sqrt{2}) a'/4$ at $z = (2 - \sqrt{2})/\mu'_t$. The distributions for the three cases described here are summarized in table 2.1.

Despite the fact that the model incorporating two sources of unequal magni-

	Pencil Beam	1 source	2 equal sources	2 unequal sources
Magnitude		a'	$a'/2$	$((2 \pm \sqrt{2})/4) a'$
Position		$1/\mu'_t$	$0, (2/\mu'_t)$	$(2 \mp \sqrt{2})/\mu'_t$
Moments: 0	a'	a'	a'	a'
1	a'/μ'_t	a'/μ'_t	a'/μ'_t	a'/μ'_t
2	$2a'/\mu_t'^2$	$a'/\mu_t'^2$	$2a'/\mu_t'^2$	$2a'/\mu_t'^2$
3	$6a'/\mu_t'^3$	$a'/\mu_t'^3$	$4a'/\mu_t'^3$	$6a'/\mu_t'^3$

Table 2.1: Magnitude, position and moments of source distributions used to represent incident pencil beams. Each source model is described in the text. Only the model incorporating two point sources of unequal magnitude is capable of matching the dipole, quadrupole and octopole moments of the pencil beam.

tude matches a higher moment of the collimated source, we have found that it models the resulting fluence and flux distributions in the medium less accurately than the model in which the two sources are equal in magnitude. Similarly, in the diffusion approximation case, Farrell *et al.* (1992) found that a single point source provided a more accurate representation of the beam than a distribution of sources of the form given in equation 2.22. In that study, the failure of the continuous distribution was attributed to the fact that this representation has a large fraction of its weight near the surface. The diffusion approximation and, to a lesser degree, the P_3 approximation are inaccurate near boundaries. Although the equal-source representation places one source on the boundary, this source contains only half of the total source amplitude and is offset by the other source, which is located deeper in the sample. In the case of unequal sources, the larger source, which com-

prises 85% of the source amplitude, is located less than one mean free path from the boundary. Both of the two-source models presented are only approximations of the true source distribution. The choice of which to use should be determined by which provides more accurate expressions for the reflectance recovered from samples similar to those we expect to encounter experimentally. In the following chapters, we have therefore adopted the equal 2-source beam representation.

2.1.5 Detector modelling

The discussion so far has focused on the modelling of light propagation in scattering media. An equally important consideration from the experimental point of view is the collection of light by detectors. For any given detector, we can define a function $\tilde{S}(\mathbf{r}, \hat{s})$ equal to the response of the detector per unit radiance at point \mathbf{r} in direction \hat{s} (Williams, 1991). The value of the response function can be specified in the dimensions of a given detector's readout (*i.e.* mV, counts per second, *etc.*), however we will adopt the convention of defining the response as the intensity of light captured by the detector. The signal R_{det} registered by the detector is given by the integration over all space and solid angle of the product of the radiance and the detector's response function,

$$R_{det}(\mathbf{r}) = \int_{4\pi} \int_V L(\mathbf{r}, \hat{s}) \tilde{S}(\mathbf{r}, \hat{s}) d\Omega d^3\mathbf{r}. \quad (2.26)$$

A typical example in tissue optics is the collection of light by an optical fiber on the sample surface. The fiber can be modelled as a detector which collects radiance at a single point on the surface within a range of angles given by its

numerical aperture. The detector function takes the form

$$\tilde{S}(\mathbf{r}, \hat{s}) = \begin{cases} T_{Fresnel}(\hat{s} \cdot \hat{n})(\hat{s} \cdot \hat{n})\delta(\mathbf{r} - \mathbf{r}_f)\delta(\mathbf{z}) & (\hat{s} \cdot \hat{n}) > \cos(\theta_{NA}) \\ 0 & \text{otherwise,} \end{cases} \quad (2.27)$$

where $T_{Fresnel}(\hat{s} \cdot \hat{n})$ is the Fresnel transmission coefficient for unpolarized light, \hat{n} is the outward normal to the tissue surface, and \mathbf{r}_f and θ_{NA} are the radial position and acceptance angle of the fiber, respectively. The delta functions ensure that only radiance at the fiber's position contributes to its response. The detected signal in this case is given by

$$R_{det}(\mathbf{r}) = \int_{\Omega_{detector}} T_{Fresnel}(\hat{s} \cdot \hat{n})L(\mathbf{r}, \hat{s})(\hat{s} \cdot \hat{n}) d\Omega, \quad (2.28)$$

where $\Omega_{detector}$ is the solid angle defined by the detector's numerical aperture. This expression agrees with that obtained by Kienle and Patterson (1997).

In the diffusion approximation, the expansion of the radiance given in equation 2.5a can be substituted into equation 2.28, giving

$$R_{det}(\mathbf{r}) = C_\Phi \Phi(\mathbf{r}) + C_j j_z(\mathbf{r}), \quad (2.29)$$

where j_z is the z component of the flux, and the constants C_Φ and C_j depend on the index mismatch at the surface and the detector's numerical aperture and are determined by numerical integration. In the P_3 approximation, an analogous approach is taken. The reflectance due to an isotropic point source at depth z_0

can be shown to take the form

$$R_{det}(\mathbf{r}) = \sum_{l=0}^3 \frac{2l+1}{4\pi} \Psi_l(\mathbf{r}) S_l(\mathbf{r}). \quad (2.30)$$

The functions S_0 through S_3 are found by substituting the P_3 radiance expansion (equation 2.12) into equation 2.28 and setting the resulting expression equal to equation 2.30, and are given by

$$S_0 = k_1 \quad (2.31)$$

$$S_1 = k_2 \left(\frac{z_0}{(\rho^2 + z_0^2)^{1/2}} \right) \quad (2.32)$$

$$S_2 = k_3 \left(\frac{3z_0^2}{2(\rho^2 + z_0^2)^{1/2}} \right) + k_4 \left(\frac{3\rho^2}{2(\rho^2 + z_0^2)^{1/2}} \right) - \frac{k_1}{2} \quad (2.33)$$

$$S_3 = k_5 \left(\frac{5z_0^3}{2(\rho^2 + z_0^2)^{3/2}} \right) + k_6 \left(\frac{15z_0\rho^2}{2(\rho^2 + z_0^2)^{3/2}} \right) - \quad (2.34)$$

$$k_2 \left(\frac{3z_0}{2(\rho^2 + z_0^2)^{1/2}} \right), \quad (2.35)$$

where ρ is the projection along the surface of the distance from the detector to the point source, and constants k_1 through k_6 are determined by numerical integration (Hull and Foster, 2001). The total reflectance is found by summing the contributions of all of the real and image sources used to represent the light source.

Previous experiments in our laboratory have used the radial dependence of R_{det} to determine the optical properties of tissue from radially resolved measurements of diffuse reflectance. The spectral analysis of experimental data described

in chapter 4, on the other hand, uses the diffuse reflectance measured at a single source-detector separation and reasonable assumptions about the wavelength dependence of the absorption and scattering coefficients to extract quantitative information about the concentrations of absorbers and scatterers within the turbid medium. The ability of the diffusion, P_3 and diffusion- P_3 hybrid reflectance expressions to model the reflectance resulting from illumination by an optical fiber on the surface of the medium is illustrated in figure 2.2. Source-detector separations of 1.53 mm (2.2(a)) and 0.73 mm (2.2(b)) were investigated. The open symbols in each plot indicate the results of a Monte Carlo simulation in which the source and detector were both modelled as small fibers with 0.22 numerical aperture. A single Monte Carlo simulation was performed with μ'_s equal 1.0 mm^{-1} and μ_a equal to 0.005 mm^{-1} . The distribution of pathlengths travelled by photons collected by the detector was scored. The detected signal at higher values of μ_a was then computed based on this distribution, according to the method of Kienle and Patterson (1996), as detailed in section 2.3.2.

At both source-detector separations, the diffusion approximation overestimates the reflectance over the full range of albedos. This is expected because the diffusion theory is valid only for source-detector separations larger than one transport mean free path and only for high transport albedo. The hybrid solution accurately models the reflectance at high albedo but begins to deviate as the sample becomes more absorbing. Surprisingly, the P_3 approximation models the reflectance less accurately than the hybrid expression at this short source-detector separation. In the fitting described in chapter 4, the transport albedo is expected to be greater than approximately 0.6 except at wavelengths corresponding to the strongest ab-

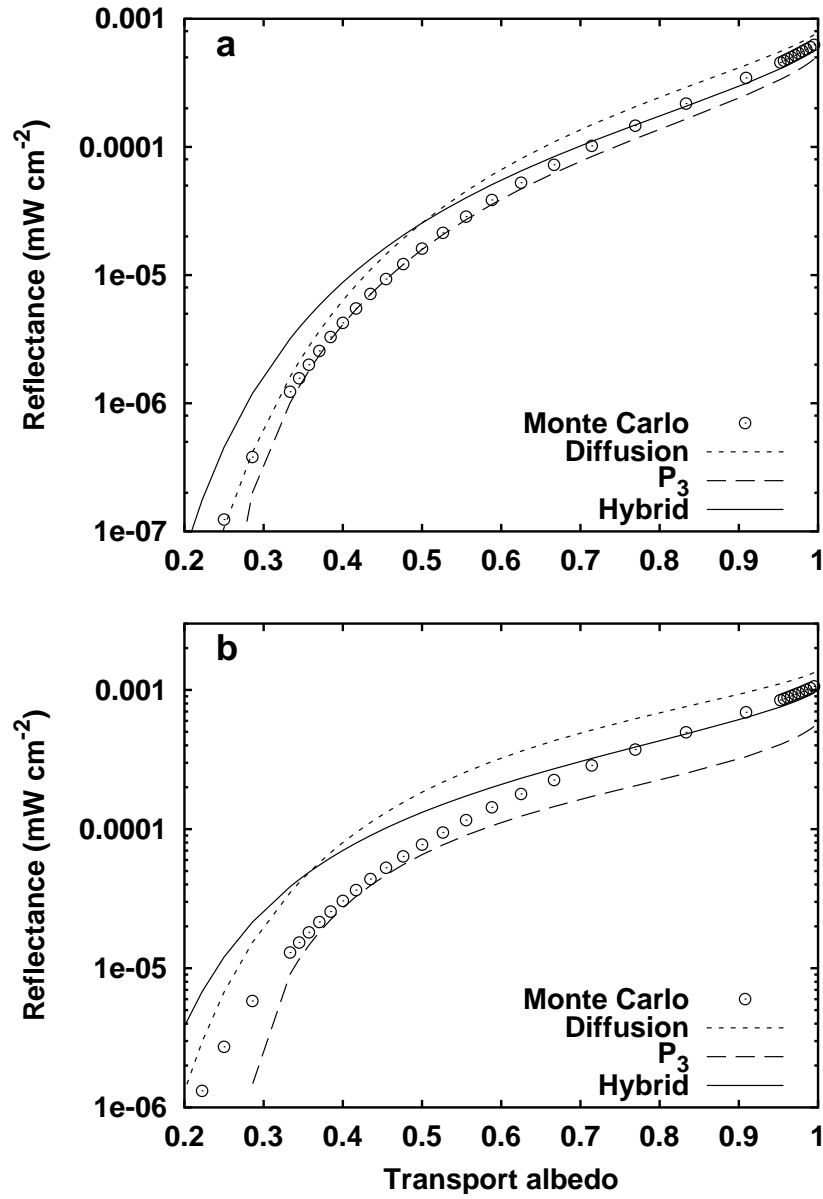


Figure 2.2: Comparison of the diffusion (\cdots), P_3 ($- - -$) and diffusion- P_3 hybrid ($—$) reflectance expressions with the results obtained from Monte Carlo simulation (\circ) for source-detector separations of (a) 1.53 mm and (b) 0.73 mm for a range of transport albedos.

sorption bands of hemoglobin. Over this range of albedo, the hybrid expression provides more accurate results than either the diffusion or P_3 approximations. We will therefore use the diffusion- P_3 hybrid expression in the analysis described in chapter 4.

2.2 Adjoint radiative transport theory

An alternative approach to the modelling of the light collected by a detector is the solution of the adjoint Boltzmann equation (Williams, 1991). Under this formalism, the quantity of interest is the importance $\tilde{L}(\mathbf{r}, \hat{s})$, which describes the probability that a photon moving in direction \hat{s} at position \mathbf{r} will contribute to the signal in a given detector. $\tilde{L}(\mathbf{r}, \hat{s})$ obeys the adjoint Boltzmann equation,

$$-\nabla \cdot \tilde{L}(\mathbf{r}, \hat{s})\hat{s} = -\mu_t \tilde{L}(\mathbf{r}, \hat{s}) + \mu_s \int_{4\pi} \tilde{L}(\mathbf{r}, \hat{s}') f(\hat{s}, \hat{s}') d\Omega' + \tilde{S}(\mathbf{r}, \hat{s}). \quad (2.36)$$

This equation is the time-reversal of the forward Boltzmann equation; solutions to this equation represent the propagation of radiance backward from a detector to its point of origin. The Green's functions of the adjoint equation are identical to those of the forward equation with the exception that the sign of \hat{s} is reversed. The Green's functions in the diffusion and P_3 approximations to adjoint radiative transport can therefore be obtained from those in the corresponding forward radiative transport approximations by reversing the direction of \hat{s} . We will refer to the resulting expressions as the adjoint diffusion and adjoint P_3 approximations. It should be noted that equation 2.36 and the results which follow from it are strictly valid only when the scattering phase function $f(\hat{s}, \hat{s}')$ is invariant under time reversal (Case and Zweifel, 1967). In the following discussion, we will assume that this condition is satisfied, as it is by any phase function which can be written in terms of $(\hat{s} \cdot \hat{s}')$, including the Henyey-Greenstein function.

The usefulness of adjoint formalism arises from the optical reciprocity theorem (Case and Zweifel, 1967), which states that the radiance at position \mathbf{r}_1 and

direction \hat{s}_1 produced by a point source at \mathbf{r}_2 emitting in direction \hat{s}_2 is identical to the radiance produced at position \mathbf{r}_2 and direction $-\hat{s}_2$ produced by a point source at \mathbf{r}_1 emitting in direction $-\hat{s}_1$. In terms of Green's functions, this can be expressed,

$$G(\mathbf{r}_1, \hat{s}_1 \rightarrow \mathbf{r}_2, \hat{s}_2) = G(\mathbf{r}_2, -\hat{s}_2 \rightarrow \mathbf{r}_1, -\hat{s}_1), \quad (2.37)$$

where $G(\mathbf{r}_1, \hat{s}_1 \rightarrow \mathbf{r}_2, \hat{s}_2)$ is the Green's function solution to the Boltzmann transport equation. The radiance L can be expanded in terms of the source distribution and Green's functions as

$$L(\mathbf{r}, \hat{s}) = \int_{4\pi} \int_{V'} S(\mathbf{r}', \hat{s}') G(\mathbf{r}', \hat{s}' \rightarrow \mathbf{r}, \hat{s}) d\Omega' d^3\mathbf{r}'. \quad (2.38)$$

With this expansion, the detected signal (equation 2.26) takes the form

$$R_{det} = \int_{4\pi} \int_V \int_{4\pi} \int_{V'} S(\mathbf{r}', \hat{s}') G(\mathbf{r}', \hat{s}' \rightarrow \mathbf{r}, \hat{s}) \tilde{S}(\mathbf{r}_2, \hat{s}_2) d\Omega' d^3\mathbf{r}' d\Omega d^3\mathbf{r}. \quad (2.39)$$

With the use of equation 2.37, this expression can be rewritten as

$$R_{det} = \int_{4\pi} \int_V \int_{4\pi} \int_{V'} S(\mathbf{r}', \hat{s}') G(\mathbf{r}, -\hat{s} \rightarrow \mathbf{r}', -\hat{s}') \tilde{S}(\mathbf{r}, \hat{s}) d\Omega' d^3\mathbf{r}' d\Omega d^3\mathbf{r}, \quad (2.40)$$

where $G(\mathbf{r}, -\hat{s} \rightarrow \mathbf{r}', -\hat{s}')$ is the Green's function of the adjoint Boltzmann equation. The convolution of the adjoint Green's function with the detector function

\tilde{S} is equal to the importance. Equation 2.40 therefore simplifies to

$$R_{det} = \int_{4\pi} \int_V S(\mathbf{r}, \hat{s}) \tilde{L}(\mathbf{r}, \hat{s}) d\Omega d^3\mathbf{r}, \quad (2.41)$$

which demonstrates that the detected signal can be represented by the integral of the product of the importance and the source distribution.

In the case where both the source and the detector are optical fibers, the adjoint radiative transport solutions in the diffusion and P_3 approximations are identical to the corresponding forward solutions. No advantage is conferred by an adjoint solution in this case. The adjoint solution does offer an advantage over its forward counterpart in cases where the source distribution is complicated and L is expensive to calculate. For example, this formalism has been applied to Monte Carlo simulations of neutron transport where the quantity of interest is the radiance captured by a small detector irradiated by a large extended source (Maynard, 1961; Williams, 1991). In a forward simulation, statistically meaningful results would require that many particles be traced from each point in the extended source. Few of these particles ever reach the detector, with the result that a great deal of computational time is spent tracing particles which do not contribute to the detected signal. In contrast, the adjoint simulation tracks particles backward in time from the detector to their points of origin. In the example presented by Maynard (1961), the source occupies a significant portion of the volume of interest, so a large fraction of the particles traced backward from the detector do in fact originate at the source and therefore contribute to the detected signal. The result is a much more efficient computation of the total signal than could

be obtained using a forward model. Furthermore, unlike the forward model, the adjoint calculation can be performed in the limit where the detector becomes infinitely small and/or has an infinitely narrow acceptance angle.

2.3 Forward-adjoint fluorescence model

In the case of fluorescence in turbid media, the source is a collection of fluorescing molecules distributed throughout the volume of interest. The corresponding source function is given by the rate of generation of fluorescence at a given point in that volume. This in turn is determined by the distribution of excitation light in the medium and by the distribution and photophysical properties of the fluorophores. Because absorption of excitation light by the fluorophore is isotropic, it depends only on the fluence term of the excitation radiance. Similarly, because emission is isotropic, the source function has no angular dependence, and can be written as a function of \mathbf{r} ,

$$S_0(\mathbf{r}) = \mu_{af}(\mathbf{r})\Phi_x(\mathbf{r})\phi_f(\lambda_x/\lambda_m), \quad (2.42)$$

where ϕ_f and μ_{af} are the fluorescence quantum yield and excitation-wavelength absorption coefficient of the fluorophore, respectively, $\Phi_x(\mathbf{r})$ is the fluence of excitation light, and the wavelength ratio (λ_x/λ_m) accounts for the difference in photon energy between the excitation and emission wavelengths. Here and in the following equations, the subscripts x and m indicate functions of the optical properties encountered at the excitation and emission wavelengths, respectively. The dependence of the fluorescence intensity on emission wavelength is contained in the variable ϕ_f , which may be wavelength dependent.

Using the source term of equation 2.42, the adjoint integral becomes

$$\begin{aligned}
 R_{det} &= (\lambda_x/\lambda_m) \int_V \int_{4\pi} \mu_{af}(\mathbf{r}) \Phi_x(\mathbf{r}) \phi_f \tilde{L}_m(\mathbf{r}, \hat{s}) d\Omega d^3r \\
 &= (\lambda_x/\lambda_m) \int_V \mu_{af}(\mathbf{r}) \Phi_x(\mathbf{r}) \phi_f \int_{4\pi} \tilde{L}_m(\mathbf{r}, \hat{s}) d\Omega d^3r \\
 &= (\lambda_x/\lambda_m) \int_V \mu_{af}(\mathbf{r}) \Phi_x(\mathbf{r}) \phi_f \tilde{\Phi}_m(\mathbf{r}) d^3r,
 \end{aligned} \tag{2.43}$$

where $\tilde{\Phi}(\mathbf{r})$ is the positional importance as defined by Crilly *et al.* (1997). The positional importance is the adjoint analog of the fluence, and describes the probability that a photon emitted at \mathbf{r} in any direction will be detected.

Under the assumption that the fluorophores are uniformly distributed and have uniform quantum yield, equation 2.43 can be further simplified, giving

$$R_{det} = (\lambda_x/\lambda_m) \mu_{af} \phi_f \int_V \Phi_x(\mathbf{r}) \tilde{\Phi}_m(\mathbf{r}) d^3r. \tag{2.44}$$

Hence, the fluorescence signal captured from a turbid medium can be determined entirely by the fluence at the excitation wavelength, the positional importance at the emission wavelength and the properties of the fluorophores present in the sample.

2.3.1 Solutions in infinite media

Consider the case of an isotropic point source of excitation light and an isotropic point fluorescence detector in an infinite medium. Because both the source and the detector possess spherical symmetry, Φ_x and $\tilde{\Phi}_m$ depend only on the scalar distance from the source and detector, respectively. In this case, equation 2.44

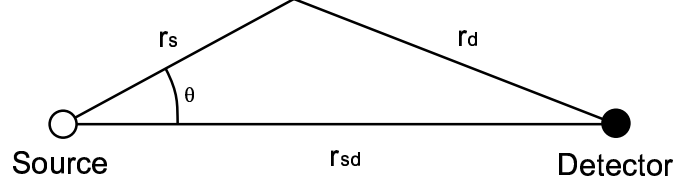


Figure 2.3: Geometry of the forward-adjoint integral for an isotropic point excitation source and an isotropic fluorescence detector embedded in an infinite scattering medium.

can be expressed in spherical coordinates as

$$R_{det} = (\lambda_x/\lambda_m)\mu_{af}\phi_f \int_{r=0}^{\infty} \int_{\theta=0}^{\pi} \int_{\phi=0}^{2\pi} \Phi_x(r_s)\tilde{\Phi}_m(r_d)r_s^2 dr_s d\theta d\phi. \quad (2.45)$$

The geometry of this integral is shown in figure 2.3. The fluence expressions in the diffusion and P_3 approximations can both be expressed as a sum of one or more factors of the form

$$\Phi = C \frac{e^{-br}}{r}. \quad (2.46)$$

Substituting expressions of this form into equation 2.44 yields an expression for the detected signal that is a sum of integrals of the form

$$I = 2\pi C_x C_m \int_{r=0}^{\infty} \int_{\theta=0}^{\pi} \frac{e^{-b_m r_d} e^{-b_x r_s}}{r_s r_d} r_s^2 dr_s \sin \theta d\theta, \quad (2.47)$$

where we have made use of the symmetry of the problem to replace the integral in ϕ with a factor of 2π . Using the law of cosines we can write r_d as $\sqrt{r_{sd}^2 + r_s^2 - 2r_d r_s \cos \theta}$. The terms in equation 2.47 that involve θ and $d\theta$ can

be expressed in terms of r_d and dr_d , allowing the integral in θ to be recast as an integral in r_d . With this transformation, equation 2.47 can be solved analytically, yielding

$$I = \frac{-4\pi C_x C_m}{r_{sd}(b_x^2 - b_m^2)} (e^{-b_m r_{sd}} - e^{-b_x r_{sd}}). \quad (2.48)$$

In the diffusion approximation, the fluence and importance each consist of a single term of the form given in equation 2.46, with C and b equal to $(1/4\pi D)$ and μ_{eff} , respectively. In this case, equation 2.45 reduces to

$$R_{det} = \frac{(\lambda_x/\lambda_m)\phi_f\mu_{af}}{4\pi D_x D_m r_{sd}(\mu_{eff(x)}^2 - \mu_{eff(m)}^2)} (e^{-\mu_{eff(m)} r_{sd}} - e^{-\mu_{eff(x)} r_{sd}}). \quad (2.49)$$

This expression agrees with that derived by Nichols (1996) for the fluorescence fluence in infinite media resulting from a point source of excitation light. Nichols derived his expression by convolving the excitation light distribution with the Green's function for forward propagation of the fluorescence. Because the emission and detection of fluorescence are both isotropic, the optical reciprocity theorem requires that this approach and our forward-adjoint derivation yield the same solution. In the form presented above, equation 2.49 contains a singularity when the values of μ_{eff} at the excitation and emission wavelengths are the same. In this case, L'Hospital's rule yields the limiting case expression,

$$\lim_{\mu_{eff(x)} \rightarrow \mu_{eff(m)}} R_{det} = \frac{(\lambda_x/\lambda_m)\phi_f\mu_{af}}{8\pi D_x D_m \mu_{eff}} (e^{-\mu_{eff} r_{sd}}). \quad (2.50)$$

As the difference in μ_{eff} at the excitation and emission wavelengths approaches zero, equation 2.49 approaches equation 2.50 smoothly and continuously.

In the P_3 approximation, the expressions for the fluence and positional importance each contain one asymptotic and one transient term. C and b are replaced by $(-\nu^-/B^-)$ and ν^- , respectively, for the asymptotic terms and by $(-\nu^+/B^+)$ and ν^+ for the transient terms. R_{det} then takes the form of the sum

$$R_{det} = 4\pi(\lambda_x/\lambda_m)\phi_f\mu_{af} \sum_{i=(+,-)} \sum_{j=(+,-)} \frac{B^i B^j}{\nu_x^i \nu_m^j ((\nu_x^i)^2 - (\nu_m^j)^2) r_{sd}} \left(e^{-\nu_m^j r_{sd}} - e^{-\nu_x^i r_{sd}} \right), \quad (2.51)$$

which includes a total of four terms. The values of B^\pm and ν^\pm are given by equations 2.16 and 2.14, respectively. A limiting expression of the form of equation 2.50 must be employed to resolve the singularity in any term in which ν_x^i and ν_m^j are equal.

To the test the accuracy of the diffusion and P_3 expressions for fluorescence in an infinite medium, we have performed Monte Carlo simulations of fluorescence propagation. The Monte Carlo routine is adapted from published sources (Prah, 1999b; Wang and Jacques, 1994) and incorporates the implicit capture variance reduction mechanism of Prah *et al.* (1989). In this routine, excitation photon packets are launched isotropically from the origin with an initial weight of 1.0 and propagated through the medium. At each scattering event, a portion of the photon's weight is deposited due to absorption, a fluorescence photon packet is created, and the remaining excitation photon weight is scattered. The fluorescence photon packets are propagated by the same method, and the weight they deposit in the sample is recorded. The medium is divided into concentric spherical shells. As the simulation progresses, the total weight of fluorescence photons absorbed within each shell is recorded, as is its standard error. The simulation continues

until the relative uncertainty reaches a preset level. Because the absorption is isotropic, the absorbed power at a given point in the medium is proportional to the fluence at that point and hence to the signal that would be measured by an isotropic detector.

In figure 2.4, the fluorescence signal as a function of source-detector separation determined by Monte Carlo simulation is compared with that predicted by equations 2.49 and 2.51. In both panels, the medium μ_s and g were set at 10 mm^{-1} and 0.9, respectively, at both the excitation and emission wavelengths. In panel (a), μ_a at both wavelengths was 0.01 mm^{-1} . Under these conditions, both the diffusion and P_3 approximations accurately model the fluorescence remote from the excitation source. At distances less than 1 mm from the source, the diffusion approximation begins to break down. The P_3 expression is accurate as close as 0.3 mm from the source. Figure 2.4(b) illustrates the corresponding plots for a medium with μ_a of 1 mm^{-1} at both wavelengths. In this case, the diffusion theory expression overestimates the fluorescence intensity by a factor of 2 even far from the source. The P_3 expression, however, accurately models the fluorescence distribution at all but the closest source-detector separations.

2.3.2 Solutions in semi-infinite media

Like diffuse reflectance measurements, fluorescence measurements are often made using optical fibers to interrogate samples that can be considered semi-infinite. In this case, the expressions for the excitation fluence and the positional importance at the detection wavelength must include the effects of boundaries. The imposition of a boundary breaks the spherical symmetry of the integral in equation 2.77.

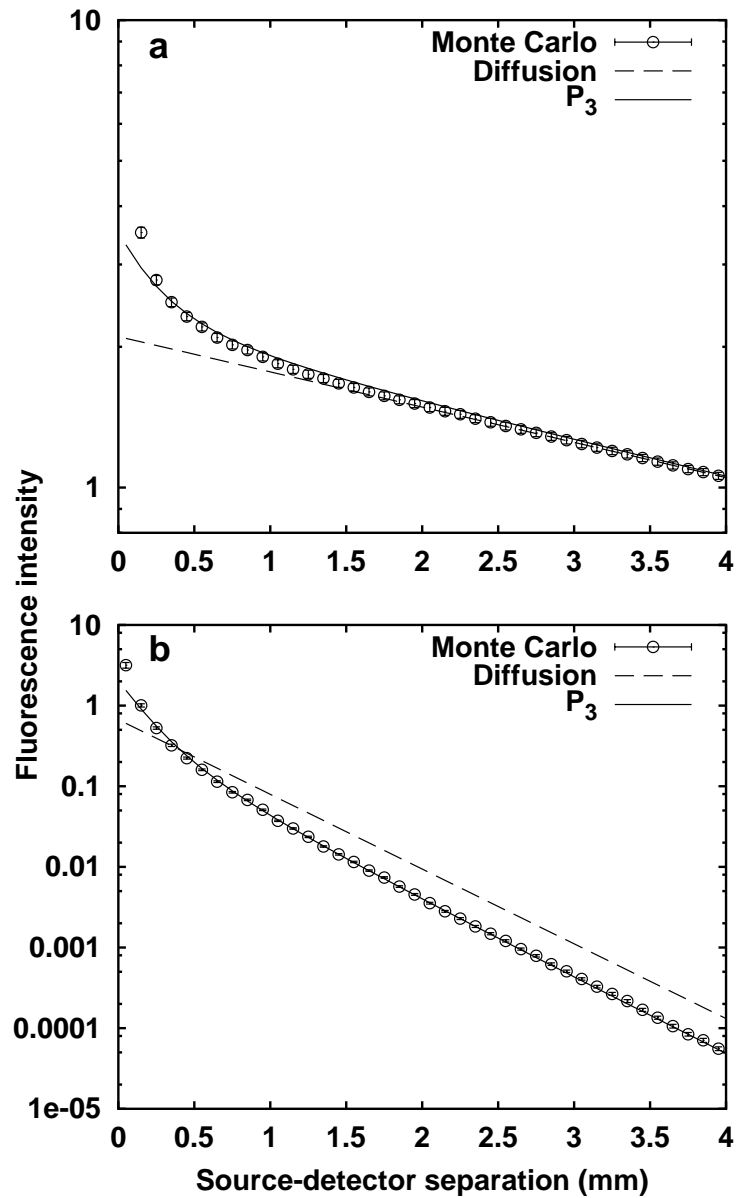


Figure 2.4: Comparison of the forward-adjoint fluorescence expressions in the diffusion and P_3 approximations with the results of Monte Carlo simulation. In each case $\mu_s = 10 \text{ mm}^{-1}$ and $g = 0.9$. μ_a was set to 0.01 (a) or 1 mm^{-1} (b). The P_3 expression offer a significant improvement over the diffusion theory in low-albedo media and near the excitation source.

The integral can be expressed in cylindrical coordinates, however in this case, the dependence on r_d and the integral over θ cannot be collapsed into a single integral. Numerical integration is therefore required to evaluate the detected signal in the semi-infinite geometry.

A further difficulty arises from the fact that the representation of beams as point sources is only approximate. Modelling of a beam as a sum of point sources provides accurate expressions for the reflectance only at points sufficiently distant from the source. In a study comparing radiative transport-derived reflectance expressions with Monte Carlo simulations, Wang and Jacques (2000) found that the greatest source of error in the diffusion approximation expression arose from the representation of the beam. This difficulty is compounded in the case of forward-adjoint integral, which requires integration over a volume that includes regions immediately adjacent to the source. In the case of a normally incident pencil beam, the fluence immediately beneath the beam is not well modelled by a finite number of point sources.

An alternative strategy is the use of scaled Monte Carlo simulation. The scaling of a single Monte Carlo simulation of light propagation in tissue for the fitting of diffuse reflectance measurements was investigated by Kienle and Patterson (1996), whose model we have adapted to the forward-adjoint case and whose method is presented here. Although this method was originally developed to model the diffuse reflectance collected at the sample surface, it is equally applicable to the determination of the fluence at any position within a turbid medium.

The first step in the scaled Monte Carlo method is to use a Monte Carlo simulation to generate a reference fluence distribution, which will serve as the

basis for computing the fluence in media with arbitrary optical properties. This reference simulation propagates photons through the medium and records the fluence as a function of position and photon pathlength. The results of this simulation can be used to calculate the fluence in a medium with arbitrary μ_s by a linear scaling of the dimensions of the fluence distribution. Let $\Phi_{MC}(\rho, z, l)$ be the fluence distribution obtained from a Monte Carlo simulation performed with scattering coefficient $\mu_{s_{MC}}$, expressed as function of position (ρ, z) and pathlength l . Then the fluence Φ for arbitrary μ_s is given by

$$\Phi(\rho, z, l) = c^3 \Phi_{MC}(c\rho, cz, cl), \quad (2.52)$$

where the scale factor c is equal to $(\mu_s/\mu_{s_{MC}})$, and reflects the fact that Φ and Φ_{MC} are identical when ρ , z , and l are expressed in units of the scattering mean free path. The factor of c^3 results from the fact that fluence has dimensions of energy per unit area per unit time. The scaling of the area gives a factor of c^2 , and the scaling of time gives another factor of c . The results of equation 2.52 assume that all the dimensions of the problem are scaled, including the values of μ_a and μ'_s . The values of dimensionless constants such as the albedo and the scattering anisotropy are therefore unchanged by the scaling.

The scaled Monte Carlo method is not limited to media with the same albedo as the reference simulation. The fluence in media with arbitrary μ_a can be calculated by the application of Beer's Law. In the case of transmission through a non-scattering medium of thickness t , Beer's law states that the fluence transmitted

through the sample is given by

$$\Phi = \Phi_0 e^{-\mu_a t}, \quad (2.53)$$

where Φ_0 is the incident fluence. In scattering media, there are an infinite number of possible paths photons may take from the source to any given point in the tissue. In this case, Beer's Law takes the form

$$\Phi(\rho, z) = \int_{l=0}^{\infty} \Phi_0(\rho, z, l) e^{-\mu_a l} dl, \quad (2.54)$$

where $\Phi_0(\rho, z, l)$ is the fluence per unit pathlength due to photons that would reach the point (ρ, z) after traversing a total distance l within the sample in the absence of absorption. The reference Monte Carlo simulation, scaled as described above, can provide $\Phi_0(\rho, z, l)$. The fluence distribution at arbitrary μ_a and μ'_s can then be calculated by

$$\Phi(\rho, z) = \int_{l=0}^{\infty} c^3 \Phi_{MC}(c\rho, cz, cl) e^{-(\mu_a - c\mu_{a_{MC}})l} dl, \quad (2.55)$$

where c is the scaling constant equal to $(\mu_s/\mu_{s_{MC}})$, and $\mu_{a_{MC}}$ is the absorption coefficient used in the reference simulation. The positional importance takes an identical form and can be derived from the same Monte Carlo simulation.

The fluorescence signal in the forward-adjoint model is given by the volume integral of the product of the fluence and the positional importance. In terms of

pathlength integrals, equation 2.44 takes the form

$$R_{det} = (\lambda_x/\lambda_m)\mu_{af}\phi_f \int_V \int_{l_x}^{\infty} \int_{l_m}^{\infty} \Phi_x(\rho, z, l_x) \tilde{\Phi}_m(\rho, z, l_m) dl_m dl_x d^3r. \quad (2.56)$$

Substituting the scaled Monte Carlo expressions for $\Phi_x(\rho, z, l_x)$ and $\tilde{\Phi}_m(\rho, z, l_m)$ gives

$$\begin{aligned} R_{det} = (\lambda_x/\lambda_m)\mu_{af}\phi_f \int_{l_x}^{\infty} \int_{l_m}^{\infty} \int_V c_x^3 c_m^3 \\ \Phi_{MC}(c_x\rho, c_x z, c_x l_x) e^{-(\mu_{ax} - c_x \mu_{aMC})l_x} \\ \Phi_{MC}(c_m\rho, c_m z, c_m l_m) e^{-(\mu_{am} - c_m \mu_{aMC})l_m} d^3r dl_x dl_m, \end{aligned} \quad (2.57)$$

where c_x and c_m are the scaling factors at the excitation and emission wavelengths, respectively. This expression is computationally intensive in that it involves the evaluation of a 5-dimensional integral. In order to simplify the process of calculating R_{det} , we define the function $R_{det MC}(l_x, l_m)$ equal to the fluorescence signal contribution from photons that travel a distance l_m prior to detection and that are excited by photons that travel a distance l_x prior to generating fluorescence under the conditions of the reference Monte Carlo simulation. $R_{det MC}(l_x, l_m)$ is given by

$$\begin{aligned} R_{det MC}(l_x, l_m) = (\lambda_x/\lambda_m)\mu_{af}\phi_f \int_V c_x^3 c_m^3 \\ \Phi_{MC}(c_x\rho, c_x z, c_x l_x) \Phi_{MC}(c_m\rho, c_m z, c_m l_m) d^3r. \end{aligned} \quad (2.58)$$

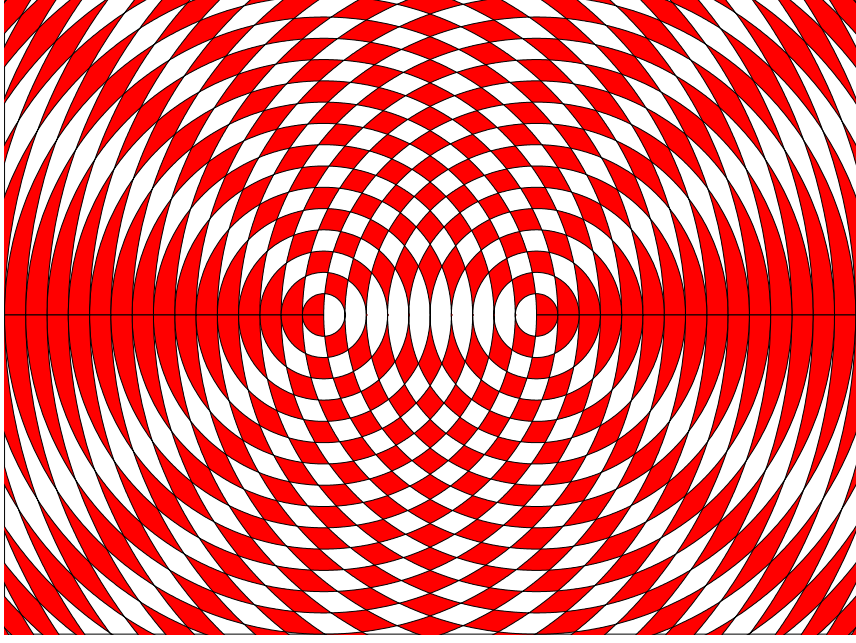


Figure 2.5: Division of sample volume into annular bins for the scaled Monte Carlo forward-adjoint calculations. Each bin consists of the intersection of an annulus centered on the source position and another centered on the detector position. In the figure, alternating bins are shaded for clarity.

This integral can be cast in terms of the depth z and the cylindrical distances from the source and detector, ρ_s and ρ_d , respectively. This has the effect of dividing the volume into bins consisting of the intersections of annuli centered at the source and detector, as illustrated in figure 2.5. The resulting expression is

$$R_{det\ MC}(l_x, l_m) = (\lambda_x/\lambda_m)\mu_{af}\phi_f \int_{\rho_s=0}^{\infty} \int_{\rho_d=0}^{\infty} \int_{z=0}^{\infty} c_x^3 c_m^3 \Phi_{MC}(c_x \rho, c_x z, c_x l_x) \Phi_{MC}(c_m \rho, c_m z, c_m l_m) a(\rho_s, d\rho_s, \rho_d, d\rho_d) dz, \quad (2.59)$$

where $a(\rho_s, d\rho_s, \rho_d, d\rho_d)$ is the area of intersection of annuli of radii ρ_s and ρ_d and thicknesses $d\rho_s$ and $d\rho_d$ centered on the source and detector, respectively. The function a accounts for the dependence of the fluorescence signal on the source-detector separation. In practice, the reference Monte Carlo simulation is computationally expensive and the fluence can be recorded for only a finite number of values of ρ, z and l . The integral in equation 2.59 must therefore be approximated by a summation. Instead of scaling the arguments of Φ_{MC} , which would require either interpolation or multiple Monte Carlo simulations, we scale the variables of integration. Implementing this scaling and replacing the integral with a summation gives the approximation

$$\begin{aligned}
 R_{det\ MC}((1/c_x)l_x, (1/c_m)l_m) \approx \\
 (\lambda_x/\lambda_m)\mu_{af}\phi_f \sum_i \sum_j \sum_k c_x^3 c_m^3 \Phi_{MC}(\rho_i, z_k, l_x) \Phi_{MC}(\rho_j, (c_m/c_x)z_k, l_m) \\
 a((1/c_x)\rho_i, (1/c_x)\Delta\rho_i, (1/c_m)\rho_j, (1/c_x)\Delta\rho_j) \Delta z_k, \quad (2.60)
 \end{aligned}$$

where z_k and Δz_k are the depth and thickness of the k^{th} depth bin, respectively, and the ρ and $\Delta\rho$ variables are the radii and thicknesses of the corresponding radial bins. Interpolation is required to obtain $\Phi_{MC}(\rho_j, (c_m/c_x)z_k, l_m)$, however the interpolation is in only the z dimension, making it relatively computationally efficient.

Equation 2.60 can be used to build up a library of $R_{det\ MC}$ matrices for a range of scattering coefficients and source-detector separations. The fluorescence signal at a given source-detector separation in the case of arbitrary absorption

coefficients is then approximated by the sum

$$\begin{aligned}
 R_{det} \approx \sum_i \sum_j R_{det\ MC}((1/c_x)l_{xi}, (1/c_m)l_{mj}) \\
 \exp[(1/c_x)l_{xi}(\mu_{ax} - (c_x)\mu_{a_{MC}})] \\
 \exp[(1/c_m)l_{mi}(\mu_{am} - (c_m)\mu_{a_{MC}})]\Delta l_{xi}\Delta l_{mi}. \quad (2.61)
 \end{aligned}$$

The fluorescence signal in media with arbitrary μ_s and μ_a at both the excitation and emission wavelengths can be found using equation 2.61. Signal from media whose μ_s is not included in the library of $R_{det\ MC}$ matrices can be found by linear interpolation. As noted previously, the scaling of the fluence and positional importance distributions has no effect on dimensionless quantities. This includes the scattering anisotropy and the numerical apertures of the source used in the reference Monte Carlo simulation. Additional simulations are required to evaluate the effects of changing these parameters. In the applications described in chapter 5, we have matched the numerical aperture in the reference simulation to that of our source and detector fibers, 0.22. We have also assumed a constant scattering anisotropy of 0.9. While it is likely that many tissues and tissue-simulating phantoms may exhibit anisotropies that deviate from this value, it is also likely that similarity relations will ensure that the anisotropy has little effect on the fluence distribution except through its effect on μ'_s . Because constant g is assumed, the scaling described above with respect to μ_s can be expressed equivalently in terms of μ'_s .

The choices of optical properties and tissue dimensions to use for the refer-

ence Monte Carlo simulation are determined by the conditions under which the fluorescence signal must be calculated. In the case of tissue and tissue-simulating phantoms, μ'_s is generally expected to be approximately 0.5 to 5 mm⁻¹. We have therefore chosen to perform the reference simulation with $\mu_{s_{MC}}$ of 10.0 mm⁻¹ and g of 0.9, for a μ'_s of 1.0 mm⁻¹. For the cases in which we wish to calculate fluorescence signal, we do not expect the value of μ_a to be less than 0.001 mm⁻¹. We can therefore set $\mu_{a_{MC}}$ to 0.001 mm⁻¹ without losing important information at long pathlengths. In general, it is advantageous to use as high a value of $\mu_{a_{MC}}$ as possible to increase the speed of the reference Monte Carlo simulation. Finally, the volume of tissue included in the simulation must be determined. Near the source and at short path length, the distribution of fluence changes rapidly. It is therefore desirable to sample the fluence at the shortest practical intervals. Because the signal at low μ_a may include contributions from volumes far from the source or detector and from photons with large pathlengths, it is advantageous to extend the matrix which records the fluence to include the largest practical volume and pathlength. The difficulty in satisfying both of these conditions is that the resulting matrices can become impractically large. To address this problem, we have modified our Monte Carlo routine to use bins whose size increases linearly with increasing ρ , z and l . Hence, the regions where the fluence changes most rapidly are sampled frequently, and a large volume of the ρ , z , l space is included. The only effect on the derivation outlined above is that Δz , $\Delta \rho$ and Δl are not constant.

2.4 Absorber packaging effects

In the derivation of diffuse reflectance and fluorescence expressions presented in this chapter, we have assumed that a medium's absorption coefficient is directly proportional to the concentration of absorber in the medium. Specifically,

$$\mu_a = N\sigma_a, \quad (2.62)$$

where N is the number density of absorber molecules and σ_a is the absorption cross section of each absorber molecule. The linearity of equation 2.62 is essential to the practice of absorption spectrophotometry and to the ability of diffuse reflectance and fluorescence expressions outlined above to relate the concentration of absorbers to measured signals. Equation 2.62 assumes that the absorber molecules are homogeneously distributed throughout the sample. This assumption is valid in the case of solutions and for suspensions in which the size of the absorbing particles is sufficiently small.

Tissues and tissue simulating phantoms containing erythrocytes, however, represent a special case; they consist of a bulk sample that is free of absorber mixed with a small volume of particles in which the absorber is concentrated. The effective μ_a of such a suspension is lower than that found by substituting the mean number density of hemoglobin molecules into equation 2.62. This 'pigment packaging' effect was first investigated by Duysens (1956) in the context of assessing the absorption coefficient of chlorophyll in photosynthetic cells. That study provided a detailed quantitative model of the effect of pigment packaging on the measured absorption spectrum, which we have adopted in the following discussion.

We first consider a nonscattering suspension of depth l illuminated by a beam of area A . In the simplest case, the suspension consists of a single particle of area a_p and volume v_p . We define the particle transmission T_p as the fraction of light incident on the particle that is transmitted through it. The total transmission through the sample T_1 consists of a fraction of the beam $(A - a_p)/A$ that misses the particle and a fraction a_p/A that strikes it. The expression for T_1 is given by

$$T_1 = (A - a_p)/A + (a_p/A) T_p = 1 - (a_p/A)(1 - T_p). \quad (2.63)$$

Equation 2.63 can be generalized to a suspension with an arbitrary number of particles. If the suspension is composed of N identical particles per unit volume, then the total number of particles in the volume interrogated by the beam is NAl . The transmission through the entire sample is the product of the transmissions through NAl single-particle suspensions,

$$T = (T_1)^{NAl}. \quad (2.64)$$

Equation 2.64 is essentially a statement of Beer's law, which is valid for suspensions as long as the fractional volume occupied by absorbing particles is small (Duyssens, 1956). The effective absorption coefficient of the suspension $\mu_a(sus)$ is found by solving the equation

$$I = I_0 e^{-\mu_a(sus)l} = I_0 T, \quad (2.65)$$

yielding

$$\mu_a(sus) = -NA \ln [1 - (a_p/A)(1 - T_p)] \approx Na_p(1 - T_p), \quad (2.66)$$

where the approximation is valid when $(a_p/A) \ll 1$. In practice, this requirement is satisfied for suspensions in which the volume fraction occupied by absorbing particles is much less than one. In tissues and tissue simulating phantoms, erythrocytes occupy approximately 1.6% of the total volume. As expected, $\mu_s(sus)$ depends linearly on the number density of absorbing particles and is independent of the geometry of the beam.

By comparison, the absorption coefficient of a solution containing the same number of absorber molecules $\mu_a(sol)$ is given by

$$\mu_a(sol) = \mu_a \frac{V_{Particles}}{V_{Total}} = \mu_a \frac{NA v_p}{Al} = \mu_a N v_p, \quad (2.67)$$

where μ_a is the absorption coefficient within each particle, and $V_{Particles}/V_{Total}$ is the volume fraction occupied by absorbing particles. Combining equations 2.66 and 2.67, we obtain the expression for the distortion of the spectrum due to pigment packaging,

$$Q = \frac{\mu_a(sus)}{\mu_a(sol)} = (1 - T_p) \frac{a_p}{v_p \mu_a}. \quad (2.68)$$

It is evident from equation 2.68 that the distortion due to pigment packaging is highly dependent on the absorption coefficient within the particles and on the particle size. On the other hand, Q is independent of particle concentration. Hence, if the particle size and absorption coefficient inside the particles is known, a single

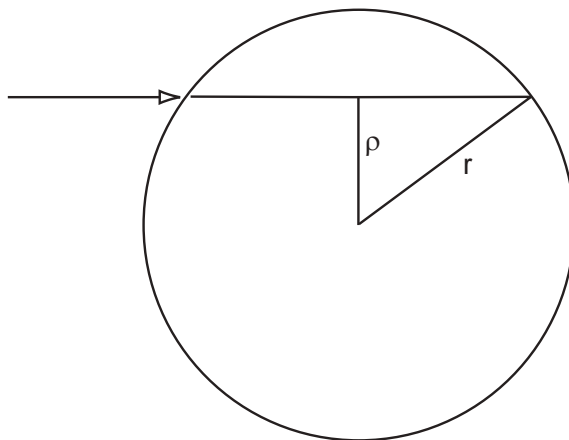


Figure 2.6: Geometry of a single spherical absorbing particle. The probability of transmission of a photon incident on the particle (arrow) is determined by the pathlength it travels through the particle, which is in turn determined by the distance ρ between its point of incidence and the central axis of the sphere.

distorted spectrum can be constructed. The effective μ_a of any suspension can then be found by multiplying the distorted spectrum by the particle concentration, which will be proportional to the bulk average absorber concentration.

To determine the distorted spectrum, some prior knowledge of the size and shape of the absorbing particles is required. For simplicity, we consider spherical particles of radius r . In this case, (a_p/v_p) is equal to $(3/4r)$. The transmission through a particle depends on the length of the photon path through it, which in turn depends on the position on the face of the particle where the photon is incident, as illustrated in figure 2.6. The mean transmission can be found by

integrating the transmission over the cross section of the absorber, giving

$$T_p = \frac{1}{a_p} \int_0^r 2\pi\rho e^{-2\mu_a\sqrt{r^2-\rho^2}} d\rho = \frac{2}{(2\mu_a r)^2} [1 - (2\mu_a r + 1) e^{-2\mu_a r}] , \quad (2.69)$$

where $(2\mu_a r)$ is the optical depth of the particle as defined by Duysens (1956). Equations 2.68 and 2.69 allow calculation of the flattening of the absorption spectrum of hemoglobin in erythrocytes relative to its spectrum in clear solution. To calculate the magnitude of this effect, we make the following assumptions. Erythrocytes can be approximated by spheres of radius $5\text{ }\mu\text{m}$ occupying 1.6% of the total sample volume. In figure 2.7(a), the value of Q resulting from this geometry is plotted as a function of the μ_a of the absorbing particles. In tissue, the volume-averaged hemoglobin concentration is approximately $50\text{ }\mu\text{M}$. Because erythrocytes comprise only 1.6% of the tissue volume, each must contain a hemoglobin concentration of approximately 3.1 mM . The value of Q as a function of wavelength resulting from this hemoglobin concentration is shown in figure 2.7(b).

In figure 2.8, the absorption spectra of $50\text{ }\mu\text{M}$ hemoglobin in clear solution is compared with the flattened spectrum resulting from the same volume-averaged concentration being confined to $10\text{ }\mu\text{m}$ -diameter spherical particles, as given by equations 2.68 and 2.69. Both plots are based on hemoglobin spectra taken from several sources (Prahl, 1999a; Van Assendelft, 1970; Wray *et al.*, 1988; Zijlstra *et al.*, 1991), as described in section 4.2.2.1. At wavelengths greater than 650 nm , the absorption cross section of hemoglobin is relatively small, and the packaging of hemoglobin in the erythrocytes distorts the absorption spectrum by less than

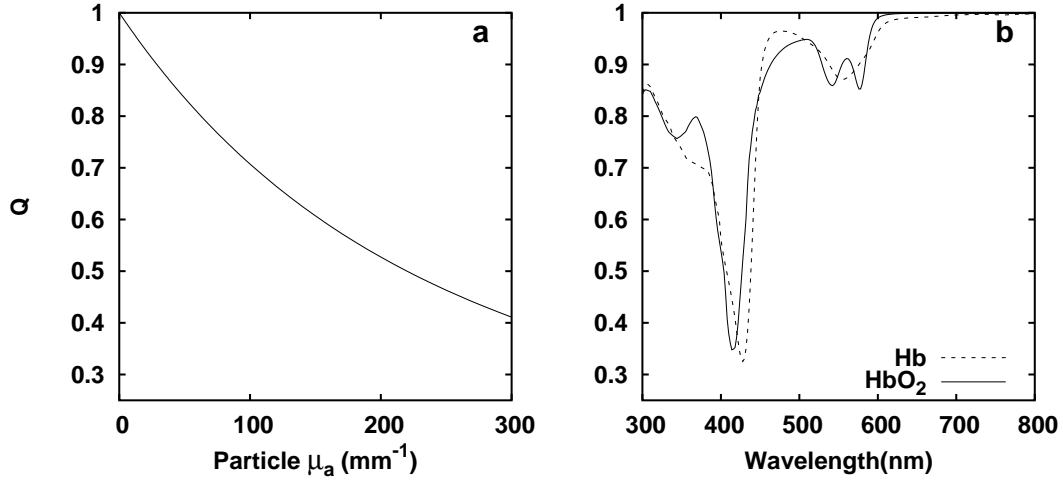


Figure 2.7: Value of Q resulting from the packaging of an absorber into a 1.6% suspension of $10\ \mu\text{m}$ diameter spherical particles, plotted as a function of (a) the μ_a of the absorbing particles and (b) wavelength for the specific case of deoxy (---) and oxy (—) hemoglobin. A mean hemoglobin concentration in the medium of $50\ \mu\text{M}$ was assumed. As defined in equation 2.68, Q is the ratio of the μ_a of the suspension to that of a solution with the same mean absorber concentration.

1%. The distortion in the visible absorption peaks is as great as 15% and can exceed 65% in the Soret absorption band.

The preceding derivation did not take into account the effects of the scattering of light within the sample. The experiments described in the remainder of this work are confined to samples in which scattering plays a significant role in the transport of light. It is apparent from equation 2.68, however, that the distortion of the absorption spectrum due to pigment packaging is independent of the beam geometry and of the length of the path taken through the tissue. The same distortion derived above for the case of clear solutions will therefore apply to scattering solutions.

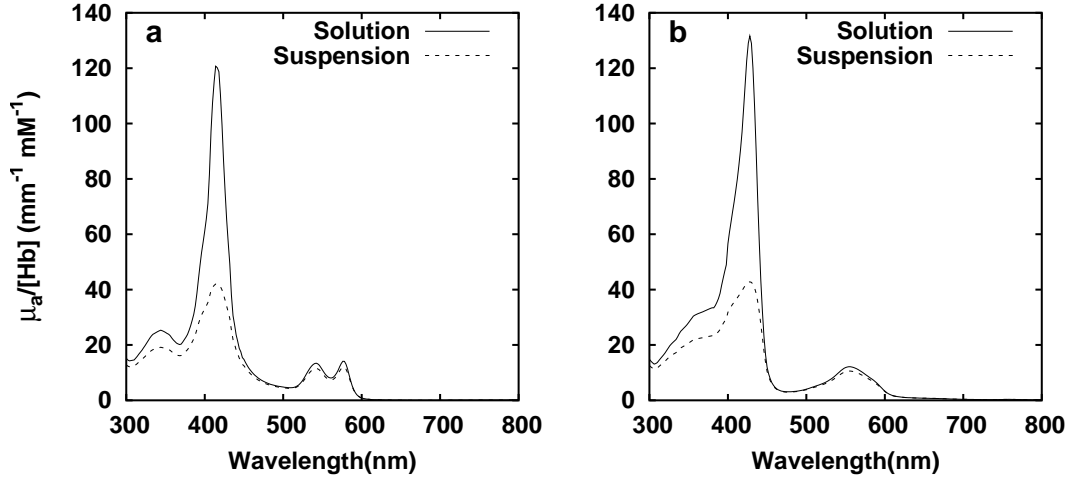


Figure 2.8: Comparison of the spectra of hemoglobin in solution and suspension for (a) oxy- and (b) deoxyhemoglobin. In each case, the millimolar absorption coefficient of $50 \mu\text{M}$ hemoglobin in clear solution (—) is compared with that of a suspension where hemoglobin at the same mean concentration is sequestered into spherical particles of diameter $10 \mu\text{m}$ (- - -).

In chapters 4 and 5, we make use of algorithms that are informed by the known absorption spectra of oxy- and deoxyhemoglobin to extract information about optical properties from measurements of diffuse reflectance and fluorescence collected from tissue and tissue-simulating phantoms. It is essential to include the effects of pigment packing when specifying the absorption basis spectra used by the fitting routine. In those chapters, it is shown that ignoring this effect can lead to significant underestimation of the reflectance and a corresponding overestimation of the extent to which fluorescence emission spectra are distorted by hemoglobin absorption, especially at short wavelengths.

2.5 Spectral analysis and fitting techniques

Problems involving fitting a theoretically derived model to an observed set of data can be characterized as either linear or nonlinear. The defining characteristic of the linear problem is a model which approximates the measured data as a linear superposition of known basis functions. The fitting of fluorescence spectra in chapter 3, polynomial fitting and linear regression are all examples of linear fitting problems. In addition, some problems which appear nonlinear, such as the extraction of the Hill parameters of hemoglobin from saturation measurements demonstrated in chapter 4, can be converted to a linear form, allowing linear fitting techniques to be applied. In the case where the model cannot be recast in linear form, iterative fitting techniques are required. The linear and nonlinear fitting routines used in the remainder of this thesis are outlined in the following sections.

2.5.1 Singular value decomposition fitting

The linear least squares fitting problem consists of modelling a measured data vector \mathbf{y} as a linear combination of the columns of a basis matrix \mathbf{X} ,

$$\mathbf{y} \approx \mathbf{X}\mathbf{a}, \tag{2.70}$$

where the elements of the vector \mathbf{a} are the amplitudes of the basis vectors to be determined by the fit. In order to incorporate the measurement uncertainty into

the fit, it is useful to define a design matrix \mathbf{A} and a vector \mathbf{b} according to

$$\mathbf{A} = \begin{bmatrix} 1 \\ \frac{1}{\sigma} \end{bmatrix} \mathbf{X} \quad (2.71a)$$

and

$$\mathbf{b} = \begin{bmatrix} 1 \\ \frac{1}{\sigma} \end{bmatrix} \mathbf{y}, \quad (2.71b)$$

where $\begin{bmatrix} 1 \\ \frac{1}{\sigma} \end{bmatrix}$ is a diagonal matrix whose elements are the uncertainties measured at each data point. The incorporation of $\begin{bmatrix} 1 \\ \frac{1}{\sigma} \end{bmatrix}$ ensures that data points with large uncertainty constrain the fit less than those with small uncertainty. The best fit is that which minimizes χ^2 , defined by

$$\chi^2 = \|\mathbf{A}\mathbf{a} - \mathbf{b}\|^2. \quad (2.72)$$

The classical least squares (CLS) solution is obtained by setting the derivative of equation 2.72 with respect to \mathbf{a} equal to zero and solving the resulting set of equations to find the minimum of χ^2 . This solution works adequately in selected circumstances, however in cases where \mathbf{A} is nearly singular, the CLS solution will often give a solution in which combinations of basis spectra are given large amplitudes of opposite sign, with the result that they contribute very little to the minimization of χ^2 .

2.5.1.1 SVD Fitting Algorithm

Singular value decomposition fitting is a linear fitting algorithm which is superior to classical least squares algorithms in cases where the basis vectors being fit are

non-orthogonal. The algorithm described here is based on that of Press *et al.* (1992), whose notation we have adopted. The singular value decomposition of the matrix \mathbf{A} is defined by the equation

$$\mathbf{A} = \mathbf{U}\mathbf{w}\mathbf{V}^T, \quad (2.73)$$

where \mathbf{U} is an orthogonal matrix, \mathbf{V}^T is the transpose of the orthogonal matrix \mathbf{V} and the matrix \mathbf{w} is a diagonal matrix whose elements are known as the singular values of the decomposition. In the linear fitting problem, the amplitudes of the basis vectors are given by

$$\mathbf{a} = \mathbf{V}\mathbf{m}\mathbf{U}^T\mathbf{b}, \quad (2.74)$$

where \mathbf{m} is the diagonal matrix whose elements are the inverses of the corresponding elements of \mathbf{w} . The variances in the amplitude are equal to the diagonal elements of the matrix \mathbf{v}_a , given by

$$\mathbf{v}_a = \mathbf{V}\mathbf{m}\mathbf{m}\mathbf{V}^T. \quad (2.75)$$

The uncertainty in each amplitude is found by taking the square root of the corresponding variance found in equation 2.75. These equations give the same results as the CLS solution and are equally subject to the difficulties introduced by a singular or nearly singular fitting matrix. This problem can be avoided by replacing the matrix \mathbf{m} with a modified singular value matrix \mathbf{m}^* whose elements

are given by

$$\mathbf{m}^*_i = \begin{cases} 1/\mathbf{w}_i, & \mathbf{w}_i > w_{max}\gamma_{tol} \\ 0, & \mathbf{w}_i < \mathbf{w}_{max}\gamma_{tol} \end{cases}, \quad (2.76)$$

where w_{max} is the largest element of \mathbf{w} , and γ_{tol} is a predetermined cutoff tolerance. The application of equation 2.76 removes basis vectors from the fit if their corresponding singular values are too small, *i.e* if they do not contribute sufficiently to the reduction of χ^2 . The effect of varying γ_{tol} is illustrated by a plot of $\|\mathbf{a}\|$ versus χ^2 , known as an L-curve (Hansen, 1994). The L-curve for a typical fitting problem is illustrated in figure 2.9. The specific data used to produce figure 2.9 came from an *in vivo* fluorescence emission spectrum being fit as a sum of the spectra of known fluorophores as described in chapter 3, however the characteristics of the L-curve are not unique to this problem. When the amplitude constraint is very loose (γ_{tol} very small), the result is the CLS solution (Press *et al.*, 1992). Conversely, an overly stringent amplitude constraint (large γ_{tol}) forces the amplitudes of all the basis vectors to zero, at the obvious expense of χ^2 . The ideal choice of γ_{tol} is that which results in a fit as close as possible to the lower left corner of the L-curve. In practice, the choice of the cutoff is relatively forgiving, and fits resulting from inappropriate constraints are obvious.

In the cases where many basis vectors are involved in the fit, it may be desirable to specify *a priori* those basis vectors which are the expected to be the most important to the fit and to make them less likely to be truncated by the SVD algorithm. This is accomplished by multiplying each basis vector by a predetermined weight. Those vectors given large weight require only small amplitudes

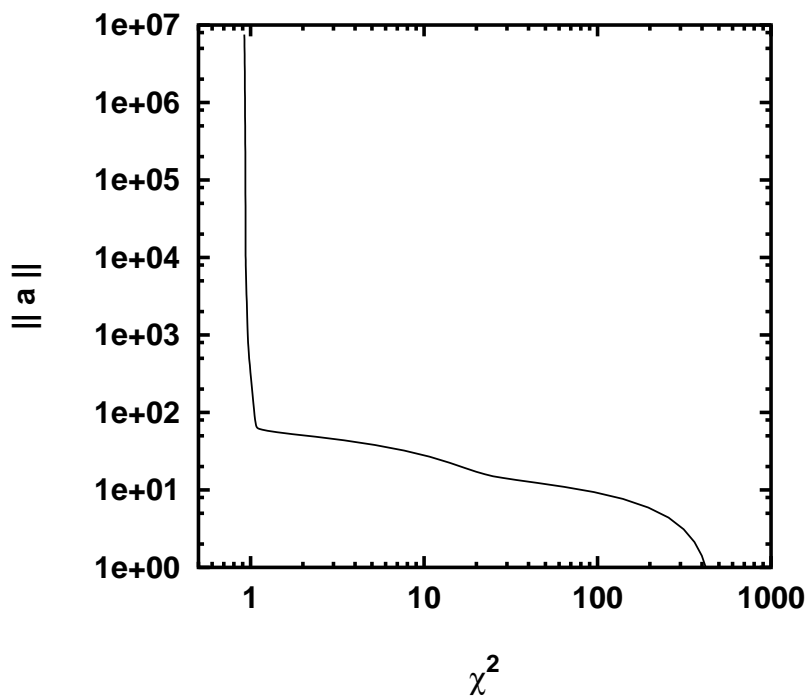


Figure 2.9: The L-curve of a typical SVD fitting problem. As more basis vectors are truncated, $\|a\|$ decreases, while a good fit is maintained. If basis vectors necessary to the fit are truncated, $\|a\|$ is further decreased, but at the expense of χ^2 . The curve shown is that derived from a typical *in vivo* fluorescence spectrum, as described in chapter 3.

to contribute significantly to the fit, so they are unlikely to cause $\|a\|$ to become large enough to trigger truncation. Conversely, vectors with small weight will contribute significantly to the fit only if the elements of \mathbf{a} to which they correspond are very large, making them more likely to be truncated. It should be noted that the influence of the weighting is limited to cases where the SVD amplitude con-

straint is sufficiently strict to cause truncation of the less important basis vectors.

In the CLS case, the weights have no effect.

2.5.1.2 Fourier Series

In the spectral analysis described in chapter 3, the basis vectors are the spectra of known fluorophores that are expected to contribute to the *in vivo* fluorescence emission. A 61-term Fourier synthesis is also included in the analysis in order to account for the possible presence of other spectral contributions and to account for changes in autofluorescence that occur during the experiment. The weighting of a Fourier series always implies some prior knowledge. In this case, the emission spectrum is expected to be well approximated by a sum of Lorentzian peaks. The N-term Fourier series which provides the best fit to any spectrum is given by the spectrum's N-term Fourier expansion, which is a finite approximation to the spectrum's Fourier transform. The Fourier transform of a Lorentzian is a decreasing exponential, so it is reasonable to make the weights of the Fourier components decrease exponentially with increasing wavenumber. An additional benefit of this scheme, especially when it is used for determining the spectra of unknown fluorophores, is that the low relative weighting of the higher frequency terms has the effect of filtering out high-frequency noise from the measured data.

Ideally, the relative weighting of the basis vectors should reflect their expected contributions to the measured data. In the analysis reported in chapter 3, the basis spectra are given a weight of 100. The most heavily weighted term in the Fourier synthesis is the constant term, with an initial weight of 2. These values provide reliable fits to all the data presented, but their exact values are not critical.

In fact, while it is important to give the Fourier terms a small weighting relative to those of the basis vectors, the SVD fits are remarkably insensitive to the relative weighting assigned among the various basis spectra themselves. To summarize, the basis spectra and the Fourier series are fit to the fluorescence data, f_{Total} , using the following equation,

$$f_{Total}(\lambda) = \sum_{i=1}^N A_i(100)f_i(\lambda) + (2.0)B_0 + \sum_{k=1}^{30} (2.0e^{-k/20}) \times \left[B_k \sin\left(\frac{\pi k(\lambda - \lambda_i)}{\lambda_f - \lambda_i}\right) + C_k \cos\left(\frac{\pi k(\lambda - \lambda_i)}{\lambda_f - \lambda_i}\right) \right] \quad (2.77)$$

where A_i and $f_i(\lambda)$ are the amplitude and basis spectrum of the i^{th} of N total fluorophores, respectively. The numbers in the small parentheses denote the weights used in the SVD fitting, as described above. The value of 20 in the exponentially decaying weights was determined empirically. The spectral amplitudes A_i , B_k and C_k are returned by the SVD algorithm.

2.5.2 Nonlinear fitting algorithms and uncertainty propagation

In cases where the model being fit to the data is nonlinear, an iterative algorithm must be utilized. In this case, we define an N -dimensional data vector \mathbf{y} and a vector \mathbf{x} whose elements are the values of the independent variable at which each measurement was made. The theoretical model we wish to fit to the data is represented by the function $f(\mathbf{x}; \mathbf{a})$. The elements of the M -dimensional vector \mathbf{a} are the parameters to be determined by the fitting algorithm. For example,

in the case of spectral analysis described in chapter 4, the elements of \mathbf{y} are the values of the reflectance measured at wavelengths \mathbf{x} , and the elements of \mathbf{a} are the concentrations of absorbers and the parameters of the scattering spectrum used to model the reflectance.

The goal of the fitting algorithm is the minimization of χ^2 , defined by

$$\chi^2 = \sum_{i=1}^N \left(\frac{y_i - f(x_i; \mathbf{a})}{\sigma_i} \right)^2, \quad (2.78)$$

where σ_i is the uncertainty in the measured data at point x_i . The strategy for accomplishing this minimization is conceptually straightforward. First, the algorithm is supplied with a vector \mathbf{a}_0 which represents a starting point in the M -dimensional space of possible solutions. The algorithm then takes a series of steps in M -space designed to lead it to a minimum in χ^2 . The direction and length of the first step is determined by the local value of χ^2 and its gradient. After each step, the value of χ^2 and its gradient are recalculated, and the length and direction of the next step are determined. In cases where the χ^2 surface is quadratic in \mathbf{a} , a single iteration yields the best fit. In cases where the relation between χ^2 and \mathbf{a} is only approximately quadratic, multiple iterations are necessary. The process is repeated until a predetermined set of convergence conditions is met. Because the algorithm calculates each step based only on the local value of χ^2 and its gradient, it is possible that it may find a local minimum. In order to increase the chances that a true global minimum is found, any fit whose χ^2 is greater than a preset threshold χ_t^2 is repeated with a different initial value of \mathbf{a} .

The specific fitting algorithm used in the following chapters is a subspace

trust region minimization method implemented in the Optimization Toolbox of Matlab. The details of the fitting algorithm itself are beyond the scope of this work, and have been described in detail by others (More, 1977, Matlab Software Manual). The algorithm as provided does not take into account the uncertainty in the measured data, and minimizes the function

$$\sum_{i=1}^N (y_i - f(x_i; \mathbf{a}))^2. \quad (2.79)$$

In order to force the algorithm to calculate χ^2 according to equation 2.78, the values of y_i and $f(x_i; \mathbf{a})$ passed to the algorithm are replaced with y_i/σ_i and $f(x_i; \mathbf{a})/\sigma_i$, respectively.

With this modification, the fitting program returns the best fit value of \mathbf{a} and the Jacobian matrix \mathbf{J}_σ , defined by

$$\mathbf{J}_\sigma = \begin{pmatrix} \frac{1}{\sigma_1} \frac{\partial f(x_1)}{\partial a_1} & \frac{1}{\sigma_1} \frac{\partial f(x_1)}{\partial a_2} & \dots & \frac{1}{\sigma_1} \frac{\partial f(x_1)}{\partial a_M} \\ \frac{1}{\sigma_2} \frac{\partial f(x_2)}{\partial a_1} & \frac{1}{\sigma_2} \frac{\partial f(x_2)}{\partial a_2} & \dots & \frac{1}{\sigma_2} \frac{\partial f(x_2)}{\partial a_M} \\ \vdots & \vdots & \ddots & \vdots \\ \frac{1}{\sigma_N} \frac{\partial f(x_N)}{\partial a_1} & \frac{1}{\sigma_N} \frac{\partial f(x_N)}{\partial a_2} & \dots & \frac{1}{\sigma_N} \frac{\partial f(x_N)}{\partial a_M} \end{pmatrix}. \quad (2.80)$$

The matrix \mathbf{J} can be used to determine the uncertainties in the fitted parameters. Following the notation of Press *et al.* (1992), we define the matrix α as

$$\alpha = \mathbf{J}_\sigma \mathbf{J}_\sigma^T, \quad (2.81)$$

where \mathbf{J}_σ^T is the matrix transpose of \mathbf{J}_σ . It can be demonstrated that α is the

matrix inverse of \mathbf{C} , the covariance matrix of the fit. The standard error in the fitted parameter \mathbf{a}_j is given by

$$\sigma^2(\mathbf{a}_j) = \mathbf{C}_{jj}. \quad (2.82)$$

Two notes of caution on this definition of uncertainty are in order. First, this definition is based on propagation of errors and therefore takes into account only the effect of variations in the data on the final value of \mathbf{a} . It does not indicate the goodness of fit which produces that value of \mathbf{a} . For example, a very poor fit resulting from the fitting algorithm finding a local minimum of χ^2 can return small uncertainty in \mathbf{a} , despite the fact that the returned value of \mathbf{a} is far from the global minimum of χ^2 .

Second, the method outlined above makes use of the fact that the χ^2 surface is approximately linear within a small region. The uncertainties in the fitted parameters are extrapolated linearly based on the local gradient of the χ^2 surface. The validity of the uncertainty estimates is therefore limited to the region where the surface is approximately linear. While it is computationally expensive to determine the limits of this linearity, in the cases described here, it is sufficient to note that very large values of $\sigma^2(\mathbf{a}_j)$ should be interpreted as indicators of a poor fit rather than quantitative measures of uncertainty.

2.6 Modelling of bleaching *via* multiple simultaneous mechanisms

Previous work in our laboratory has established a model of photodynamic damage and sensitizer photobleaching based on the diffusion and consumption of oxygen during irradiation of sensitized multicell tumor spheroids (Georgakoudi and Foster, 1998; Georgakoudi *et al.*, 1997). In this model, oxygen is consumed by cellular metabolism and by photochemical reactions and is resupplied by diffusion from the surrounding medium. Irreversible photobleaching reduces the sensitizer concentration and hence the rate of photochemical oxygen consumption. The oxygen distribution in the spheroid is therefore sensitive to the mechanism of photobleaching. The oxygen concentration in a spheroid during PDT can be monitored by an oxygen-sensitive electrode, providing an indirect measure of photobleaching. The coupling of numerical integration of the relevant time-dependent diffusion-with-reaction equations with an iterative fitting algorithm has allowed the interpretation of electrode measurements in terms of fundamental photophysical parameters. In the case of bleaching mediated by reactions between singlet oxygen and the sensitizer, the ratio of the reaction rate constant for irreversible photobleaching to that for the deposition of photodynamic damage can be determined, allowing a direct mapping between the bleaching of the sensitizer and the deposited photodynamic dose (Georgakoudi *et al.*, 1997). Georgakoudi and Foster (1998) have demonstrated that the diffusion-with-consumption model can identify cases where the bleaching is mediated by reactions not directly involving oxygen, such as those between the sensitizer triplet state and cellular targets.

These prior studies have been interpreted using models where the bleaching was assumed to proceed *via* one predominant mechanism or another but not *via* multiple mechanisms simultaneously. In the following sections, we develop a simultaneous singlet oxygen- and triplet-mediated bleaching (SSTB) model that extends the singlet oxygen-mediated bleaching model developed by Georgakoudi *et al.* (1997) to include bleaching by reactions between the triplet state sensitizer and cellular substrates. We show that the timecourse of irreversible photobleaching predicted by the SSTB model is dependent on the initial concentration of the sensitizer. When the initial sensitizer concentration is high, the photobleaching proceeds primarily through reactions involving singlet oxygen. As the initial sensitizer concentration is decreased, sensitizer triplet reactions play an increasingly important role.

In chapter 3 this observation is invoked to reconcile apparently conflicting experimental evidence concerning the photobleaching of the sensitizer Photofrin. Based on electrode measurements of oxygen in spheroids, Georgakoudi *et al.* (1997) concluded that Photofrin bleaches predominantly *via* singlet oxygen reactions. However, the irradiance dependent photobleaching that is the hallmark of singlet oxygen-mediated bleaching is not observed in the *in vivo* fluorescence photobleaching described in chapter 3. The initial sensitizer concentrations in the two cases differ significantly; both sets of experimental results are therefore consistent with predictions of the SSTB model.

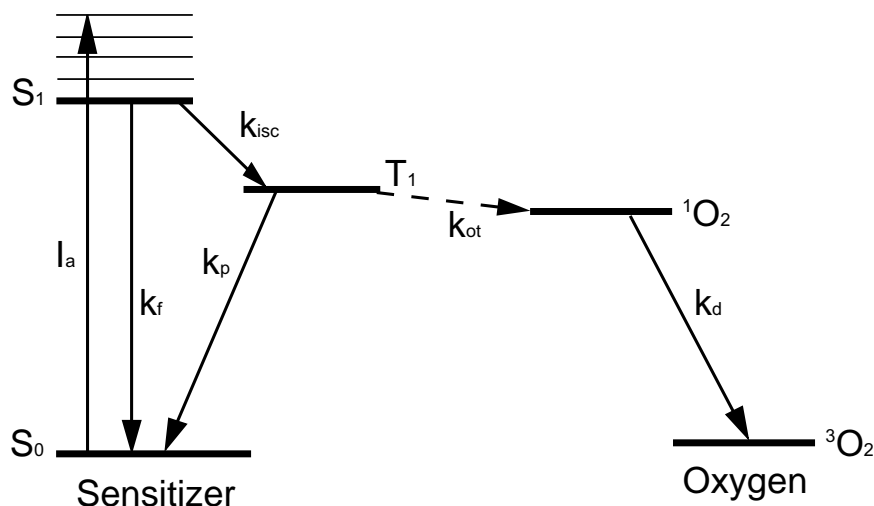


Figure 2.10: Jablonksi diagram of photosensitized singlet oxygen formation involving a type II photosensitizer. The rate constants for monomolecular transitions (—) and bimolecular energy transfer (---) are indicated. Irreversible reactions of the sensitizer with 1O_2 or with cellular substrates are omitted for clarity.

2.6.1 Basic kinetic equations

The energy level diagram shown in figure 2.10 illustrates the interactions between the sensitizer and oxygen that lead to tissue sensitization. The population of the sensitizer ground state (S_0) is reduced reversibly by optical excitation and replenished by decay from the excited singlet (S_1) and triplet (T_1) states. Radiative decay from S_1 to S_0 can be detected as fluorescence emission. Nonradiative decay and intersystem crossing to T_1 also reduce the population of the S_1 state. The excited triplet state gains population through intersystem crossing from S_1 and loses it by collisional energy transfer to ground state oxygen and by decay to S_0 , which for most sensitizers is predominantly nonradiative.

In addition, molecules in the S_1 or T_1 state may react with cellular targets (A), leading to irreversible photobleaching. Ground state sensitizer molecules may be irreversibly bleached by reactions with $^1\text{O}_2$ molecules, which may produce detectable fluorescent photoproducts (P). We will ignore the possibility that $^1\text{O}_2$ can react with S_1 or T_1 . This is justified by the fact that the irradiances employed in PDT are low enough that the vast majority of the sensitizer population, and hence of the sensitizer- $^1\text{O}_2$ reactions, occurs in the S_0 state. The reactions that lead to destruction of the sensitizer can be summarized by the rate equations



where SO and SA represent the products of irreversible reactions of the sensitizer with $^1\text{O}_2$ and with cellular targets, respectively. The rates of population change of the sensitizer's energy levels can be represented by the set of differential equations

$$\frac{d[S_0]}{dt} = -I_a + k_f[S_1] + k_p[T_1] + k_{ot}[T_1][^3\text{O}_2] - k_{os}[S_0][^1\text{O}_2], \quad (2.84a)$$

$$\frac{d[S_1]}{dt} = I_a - k_f[S_1] - k_{isc}[S_1] - k_{sa}[A][S_1] \quad (2.84b)$$

$$\frac{d[T_1]}{dt} = k_{isc}[S_1] - k_p[T_1] - k_{ot}[T_1][^3\text{O}_2] - k_{ta}[A][T_1], \quad (2.84c)$$

which explicitly account for all of the reactions listed in equations 2.83 and de-

picted in figure 2.10. For most sensitizers, molecules in the S_1 state make the transition to T_1 or decay back to S_0 very quickly; typical S_1 lifetimes are on the order of 10 ns. Because each molecule spends only a small fraction of its time in the S_1 state, reactions between S_1 molecules and substrates are unlikely. The $k_{sa}[A][S_1]$ term in equation 2.84b can therefore be neglected.

Singlet oxygen is created by collisions between ground state oxygen ($^3\text{O}_2$) and sensitizer triplets. Once $^1\text{O}_2$ is formed, it can decay back to the ground state or react with sensitizer molecules or other acceptors. The reactions that irreversibly consume oxygen are



where AO represents the products of oxidative reactions between $^1\text{O}_2$ and cellular substrates. The damage to cells by $^1\text{O}_2$ occurs as a result of the reactions described by equation 2.85b. The oxygen kinetics are given by

$$\frac{d[^3\text{O}_2]}{dt} = -S_\Delta k_{ot}[T_1][^3\text{O}_2] + k_d[^1\text{O}_2] \quad (2.86a)$$

$$\frac{d[^1\text{O}_2]}{dt} = S_\Delta k_{ot}[T_1][^3\text{O}_2] - k_d[^1\text{O}_2] - k_{oa}[A][^1\text{O}_2] - k_{os}[S_0][^1\text{O}_2]. \quad (2.86b)$$

The definitions of all the variables in equations 2.84 and 2.86 are listed in table 2.2. Because the excitation, intersystem crossing and decay events are very rapid compared to bulk changes in either sensitizer or oxygen concentration, $[S_1]$, $[T_1]$, and $[^1\text{O}_2]$ rapidly come to equilibrium with the concentrations of their respec-

Symbol	Definition	Units
I_a	Rate of photon absorption	s^{-1}
ϕ_t	Sensitizer triplet yield	
S_Δ	Fraction of T_1 - 3O_2 reactions which produce 1O_2	
S_P	Fraction of S_0 - 1O_2 reactions which produce photoproduct	
σ_{S_0}	Absorption cross section of S_0	cm^2
Φ_i	Irradiance of incident light	$mW\ cm^{-2}$
$[S_0]$	Sensitizer ground state	M
$[S_1]$	Sensitizer singlet excited state	M
$[T_1]$	Sensitizer triplet excited state	M
$[P]$	Fluorescent photoproducts	M
$[^3O_2]$	Triplet oxygen	M
$[^1O_2]$	Singlet oxygen	M
$[A]$	Cellular targets	M
k_f	$S_1 \rightarrow S_0$	s^{-1}
k_p	$T_1 \rightarrow S_0$	s^{-1}
k_{isc}	$S_1 \rightarrow T_1$ (Intersystem crossing)	s^{-1}
k_d	$^1O_2 \rightarrow ^3O_2$	s^{-1}
k_{ot}	Reaction of 3O_2 with T_1	$M^{-1}s^{-1}$
k_{os}	Reaction of 1O_2 with S_0	$M^{-1}s^{-1}$
k_{oa}	Reaction of 1O_2 with A	$M^{-1}s^{-1}$
k_{sa}	Reaction of S_1 with A	$M^{-1}s^{-1}$
k_{ta}	Reaction of T_1 with A	$M^{-1}s^{-1}$

Table 2.2: Definitions and units of variables used in the kinetic analysis of simultaneous triplet- and 1O_2 -mediated bleaching.

tive ground states. To find the instantaneous equilibrium concentrations of these species, we set their time derivatives to zero. First, equations 2.84b and 2.84c are set equal to zero to give

$$I_a = k_f[S_1] + k_{isc}[S_1] \quad (2.87a)$$

$$k_{isc}[S_1] = k_p[T_1] + k_{ot}[T_1][^3\text{O}_2] + k_{ta}[A][T_1], \quad (2.87b)$$

respectively. Combining these equations and substituting into equation 2.84a gives

$$\frac{d[S_0]}{dt} = -k_{ta}[A][T_1] - k_{os}[S_0][^1\text{O}_2], \quad (2.88)$$

consistent with the interpretation that only reactions between $^1\text{O}_2$ and S_0 or between T_1 and cellular substrates result in irreversible loss of sensitizer concentration.

The oxygen equations (2.86) can also be solved for their instantaneous equilibrium solutions to find the instantaneous concentration of $^1\text{O}_2$. The first step is to set equation 2.86b equal to zero and solve for $[^1\text{O}_2]$, which gives

$$[^1\text{O}_2] = \frac{S_\Delta k_{ot}[T_1][^3\text{O}_2]}{k_d + k_{oa}[A] + k_{os}[S_0]}. \quad (2.89)$$

Because $k_{os}[S_0]$ is generally much less than $k_{oa}[A]$, it can be dropped from the denominator of equation 2.89. Solving equation 2.87a for $[S_1]$ and equation 2.87b

for $[T_1]$ then gives

$$[S_1] = \frac{I_a}{k_f + k_{isc}} \quad (2.90a)$$

$$[T_1] = \frac{k_{isc}[S_1]}{k_p + k_{ot}[^3O_2] + k_{ta}[A]}. \quad (2.90b)$$

Combining equations 2.89 and 2.90 and noting that the triplet yield $\phi_t = k_{isc}/(k_{isc} + k_f)$, we obtain

$$[^1O_2] = S_{\Delta}\phi_t I_a \left(\frac{k_{ot}[^3O_2]}{k_{ot}[^3O_2] + k_p + k_{ta}[A]} \right) \left(\frac{1}{k_d + k_{oa}[A]} \right), \quad (2.91)$$

which differs from the corresponding expression for 1O_2 mediated bleaching (Georgakoudi and Foster, 1998, Eq. 9) only by the addition of the triplet-mediated bleaching term $k_{ta}[A]$. It is important to consider that the rate of photon absorption, I_a , that appears in these expressions depends on the sensitizer concentration. Specifically, I_a can be expressed as

$$I_a = [S_0] \frac{\sigma_{S_0} \Phi_i}{h\nu}, \quad (2.92)$$

where Φ_i and $h\nu$ are the fluence rate and energy per photon of the irradiation light, respectively, and σ_{S_0} is sensitizer's ground state absorption cross section. Finally, combining equations 2.88, 2.90b and 2.91, we obtain the instantaneous rate of photobleaching due to simultaneous 1O_2 - and T_1 -mediated bleaching in

terms of the concentrations of the ground state sensitizer and oxygen,

$$\begin{aligned} \frac{d[S_0]}{dt} &= -k_{ta}[A][T_1] - k_{os}[S_0][^1O_2] \\ &= - \left(\frac{\left(\frac{\sigma_{S_0} \Phi_i}{h\nu} \right) [S_0] \phi_t}{k_p + k_{ot}[^3O_2] + k_{ta}[A]} \right) \left[k_{ta}[A] + \frac{k_{os}[S_0] S_{\Delta} k_{ot}[^3O_2]}{k_d + k_{oa}[A]} \right]. \end{aligned} \quad (2.93)$$

2.6.2 Solutions under conditions of constant oxygen concentration

A complete solution of equation 2.93 must account for the fact that $[^3O_2]$ will be modified by treatment. This solution requires the use of numerical integration methods and the incorporation of oxygen diffusion into the model. However, the implications of the SSTB model can be illustrated by a simplified analysis in which the local oxygen concentration is held constant. With the substitutions

$$C_1 = \frac{\left(\frac{\sigma_{S_0} \Phi_i}{h\nu} \right) \phi_t k_{ta}[A]}{k_p + k_{ot}[^3O_2] + k_{ta}[A]} \quad (2.94a)$$

and

$$C_2 = \frac{k_{os} S_{\Delta} k_{ot}[^3O_2]}{k_{ta}[A](k_d + k_{oa}[A])}, \quad (2.94b)$$

the equilibrium concentrations of 1O_2 (equation 2.91) and of T_1 (equation 2.90b) can be written

$$[^1O_2] = \frac{C_1 C_2}{k_{os}} [S_0] \quad (2.95)$$

and

$$[T_1] = \frac{C_1}{k_{at}[A]}[S_0], \quad (2.96)$$

respectively, reducing equation 2.93 to a Bernoulli equation,

$$\frac{d[S_0]}{dt} = -C_1[S_0] - C_1C_2[S_0]^2. \quad (2.97)$$

The first term on the RHS of equation 2.97, which describes triplet-mediated bleaching, is linear in $[S_0]$ because triplet bleaching depends only on the population of T_1 , which is proportional to that of S_0 . The rate of 1O_2 -mediated bleaching, on the other hand, is second order in $[S_0]$ because both the production of 1O_2 molecules and the number of sensitizer molecules available for reaction with them are proportional to $[S_0]$. Note that equation 2.97 is valid only when C_1 and C_2 are constants, *i.e.* under conditions of constant oxygen concentration.

Equation 2.97 can be reduced to a linear differential equation by the change of variables to $\nu = 1/[S_0]$ and solved by standard techniques (Nagel and Saff, 1993). The resulting expression for the time-dependent sensitizer concentration is

$$[S_0]_{(t)} = \left[\left(\frac{1}{[S_0]_0} + C_2 \right) e^{C_1 t} - C_2 \right]^{-1}, \quad (2.98)$$

where $[S_0]_0$ is the initial concentration of the sensitizer. In the limit where the bleaching is entirely triplet sensitizer-mediated (*i.e.*, $k_{os} = 0$), the bleaching expression takes the form of a simple exponential in time,

$$[S_0]_{(t)} = [S_0]_0 e^{-C_1 t}. \quad (2.99)$$

In this limit, abundant oxygen inhibits bleaching by quenching the T_1 state, reducing its lifetime. This is reflected in equation 2.99 *via* C_1 , which decreases with increasing $[^3\text{O}_2]$, yielding the correct oxygen dependence. In the special case where $(k_p + k_{ot}[^3\text{O}_2]) \gg k_{ta}[T]$, equation 2.99 reduces to the corresponding expression found by Patterson (1998), who considered only the T_1 -mediated mechanism in his derivation. In the opposite limit of purely $^1\text{O}_2$ -mediated bleaching (*i.e.*, $k_{ta} = 0$), the corresponding expression is

$$[S_0]_{(t)} = \left[\frac{1}{[S_0]_0} + C_1 C_2 t \right]^{-1}. \quad (2.100)$$

As noted by Georgakoudi *et al.* (1997), $^1\text{O}_2$ -mediated bleaching does not follow a simple exponential, even when the effects of oxygen consumption are ignored.

The reactions which cause irreversible photobleaching may lead to the formation of fluorescent photoproducts. Under the assumption that photoproducts are formed only as a result of reactions between S_0 and $^1\text{O}_2$, the photoproduct concentration $[P]$ as a function of time is given by

$$[P]_{(t)} = \int_0^t S_P k_{os}[^1\text{O}_2]_{(t')} [S_0]_{(t')} dt' = C_1 C_2 S_P \int_0^t [S_0]_{(t')}^2 dt', \quad (2.101)$$

where S_P is the fraction of $^1\text{O}_2$ - S_0 reactions which produce photoproduct. It is possible that photodynamic damage is caused by reactions involving either $^1\text{O}_2$ or T_1 and cellular targets. However, because each sensitizer molecule can participate in at most one $T_1 - A$ reaction but may provide energy for the formation of many $^1\text{O}_2$ molecules, we will not include triplet sensitizer reactions in our definition of

dose. The cumulative photodynamic dose is therefore given by the time integral of the rate of $^1\text{O}_2$ reactions,

$$\int_0^t k_{oa}[A][^1\text{O}_2]_{(t')} dt' = \frac{k_{oa}[A]}{k_{os}} C_1 C_2 \int_0^t [S_0]_{t'} dt'. \quad (2.102)$$

Many of the variables needed to calculate C_1 and C_2 have not been measured individually, although ratios among them often are available in the literature. In terms of these measurable ratios, C_1 and C_2 can be expressed as

$$C_1 = \frac{(\sigma_{S_0} \phi_t / h\nu) (k_{ta}[A]/k_{ot}) \Phi_i}{(k_p/k_{ot}) + [^3\text{O}_2] + (k_{ta}[A]/k_{ot})} \quad (2.103a)$$

and

$$C_2 = \frac{(k_{os}/k_{oa}[A]) (\beta_{PDT}/[S_0]) [^3\text{O}_2]}{(k_{ta}[A]/k_{ot}) (\sigma_{S_0} \phi_t / h\nu)}, \quad (2.103b)$$

respectively, where β_{PDT} is the ratio of oxygen consumption rate to irradiance (Georgakoudi *et al.*, 1997), given by

$$\beta_{PDT} = \frac{S_{\Delta} \phi_t I_{a(t=0)}}{\Phi_i} \left(\frac{k_{oa}[A]}{k_d + k_{oa}[A]} \right). \quad (2.104)$$

Measured values of the terms in parentheses in equations 2.103a and 2.103b for the sensitizer Photofrin are listed in table 2.3 and have been adopted in the following discussion. The calculation of the quantity $(\beta_{PDT}/[S_0])$ requires knowledge of the sensitizer concentration in the spheroids in which β_{PDT} was measured. Based on the previous work of Nichols and Foster (1994), the concentration of sensitizer in those spheroids can be estimated at $102 \mu\text{g ml}^{-1}$. Because Photofrin is a

Variable	Value	Source
$\left(\frac{k_{os}}{k_{oa}[A]}\right)$	76 M ⁻¹	Georgakoudi <i>et al.</i> (1997)
$\left(\frac{k_p}{k_{ot}}\right)$	1.19×10^{-5} M	Georgakoudi <i>et al.</i> (1997)
$\left(\frac{k_{ta}[A]}{k_{ot}}\right)$	6×10^{-9} M	
β_{PDT}^*	1.87×10^{-3} M cm ² J ⁻¹	Georgakoudi <i>et al.</i> (1997)
$[S_0]_0^*$	1.70×10^{-4} M	Nichols and Foster (1994)
$\left(\frac{\beta_{PDT}}{[S_0]}\right)$	11 cm ² J ⁻¹	
σ_{S_0}	1.8×10^{-17} cm ²	Measured in clear solution
ϕ_t	0.63	Foster <i>et al.</i> (1991)
$(\sigma_{S_0}\phi_t/h\nu)$	29 cm ² J ⁻¹	
S_P	1	

Table 2.3: Numerical values assigned to variables describing photobleaching kinetics. The values used for the generation of figures 2.11, 2.12 and 2.13 are listed with the rationale for their adoption or published sources from which they were taken. S_p is set to 1 for convenience, and $(k_{ta}[A]/k_{ot})$ was chosen to illustrate the effects of triplet-mediated bleaching at various values of $[S_0]_0$. Parameters taken from Georgakoudi *et al.* (1997) were measured with the sensitizer Photofrin. The values indicated by asterisks (*) are dependent on the initial Photofrin concentration in the spheroids in which they were measured, however they are used only to calculate their ratio, which is concentration-independent.

mixture of porphyrins rather than a pure compound, it does not have a defined molecular weight, however its average weight per mole of porphyrin rings has been estimated at 600 g (Moan and Berg, 1991). The molar concentration of Photofrin corresponding to $102 \mu\text{g ml}^{-1}$ is therefore $170 \mu\text{M}$.

The only value listed in table 2.3 that has not been obtained experimentally is $(k_{ta}[A]/k_{ot})$. In chapter 3, it is shown that a comparison between *in vivo* fluorescence photobleaching measurements and previous oxygen electrode measurements in spheroids (Georgakoudi *et al.*, 1997) can be used to constrain the $(k_{ta}[A]/k_{ot})$ of Photofrin, and a rationale is presented for estimating its value at approximately 6×10^{-9} M. For purposes of the current discussion, we will adopt this value. The general qualitative results presented below are not sensitive to the particular choice of $(k_{ta}[A]/k_{ot})$; a different value of $(k_{ta}[A]/k_{ot})$ can be offset by a change in initial sensitizer concentration.

The SSTB model predicts remarkably different bleaching behavior for systems with different initial sensitizer concentrations. When $[S_0]_0$ is large, the bleaching is dominated by $^1\text{O}_2$ reactions and exhibits the oxygen dependence expected of $^1\text{O}_2$ mediated bleaching. At intermediate $[S_0]_0$, the oxygen dependence of the photobleaching disappears, and at low $[S_0]_0$ it reverses, indicating an increasing contribution from T_1 reactions. The details of the photobleaching, photoproduct formation and dose deposition in each of these three regimes are illustrated in the following sections.

First, we will consider an initial sensitizer concentration of $170 \mu\text{M}$, a case where the SSTB model predicts that bleaching is dominated by $^1\text{O}_2$ reactions. To demonstrate the effects of varying oxygen concentration, we compare the bleach-

ing behavior when $[^3\text{O}_2]$ is equal to $67\ \mu\text{M}$, typical of well-oxygenated tissue (Boag, 1969) with the case of $[^3\text{O}_2]$ equal to $5\ \mu\text{M}$. The resulting photobleaching, photoproduct accumulation and dose deposition curves are plotted as functions of irradiation fluence in figure 2.11. The concentrations of the sensitizer (2.11(a)) and its photoproduct (2.11(b)) are expressed as fractions of $[S_0]_0$. The concentration of reacted $^1\text{O}_2$ deposited in the medium is plotted in panel (c). In each panel, the curves for the high (---) and low (—) oxygen concentration cases are plotted on the same scale. In this case, the initial sensitizer concentration is sufficiently high that bleaching is initially dominated by $^1\text{O}_2$ -mediated processes. As expected, the bleaching proceeds more rapidly in the well-oxygenated medium than in the poorly-oxygenated medium and leads to a more rapid accumulation of photoproduct. If the sensitizer were not able to bleach *via* a triplet-mediated mechanism, each reaction between the sensitizer and $^1\text{O}_2$ would generate an average of S_P molecules of photoproduct, so the accumulation of photoproduct would be directly proportional to the fraction of the initial sensitizer that had bleached. The fraction of sensitizer bleached would also be directly related to the total amount of $^1\text{O}_2$ deposited in tissue (Georgakoudi *et al.*, 1997), allowing either photobleaching or photoproduct accumulation to serve as a surrogate reporter of photodynamic dose. In contrast, when a triplet-mediated mechanism is available, a lowering of the oxygen concentration causes more of the sensitizer molecules to bleach without forming photoproducts, which in turn leads to a lower total production of photoproduct. In addition, the dose deposited for a given amount of bleaching becomes dependent on the local oxygen concentration, as shown in figure 2.11(c). In both the low- and high-oxygen cases, the deposition of dose continues even after

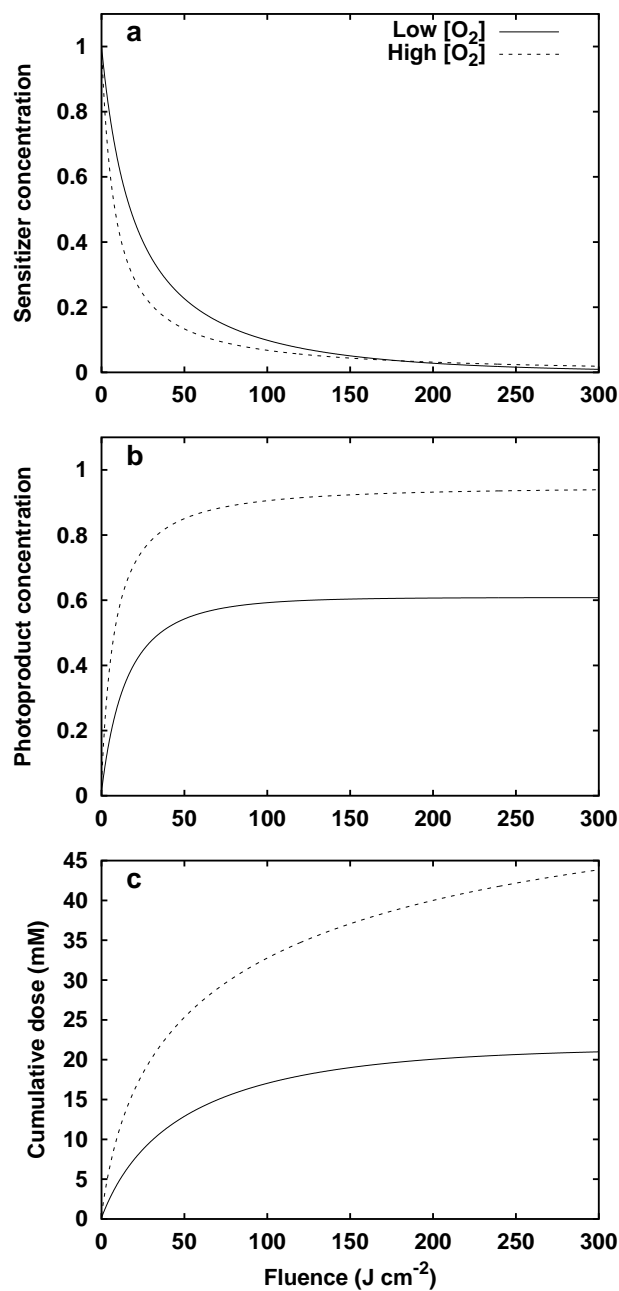


Figure 2.11: Concentrations of (a) ground state sensitizer and (b) photoproduct predicted by kinetic equations for mixed-mechanism bleaching in the case of constant oxygen and (c) the corresponding cumulative dose of reacted $^1\text{O}_2$ for media at high (---) and low (—) oxygen concentration. The initial sensitizer concentration was set at $170 \mu\text{M}$

the accumulation of photoproduct appears to have levelled off. This is a result of the fact that photoproduct accumulation, like $^1\text{O}_2$ -mediated photobleaching, has a second-order dependence on $[S_0]$, while the deposition of dose is linearly proportional to $[S_0]$ for a given oxygen concentration and irradiance.

Corresponding plots for a five-fold lower initial sensitizer concentration of $34\ \mu\text{M}$ are shown in figure 2.12. Here the bleaching initially exhibits an oxygen dependence similar to that observed in the higher concentration case. As irradiation proceeds, however, the triplet-mediated bleaching mechanism becomes more important, and the oxygen dependence reverses. In this case, careful measurement would be required to discern any oxygen dependence in the bleaching curve over the range of fluences shown, despite the fact that the total deposited doses in the high and low oxygen cases differ significantly.

When $[S_0]_0$ is lowered further to $17\ \mu\text{M}$, the bleaching is more rapid at lower oxygen concentration from the onset of irradiation. At lower oxygen concentration, triplet sensitizer molecules are less likely to be quenched by oxygen, so they have more opportunity to react with cellular substrates. The result is that triplet-mediated bleaching is more efficient at low oxygen concentration, as shown in figure 2.13(a). Despite the fact that it is primarily the triplet mechanism which determines the oxygen dependence of bleaching in this case, it is not accurate to say that the photobleaching is dominated by triplet interactions. In fact, at high oxygen concentration approximately 60% of the bleaching is accomplished *via* $^1\text{O}_2$ reactions, as indicated by the photoproduct accumulation shown in figure 2.13(b). The dose deposition in the low oxygen case shown here provides justification for our previous assumption that tissue damage caused by $T_1 - A$ reactions was

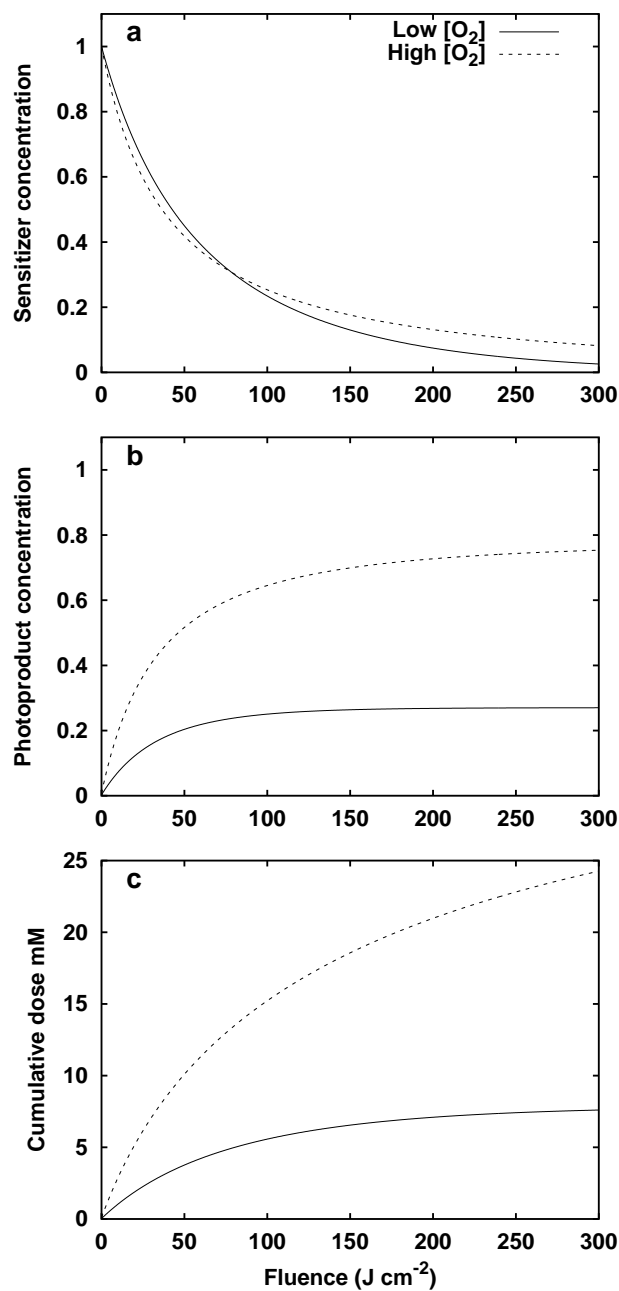


Figure 2.12: Concentrations of (a) ground state sensitizer and (b) photoproduct predicted by kinetic equations for mixed-mechanism bleaching in the case of constant oxygen and (c) the corresponding cumulative dose of $^1\text{O}_2$ for media at high (---) and low (—) oxygen concentration. The initial sensitizer concentration was set at $34 \mu\text{M}$

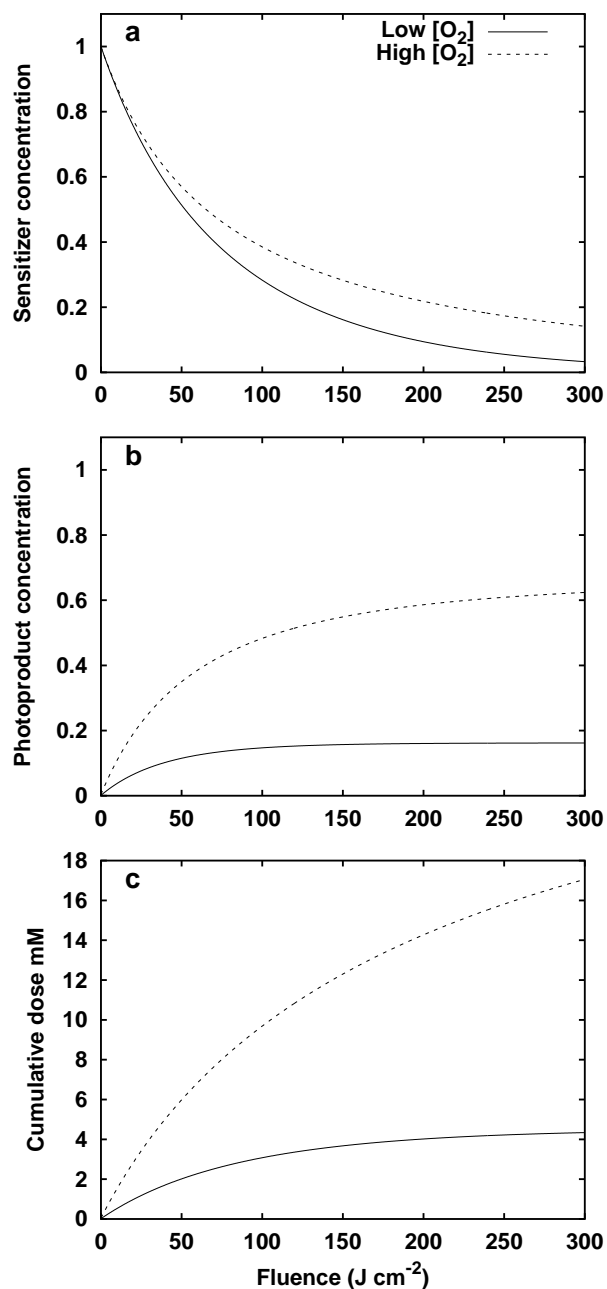


Figure 2.13: Concentrations of (a) ground state sensitizer and (b) photoproduct predicted by kinetic equations for mixed-mechanism bleaching in the case of constant oxygen and (c) the corresponding cumulative dose of $^1\text{O}_2$ for media at high (---) and low (—) oxygen concentration. The initial sensitizer concentration was set at $17 \mu\text{M}$

negligible. Even if all of the bleaching were caused by these reactions, the total reacted triplet dose could not exceed $17 \mu\text{M}$. Under conditions of reduced $[^3\text{O}_2]$, the deposited $^1\text{O}_2$ dose is on the order of 4 mM , indicating that the relative contribution of triplet reactions to photodynamic dose will be significant only at extremely low oxygen concentrations. A sensitizer with a higher $(k_{ta}[A]/k_{ot})$ would deposit less $^1\text{O}_2$, but its reacted triplet dose could still not exceed $[S_0]_0$.

2.6.3 Effect of limited $^1\text{O}_2$ diffusion length

In the analysis presented above, it has been assumed that the rate of reaction between $^1\text{O}_2$ and the ground state sensitizer is proportional to the product of $[^1\text{O}_2]$ and $[S_1]$. This derivation implicitly assumes that the $^1\text{O}_2$ and sensitizer molecules are randomly distributed. In fact, it has been shown by Moan and Berg (1991) that $^1\text{O}_2$ molecules created in sensitized cells diffuse only 10 to 20 nm before reacting, so a $^1\text{O}_2$ molecule is exposed to a very small volume of tissue which necessarily includes the sensitizer molecule which created it. The probability that the $^1\text{O}_2$ molecule will react with its parent sensitizer molecule is therefore greater than that predicted by an analysis based on homogeneous reaction kinetics. To compensate for this effect, we can replace occurrences of $k_{os}[^1\text{O}_2][S_0]$ in the kinetic equations with the quantity $(k_{os}[^1\text{O}_2][S_0] + \frac{1}{vN_A})$, where v is the volume accessible to a $^1\text{O}_2$ molecule and N_A is Avogadro's number. When $[S_0]$ is large, this additional term has little effect. In the small $[S_0]$ limit the predicted number of sensitizer molecules within the volume sampled by $^1\text{O}_2$ approaches 1, consistent with the observation that this volume always contains at least the parent sensitizer molecule. This substitution has the effect of adding a component to the $^1\text{O}_2$ -

mediated bleaching that is linear in $[S_0]$, reducing the dominance of the triplet-mediated bleaching mechanism at low sensitizer concentration. For reasonable values of v , this effect can be offset by an increase in $(k_{ta}[A]/k_{ot})$, and the three regimes of oxygen dependence illustrated by figures 2.11, 2.12 and 2.13 are still observed, although the difference in bleaching rate between the high and low oxygen cases diminishes with decreasing v (data not shown).

2.6.4 Implications of multiple-mechanism bleaching for PDT dosimetry

As shown in figures 2.11, 2.12 and 2.13, the relationship between the sensitizer photobleaching and dose deposition when multiple bleaching mechanisms are present is highly dependent on the initial concentration of the sensitizer. At high $[S_0]_0$, the photobleaching of the sensitizer can serve as a reporter of deposited dose. However, as the concentration is lowered the accuracy of bleaching-based dosimetry degrades. At the lowest sensitizer concentration investigated here, monitoring of photobleaching would lead one to conclude that a greater photodynamic dose had been deposited in the low-oxygen case than in the well-oxygenated case when in fact the opposite is true. This observation motivates careful attention to the bleaching mechanism of sensitizers for which photobleaching is considered as a means of real-time dosimetry. If, as we have assumed, the deposition of dose and the formation of photoproducts are both mediated solely by 1O_2 , the accumulation of photoproduct may serve as a more accurate measure of dose than the bleaching of the sensitizer in cases where multiple bleaching mechanisms are

present. A potential complication is the fact that the photoproduct itself may undergo photobleaching, an effect that this analysis has neglected but which has been observed *in vivo* (Chapter 3 of this thesis; Robinson *et al.*, 1998).

It should be acknowledged that the model described here is a significant simplification of the true *in vivo* situation, in which the consumption and transport of oxygen may play important roles and significant gradients in oxygen concentration may develop during PDT. However, the cases considered here represent two limiting cases of the *in vivo* bleaching dynamics. If the irradiance is sufficiently low, PDT may be performed with little perturbation of the local oxygen concentration, corresponding to the well-oxygenated cases shown above. Conversely, if the irradiance is high enough, volumes of tissue not immediately adjacent to vasculature may be rendered hypoxic almost immediately and not recover during the duration of PDT, a situation analogous to the low-oxygen cases shown here. Any situation encountered during PDT *in vivo* is likely to fall between these extremes, so we expect the trends observed in the current simplified model to be reproduced at least qualitatively in real systems.

References

- Boag, J. W. (1969), Oxygen diffusion and oxygen depletion problems in radiobiology. In *Current Topics in Radiation Research*, Ebert, M. and Howard, A., editors, volume 5, pages 141–195. North-Holland, Amsterdam/London.
- Case, K. M. and Zweifel, P. F. (1967). *Linear Transport Theory*. Addison-Wesley, Reading, MA.
- Crilly, R. J., Cheong, W.-F., Wilson, B. C., and Spears, J. R. (1997). Forward-adjoint fluorescence model: Monte carlo integration and experimental validation. *Appl. Opt.* **36**:6513–6519.
- Duysens, L. N. M. (1956). The flattening of the absorption spectrum of suspensions, as compared with that of solutions. *Biochim. Biophys. Acta.* **19**: 1–12.
- Farrell, T. J., Patterson, M. S., and Wilson, B. (1992). A diffusion theory model of spatially resolved, steady-state diffuse reflectance for the noninvasive determination of tissue optical properties *in vivo*. *Med. Phys.* **19**:879–888.
- Fishkin, J. B., Fantini, S., vande Ven, M. J., and Gratton, E. (1996). Gigahertz photon density waves in a turbid medium: Theory and experiments. *Phys. Rev. E.* **53**:2307–2319.
- Foster, T. H., Murant, R. S., Bryant, R. G., Knox, R. S., Gibson, S. L., and Hilf, R. (1991). Oxygen consumption and diffusion effects in photodynamic therapy. *Rad. Res.* **126**:296–303.
- Georgakoudi, I. and Foster, T. H. (1998). Singlet oxygen- *versus* nonsinglet oxygen-mediated mechanisms of sensitizer photobleaching and their effects on photodynamic dosimetry. *Photochem. Photobiol.* **67**:612–625.
- Georgakoudi, I., Nichols, M. G., and Foster, T. H. (1997). The mechanism of Photofrin photobleaching and its consequences for photodynamic dosimetry. *Photochem. Photobiol.* **65**:135–144.
- Hansen, P. C. (1994). Regularization tools: A Matlab package for analysis and solution of discrete ill-posed problems. *Numerical Algorithms.* **6**:1–35.
- Haskell, R. C., Svaasand, L. O., Tsay, T.-T., Feng, T.-C., McAdams, M. S., and Tromberg, B. J. (1994). Boundary conditions for the diffusion equation in radiative transfer. *JOSA A.* **11**:2727–2741.

- Henye, I. and Greenstein, J. (1941). Diffuse radiation in the galaxy. *Astrophys. J.* **93**:70–83.
- Hull, E. L. and Foster, T. H. (2001). Steady-state reflectance spectroscopy in the P_3 approximation. *JOSA A*. **18**:584–599.
- Ishimaru, A. (1997). *Wave propagation and scattering in random media*. IEEE Press, New York.
- Jacques, S. L., Alter, C. A., and Prahl, S. A. (1987). Angular dependence of HeNe laser light scattering by human dermis. *Lasers Life Sci.* **1**:309–333.
- Kienle, A. and Patterson, M. (1996). Determination of the optical properties of turbid media from a single Monte Carlo simulation. *Phys. Med. Biol.* **41**: 2221–2227.
- Kienle, A. and Patterson, M. (1997). Improved solutions of the steady-state and the time-resolved diffusion equations for reflectance from a semi-infinite turbid medium. *JOSA A*. **14**:246–254.
- Maynard, C. (1961). An application of the reciprocity theorem to the acceleration of Monte Carlo calculations. *Nuc. Sci. Eng.* **10**:97–101.
- Moan, J. and Berg, K. (1991). The photodegradation of porphyrins in cells can be used to estimate the lifetime of singlet oxygen. *Photochem. Photobiol.* **53**: 549–553.
- More, J. J. (1977), The Levenberg-Marquardt algorithm: Implementation and theory. In *Numerical Analysis*, Watson, G. A., editor, volume 630 of *Lecture Notes in Mathematics*, pages 105–116. Springer Verlag.
- Nagel, R. K. and Saff, E. B. (1993). *Fundamentals of Differential Equations*. Addison-Wesley, Reading, MA, third edition.
- Nichols, M. G. and Foster, T. H. (1994). Oxygen diffusion and reaction kinetics in the photodynamic therapy of multicell tumour spheroids. *Phys. Med. Biol.* **39**:2161–81.
- Nichols, M. G., (1996). *Transport of oxygen and light in model tumor systems*. PhD thesis, University of Rochester, Rochester, NY.
- Patterson, M. S., (1998). Personal communication.
- Prahl, S. A., (1999a). Optical properties of hemoglobin. Available from the website omlc.ogi.edu.

- Prahl, S. A., (1999b). small_mc. Available from the website omlc.ogi.edu.
- Prahl, S. A., Keijzer, M., Jacques, S. L., and Welch, A. J. (1989). A Monte Carlo model of light propagation in tissue. *SPIE Institute Series*. **IS5**:102–111.
- Press, W. H., Teukolsky, S. A., Vetterling, W. T., and Flannery, B. P. (1992). *Numerical Recipes in C: The Art of Scientific Computing*. Cambridge University Press, New York, second edition.
- Robinson, D. J., de Bruijn, H. S., van der Veen, N., Stringer, M. R., Brown, S. B., and Star, W. M. (1998). Fluorescence photobleaching of ALA-induced protoporphyrin IX during photodynamic therapy of normal hairless mouse skin: The effect of light dose and irradiance and the resulting biological effect. *Photochem. Photobiol.* **67**:140–149.
- Schuster, A. (1905). Radiation through a foggy atmosphere. *Astrophys. J.* **21**: 1–22.
- Van Assendelft, O. W. (1970). *Spectrophotometry of Haemoglobin Derivatives*. Charles C. Thomas, Springfield, IL.
- Wang, L. and Jacques, S. L. (1994). Optimized radial and angular positions in Monte Carlo modeling. *Med. Phys.* **21**:1081–1083.
- Wang, L. V. and Jacques, S. L. (2000). Source of error in calculation of optical diffuse reflectance from turbid media using diffusion theory. *Comput. Methods Programs Biomed.* **61**:163–170.
- Williams, M. L. (1991). Generalized contribution response theory. *Nuc. Sci. Eng.* **108**:355–383.
- Wray, S., Cope, M., Delpy, D. T., Wyatt, J. S., and Reynolds, E. O. R. (1988). Characterization of the near-infrared absorption spectra of cytochrome aa₃ and hemoglobin for the noninvasive monitoring of cerebral oxygenation. *Biochim. Biophys. Acta.* **933**:184–192.
- Zijlstra, W. G., Bursma, A., and Meeuwssen-van der Roest, W. P. (1991). Absorption spectra of human fetal and adult oxyhemoglobin, de-oxyhemoglobin, carboxyhemoglobin, and methemoglobin. *Clin. Chem.* **37**:1633–1638.

Chapter 3

In Vivo Photobleaching

3.1 Introduction

A problem of continuing interest in the study of PDT is the definition and measurement of photodynamic dose. It is believed that the majority of photosensitizers accomplish their cytotoxic effect through the production of $^1\text{O}_2$ and other reactive oxygen species (Dougherty *et al.*, 1998). For many sensitizers, the same or similar mechanism is also responsible for the degradation of the sensitizer molecules, which is observable as irreversible photobleaching. The photobleaching of the sensitizer can therefore be utilized to optimize PDT dosimetry, a scheme described by Wilson *et al.* (1997) as implicit dosimetry. Such a dosimetry method takes into account all of the factors involved in the deposition of photodynamic dose, without the need to measure them explicitly. In the case of purely $^1\text{O}_2$ -mediated bleaching with spherical boundary conditions, Georgakoudi and Foster (1998b) have developed a rigorous model which quantitatively relates the fraction of sensitizer bleached to the deposited $^1\text{O}_2$ dose. While the *in vivo* situation is complicated

by tissue geometry and optical variations, it can be expected that photobleaching will still be predictive of photodynamic dose deposition.

Under PDT treatment conditions in which photodynamic oxygen consumption is significant enough to limit type-II photochemistry, a predominantly $^1\text{O}_2$ -mediated photobleaching mechanism would be expected to become relatively inefficient. Unless other oxygen-independent bleaching mechanisms were to become important under conditions of low tissue oxygen tension *in vivo*, an irradiance dependence to the rate of photobleaching would be anticipated such that the photodegradation of the sensitizer for a given fluence would be greater at relatively lower irradiance.

Previous work in our laboratory has examined photosensitizer bleaching indirectly through its effect on the oxygen concentration measured at the surface of multicell tumor spheroids during irradiation (Coutier *et al.*, 2001; Georgakoudi and Foster, 1998b; Georgakoudi *et al.*, 1997). Analysis of these time-dependent changes in oxygen concentration suggests that the bleaching of the sensitizers Photofrin, *meso*-tetrahydroxyphenyl chlorin (mTHPC) and aminolevulinic acid (ALA)-induced protoporphyrin IX (PpIX) in EMT6 spheroids is mediated predominantly by a self-sensitized $^1\text{O}_2$ reaction mechanism. Recent direct observations of fluorescence photobleaching have confirmed these results in the case of spheroids (Bigelow *et al.*, 2002). For the case of PpIX, this result is qualitatively consistent with a finding published by Krieg and Whitten (1984), who concluded that the detailed mechanism of PpIX bleaching in erythrocyte ghosts involved reaction of $^1\text{O}_2$ with an intermediate oxidizable amino acid. An oxygen dependence to the rate of Photofrin bleaching is consistent with results reported by Spikes

(1992), although the extent of the role of $^1\text{O}_2$ was not clear in that study, which was performed using a variety of model environments in fluid solution.

In considering an experimental approach to quantitative or semiquantitative fluorescence spectroscopy of photosensitizers in tissue, it is necessary to acknowledge that fluorescence measurements during PDT *in vivo* are conducted against a background of tissue optical properties that may not be assumed to remain constant. The effects that tissue optical properties may have on the apparent photobleaching kinetics measured *in vivo* were considered by Jacques *et al.* (1993). Wavelength-dependent tissue absorption and scattering may distort fluorescence spectra (Keijzer *et al.*, 1989), and these background optical properties may change during irradiation in response to cellular and physiologic responses to photodynamic damage. Several groups working in the field of tissue optics have addressed the problem of performing fluorescence spectroscopy in highly scattering and absorbing media such as tissue (for example, Gardner *et al.*, 1996; Müller *et al.*, 2001; Wu *et al.*, 1993). In designing the experiments described in this chapter, we have implemented a modification of the approach of Wu *et al.* (1993), which involves correction of the measured fluorescence using the reflectance spectrum measured in the same geometry. This empirical method has allowed us to collect fluorescence spectra undistorted by changing optical properties.

A further complexity arises in the particular case of spectroscopy of sensitized tissue in that the fluorescence emission spectrum may change qualitatively in response to irradiation as sensitizer photoproducts and, under certain conditions, other chemical species contribute significantly to the measurement (Dietel *et al.*, 1996; Gudgin Dickson and Pottier, 1995; König *et al.*, 1993, and references

therein). Thus, appropriate methods of spectral analysis are required in order to separate the contributions of the various fluorescing species. The purpose of these studies was to incorporate such spectroscopic techniques and methods of analysis into an experimental investigation of the kinetics of sensitizer photobleaching and photoproduct formation in normal rat skin *in vivo*. Three sensitizers were investigated, all of which are currently being used in clinical treatment or clinical trials in the U.S. and/or Europe. A brief summary of the current state of investigation of each sensitizer is given below.

3.1.1 ALA-induced PpIX

ALA is unique among PDT drugs currently under investigation in that it is not itself a sensitizer, but rather a prodrug which induces the formation of the photosensitizer PpIX within target tissues. This strategy makes use of the biosynthetic mechanism responsible for the creation of heme in mammalian cells (Peng *et al.*, 1997). The first step in heme synthesis is the formation of ALA in the mitochondria through the action of the enzyme ALA synthase. The ALA crosses the mitochondrial membrane and enters the cytosol, where it undergoes a series of enzymatic reactions which combine a total of eight ALA molecules to form one molecule of uroporphyrinogen III. A further reaction converts uroporphyrinogen III to coproporphyrinogen III. In order for heme synthesis to proceed, coproporphyrinogen III must be taken into the mitochondria and converted to protoporphyrinogen IV and subsequently into PpIX. Under normal circumstances, the enzyme ferrochelatase acts to incorporate iron into the PpIX produced in the mitochondria, forming heme. Both the formation and the enzymatic action of

ALA synthase are inhibited by the presence of heme (Stryer, 1988). Because of this negative feedback, the production of heme is a self-regulating process. By administering excess ALA, it is possible to upset the natural regulation of the heme synthesis pathway. The introduction of ALA that is not created by ALA synthase bypasses the step at which the heme synthesis pathway is inhibited by free heme. The downstream steps in the pathway proceed uninhibited. In this case, the rate of incorporation of iron into the porphyrin ring by ferrochelatase is outstripped by the production of PpIX. PpIX, unable to be converted to heme, builds up in the mitochondria. In addition, if the mitochondria are unable to complete the formation of PpIX, the intermediate products uroporphyrinogen III and coproporphyrinogen III, instead of being used in downstream steps of heme synthesis, can undergo reactions in the cytosol which produce the water-soluble porphyrins uro- and coproporphyrin, respectively (Dietel *et al.*, 1997).

Reports in the literature of experimental investigation of the irradiance dependence of *in vivo* PpIX photobleaching are conflicted. In a pair of papers, Robinson and his colleagues have described, among other things, an irradiance dependence of the rate of PpIX photobleaching in normal mouse skin and in UVB-induced skin tumors that is qualitatively consistent with an oxygen-dependent bleaching mechanism (Robinson *et al.*, 1998; 1999). Studies by Sørensen *et al.* (1998), who also reported results of experiments performed with ALA-sensitized normal mouse skin over a wide range of irradiances, and by Iinuma *et al.* (1999), who worked with ALA-sensitized tumors in rats, found no evidence for an irradiance dependence of the efficiency of PpIX photobleaching. The resolution of this apparent discrepancy is important not only from a mechanistic perspective but also for the

ongoing evaluation of the potential of photosensitizer bleaching to report useful dosimetry.

3.1.2 mTHPC

mTHPC is a promising second-generation photosensitizer. Several investigators have reported mTHPC to be the most potent of all the photosensitizers being studied presently. A clinical study performed in patients with diffuse malignant mesothelioma reported a 10 mm deep tumor necrosis with a dose of 0.3 mg kg^{-1} mTHPC activated after 48 h with 10 J cm^{-2} at 652 nm (Ris *et al.*, 1991; 1996). Similar successful tumor responses have been reported by Baas *et al.* (2001); Savary *et al.* (1997) and Mlkvy *et al.* (1998) among others, using fluences of 10 to 20 J cm^{-2} and an even lower mTHPC dose of 0.15 mg kg^{-1} .

The photobleaching of mTHPC has been investigated by several groups. One of the earliest such studies was conducted by Ma *et al.* (1994b), who compared the loss of mTHPC fluorescence with that of *meso*-tetrahydroxyphenyl porphyrin (mTHPP) and Photofrin during irradiation of sensitized cells with broadband light at 375-450 nm. They reported that the rate of mTHPC bleaching with respect to time was much higher than that of Photofrin or mTHPP. Measurements to investigate the mTHPC bleaching kinetics *in vivo* were performed by Forrer *et al.* (1995), who found that the decay of mTHPC fluorescence was consistent with a theory based on the assumption that $^1\text{O}_2$ was the agent responsible for bleaching. Hadjur *et al.* (1998) showed evidence that supported the involvement of $^1\text{O}_2$ in the *in vitro* photodegradation of mTHPC in 10% fetal calf serum. A study performed in collaboration with our laboratory by Coutier *et al.* (2001) addressed the impact

of irradiance on the photobleaching of mTHPC-sensitized tumor spheroids as well as on the PDT-induced cell toxicity. A decrease in incident irradiance resulted in a greater rate of mTHPC bleaching *vs* fluence as well as a decrease in the fraction of cells surviving treatment, as expected in the presence of oxygen concentration gradients with a sensitizer whose photodynamic damage and bleaching are both mediated by $^1\text{O}_2$. These results are consistent with prior reports by Ma *et al.* (1994a) and Melnikova *et al.* (1999b), where $^1\text{O}_2$ was identified as the major toxic agent in mTHPC photosensitization and with the *in vivo* results of Blant *et al.* (1996), who observed more efficient treatment of Syrian hamster cheek pouch tumors at lower irradiance.

3.1.3 Photofrin

Photofrin was the first photosensitizing drug to gain health agency approval for use in patients and is currently the most widely used clinically (Dougherty *et al.*, 1998), however the details of its *in vivo* dose deposition and photobleaching behavior are still not completely understood. Much of the early research on the irradiance dependence of the biological response to Photofrin PDT was performed at the University of Rochester in our laboratory and that of Dr. Russel Hilf. Using the R3230AC tumor model in rats, Gibson *et al.* (1990) observed significantly enhanced tumor response to Photofrin PDT when the irradiation was divided into two sessions separated by a dark interval or when the treatment irradiance was reduced from 200 to 50 mW cm⁻². Subsequent studies using this tumor model (Foster *et al.*, 1991; Gibson *et al.*, 1994) and xenografts of human mesothelioma in nude mice (Feins *et al.*, 1990; Gibson *et al.*, 1994) confirmed this irradiance

dependence and observed an even greater enhancement when the treatment was performed at 100 mW cm^{-2} delivered in 30 s doses separated by 30 s dark intervals. Later, similar irradiance dependence was reproduced by Sitnik and Henderson (1998a) in mice bearing radiation-induced fibrosarcoma (RIF) tumors. Foster *et al.* (1991) argued on the basis of a simple oxygen diffusion model that these effects could be explained by the photochemical consumption of oxygen, which is more significant during higher irradiance treatment. Direct measurements of tissue oxygenation during Photofrin-PDT have confirmed a significant reduction of local oxygen concentration (Henderson *et al.*, 2000; Tromberg *et al.*, 1990). In one such set of experiments, Sitnik and Henderson (1998b) demonstrated that the depletion of oxygen in murine RIF tumors is irradiance dependent.

The quantitative predictions of the oxygen diffusion model in spherical geometry were tested by Foster *et al.* (1993), who irradiated Photofrin-sensitized multicell tumor spheroids with various irradiances of 630 nm light. In that study, it was shown that decreasing the treatment irradiance decreased the fraction of cells that survived PDT, as measured by a colony forming assay. This decrease was consistent with a model in which a portion of the spheroid was rendered hypoxic by photochemical and metabolic oxygen consumption and hence protected from photodynamic damage. In a subsequent study, Nichols and Foster (1994) made direct measurements of the oxygen consumption at the edge of spheroids during irradiation and used the oxygen diffusion-with-consumption model to estimate the reacted dose of $^1\text{O}_2$ as a function of radial position in the spheroid. It was shown that the fraction of cells killed by treatment in the 1993 study was highly correlated with the volume fraction of the spheroid that received a thresh-

old dose of 323 μM of $^1\text{O}_2$. These results and those of the previous animal studies are consistent with oxygen consumption and cell killing resulting from the reaction of $^1\text{O}_2$ with cellular targets. Georgakoudi *et al.* (1997) extended the oxygen diffusion-with-consumption model to include the effects of photobleaching of the sensitizer and used this improved model to demonstrate that the photobleaching of Photofrin in spheroids undergoing PDT is also predominantly mediated by $^1\text{O}_2$.

Fluorescence photobleaching *in vivo* has long been recognized as a factor in PDT sensitized by Photofrin. Early observations of photobleaching (Mang *et al.*, 1987; Moan, 1986) lead to the development of a definition of photodynamic dose which included the effects of photobleaching (Potter *et al.*, 1987) and to the suggestion that photobleaching could be exploited to reduce unwanted Photofrin-induced skin photosensitivity (Boyle and Potter, 1987). These studies did not address the question of whether the photobleaching of Photofrin was irradiance-dependent. Based on the observations in spheroids, however, it is reasonable to expect the photobleaching of Photofrin and the deposition of dose *in vivo* to be mediated by $^1\text{O}_2$ and hence dependent on the tissue oxygen concentration. It is therefore expected that high irradiance PDT will lead to a reduction in the rate of photobleaching commensurate with the observed reduction in biological response. This chapter will present the first direct experimental test of the irradiance dependence of Photofrin photobleaching using *in vivo* fluorescence spectroscopy.

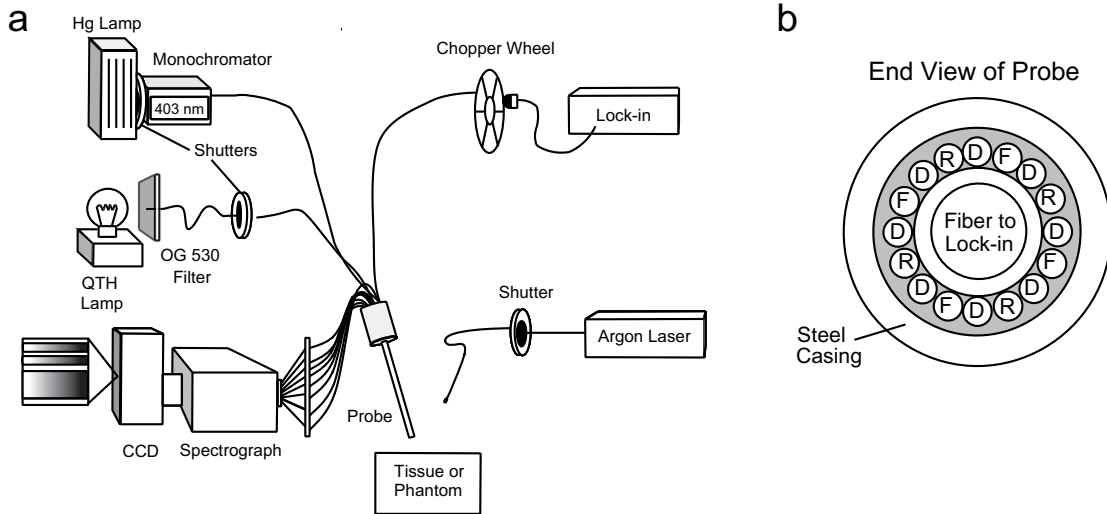


Figure 3.1: (a) Schematic diagram of the system for performing fluorescence and reflectance spectroscopy during PDT and (b) end view of the spectroscopy probe showing source-detector fiber geometry. F: fluorescence excitation fiber; R: reflectance source fiber; D: detection fiber to spectrograph and CCD. The central fiber carries diffusely reflected 403 nm light to the photodiode and lock-in amplifier.

3.2 Experimental methods and data analysis

3.2.1 Instrumentation

The experiments described in this chapter use a fiber-based optical probe designed to allow collection of fluorescence and diffuse reflectance in the same source-detector geometry. Reflectance is collected in the spectral window corresponding to that of the detected fluorescence emission (575 to 720 nm) and at the excitation wavelength (403 nm) in order to correct the fluorescence for the effects of tissue optical properties. Schematic diagrams of the probe and of the entire spectroscopy system are shown in figure 3.1. The probe consists of four fluorescence

excitation source fibers, four reflectance source fibers and eight detection fibers, each of which has a 200 μm core diameter and a numerical aperture of 0.22. As illustrated in figure 3.1b, the fibers are arranged such that each detection fiber is adjacent to a fluorescence excitation fiber on one side and a reflectance source fiber on the other. These fibers are evenly spaced around the circumference of a 400 μm core diameter silica fiber, which monitors diffusely reflected excitation light. The 17 fibers are cemented together and encased in a steel tube of diameter 3.2 mm. The probe is placed 8 mm above the surface of the tissue or tissue simulating phantom being studied. It is oriented at an angle sufficient to exclude specular reflectance.

The four probe reflectance source fibers are illuminated by the output of a 365 μm core diameter transfer fiber that is coupled to a 250 W quartz tungsten halogen (QTH) lamp, as shown in figure 3.1a. In order to minimize the excitation of fluorescence during the reflectance measurement, a longpass filter (OG 530, Schott, Duryea, PA) is placed between this lamp and the transfer fiber. The fluorescence excitation source is a 100-W mercury arc lamp (model 60100, Oriel, Stratford, CT). Light from this source passes through a monochromator (model 77250 Oriel) centered at 403 nm and is then coupled into a 1 mm core diameter transfer fiber, which illuminates the four fluorescence excitation fibers of the probe. For the purposes of these studies, the excitation wavelength was chosen as 403 nm to confine the excitation of fluorescence to the most superficial layer of the tissue. This wavelength also coincides with a peak in the mercury lamp spectrum and with the approximate location of the Soret band of the chlorin- and porphyrin-based sensitizers' absorption spectra. The output of both lamps is monitored by

optical fibers to allow correction for variations in lamp intensity, and both sources can be blocked by electronically controlled mechanical shutters (Uniblitz, Vincent Associates, Rochester, NY).

The eight, 200 μm detection fibers as well as the two fibers used to monitor lamp intensities are connected *via* a fiber patch panel to ten, 300 μm fibers terminating in a linear ferrule, which in turn is positioned at the focal plane of a 0.275 m imaging spectrograph (Acton Research Corporation, Acton, MA). The fibers are imaged through a 300 g mm^{-1} diffraction grating onto the surface of a nitrogen-cooled, 512 X 512 pixel, 16 bit charge-coupled device (CCD) array (Princeton Instruments, Trenton, NJ). The dispersion of the grating and the detector area are such that each measurement includes approximately 146 nm of the fluorescence or reflectance spectrum.

In order to maximize signal recovery, regions on the CCD comprising four pixels along the wavelength axis and 220 pixels along the slit axis are binned to create a single superpixel. Because each superpixel includes contributions from all eight detection fibers, the measured signal is the sum of the emission collected by these eight fibers. The four-pixel binning in wavelength limits the spectral resolution to 1.14 nm.

Diffuse reflectance at 403 nm is collected by the probe's center fiber and passes through an optical chopper to a silicon photodiode (S2386-18L, Hamamatsu Corporation, Bridgewater, NJ). A short-pass filter (BG 28, Schott) prevents detection of fluorescence by the photodiode. The photodiode output is monitored by a lock-in amplifier (SR-510, Stanford Research Systems, Sunnyvale, CA), digitized and stored on a computer. The measurement of reflected excitation light by

the photodiode is limited by electronic noise, whereas the CCD's signal-to-noise ratio is limited by the intensity of the fluorescence. Placing the optical chopper in the photodiode detection path rather than at the excitation source allows the lock-in amplifier to reduce electronic noise without reducing the intensity of the fluorescence signal. In the Photofrin experiments, the photodiode and lock-in were replaced with a UV-sensitive silicon detector and power meter (Newport Corp). This detector is less sensitive to electronic noise, and includes its own amplification system, negating the need for a lock-in amplifier.

The sequence of data collection is controlled by an electronic timing circuit designed and built for these experiments. Before the first measurement the excitation and reflectance sources are blocked by closed shutters. The reflectance source shutter is opened first, and the CCD acquires the reflectance spectrum in the emission spectral window. Then, the reflectance source shutter is closed, and the fluorescence excitation shutter is opened. The CCD acquires the fluorescence spectrum, and the intensity of the diffusely reflected 403 nm excitation light is recorded. The excitation shutter is then closed. When PDT irradiation is administered, a third shutter interrupts the treatment laser beam during reflectance and fluorescence measurements. In the photobleaching experiments, the laser shutter is held open for the specified treatment interval, after which the sequence of data acquisition resumes. The cycle is then repeated. During the early stages of a photobleaching experiment when there is abundant fluorescence signal, the total duration of the laser beam interruption is under 2 s. As the fluorescence is bleached, the length of the interruption is increased as needed to a maximum of 6 s by the end of the experiment.

Before any spectral analysis is done, the signal measured by the CCD is first corrected for instrument effects. The CCD controller electronics add a fixed offset to each pixel before transferring the data to the computer. This offset is corrected automatically in software (WinSpec, Princeton Instruments). To correct for the optical throughput of the system, the measured fluorescence data are then multiplied by a wavelength-dependent calibration function, which is obtained experimentally by comparing the measured and known spectra of a standard irradiance source (Model LS-1-CAL, Ocean Optics, Dunedin, FL). Each reflectance spectrum is then divided by the reflectance spectrum of a Lambertian reflector (CAT 849 1656, Scientific Imaging Systems, Eastman Kodak Company, Rochester, NY) in order to correct for the QTH lamp emission spectrum and the optical throughput of the reflectance source fibers. Finally, all spectra are corrected for variations in lamp intensity.

3.2.2 Empirical correction for changes in tissue optical properties

Changes in the measured fluorescence from an absorbing and scattering system may be due either to changes in the actual fluorophore concentration or to changes in the optical properties of the medium. In order to minimize the possibly confounding effects of tissue optical properties, which during PDT may be dynamic, we utilize a modification of the method suggested by Wu *et al.* (1993), in which the measured fluorescence signal is divided by the reflectance signal measured in the same wavelength window. In addition, we have found experimentally that division

of the fluorescence by the diffuse reflectance at 403 nm raised to the 0.8 power provides a significant improvement to the correction. The value of the exponent (0.8) was determined from measurements of PpIX in tissue-simulating phantoms and is likely to be specific to the particular experimental probe being used. Because the source-detector geometry is nearly identical for all measurements, the optical properties sampled by the fluorescence and both reflectance measurements are approximately the same.

In order to test the ability of our probe and method of analysis to report relative fluorophore concentrations in the presence of physiologically relevant absorption and scattering, experiments were performed in a tissue-simulating phantom. The phantom consisted of 100 mL of buffered, 0.9% saline and 10 mL of 10% Liposyn II (Abbott Labs, North Chicago, IL). This 0.9% lipid volume phantom has a transport scattering coefficient of approximately 1 mm^{-1} at 630 nm, which is similar to that of the tissue (van Staveren *et al.*, 1991). The phantom was kept at constant temperature and stirred throughout the experiment. In order to produce fluorescence, 2.4 mg ml^{-1} PpIX (Porphyrin Products, Logan, UT) was added to the phantom.

To study the effects of ambient absorption changes on the fitted, relative fluorophore concentration returned by our algorithm, a small, fixed concentration of the weakly fluorescent water-soluble porphyrin manganese *meso*-tetra (4 sulfonatophenyl) porphine (MnTPPS) was added sequentially to a final concentration of 0.32 mg ml^{-1} , with reflectance at excitation and emission wavelengths and fluorescence spectra being acquired after each addition. The absorption spectrum of

MnTPPS is similar to that of hemoglobin, with a strong absorption band around 400 nm and weaker absorption in the PpIX emission range.

The initial PpIX fluorescence spectrum (with no absorber added), basis spectra accounting for the slight fluorescence of MnTPPS and lipids, and a 61-term Fourier synthesis were fit to each of the corresponding fluorescence spectra using the singular value decomposition (SVD) fitting algorithm described in section 2.5.1.1).

In figure 3.2, the estimate of the PpIX spectral amplitude returned by SVD is plotted as a function of the normalized integrated reflectance at the excitation wavelength for two cases: (1) with no correction for optical properties (solid circles); and (2) with correction of the fluorescence spectrum and amplitude using division by the emission wavelength reflectance and by the excitation wavelength reflectance raised to the 0.8 power (open circles). In both the corrected and uncorrected cases, the PpIX amplitudes are normalized to that obtained in the presence of a value of the integrated reflectance typical of that encountered *in vivo* prior to treatment. The dashed horizontal line represents the actual normalized PpIX concentration, which was not changed during the experiment. This correction is able to render the fluorescence measurement immune to the effects of background absorption changes over a range of reflectance changes at least three times greater than that encountered in the course of our *in vivo* experiments.

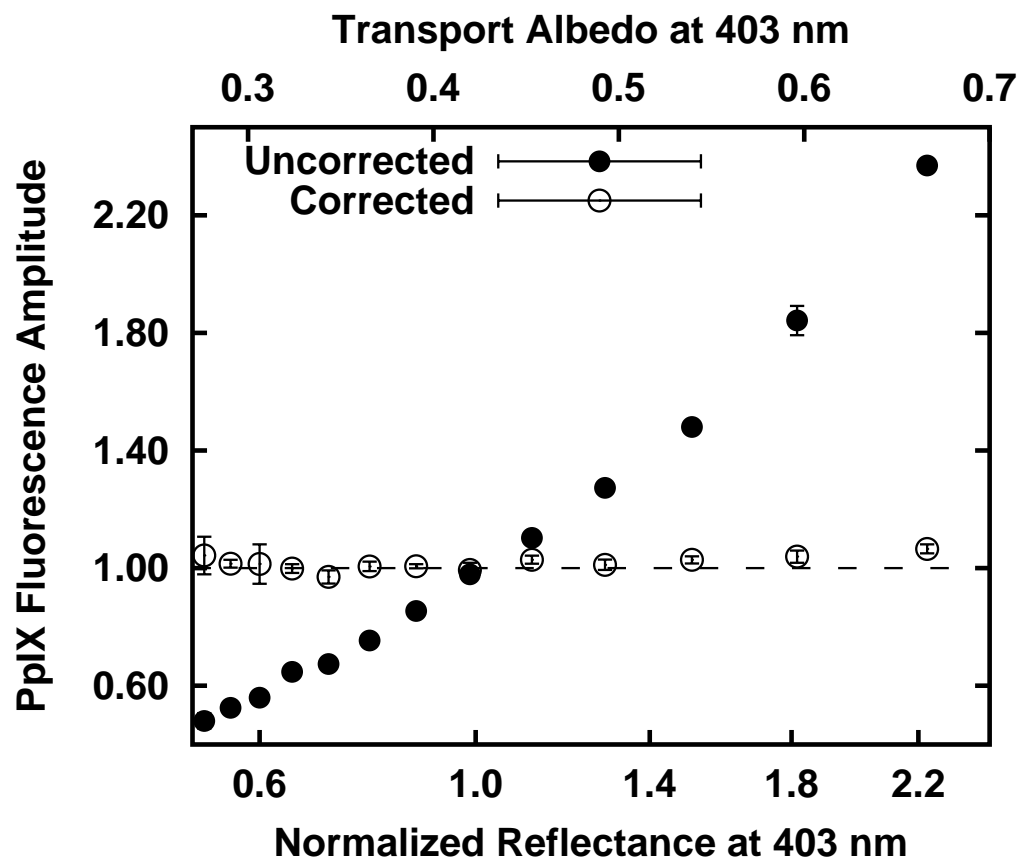


Figure 3.2: Correction of fluorescence for changes in optical properties. The fitted fluorophore (PpIX) concentration is plotted as a function of the normalized reflectance at 403 nm measured in a scattering emulsion. The reflectance was varied by addition of MnTPPS. The filled circles (\bullet) depict fluorescence estimates that have not been corrected for absorption changes, and the open circles (\circ) illustrate the corrected estimates. The dashed horizontal line indicates the actual concentration, which did not change during the experiment. Error bars indicate the standard deviations from six measurements. The transport albedo of the scattering emulsion at 403 nm is indicated on the top horizontal axis. This range of concentrations provided variations in reflectance intensity much greater than those observed during PDT of normal rat skin.

3.2.3 Construction of basis spectra for fluorescence photobleaching analysis

The emission spectrum, corrected for instrument response and tissue optical properties as described above, is analyzed as a linear combination of basis fluorescence spectra using the SVD algorithm described in section 2.5.1. Briefly, basis spectra corresponding to autofluorescence, the photosensitizer being studied, other fluorophores which evolve during treatment and a 61-term Fourier series are fit to the instrument- and reflectance-corrected fluorescence data, f_{Total} , using the equation,

$$f_{Total}(\lambda) = \sum_{i=1}^N A_i(100)f_i(\lambda) + (2.0)B_0 + \sum_{k=1}^{30} (2.0e^{-k/20}) \times \left[B_k \sin\left(\frac{\pi k(\lambda - \lambda_i)}{\lambda_f - \lambda_i}\right) + C_k \cos\left(\frac{\pi k(\lambda - \lambda_i)}{\lambda_f - \lambda_i}\right) \right] \quad (3.1)$$

where A_i and $f_i(\lambda)$ are the amplitude and known spectrum of the i^{th} of N total fluorophores, respectively. The numbers in the small parentheses denote the weights used in the SVD fitting, as described in section 2.5.1. The spectral amplitudes A_i , B_k and C_k are returned by the SVD algorithm. Each sensitizer requires its own set of basis spectra, as described in the following sections.

3.2.3.1 ALA-PpIX

In this case, the basis fluorescence spectra used in the analysis are those of PpIX, two photoproducts of PpIX, uroporphyrin/coproporphyrin (Up/Cp), and the measured autofluorescence of rat skin. All basis spectra are derived from measure-

ments performed *in vivo*. In each instance the *in vivo* data used to create the basis spectra were first corrected for optical properties as described above.

An average autofluorescence spectrum was constructed from the average of 60 *in vivo* measurements of the skin of three animals that had not received ALA. Rat skin autofluorescence typically contains the signature of naturally occurring porphyrins, which is spectrally indistinguishable from ALA-induced PpIX. In order to remove this contribution, the fluorescence of preformed PpIX (Porphyrin Products, Logan, UT) in a lipid emulsion was measured. This spectrum, scaled appropriately, was subtracted from the average autofluorescence to yield a spectrum which is the average non-porphyrin autofluorescence.

An initial PpIX spectrum was constructed from the average of 21 *in vivo* measurements of the skin fluorescence of 21 animals 3 h after systemic administration of 200 mg kg⁻¹ ALA. At this time point, PpIX is the dominant fluorophore in the 620 to 720 nm range; however, there is still a strong contribution from autofluorescence, especially at shorter wavelengths. This contribution was removed by subtracting the average non-porphyrin autofluorescence found previously as described above. The resulting spectrum is the *in vivo* fluorescence spectrum of PpIX, without contamination from autofluorescence, and constitutes the PpIX basis spectrum used in the subsequent spectral analysis.

While the average autofluorescence is useful in constructing a PpIX basis spectrum, in fact each animal's autofluorescence is different. To account for this, an individual autofluorescence basis spectrum is constructed for each animal prior to PDT. The initial (pre-irradiation) spectrum obtained 3 h after ALA injection is fit using SVD as a combination of the average non-porphyrin autofluorescence,

the PpIX basis spectrum, and a 61-term Fourier series as described above. Here the Fourier series accounts for differences between the average non-porphyrin autofluorescence and the individual animal's autofluorescence. The autofluorescence basis spectrum for a particular animal is therefore the sum of the fitted average non-porphyrin autofluorescence and the Fourier series contribution. This spectrum is free of any contribution from PpIX.

The PDT-induced PpIX photoproduct fluorescence near 676 nm has been attributed to hydroxyaldehyde chlorins produced by the photodynamic degradation of PpIX (Wessels *et al.*, 1993, and references therein). As this is the primary photoproduct of PpIX, we will refer to it as photoproduct I. In keeping with our practice of using spectra measured *in vivo* for PpIX and autofluorescence, we use the *in vivo* spectrum of photoproduct I to construct its basis spectrum. Six PDT irradiation experiments were chosen in which the photoproduct I peak at approximately 676 nm was cleanly separated from other spectral features. From these experiments, a total of 38 spectra were used, all acquired after sufficient irradiation to produce detectable photoproduct I. Each was fitted by SVD using a combination of PpIX, autofluorescence and the Fourier series. The fitted contributions of autofluorescence and of PpIX were subtracted from each spectrum, leaving the spectrum of photoproduct I plus small contributions from unknown fluorophores. These 38 subtracted spectra were averaged, and a single Lorentzian was fit to the resulting spectrum using a nonlinear fitting algorithm. The best fit Lorentzian, centered at 675.7 nm with a width of 27 ± 3 nm was adopted as the photoproduct I basis spectrum. The uncertainty in the center wavelength was smaller than the spectral resolution of the measurement.

A second fluorescent photoproduct with an emission peak near 652 nm has been observed by Bandanas *et al.* (2000) in cell suspensions. A fluorescence emission peak in the same region of the spectrum is evident in our *in vivo* data. For clarity, we will refer to this photoproduct as product II. The basis spectrum of product II was generated in the same manner as that of product I. Ninety-five spectra from six experiments were selected, all of which contained a distinct contribution from product II. A Lorentzian peak was fit to the average of these spectra after the fitted contributions of PpIX, autofluorescence and product I were subtracted, as described above. The resulting Lorentzian is centered at 654 ± 2 nm and has a width of 15 ± 3 nm.

Dietel *et al.* (1996) have identified a fluorescence peak in the spectral region near 620 nm in Ehrlich ascite carcinoma cells incubated with ALA and have assigned it to the presence of water soluble Up and Cp. Heil *et al.* (1997) have detected similar spectra in the bladder contents of rats after instillation with ALA. In order to create Up and Cp basis spectra, we have measured the fluorescence spectra of preformed Up and Cp (Porphyrin Products) in saline solutions of varying pH and in saline solutions containing lipids. In agreement with the work of Polo *et al.* (1988), we find that the spectra of Up and Cp in aqueous solutions exhibit two distinct shapes depending upon the pH of the local microenvironment. In addition, we find that Up and Cp each exhibit a third form which is present only in solutions containing lipids at pH below 6.5 (Cp) or 5 (Up). Of the six spectral shapes produced *in vitro* (three for each species), only those obtained in aqueous solution at physiological pH and in lipid-containing solution have fluorescence emission peaks in the region near 620 nm.

In order to quantify which of the Up and Cp spectra are relevant to the fitting of *in vivo* data, 99 spectra from five *in vivo* experiments that produced prominent 620 nm peaks were selected. Fitted contributions of PpIX, autofluorescence and both photoproducts were subtracted and the resulting spectra were averaged. A sum of the four Up and Cp spectra with peaks near 620 nm was fit to the average spectrum. Only the spectra of Up in physiological pH aqueous solution and Cp in lipid emulsion were found to contribute significantly. The fit was repeated using only these two spectra. The resulting best fit spectrum, a sum of 51% Up in physiological pH aqueous solution and 49% Cp in lipid emulsion, was adopted as the Up/Cp basis spectrum.

The basis spectra for PpIX, both photoproducts and autofluorescence used in the SVD analysis of *in vivo* fluorescence data are shown in figure 3.3(a). A comparison of the *in vivo* PpIX emission spectrum with that of preformed PpIX in a lipid emulsion phantom is shown in figure 3.3(b). The similarity between these spectra is apparent.

The weighted sum of Up and Cp spectra used as the Up/Cp basis is shown in figure 3.3(c), along with the two spectra which comprise it. Figure 3.3(d) shows the four spectra of Up and Cp that were not used in creating the basis spectrum. The Up/Cp basis spectrum fits adequately the *in vivo* data. The fitting method used to generate this basis spectrum, however, cannot rigorously exclude the presence of other forms of Up and Cp or of other water-soluble porphyrins with similar emission spectra.

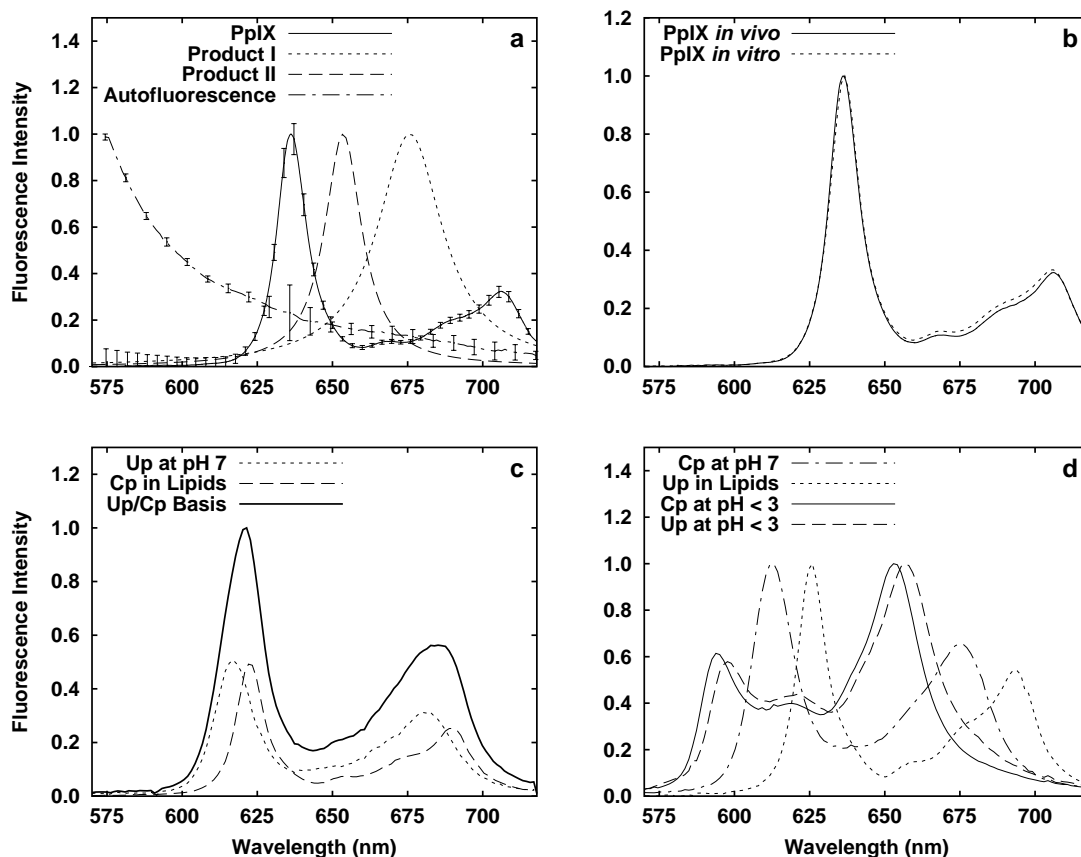


Figure 3.3: Basis spectra used in SVD fitting of *in vivo* fluorescence measured from PpIX-sensitized normal rat skin. (a) Spectra of PpIX, both photoproducts, and autofluorescence. The PpIX and autofluorescence spectra are averages of *in vivo* measurements, as described in section 3.2.3.1. In both cases, the error bars indicate standard deviations. The increased uncertainty in the autofluorescence spectrum near 635 nm is the result of the subtraction of the emission from endogenous porphyrin. The photoproducts are fitted Lorentzians at 676 and 654 nm. (b) PpIX spectra acquired *in vivo* (—) and *in vitro* (- -). (c) The spectra used to create the Up/Cp basis spectrum. The measured spectra are normalized such that the sum (heavy line) has a maximum peak of height 1. (d) The spectra of Cp at pH 7 in aqueous solution, Up in a lipid emulsion and Cp and Up at pH 3 in aqueous solution.

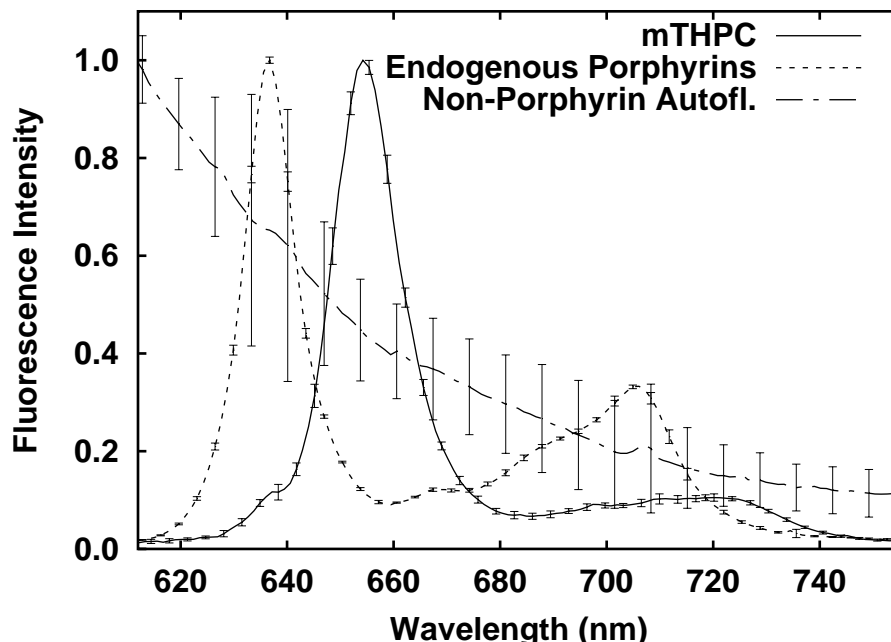


Figure 3.4: Basis spectra used in SVD analysis of fluorescence spectra obtained from mTHPC-sensitized normal rat skin *in vivo*. The solid line represents the emission spectrum of mTHPC, the dashed line, endogenous porphyrins and the dash dot line, non-porphyrin autofluorescence. Each spectrum is an average taken from several animals. Errorbars indicate standard deviations.

3.2.3.2 mTHPC

In the case of mTHPC sensitization, the *in vivo* spectra are composed of mTHPC fluorescence and tissue autofluorescence, and the basis spectra used in the fitting are chosen accordingly. Autofluorescence is broken into two components, one of which is similar to the non-porphyrin autofluorescence used in the analysis of PpIX photobleaching. The second component is emission from naturally occurring porphyrins in the tissue. Because the proportions of the two components may vary with time and among animals, it is necessary to treat them as separate

basis spectra. In the case of ALA-sensitized tissue, the inclusion of PpIX as a basis spectrum accounted for any endogenous porphyrin fluorescence implicitly. In the case of mTHPC a basis spectrum distinct from those of non-porphyrin autofluorescence and mTHPC is required. As noted previously, the spectrum of the endogenous porphyrin emission is indistinguishable from that of PpIX. The spectrum of preformed PpIX (Porphyrin Products, Logan, Utah) in a lipid emulsion was therefore adopted as the basis spectrum for the endogenous porphyrin component of autofluorescence. The non-porphyrin autofluorescence spectrum was constructed from the average of five *in vivo* measurements of the untreated skin of two animals. A basis spectrum different from that used for PpIX fitting was required because the data were acquired over a different wavelength range, however the two are in agreement in the region where they overlap. The mTHPC basis spectrum was constructed from 10 fluorescence spectra of normal rat skin measured 72 h after administration of 1 mg kg^{-1} mTHPC. The endogenous porphyrin and autofluorescence contributions were scaled and subtracted to yield the *in vivo* mTHPC fluorescence spectrum.

3.2.3.3 Photofrin

The basis spectrum for Photofrin was constructed by averaging the emission spectra of the normal skin of six rats after administration of 10 mg kg^{-1} Photofrin. The autofluorescence component of these spectra was isolated using the SVD fitting algorithm and subtracted prior to averaging. The autofluorescence basis spectrum used for fitting of spectra from Photofrin-treated animals is the same as that used in the case of mTHPC.

During PDT, Photofrin exhibits the formation of a fluorescent photoproduct with an emission peak at 655 nm. Moan and Kessel (1988) observed a similar peak in cell suspensions irradiated with blue and ultraviolet light. In order to generate a basis spectrum for this product, five animals were exposed to sufficient low-irradiance (5 mW cm^{-2}) irradiation to produce significant accumulation of the fluorescent photoproduct. Spectra were acquired from the skin of these animals, and the autofluorescence and Photofrin components of the spectra were identified and subtracted using the SVD fitting algorithm. The remaining spectra, containing emission only from the photoproduct, exhibited a single asymmetric emission peak centered at 655 nm. The photoproduct basis spectrum was constructed by finding a best-fit Lorentzian line shape for each side of the peak. The resulting spectrum, with half-widths of $15.3 \pm .75$ and 30.2 ± 3 on the short- and long-wavelength sides, respectively, accurately models the emission of the photoproduct with a smooth, noise-free line shape.

Each basis spectrum is normalized to a peak value of 1.0 prior to fitting. The normalized basis vectors for autofluorescence (dashed line), Photofrin (solid line) and the fluorescent photoproduct (dash-dot line) are illustrated in figure 3.5.

3.2.4 Animal preparation for *in vivo* fluorescence photobleaching measurements

Experiments were performed *in vivo* on the intact, normal skin of female Fischer rats. The autofluorescence spectrum of these animals typically contains a peak centered at approximately 675 nm, identified by Weagle *et al.* (1988) as

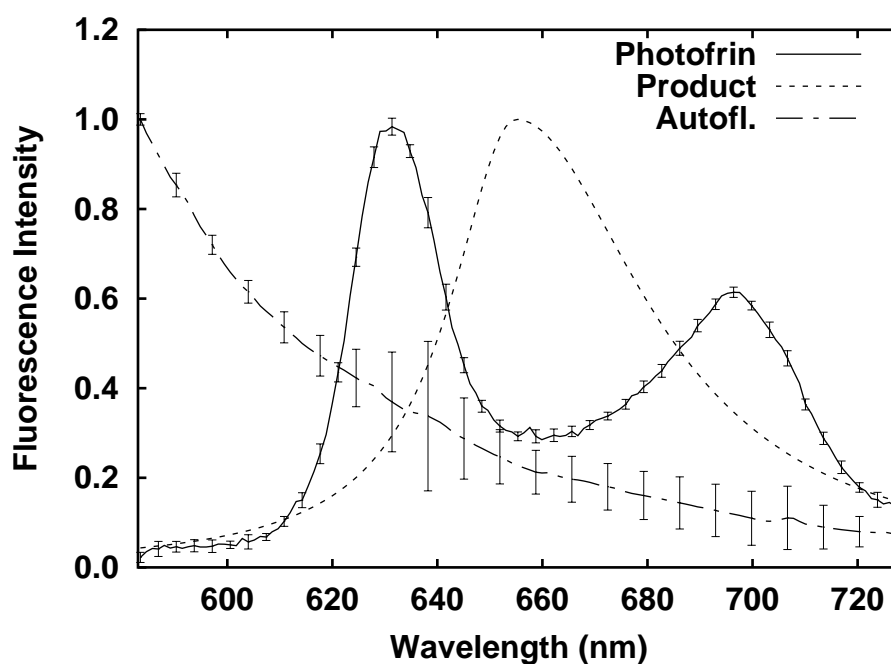


Figure 3.5: Basis spectra used for SVD fitting of fluorescence spectra obtained from Photofrin-sensitized animals. All spectra are based directly on *in vivo* measurements, as described in the text. Each data point is the average of measurements from several measurements. Errorbars indicate standard deviations.

originating from some combination of pheophytin a and pheophorbide a. Both of these fluorophores are produced by the degradation of chlorophyll found in standard laboratory rat food. The amplitude of the emission of these fluorophores is highly variable with time (Gudgin Dickson *et al.*, 1995), and it overlaps spectrally with the PpIX photoproduct emission and the emission spectra of mTHPC and Photofrin. In addition, pheophorbide a has been identified as a photosensitizer. In order to eliminate these problems, all animals used in the study were kept on a chlorophyll-free diet prepared according to the published recipe of Holmes *et al.* (1995) for a minimum of 2 weeks prior to the first treatment. Spectra taken prior to sensitizer administration indicate no detectable emission due to chlorophyll or its degradation products.

Optical measurement of the skin requires the removal of hair from the skin surface. This was accomplished by the application of the hair removal lotion Nair (Carter-Wallace, Inc., New York, NY) and subsequent rinsing with distilled water. We confirmed that Nair does not fluoresce when excited at 403 nm. In some cases, its application did appear to induce an increase in the endogenous porphyrin component of autofluorescence at timepoints of 24 to 96 hours (data not shown), however the non-porphyrin component of autofluorescence was unchanged. In cases where the hair is especially thick, it was first shortened with an electric shear. All animal care and handling were done according to guidelines established by the University Committee on Animal Resources at the University of Rochester.

3.2.5 Sensitizer administration

3.2.5.1 ALA

Prior to PDT, each animal was anesthetized with approximately 60 mg kg^{-1} ketamine hydrochloride and 6 mg kg^{-1} xylazine. ALA (Porphyrin Products) dissolved in sterile saline was administered in a dose of 200 mg kg^{-1} body weight by tail vein injection. The animals were then kept in dark conditions with access to food and water for 3 h, during which time they recovered from the initial anesthetic. Hair removal was performed prior to placing the animals in darkness.

3.2.5.2 mTHPC

The photosensitizer mTHPC was obtained from Scotia Pharmaceuticals (Surrey, UK). It was dissolved in a solvent mixture of 30% polyethylene glycol 400, 20% ethanol and 50% water, according to the manufacturer's recommendations. mTHPC was administered at a dose of 1 mg kg^{-1} body weight by tail vein injection. As with ALA, the *i.v.* injection was performed under anesthesia, after which the animals are kept in darkness for 72 h.

3.2.5.3 Photofrin

Photofrin was obtained as a powder, and was reconstituted to a concentration of 5 mg ml^{-1} in a 5% solution of dextrose in sterile water. 24 hours prior to irradiation, each rat was injected with 10 mg kg^{-1} Photofrin *via* the tail vein. The concentration of Photofrin resulted in a total injection volume of approximately $250 \text{ }\mu\text{l}$. A more sophisticated animal restraint was used for Photofrin injections

Sensitizer	dose	drug-light interval
PpIX	200 mg ALA kg ⁻¹	3 h
mTHPC	1 mg kg ⁻¹	72 h
Photofrin	10 mg kg ⁻¹	24 h

Table 3.1: Sensitizer dose and drug-light interval for each sensitizer investigated. In the case of PpIX, the dose given is that of the prodrug ALA.

than was available for the cases of ALA-PpIX or mTHPC, eliminating the need for anesthesia during the injection. Removal of hair was therefore performed immediately prior to irradiation.

The sensitizer dose and drug-light interval for each sensitizer are listed in table 3.1. These parameters were chosen to fall within the range of doses and drug-light intervals reported in the literature as effective in preclinical and clinical studies.

3.2.6 PDT irradiation conditions

Immediately before PDT, each animal was anesthetized with sodium pentobarbital at a dose of 65 mg kg⁻¹. This was sufficient to chemically restrain the animals for the duration of irradiation. In order to prevent movement during irradiation and optical measurements, the animals were also mechanically restrained with tape. In all cases, the irradiated area was on the rear flank, posterior to the femur. This location was selected to avoid possible damage to internal organs and to provide repeatable positioning of the probe.

The optical probe was placed 8 mm above the skin and fixed in place. The treatment area was irradiated with 514 nm light from an argon-ion laser (Photofrin

and PpIX) or 650 nm light from a dye laser (mTHPC). The laser light was coupled into a 365 μ m core diameter optical fiber terminated with a gradient index lens (General Fiber Optics, Fairfield, NJ). The area treated was a 1 cm diameter circle. The area interrogated by the probe was smaller than and concentric with the treatment area.

The power output of the laser was monitored with a photodiode to ensure that the desired irradiance at the skin surface was maintained. In the cases where the argon laser was used for treatment, the laser's internal photodiode and feedback control hardware were utilized. When the dye laser was used, a custom built system was employed in which a portion of the beam was diverted by a beam splitter and collected by a photodiode. The photodiode output was monitored by an analog circuit which emitted an audible signal when the incident power drifted by more than 3% from the desired value. In these instances, the dye laser was readjusted manually to restore the correct power.

In order to follow the course of photobleaching, measurements of fluorescence and reflectance were made as the treatment progressed. As described above, it was necessary to interrupt treatment at regular intervals for durations of from 2 to 6 s in order to make these measurements. Each animal was used for one experiment on each rear flank. In the case of mTHPC, animals were used for up to 4 irradiations with a single dose of sensitizer. In order to evaluate the effect of the probe's 403 nm illumination, control experiments were performed without laser irradiation. In each case, the effect of probe-induced bleaching on the *in vivo* sensitizer kinetics was smaller than the animal-to-animal variation within each group.

Sensitizer	Treatment Wavelength	Irradiances (mW cm ⁻²)
PpIX	514 nm	1, 5, 100
mTHPC	650 nm	5, 20, 50
Photofrin	514 nm	5, 100

Table 3.2: Irradiation parameters for *in vivo* PDT on normal rodent skin. In each case, the irradiances were chosen to span a range over which an irradiance dependence was observed.

The set of irradiances investigated was chosen for each sensitizer to allow comparison with previous literature and to span a range over which interesting irradiance-dependent effects could be observed. The treatment conditions are listed in table 3.2.

3.3 *In vivo* photobleaching results

3.3.1 ALA-induced PpIX

3.3.1.1 *In vivo* reflectance during PDT

To illustrate the extent of the reflectance changes observed during PDT *in vivo* under the conditions of our experiments, we have plotted in figures 3.6(a) and (b) the amplitude of the measured spectrally integrated reflectance *vs* fluence at 403 nm (the excitation wavelength) and in the fluorescence emission window respectively.

In each case, the reflectance is normalized to 1 as its initial value. Interestingly, at the lower irradiances the reflectance in both wavelength ranges increases with

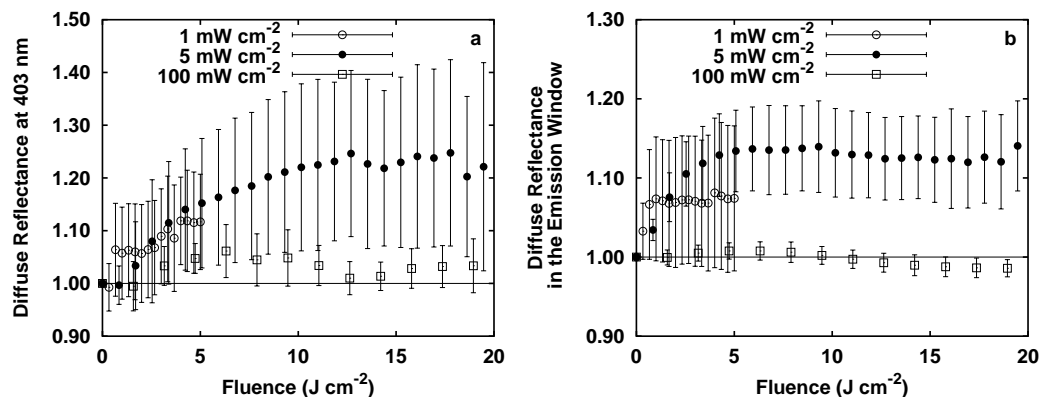


Figure 3.6: Spectrally integrated reflectance at (a) 403 nm and (b) in the interval from 575 to 720 nm in ALA-sensitized skin *in vivo* during PDT. The three irradiances used are given in the legend.

the onset of irradiation. Because the magnitude of the measured reflectance is sensitive to both scattering and absorption, the increase in reflectance could result from either a decrease in absorption or an increase in scattering in either or both wavelength intervals.

3.3.1.2 PpIX fluorescence photobleaching and photoproduct formation *in vivo*

Figure 3.7(a) shows a typical series of reflectance-corrected fluorescence spectra acquired *in vivo* from the skin of a rat treated with 514 nm light delivered at 100 mW cm⁻² 3 h after tail vein injection of 200 mg kg⁻¹ ALA. As the PpIX fluorescence diminishes as a result of bleaching, the fluorescence emission of photoproduct I near 676 nm becomes apparent. In order to illustrate the photoproduct more clearly, figure 3.7(b) shows five spectra selected from the same data set,

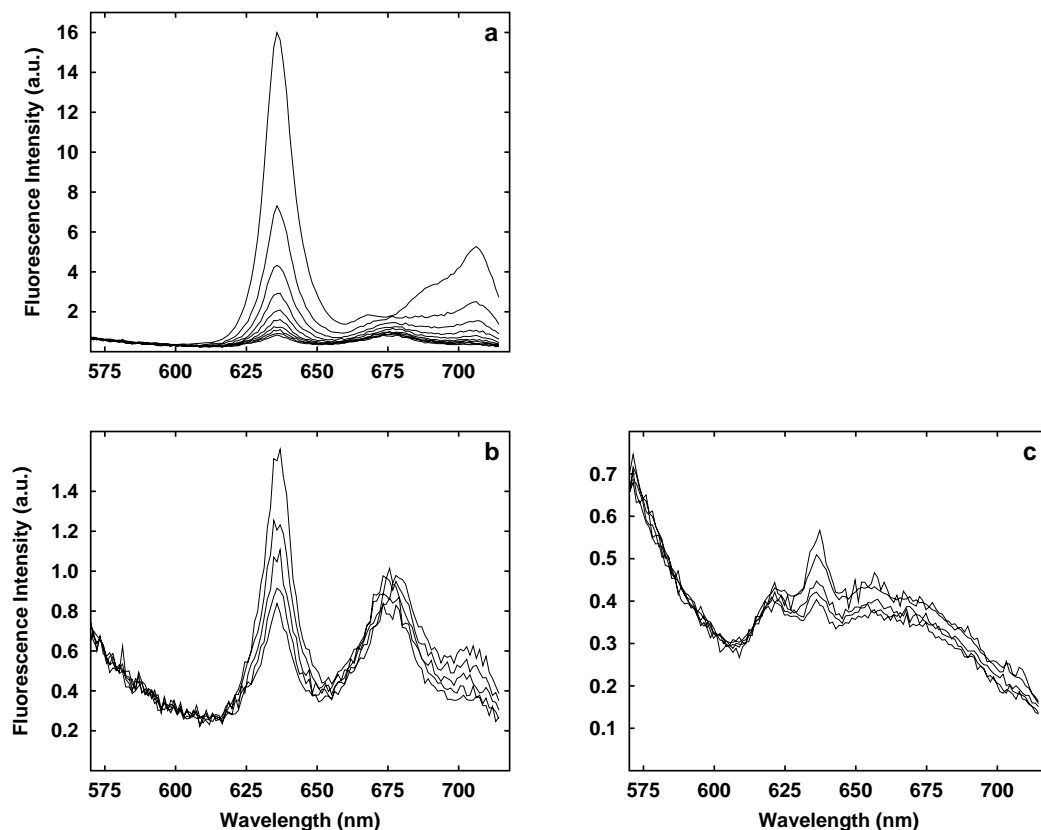


Figure 3.7: (a) A typical series of reflectance-corrected fluorescence spectra obtained from ALA-sensitized skin *in vivo* during PDT with 514 nm light and an irradiance of 100 mW cm^{-2} . Spectra shown were acquired at 3 J cm^{-2} intervals. (b) Spectra taken from the same data set at 3 J cm^{-2} intervals beginning at a fluence of 15 J cm^{-2} . (c) A typical series of spectra obtained during PDT with 514 nm light and an irradiance of 5 mW cm^{-2} . Spectra shown were acquired at intervals of 2 J cm^{-2} beginning at 10 J cm^{-2} .

which correspond to irradiation fluences of 15 to 27 J cm⁻². In these spectra, the photoproduct I emission peak is cleanly separated from the PpIX emission, and no other spectral features are evident.

Figure 3.7(c) shows five spectra obtained from the skin of an animal similarly irradiated with 10 to 18 J cm⁻² of 514 nm light delivered at 5 mW cm⁻². In this case, an emission peak near 622 nm is clearly visible, which may be assigned to Up and Cp (Dietel *et al.*, 1996). By direct observation, the photoproduct I peak is not apparent; however, an SVD fit to this data reveals that the rather featureless region of the spectrum between 640 and 680 nm actually comprises contributions from the emissions of PpIX photoproducts I and II, Up/Cp and other spectral features of unknown origin, which are detected through the Fourier terms used in the fitting function.

In figure 3.8, the results of the SVD fit to one such spectrum are shown, illustrating the ability of the Fourier terms to identify spectral features that are not accounted for with explicit basis spectra and/or to report changes in autofluorescence. The amplitude of the Fourier series component is small relative to the amplitudes of the known basis spectra, indicating that the basis spectra are accurately representing the components of the observed *in vivo* spectra.

Figure 3.9 shows the fitted spectral amplitude of PpIX as a function of fluence for 514 nm irradiation conducted at 1, 5 and 100 mW cm⁻², normalized to the initial amplitude as was done in the previous work of Robinson *et al.* (1998; 1999). Each point is the average derived from six separate experiments, and the uncertainties depicted by the error bars are the sample standard deviations. When plotted as a function of fluence, the rate of bleaching decreases as the fluence rate

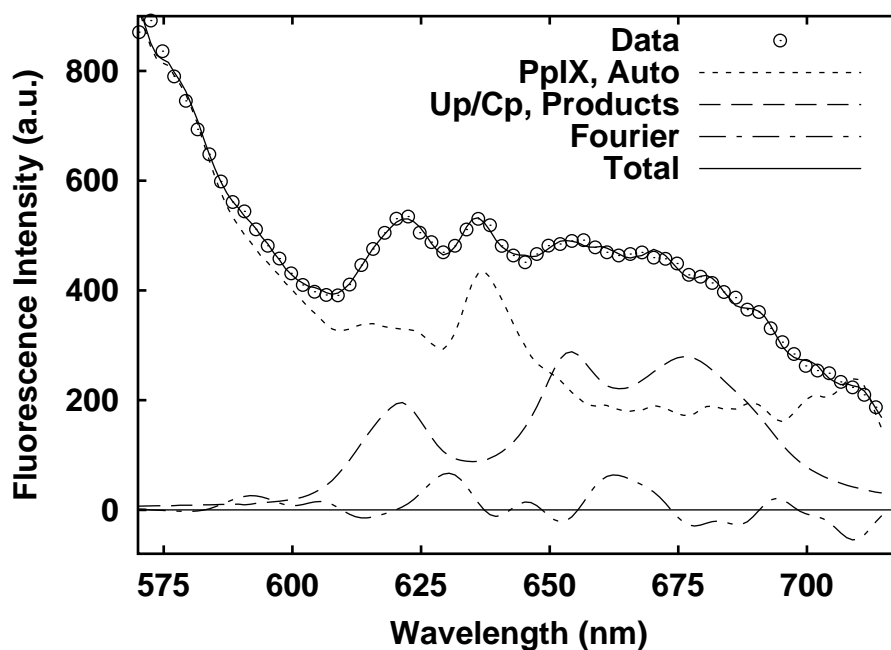


Figure 3.8: SVD analysis of a reflectance-corrected fluorescence spectrum acquired *in vivo* after 19 J cm^{-2} of 514 nm irradiation at an irradiance of 5 mW cm^{-2} . The fitted spectral contribution of each basis spectrum is shown, including that of the Fourier series. The open circles are the reflectance-corrected fluorescence spectrum, and the solid line that closely follows them is the total SVD fit to this spectrum. The uppermost dotted line is the sum of the fitted contributions of initial autofluorescence for this animal and PpIX. The lower dashed line represents the summed SVD estimates of Up/Cp (maximum at 621 nm) and the PpIX photoproducts centered at 676 nm and 654 nm. The dashed-dot line represents the SVD estimate of the contribution of the sum of the Fourier terms.

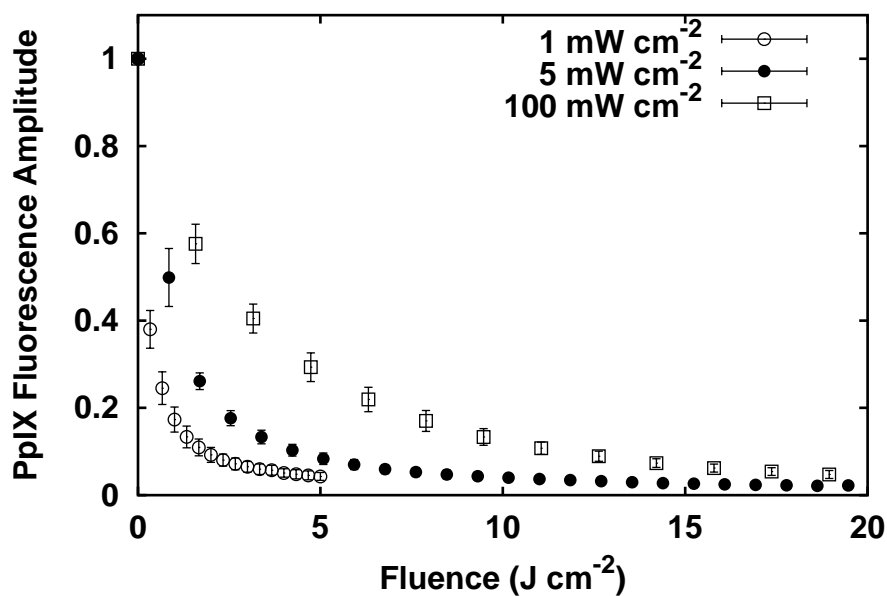


Figure 3.9: Mean spectral amplitude of PpIX as a function of fluence delivered at 1, 5 and 100 mW cm⁻² using 514 nm light ($n = 6$ for each irradiance). Amplitudes are plotted as a fraction of the initial PpIX amplitude in each case. Error bars represent the standard deviations within each group.

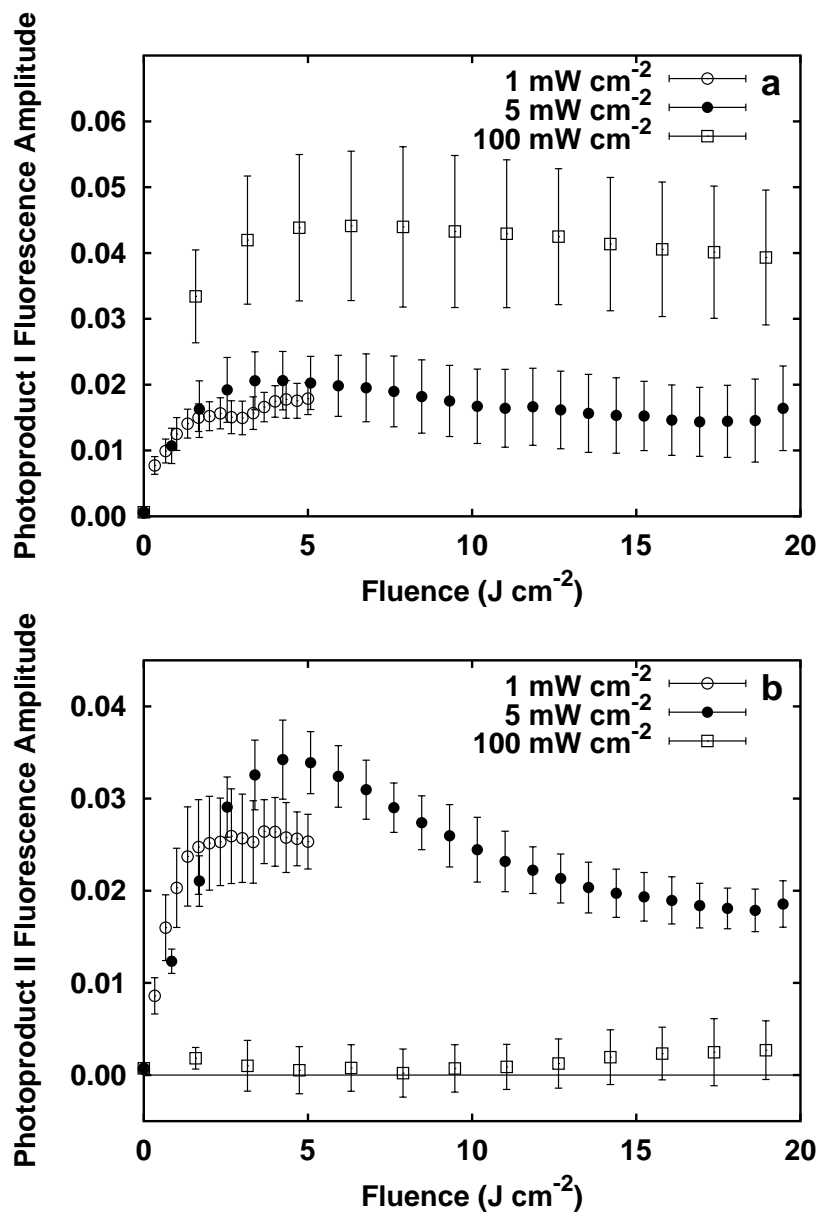


Figure 3.10: Mean spectral amplitudes of (a) photoproduct I and (b) photoproduct II as functions of fluence for 514 nm irradiation. Amplitudes are plotted as fractions of the initial PpIX amplitude in each case. Error bars represent the standard deviations within each group. Photoproduct estimates were determined from the same set of fluorescence spectra that were used to construct the PpIX photobleaching curves of figure 3.9.

is increased in a manner that is quantitatively consistent with the findings of Robinson *et al.* (1998, particularly figure 7.).

Figures 3.10(a) and (b) show the SVD estimates of the spectral amplitudes of photoproducts I and II, respectively, for these same sets of spectra. The data from each experiment are normalized to the initial PpIX amplitude and subsequently averaged. For all three irradiances, the photoproduct I intensity initially increases rapidly and then begins to decrease due to photoproduct bleaching. Greater photoproduct accumulation is observed in the 100 mW cm⁻² case than in the lower-irradiance cases. This is likely a result of the lower efficiency of photoproduct I bleaching in the oxygen-limited, high-irradiance regime. The accumulation of photoproduct II (figure 3.10(b)) is greatest in the low-irradiance cases where photoproduct I undergoes the most bleaching, suggesting that it is formed as a result of the bleaching of photoproduct I rather than of PpIX.

3.3.1.3 Up/Cp fluorescence

The PDT-induced appearance of the emission peak at 622 nm, corresponding to Up/Cp, exhibits an irradiance dependence, with the accumulation of these species being much greater in the lower-irradiance cases. In figure 3.11, the fitted amplitude of Up/Cp is plotted as a function of fluence. These estimates are normalized to the initial PpIX amplitude. A possible explanation for the irradiance dependence we observe might be that the appearance of the Up and Cp species is simply time dependent and manifests most strongly in the lower-irradiance cases because those cases require more time to deliver a given fluence. In order to rule out this possibility, we have treated two animals with 100 mW cm⁻² irradiation and mon-

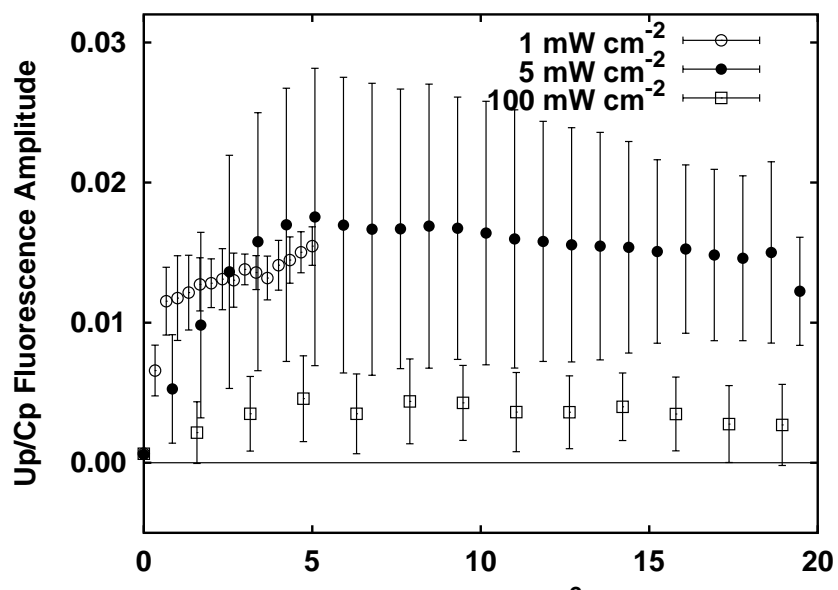


Figure 3.11: Mean spectral amplitude of Up/Cp, normalized to the initial PpIX level, as a function of fluence for 514 nm irradiation. Up/Cp estimates were determined from the same set of fluorescence spectra that were used to construct the PpIX and photoproduct curves of figure 3.9.

itored their fluorescence for 1 h after the end of treatment. No significant changes in the spectrum near 622 nm were observed.

3.3.2 Measurement of PpIX photobleaching in human tumors and normal skin *in vivo*

The opportunity to apply the techniques developed in this chapter to data obtained from human tumors was provided by a collaboration with Dr. Alan Oseroff at the Roswell Park Cancer Institute in Buffalo, New York. The clinic at Roswell Park regularly treats patients suffering from nodular basal cell carcinoma using topically applied ALA. In an effort to establish a fluorescence-based dosimetry system, preliminary fluorescence measurements have been collected from the skin of healthy volunteers and from tumor and surrounding tissue in patients being treated with PDT using 635 nm light. The fluorescence spectra were obtained by staff scientists at Roswell Park using a home-built fluorescence spectroscopy system. Fluorescence was excited by 454 nm light provided by an optical parametric oscillator and captured by a time-gated intensified CCD. The raw data were then transferred electronically to a computer in our laboratory for spectral analysis.

Differences in probe geometry and the fact that reflectance measurements, when taken, were obtained with a separate probe make optical properties correction of the type described in section 3.2.2 impossible for these data. In the cases where reflectance was measured, it varied little compared with the changes in fluorescence induced by PDT. It is therefore anticipated that the results presented here would not be significantly affected by a correction for optical properties and

that the changes observed in fluorescence spectra with irradiation are not the result of optical changes in the tissue.

In constructing the basis spectra for the spectral analysis of patient data, it was anticipated that the major components of the *in vivo* fluorescence spectrum obtained from human and rat skin treated with ALA would be similar. Therefore, the basis spectra described in section 3.2.3.1 were adopted for the fitting described here, with the exception of the autofluorescence spectrum. The human autofluorescence basis spectrum was constructed from measurements made on the unsensitized, unirradiated skin of a healthy volunteer. As shown in figure 3.12, these basis spectra fit the measured fluorescence adequately. The fluorescence spectrum shown was obtained from a basal cell carcinoma tumor on the skin of a human patient. The tumor was sensitized with topically applied ALA, and underwent 9 J cm^{-2} of irradiation at 150 mW cm^{-2} prior to the acquisition of the spectrum shown. In the cases investigated thus far, no spectroscopic signature of photoproduct II or Up/Cp was visible, however these basis spectra were included in the fit for comparison with the rodent data.

The spectral amplitudes of PpIX and photoproduct I for three sets of fluorescence spectra are shown in figure 3.13. The first set was acquired from the normal skin adjacent to a basal cell carcinoma tumor during treatment at 150 mW cm^{-2} . Because the irradiance of 150 mW cm^{-2} was specified in the clinical protocol, it was not possible to investigate lower irradiance treatment in patients. Therefore, photobleaching data for treatment at 10 and 50 mW cm^{-2} was acquired from the normal skin on the forearm of a healthy volunteer.

While the data shown here are preliminary and involve only one set of spec-

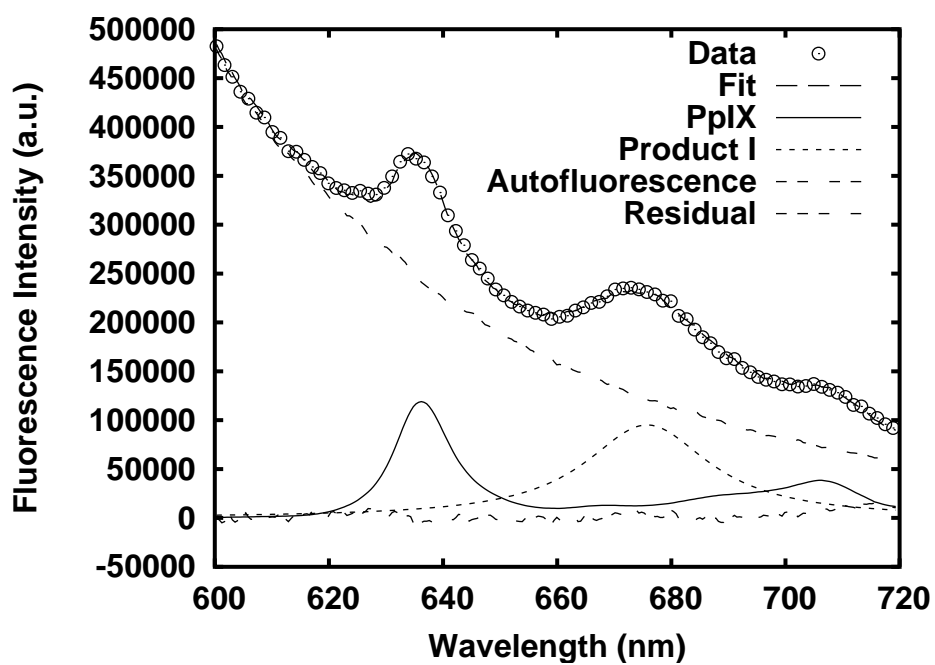


Figure 3.12: SVD analysis of a typical *in vivo* fluorescence spectrum obtained from a basal cell carcinoma tumor in a human patient after 9 J cm^{-2} of 630 nm PDT at 150 mW cm^{-2} . The spectrum labelled 'residual' is the difference between the measured fluorescence and the sum of the contributions of autofluorescence, PpIX and product I.

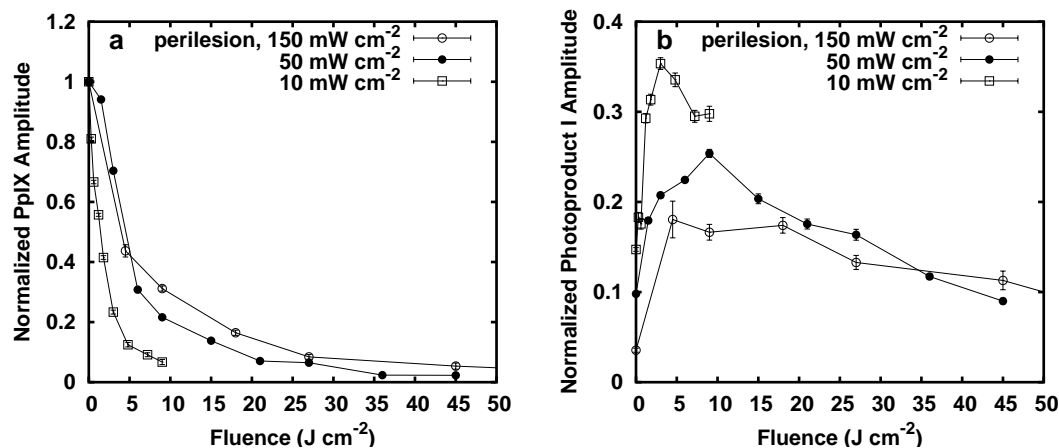


Figure 3.13: Spectral amplitudes of (a) PpIX and (b) product I returned by the SVD algorithm for sequential fluorescence spectra taken during PDT of normal skin adjacent to a basal cell carcinoma tumor at 150 mW cm⁻² and of normal skin in a healthy volunteer at 10 and 50 mW cm⁻².

tra per irradiance, several interesting features are evident. First, the irradiance dependence of the photobleaching observed in rodent skin is reproduced at least qualitatively in human skin. A quantitative comparison is difficult because different irradiances were investigated in the two cases.

In the rodent case, the accumulation of photoproduct I is greater at high irradiance than at low irradiance (see figure 3.10(a)). The product I accumulation observed in the human data is also irradiance dependent, but here higher irradiance leads to less photoproduct I accumulation. It is possible that this apparent discrepancy is due to the difference in treatment wavelength between the rodent and human experiments. If, as postulated on the basis of animal experiments, photoproduct I is bleached by photodynamic action initiated by its own excitation and subsequently forms product II, production of product II would be dependent

on efficient excitation of product I, a requirement which may not be satisfied by the 635 nm treatment light. It is possible that the production of product I is similar in the two cases, but that its bleaching and the subsequent formation of product II is observed only under 514 nm irradiation. It is also possible that some accumulation of product II occurs, but that its fluorescence is not excited efficiently by the 454 nm excitation light. A definitive comparison between the human and rodent cases will be possible only if they are treated with irradiation of identical irradiance and wavelength and interrogated with identical excitation light. However, the current pilot study does indicate that the spectral analysis methods and basis spectra developed in the laboratory can readily be applied in a clinical setting.

3.3.3 mTHPC

3.3.3.1 *In vivo* mTHPC photobleaching

A typical *in vivo* fluorescence spectrum obtained from the skin of a rat treated with mTHPC is illustrated in figure 3.14. The data were corrected for optical properties before fitting. The dominant feature is the fluorescence emission of mTHPC, with a maximum near 655 nm. The peaks near 636 and 708 nm arise from endogenous porphyrins. The SVD algorithm identifies both these components as well as the contribution from non-porphyrin autofluorescence, as indicated in the figure. The endogenous porphyrin contribution is larger than that typically found in spectra measured from the skin of rats immediately after administration of anesthetic.

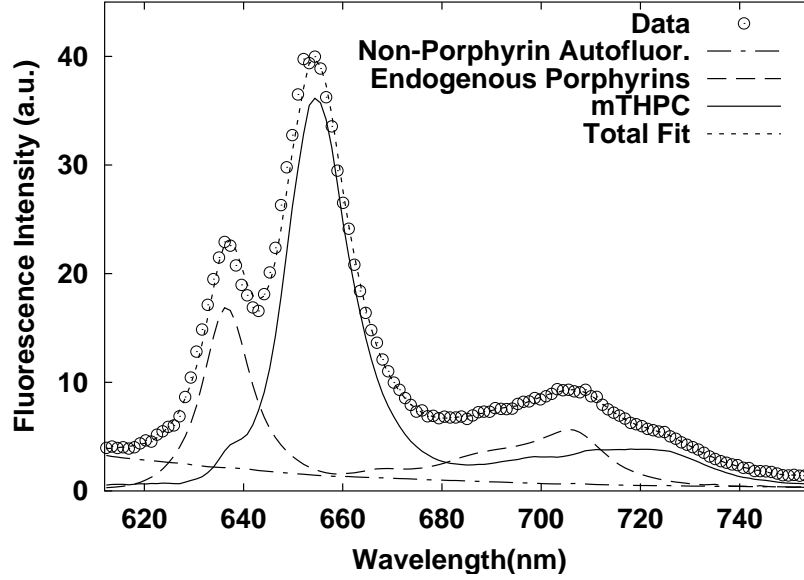


Figure 3.14: SVD analysis of a typical pre-irradiation fluorescence spectrum acquired from the skin of a rat sensitized with mTHPC. The open circles are the data points. The solid line represents the contribution from mTHPC, the dashed line, endogenous porphyrins and the dash-dot line, non-porphyrin autofluorescence. The total fit (dotted line) includes a very small contribution from the Fourier series (not shown), as described in section 2.5.1.1.

The increase in endogenous porphyrin fluorescence appears to be a long term effect of the hair removal process, which occurs in this case 72 h before treatment.

A series of reflectance-corrected fluorescence emission spectra, taken every 0.15 J cm^{-2} during treatment with 5 mW cm^{-2} irradiation, is shown in figure 3.15(a). We denote the mTHPC amplitude measured after irradiation with fluence ϕ as $A(\phi)$. The normalized mTHPC amplitude $A_n(\phi)$ is then defined as

$$A_n(\phi) = \frac{A(\phi)}{A(0)}, \quad (3.2)$$

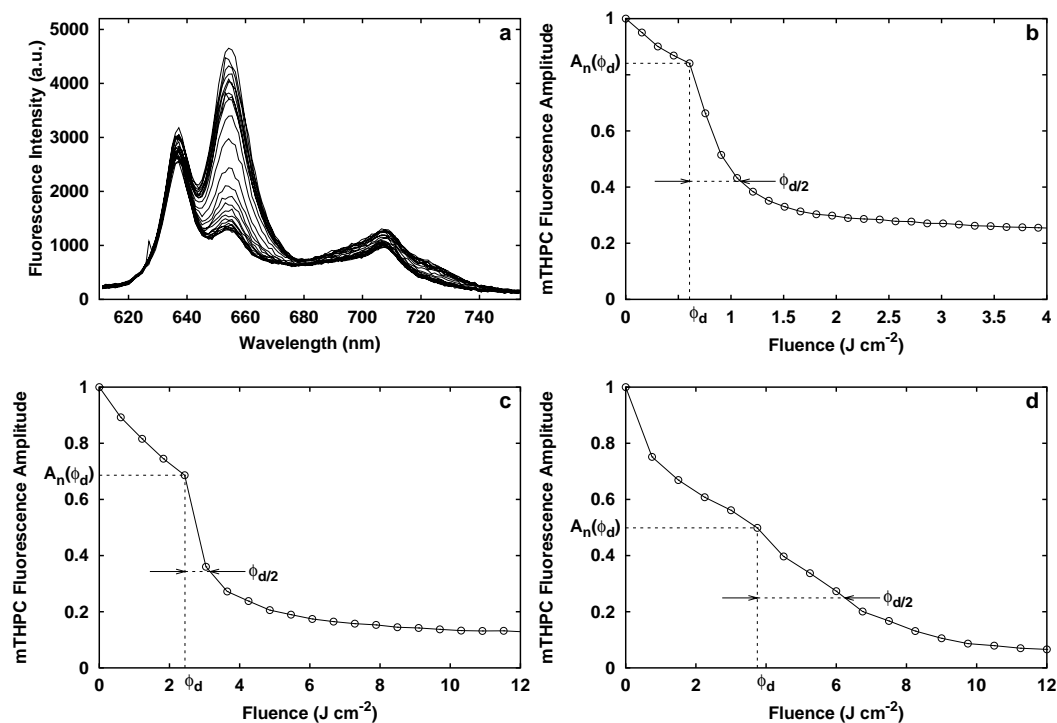


Figure 3.15: (a) Typical series of reflectance-corrected *in vivo* fluorescence emission spectra obtained from normal rat skin sensitized with mTHPC during irradiation with 650 nm light administered at 5 mW cm^{-2} . Spectra were taken at 0.15 J cm^{-2} intervals. (b) mTHPC amplitude returned by the SVD algorithm as a function of fluence for the same experiment. Each data point corresponds to one spectrum in (a). The labelled parameters $A_n(\phi_d)$, ϕ_d and $\phi_{d/2}$ are defined in the text and in the legend to Table 3.3. Representative curves for the 20 mW cm^{-2} (c) and 50 mW cm^{-2} (d) cases are also shown.

where $A(0)$ is the pre-irradiation amplitude. The normalized mTHPC amplitude, $A_n(\phi)$, is plotted as a function of fluence in figure 3.15(b). Each point in figure 3.15(b) corresponds to one spectrum in figure 3.15(a).

Bleaching of mTHPC proceeds in two phases. Initially, the spectra exhibit a gradual decrease in the intensity of the mTHPC peak. This first phase is followed by a sudden, sharp decrease in mTHPC contribution in the sixth spectrum. This is reflected in the fitted mTHPC amplitude by a discontinuous change in slope. The discontinuity is identified by the minimum in the second derivative of $A_n(\phi)$ with respect to fluence. The fluence at which the discontinuity occurs is denoted as ϕ_d . After ϕ_d , bleaching continues at an increased rate. We denote the additional fluence required to reduce the mTHPC amplitude from $A_n(\phi_d)$ to $A_n(\phi_d)/2$ as $\phi_{d/2}$. These parameters are illustrated in figure 3.15(b) and for representative 20 and 50 mW cm⁻² cases, respectively, in figures 3.15(c) and (d). The discontinuity in bleaching rate is most evident in the lower irradiance cases and is less obvious by inspection in the 50 mW cm⁻² experiments, although the second derivative analysis finds the discontinuity reproducibly even in this case. The fitted mTHPC amplitude eventually reaches a level beyond which it bleaches very slowly, despite the fact that as much as 25% of the initial fluorescence emission attributable to mTHPC remains unbleached.

The mean mTHPC amplitude as a function of fluence is plotted in figure 3.16 for the 5, 20 and 50 mW cm⁻² irradiation cases. Each point on the plot represents the mean of fitted amplitudes from 8 or 11 experiments, and the error bars indicate standard deviations within each group. The mean values of the parameters ϕ_d , $A_n(\phi_d)$ and $\phi_{d/2}$ for each irradiance are listed in table 3.3, with uncertainties

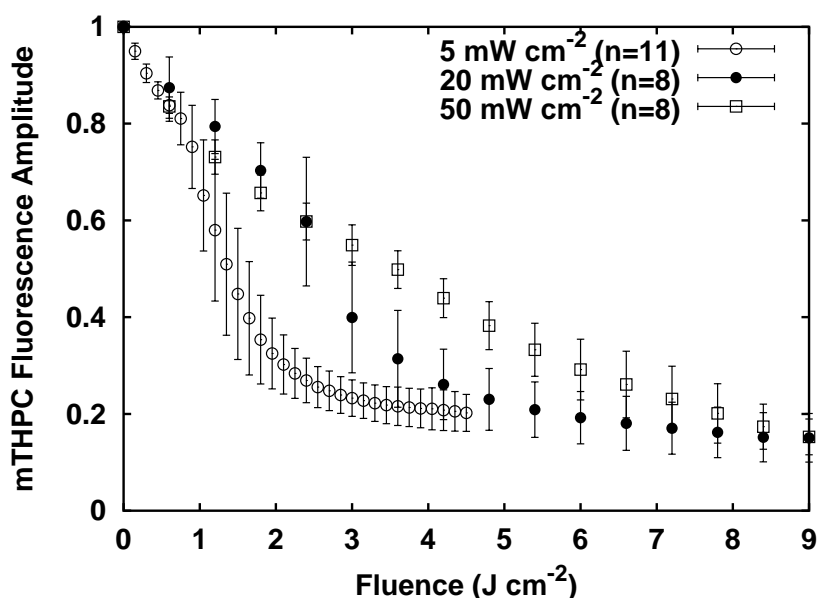


Figure 3.16: Mean mTHPC amplitude as a function of fluence for 650 nm irradiation at 5, 20 and 50 mW cm⁻². Data are normalized before averaging. Error bars represent the standard deviations within each group.

Irradiance (mW cm ⁻²)	ϕ_d (J cm ⁻²)	$A_n(\phi_d)$	$\phi_{d/2}$ (J cm ⁻²)
5 (n = 11)	0.97 ± 0.29	0.79 ± 0.006	0.61 ± 0.13
20 (n = 8)	2.37 ± 0.64	0.67 ± 0.07	1.18 ± 0.72
50 (n = 8)	5.3 ± 1.7	0.41 ± 0.09	2.6 ± 1

Table 3.3: Parameters characterizing the irradiance-dependent features of mTHPC photobleaching *in vivo*: ϕ_d , fluence at which the bleaching rate discontinuity occurs; $A(\phi_d)$, fraction of mTHPC bleached at ϕ_d ; $\phi_{d/2}$, fluence required to bleach half of $A(\phi_d)$. Values are reported as mean \pm the standard deviation for each group

equal to the sample standard deviations. Comparing the three irradiance cases, three major irradiance-dependent effects are evident. During the first phase of bleaching, there is no significant difference in bleaching rate among the three cases. The extent of the first phase, however, is dependent upon irradiance. As irradiance increases over the range of 5 – 50 mW cm⁻², the fluence at which the first phase ends, ϕ_d , increases. Second, the fraction of mTHPC amplitude remaining after the first phase of bleaching, $A(\phi_d)$, decreases. Finally, the value of $\phi_{d/2}$ increases with irradiance, indicating more efficient bleaching with lower irradiance during the second phase of bleaching. For ϕ_d and $A(\phi_d)$, the difference between any two irradiance cases was found to be significant to $P < 0.0005$ using a two-tailed t-test. The differences in $\phi_{d/2}$ were also significant for all pairwise comparisons ($P < 0.02$).

In all cases, the bleaching slows or stops, leaving a fraction of the mTHPC unbleached despite continuing irradiation. Although this bleaching-resistant fraction is difficult to quantify exactly, it appears to decrease with increasing irra-

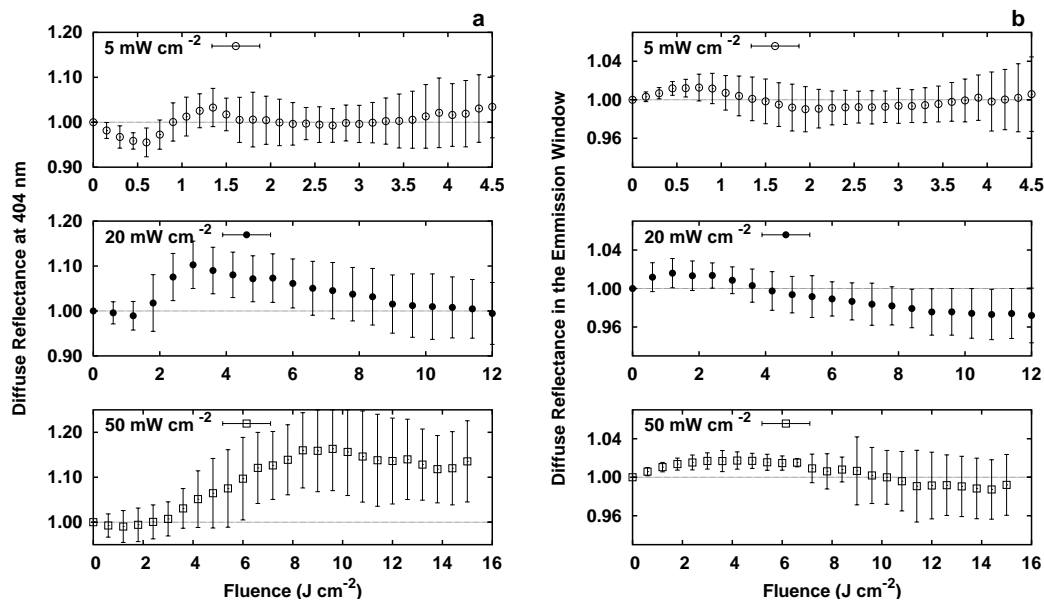


Figure 3.17: (a) Mean value of diffuse reflectance at the fluorescence excitation wavelength of 404 nm and (b) spectrally integrated reflectance in the fluorescence emission window (611 – 755 nm) measured from the skin of rats during irradiation. Data were normalized to the pre-irradiation value before averaging.

diance from approximately 20% in the 5 mW cm^{-2} case to less than 10% in the 50 mW cm^{-2} case.

3.3.3.2 *In vivo* diffuse reflectance

Figure 3.17(a) shows the reflectance measured *in vivo* at 404 nm as a function of fluence during 5, 20 and 50 mW cm^{-2} irradiation. Each point is the average of the reflectances measured from the skin of 8 or 11 different experiments. Error bars represent the standard deviation within each set. In each case, the data are normalized to their pre-irradiation value before averaging. At all three irradiances,

the 404 nm reflectance varies in a similar pattern. The reflectance first decreases, then increases, and then remains constant or slowly decreases again. The initial decrease is most prominent in the 5 mW cm⁻² case and is absent in one of the 20 mW cm⁻² experiments and in two 50 mW cm⁻² experiments (data not shown). In each case, the discontinuity in the slope of the mTHPC fluorescence amplitude occurs during the increase in reflectance at 404 nm. The spectrally integrated reflectance in the emission window is shown in figure 3.17(b). In this wavelength range, the reflectance initially increases and then decreases. The onset of the decrease occurs at approximately ϕ_d in each case. No obvious spectral signature of mTHPC absorption is visible in the reflectance spectra (data not shown).

3.3.4 Photofrin

3.3.4.1 Photofrin bleaching and photoproduct formation

Figure 3.18 illustrates the typical spectral changes observed during *in vivo* photobleaching of Photofrin. The spectra in each frame are the average of spectra taken from six experiments prior to irradiation (dashed lines) and after 9 J cm⁻² of irradiation (solid lines). Prior to averaging, the autofluorescence component of each spectrum was subtracted, and the peak was normalized to 1. Errorbars represent standard deviations. The spectra of sensitized skin irradiated at 5 mW cm⁻² (panel a) and 100 mW cm⁻² (panel b) clearly differ. In both cases, the intensities of the Photofrin emission peaks at 632 and 696 nm are significantly reduced relative to their pre-irradiation values. The appearance of photoproduct emission at 655 nm is greater in the lower irradiance case, where a distinguishable peak is

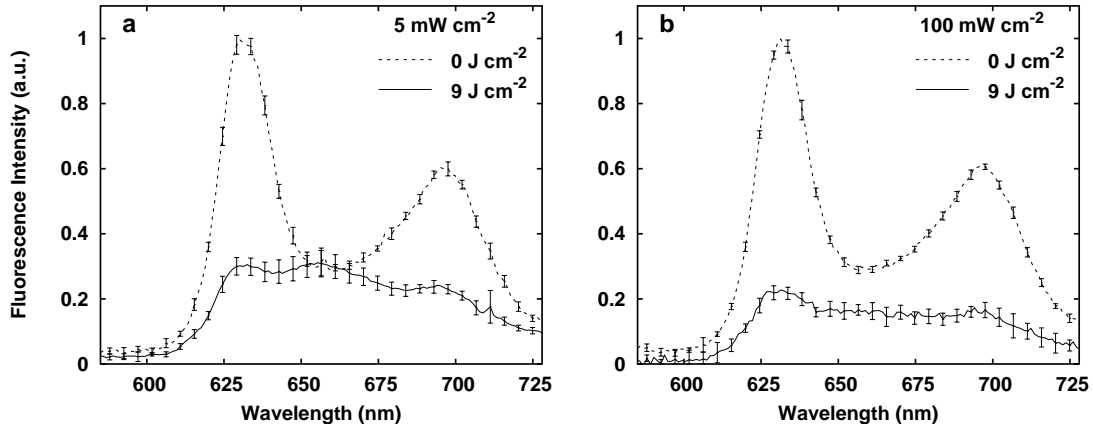


Figure 3.18: Normalized fluorescence spectra obtained from the normal skin of Photofrin sensitized rats before irradiation (dashed lines) and after 9 J cm^{-2} of 514 nm irradiation (solid lines) administered at (a) 5 and (b) 100 mW cm^{-2} . Each curve is the average of spectra taken from 6 animals; errorbars indicate standard deviations. Prior to averaging, the autofluorescence component of each spectrum was subtracted.

visible. In the 100 mW cm^{-2} case, the photoproduct emission is masked by the fact that it coincides with a valley in the emission of Photofrin. The SVD fitting algorithm can separate this component even though it is not obvious to the eye.

The amplitude of the Photofrin component of *in vivo* fluorescence as a function of irradiation fluence is plotted in figure 3.19. The data points represent the average of the amplitudes from 6 independent experiments, and the errorbars depict standard deviations within each group. The amplitudes are normalized to the initial (pre-irradiation) amplitude prior to averaging. The bleaching curves observed in the 5 and 100 mW cm^{-2} cases are not significantly different. In both cases, the bleaching is most rapid at the beginning of treatment, and slows as treatment

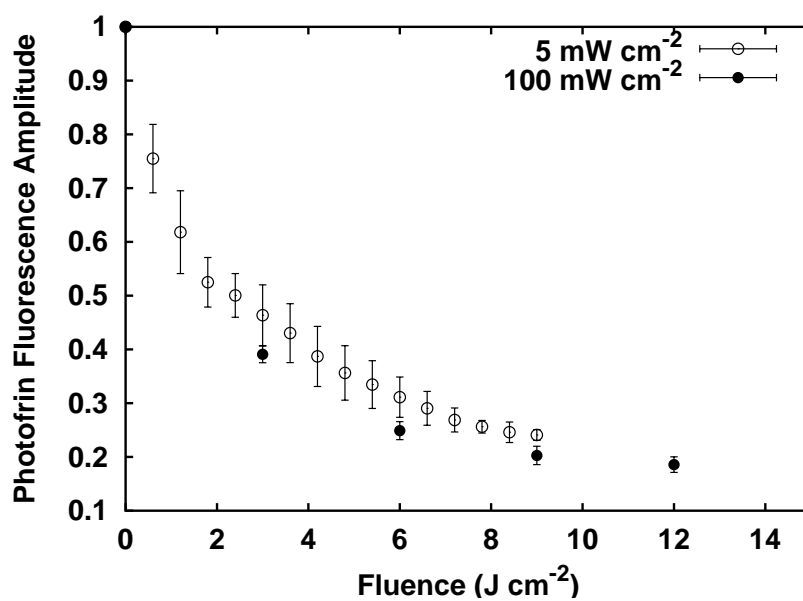


Figure 3.19: Normalized Photofrin amplitude as a function of fluence for 514 nm irradiation at 5 and 100 mW cm⁻². Each data point is the average taken from six experiments. The errorbars represent standard deviations.

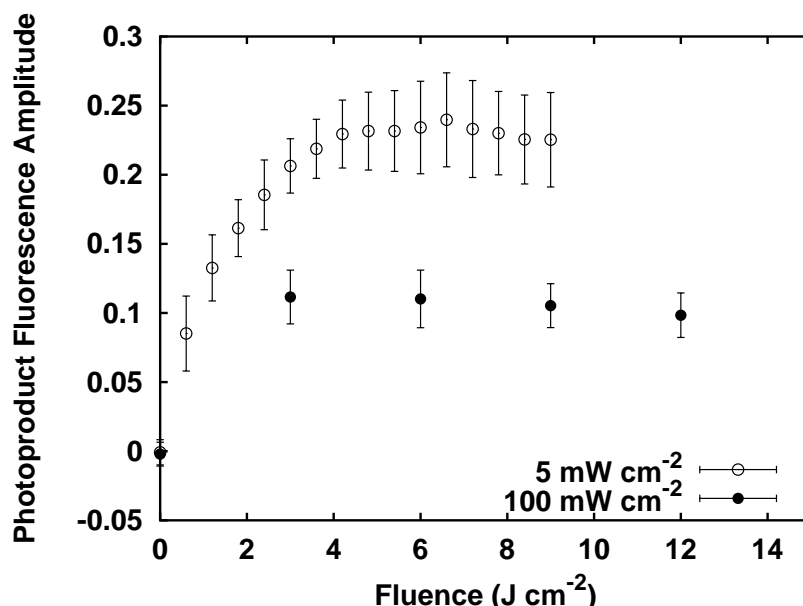


Figure 3.20: Normalized amplitude of the Photofrin photoproduct as a function of fluence for 514 nm irradiation at 5 and 100 mW cm⁻². The data here is taken from the same set of experiments used to generate the curves in figure 3.19.

progresses. The bleaching of Photofrin appears to stop when the amplitude has reached approximately 15% of its initial value.

Figure 3.20 shows a plot of the photoproduct amplitude for the same data sets. Each curve is normalized to the corresponding pre-irradiation amplitude of Photofrin prior to averaging. The PDT-induced accumulation of the photoproduct is irradiance dependent, with significantly greater accumulation in the lower irradiance case.

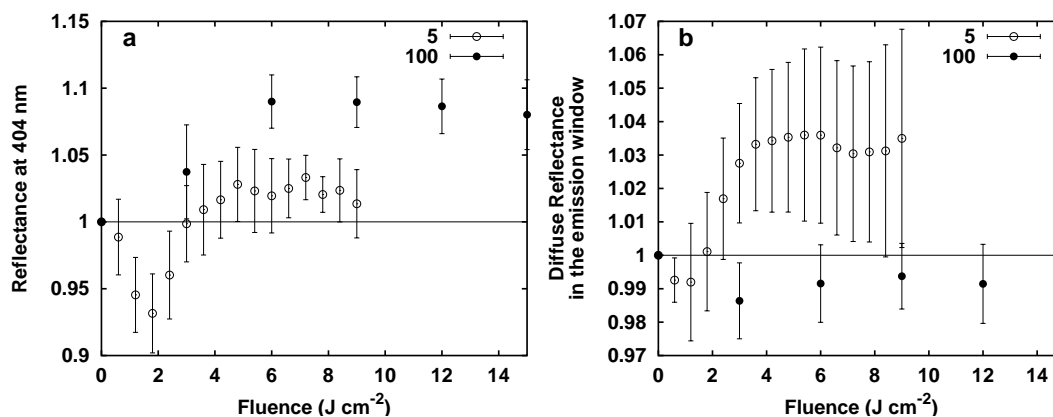


Figure 3.21: Normalized skin reflectance (a) at 404 nm and (b) integrated over the emission window during Photofrin PDT at 5 mW cm⁻² (open circles) and 100 mW cm⁻² (filled circles).

3.3.4.2 Diffuse reflectance

Figure 3.21 illustrates the reflectance recorded at the excitation wavelength (panel a) and integrated over the emission window (panel b) during PDT, taken from the same data sets used to create figures 3.19 and 3.20. The 404 nm reflectance observed during 5 mW cm⁻² irradiation first decreases and then recovers. It is possible that a similar effect occurs in the 100 mW cm⁻² case, however the frequency of data collection is such that the initial decrease may fall between samples. In the 100 mW cm⁻² case, the reflectance increases to approximately 110% of its initial value. In the emission window, the changes in reflectance are less severe than at 404 nm.

3.4 Discussion

The experiments described here demonstrate significant irradiance dependence to the photobleaching and/or photoproduct accumulation kinetics of three different sensitizers. While the behaviors of the three are very different in detail, *in vivo* fluorescence measurements can provide useful dosimetric information in each case. The similarities and differences among the three cases are discussed in the following sections.

3.4.1 Diffuse reflectance

Measurements of the reflectance at the excitation and emission wavelengths allow correction of the fluorescence for the effects of tissue optical properties. In addition, the reflectance may report changes in tissue scattering, blood volume, hemoglobin oxygenation or concentration of other absorbers. We hypothesize that the trends observed in the present studies (see figures 3.6, 3.17 and 3.21) can be explained by a combination of absorption and scattering changes.

The absorption coefficient of hemoglobin at physiological concentration and various oxygen saturations at the excitation and emission wavelengths is summarized in table 3.4. The absorption coefficient of hemoglobin in pure solution at 404 nm changes by a factor of 20% upon deoxygenation. However, when the hemoglobin is packaged in red blood cells, the magnitude of this change is reduced to less than 4% by the spectral flattening effect described in chapter 2. Because the dependence on oxygen saturation has opposite effects on the reflectance at the excitation and emission wavelengths, reflectance changes that result from shifts in

Oxygen Saturation	Mean μ_a (mm^{-1})	
	404 nm	600-700 nm
0%	1.52	0.055
50%	1.55	0.032
100%	1.58	0.0079

Table 3.4: Hemoglobin absorption relevant to reflectance measured during *in vivo* photobleaching experiments. Each column lists the mean value of tissue μ_a in the wavelength ranges at which diffuse reflectance was monitored during PDT experiments for various values of the hemoglobin oxygen saturation. The hemoglobin concentration was assumed to be 50 μM .

hemoglobin oxygen saturation can be separated from those resulting from changes in blood volume or tissue scattering, which would shift reflectance at both wavelengths in the same direction. Because of the spectral flattening effect, however, changes in reflectance at 404 nm larger than a few percent cannot be explained purely by oxygenation changes.

Upon irradiation, each of the sensitizers we investigated induces a reproducible change in the reflectance measured from the skin. The details of the reflectance response are sensitizer-specific. In the case of PpIX, the reflectance values in the two wavelength ranges both increase during irradiation, indicating that they are dominated by effects other than shifts in oxygen saturation. Specifically, ALA PDT results in visibly apparent whitening or blanching of the tissue, likely resulting from a decrease in blood volume or an increase in scattering.

Tissue treated with Photofrin-PDT also exhibits blanching at low irradiance, which is reported in the increase in reflectance at fluences greater than 4 J cm^{-2} . At high irradiance, the 404 nm reflectance increases steadily with irradiation,

while the emission window reflectance decreases slightly. This pattern is consistent with a switch from oxy- to deoxyhemoglobin resulting from photodynamic oxygen depletion. The fact that the magnitude of the change is greater at the excitation wavelength, however, makes it unlikely that these changes are due purely to changes in oxygenation. The initial decrease in reflectance in both wavelength regimes in the low irradiance case may indicate a transient increase in blood volume.

With the onset of irradiation of mTHPC-sensitized tissue, the reflectance at the excitation wavelength decreases, whereas that in the emission window increases. This is consistent with absorption changes caused by a shift from deoxy- to oxyhemoglobin, a possible result of increased blood flow in response to initial tissue damage. As in the case of Photofrin, the magnitude of the change is greater at the excitation wavelength than in the emission window, indicating the presence of changes unrelated to hemoglobin oxygenation. The subsequent irradiance-dependent increase in reflectance at 404 nm may be indicative of increased scattering resulting from tissue swelling or decreased absorption because of reduced blood oxygenation.

The measurements of integrated reflectance reported here are useful for observing general trends, however they are not sufficient to elucidate the physiological causes of changes in reflectance or even to uniquely separate the effects of changes in absorption and scattering. The variety of reflectance changes observed with different sensitizers and under different treatment irradiances motivates the development and utilization of more sophisticated reflectance measurements. Hull *et al.* (1999) have demonstrated a method of radially resolved diffuse reflectance

spectroscopy capable of identifying changes in hemoglobin saturation and concentration *in vivo*, however their method requires sampling of an area of tissue larger than the treatment field in our experiments. The need for a reflectance measurement compatible with small sample volumes motivates the development of short source-detector separation methods (Hull and Foster, 2001) and the single source-detector methods described in chapter 4.

3.4.2 ALA-induced PpIX

3.4.2.1 *In vivo* bleaching of PpIX

In the case of ALA-induced PpIX, we observe irradiance dependent photobleaching that is consistent with an oxygen-dependent photobleaching mechanism. This phenomenon has been observed during PDT conducted using 514 nm irradiation over a range of clinically relevant irradiances (figure 3.9(a)). The irradiance dependence of the rate of PpIX photobleaching and of photoproduct accumulation and subsequent bleaching is potentially significant for photodynamic dosimetry and provides direct experimental support for an oxygen-based interpretation of irradiance-dependent tumor response to PDT, which has been demonstrated for ALA-induced PpIX *in vivo* (Hua *et al.*, 1995) and for several other photosensitizers (Veenhuizen and Stewart, 1995). To the extent that photodynamic damage and photodegradation of the photosensitizer are both mediated by an oxygen-dependent photochemistry, greater photobleaching at a given fluence implies that greater photodynamic damage has also been deposited. Thus, while an enhanced tumor response to PDT administered at low irradiance has been recognized for

some time, our results and those of Robinson *et al.* (1998; 1999) provide physical evidence that this biological effect is indeed a response to increased photodynamic dose.

A second observation that has possible importance for dosimetry is the fact that the irradiance dependence to the rate of PpIX photobleaching persists down to surprisingly low irradiances. As shown in figure 3.9(a), the loss of PpIX fluorescence *vs* fluence is more efficient when the irradiance is reduced from 5 to 1 mW cm⁻². This may suggest that type-II photochemistry is limited by photochemical oxygen depletion even at these very low irradiances.

3.4.2.2 Comparison with previously published studies

The PpIX bleaching results presented here quantitatively reproduce the previously reported findings of Robinson *et al.* (1998; 1999), while differing rather dramatically from those of Sørensen *et al.* (1998) and Iinuma *et al.* (1999), who found no irradiance dependence to the rate of PpIX bleaching induced by 630 and 636 nm irradiation, respectively. While differences in tissue type, animal model and experimental setup make exact accounting for the causes of this discrepancy impossible, several factors may be identified that could account for the differences between the results of Robinson *et al.* and ours on the one hand and those of Iinuma *et al.* and Sørensen *et al.* on the other.

The important experimental differences among the four studies include the choice of PDT treatment and fluorescence excitation wavelengths, PDT treatment irradiances and the wavelength range and method of fluorescence detection, as summarized in table 3.5. Our studies in rodents and human patients make use

Study	PDT Treatment		Excitation λ (nm)	Detection	
	λ (nm)	Irradiance (mW cm ⁻²)		λ (nm)	Method
Finlay	514	1, 5, 100	403	575 – 720	SVD fitting
Robinson	514	10, 150	514	550 – 794	Nonlinear fitting
Roswell	635	10, 50, 150	454	600 – 720	SVD fitting
Sørensen	636	37.5, 75, 150, 300, 500	636	715 \pm 5	Integration
Iinuma	630	30, 100	630	675 – 720	Integration

Table 3.5: Comparison of the PDT treatment parameters and fluorescence excitation and detection wavelengths utilized in our own and three other published studies of PpIX photobleaching. ‘Roswell’ indicates the study of fluorescence spectra obtained at the Roswell Park Cancer Center and analyzed using our SVD algorithm.

of spectrally resolved data acquisition and spectral fitting to separate the fluorescence of PpIX from autofluorescence and photoproduct emission. In contrast, the Sørensen and Iinuma studies take the integrated fluorescence intensity over a pre-determined wavelength range as a measure of the PpIX concentration. This method allows signal from autofluorescence and photoproducts to be erroneously included in the reported PpIX signal. In order to assess the effect of this difference in detection schemes, we have re-analyzed the human data acquired at Roswell Park Cancer Center using methods that mimic those of Sørensen *et al.* and Iinuma *et al.* Specifically, we have taken the total signal within the wavelength range utilized by each study (see table 3.5) as the PpIX amplitude. The fluorescence amplitudes obtained using the integration ranges of the Sørensen and Iinuma studies are shown in figure 3.22(b) and (c), respectively. For comparison, panel (a) reproduces the amplitudes reported in figure 3.13 obtained with

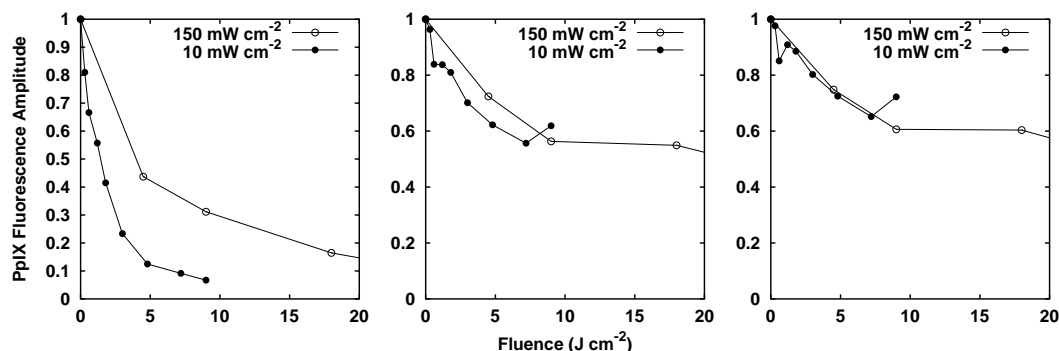


Figure 3.22: Normalized amplitude of PpIX as reported by (a) SVD analysis (see section 2.5.1) and by the spectral integration methods used by (b) Sørensen *et al.* (1998) and by (c) Iinuma *et al.* (1999). The data used are the same used to generate figure 3.13.

SVD fitting. The spectrally integrating methods fail to capture the irradiance dependence of the photobleaching in this case. It is clear from the SVD-derived amplitude of the autofluorescence basis spectrum that this is due in large part to variations in autofluorescence, however a spectrally resolved method is required to make that diagnosis. When the fluorescence spectra are adjusted for differences in autofluorescence prior to analysis, the spectrally integrating methods are capable of distinguishing an irradiance dependence, however the differences between the low and high irradiance cases are reduced (data not shown). The differences in data analysis methods do not entirely explain the discrepancy between our results and those of Iinuma and Sørensen, however the analysis depicted in figure 3.22 demonstrates the danger of using spectrally integrating methods in cases where fluorophores other than the sensitizer are present.

Another effect that may be particularly important in studies comparing

different irradiances is the oxygen dependence of the absorption spectrum of hemoglobin, which is the most important tissue chromophore in this wavelength range. Deoxyhemoglobin is significantly more absorbing than is oxyhemoglobin in the 620 – 720 nm wavelength range (Jope, 1949) where the fluorescence was excited and detected and the treatment light was delivered in the Sørensen and Iinuma studies. Conversion of oxy- to deoxyhemoglobin during PDT would increase the tissue absorption at both the excitation and emission wavelengths used in their experiments, thereby decreasing the measured fluorescence and giving rise to an apparent increase in the rate of photobleaching. Because tissue deoxygenation is expected to be more rapid and more pronounced at higher irradiance, a decreased photobleaching efficiency could be masked by the increased attenuation of the excitation light and the fluorescence emission. Interestingly, the 514 nm excitation used by Robinson *et al.* corresponds to a nearly isosbestic point in the hemoglobin spectra. Independent of the choice of excitation wavelength, the significant oxygen-dependent changes in hemoglobin absorption throughout the wavelengths corresponding to the emission spectrum of PpIX motivate careful attention to correction for optical properties in fluorescence measurements performed during PDT.

A related consequence of the wavelength dependence of tissue optical properties is the fact that the volume of tissue sampled by fluorescence measurements made with different excitation wavelengths is significantly different. To assess this effect, we have used a Monte Carlo algorithm (see appendix A) to calculate the mean depth of origin of the fluorescence captured by the detectors used in each of the studies being compared. Differences in detector geometry and tissue optical

	Mean depth of detected fluorescence (mm)		
Hb sat.	0%	50%	100%
Finlay	0.30	0.30	0.30
Robinson	0.67	0.74	0.82
Sørensen	1.26	1.42	2.03
Iinuma	1.55	1.97	3.14

Table 3.6: Mean depth of origin of fluorescence collected by the detectors used in various PpIX bleaching studies, as determined by Monte Carlo simulation.

properties at the excitation and detection wavelengths result in remarkably different depths being probed by the different methods. Table 3.6 lists the mean depth of origin of fluorescence for the detection geometry and wavelengths used in each study assuming tissue hemoglobin concentration of 50 μM at oxygen saturations of 0, 50 and 100%. Homogenous distribution of fluorophore was assumed. In reality, as treatment progresses, the upper layers of tissue will undergo more rapid bleaching, with the result that the depth at which appreciable fluorescence is created increases with irradiation (Farrell *et al.*, 1998). The depth of fluorescence collected using longer wavelength excitation as in the Iinuma and Sørensen studies decreases by approximately a factor of two in the event that the tissue becomes deoxygenated, biasing the sampled volume toward more superficial layers of tissue. This effect compounds the decrease in observed fluorescence as a result of increased absorption. The volume of tissue probed by fluorescence measurements made using shorter excitation wavelengths is insensitive to changes in hemoglobin saturation, minimizing these problems

Based on the arguments outlined above, it is plausible that the discrepancies among the four studies compared here are due in large part to differences in

treatment, excitation and detection wavelength. However, lack of knowledge of the detailed tissue optical properties and oxygen concentrations encountered in each case makes a quantitative assessment of these effects impossible.

3.4.2.3 Photoproduct dynamics

The accumulation kinetics of the two PpIX fluorescent photoproducts are consistent with production and bleaching of these photoproducts at rates that depend on irradiance. Lower irradiance PDT causes more efficient bleaching of PpIX and, presumably, more efficient photoproduct I formation. But lower irradiance also leads to more efficient photoproduct I bleaching, as evidenced by the lower net accumulation of photoproduct I (see figure 3.10). In one 100 mW cm^{-2} experiment, prolonged irradiation was observed to bleach the majority of the photoproduct I amplitude (data not shown). In this case, the disappearance of photoproduct I was accompanied by an accumulation of photoproduct II, indicating that product II is produced by the bleaching of product I rather than of the PpIX. Indeed, accumulation of photoproduct II is greatest in the low-irradiance cases, where photoproduct I undergoes the most bleaching. Photoproduct II is also photo-bleached (figure 3.10(b)); however, the lack of its significant accumulation in the 100 mW cm^{-2} case makes it impossible to determine whether this bleaching is irradiance dependent.

Another potentially interesting and unanticipated finding to emerge from spectroscopic studies of PpIX bleaching is the irradiance dependence of the appearance of Up/Cp emission near 620 nm. This peak is clearly evident in the spectrum shown in figure 3.7(c) and its amplitude *vs* fluence is summarized in figure 3.11.

Because these porphyrins are synthesized in the cytosol, their accumulation in response to PDT may be the result of photodynamic damage to the mitochondria, where the final steps of heme synthesis occur. Dietel *et al.* (1997) have observed enhanced accumulation of water-soluble porphyrins in a mouse tumor model under conditions of reduced mitochondrial viability. Thus the irradiance-dependent emission at 622 nm that we observe is spectroscopic evidence for greater mitochondrial damage at the reduced irradiances. Because the formation of Up and Cp is dependent on excess ALA, its use in dosimetry is limited to the case of ALA-induced PpIX.

It should be noted that the emission spectra of protonated Up and Cp found in aqueous solutions of very low pH exhibit peaks in the same region of the spectrum as does photoproduct II, leading to possible ambiguity in the choice of basis spectra. However, as the protonated species of Up and Cp are present only at pH of approximately 6 or lower and because we see no evidence of the secondary emission peaks of these species in our *in vivo* data, they do not appear to contribute significantly to the *in vivo* fluorescence.

Observation of photoproduct accumulation requires that spectrally resolved methods be used to separate the fluorescence contributions of the primary sensitizer and its photoproducts. Therefore, comparisons of photoproduct accumulation are only possible between our work and that of Robinson *et al.* Those authors observed only one photoproduct, which corresponds to our photoproduct I. They have demonstrated an irradiance dependence to the rate of photoproduct I formation under conditions of 514 nm irradiation and observed appreciable photoproduct I photobleaching, although the dynamics they reported are much different

than those that we observe (Robinson *et al.*, 1999). This discrepancy may be due to differences in the methods of spectral analysis. The Robinson study modelled the fluorescence emission as a superposition of Lorentzian lineshapes, but did not explicitly include a basis spectrum for product II. We note, however, that the kinetics Robinson reports for photoproduct I are qualitatively similar to the kinetics we find for the sum of the two photoproducts.

It is interesting to note that the photoproduct dynamics observed by Robinson *et al.* under 514 nm irradiation are in qualitative agreement with those we observe in the case of ALA-sensitized human skin *in vivo* irradiated with 635 nm light and excited at 454 nm (see figure 3.13). In both cases only one photoproduct was observed. It is possible that photoproduct II is not excited efficiently at 514 or 454 nm. Regardless of the excitation wavelength, the differences in product I kinetics between our rodent data on one hand and our human data and Robinson's rodent data on the other are still unexplained. The human treatments at Roswell Park and Robinson's mouse experiments both utilize topically applied ALA, in contrast to the systemic administration used in our rat experiments. To rule out the route of ALA application as a cause of the differences between the studies, we have treated two rats with topically applied ALA (data not shown) and have observed photobleaching and photoproduct accumulation indistinguishable from that observed in rats sensitized systemically.

Irradiance dependence in the rate of photoproduct formation and bleaching *in vivo* is consistent with an oxygen mediated reaction mechanism, as has been proposed by others (Gudgin Dickson and Pottier, 1995; König *et al.*, 1993, and references therein). The use of photoproduct fluorescence as a dosimeter is com-

plicated by the fact that the photoproduct itself is capable of undergoing bleaching, evident in figures 3.10(b) and (c). The fact that photoproduct production and bleaching are competing processes makes it impossible to measure the total amount of photoproduct produced or the total amount bleached at any given fluence.

3.4.3 mTHPC

Based on prior findings (Coutier *et al.*, 2001; Hadjur *et al.*, 1998), it was expected that the photobleaching of mTHPC *in vivo* would be singlet-oxygen mediated and thus exhibit an irradiance dependence similar to that of ALA-induced PpIX. However, the bleaching behavior we observe is remarkably complicated, with two distinct phases of bleaching and a number of irradiance-dependent features (see figure 3.16). Although the initial phase of bleaching does not exhibit significant irradiance dependence, the fluence required to trigger the onset of the second phase depends strongly on irradiance. Further, the mTHPC amplitude remaining at this transition decreases significantly with increasing irradiance. This indicates the presence of an irradiance-dependent phenomenon during the first phase, which is not reported by the rate of fluorescence loss. During the second phase of bleaching, the loss of fluorescence is more efficient with respect to fluence at lower irradiance. This behavior is consistent with $^1\text{O}_2$ -mediated bleaching in which the higher irradiance treatments cause more significant oxygen depletion.

A possible explanation for the two-phase nature of the *in vivo* photobleaching might be redistribution of mTHPC within the tissue. Previous work by others and by our group has investigated such a phenomenon in cells and spheroids treated

with sensitizers that localize to lysosomes (Berg *et al.*, 1991; Georgakoudi and Foster, 1998a; Peng *et al.*, 1991). In those studies, the photosensitizers were observed to relocate from the lysosomes to the cytosol of cells in response to irradiation. Oxygen concentration measurements performed at the edge of spheroids incubated with a Nile blue derivative showed a sudden increase in the oxygen consumption rate at a fluence corresponding to the observed relocation (Georgakoudi and Foster, 1998a). In contrast, the oxygen concentration changes measured in our laboratory with mTHPC-sensitized spheroids during irradiation showed no features analogous to the two-phase bleaching observed *in vivo* (Finlay *et al.*, 2002). Melnikova *et al.* (1999a) studied the subcellular localization of mTHPC in human tumor cells and saw no evidence of irradiation-induced relocation of the sensitizer. If drug relocation is responsible for the bleaching behavior we observe, it is possible that the process is unique to the *in vivo* environment.

Coutier *et al.* (2001) used the intensity of the fluorescence emission at 650 nm to directly measure the photobleaching of mTHPC in Colo 26 spheroids treated with 650 nm light at 5, 30 and 90 mW cm⁻². They observed more efficient bleaching at lower irradiance but did not observe a discontinuity in bleaching rate. However, because the fluorescence was sampled only at 5, 10, 15 and 30 J cm⁻² in that study, it is possible that this feature was missed. Indeed, in the present study, fluorescence measurements at fluence intervals as short as 0.15 J cm⁻² were required to accurately assess the shape of the bleaching curve. The presence or absence of such behavior in the spheroid model could be verified by a study whose design is informed by our *in vivo* results.

Another unusual feature of the *in vivo* fluorescence kinetics of mTHPC is the

relatively large fraction of the sensitizer that appears resistant to bleaching. The analysis of our *in vivo* fluorescence spectra is complicated by the presence of endogenous porphyrins, whose fluorescence is similar to that of PpIX. It is possible that some bleaching of these porphyrins is sensitized by mTHPC, leading to the accumulation of the fluorescent photoproducts described in section 3.2.3.1. In experiments where the endogenous porphyrin contribution is unusually high, the SVD fitting algorithm reveals slight bleaching of the endogenous porphyrins and accumulation of the 676 nm photoproduct. It is possible that the 654 nm photoproduct is present as well, but this is spectrally indistinguishable from mTHPC. The presence of this second photoproduct would cause a systematic overestimation of the mTHPC amplitude, which would become greater as treatment progressed. Although this effect may be a minor source of error in our results, its magnitude is not sufficient to completely account for the fraction of mTHPC that remains unbleached after treatment.

The complexity of the mTHPC bleaching kinetics we observe *in vivo* motivates further study. Bleaching exhibiting two distinct phases is not evident in oxygen concentration measurements performed in our laboratory with mTHPC-sensitized spheroids (data not shown) nor is it predicted by the bleaching model presented in section 2.6, which incorporates both $^1\text{O}_2$ mediated and triplet sensitizer-mediated bleaching mechanisms. It is possible that mTHPC bleaches partially *via* a mechanism or combination of mechanisms that is not directly reported by oxygen concentration or that the two-phase bleaching is the result of processes unique to the *in vivo* environment, for example, therapy-induced physiological responses such as changes in blood flow. Another possibility is the presence of multiple populations

of mTHPC within the tissue that bleach *via* mechanisms with different oxygen dependencies. Ongoing studies in our laboratory will use confocal fluorescence microscopy to observe the photobleaching of mTHPC at various distances from the center of an intact spheroid at irradiation intervals informed by our *in vivo* results. These studies will allow the fundamental photophysical processes present in both the *in vivo* and spheroid systems to be separated from factors such as blood flow and macroscopic physiological response that are unique to the *in vivo* environment.

3.4.4 Photofrin

Previous studies of the photobleaching of Photofrin conducted in our laboratory have utilized a multicell tumor spheroid model (Georgakoudi *et al.*, 1997). The experiments detailed in that paper measured the photobleaching of Photofrin indirectly *via* its effect on the oxygen concentration measured by an oxygen sensitive electrode at the edge of the spheroid. These measurements were shown to be consistent with photobleaching mediated by $^1\text{O}_2$. If Photofrin is bleached by the same mechanism *in vivo*, we expect more efficient photobleaching at lower irradiance. However, we observe no irradiance dependence in photobleaching in our *in vivo* fluorescence measurements, as shown in figure 3.19.

Despite the lack of irradiance dependence in the *in vivo* bleaching of Photofrin itself, the accumulation of photoproduct is significantly greater at lower irradiance *in vivo*, as shown in figure 3.20. This trend is expected when the photoproduct is produced by the reaction of $^1\text{O}_2$ with the primary sensitizer. Indeed, experiments reported by König *et al.* (1990) on the photobleaching of the Photofrin-like mixture

hematoporphyrin derivative (HPD) in aqueous solution showed that photoproduct formation was inhibited by $^1\text{O}_2$ scavengers, indicating direct involvement of $^1\text{O}_2$ in photoproduct production.

It is possible that our *in vivo* observations can be reconciled with the previous measurements made in spheroids by a model in which the bleaching of Photofrin can proceed either *via* $^1\text{O}_2$ reactions or through reactions between the sensitizer triplet state and cellular targets, but in which only $^1\text{O}_2$ -mediated bleaching reactions lead to photoproduct formation. The derivation of kinetic equations describing such a simultaneous singlet oxygen- and triplet-mediated bleaching (SSTB) mechanism are outlined in section 2.6 of this thesis, where it is shown that for a given set of physical parameters, the relative importance of the $^1\text{O}_2$ - and triplet-mediated mechanisms is determined by the rate constants for the possible reactions of the sensitizer and oxygen and by the concentration of the sensitizer. For the purposes of the arguments outlined below, we have adopted the values of rate constants and photophysical parameters listed in table 2.3.

First, we consider the spheroid model system. In a previous study in our laboratory, Nichols and Foster (1994) used a scintillation counting assay to observe the uptake by spheroids of [^{14}C]polyhaematoporphyrin, a radioactively labelled analogue of Photofrin. In that study, it was determined that the sensitizer concentration in spheroids under conditions identical to those employed in the subsequent photobleaching study was $102\ \mu\text{g ml}^{-1}$, or $170\ \mu\text{M}$. Figure 3.23(a) illustrates the bleaching curves predicted by the SSTB mechanism outlined in section 2.6 for spheroids at oxygen concentrations of $240\ \mu\text{M}$ (air-saturated) and $5\ \mu\text{M}$ for the range of fluences over which electrode measurements were made. The sensitizer

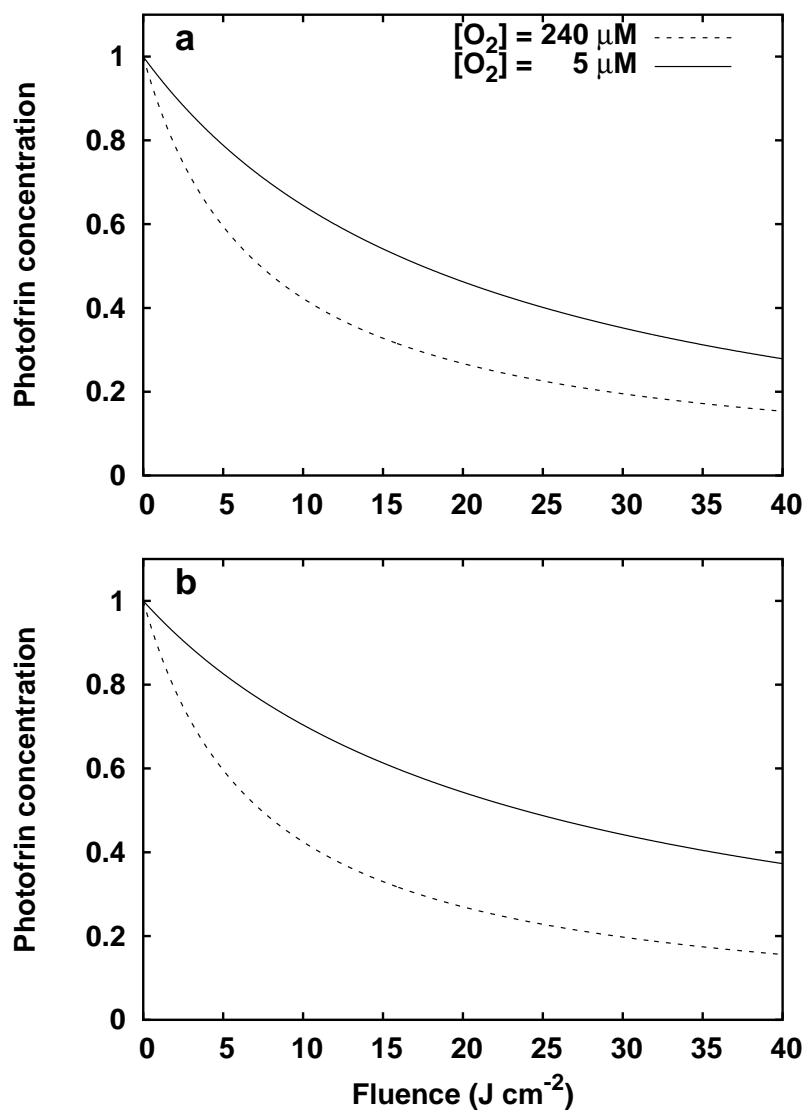


Figure 3.23: Bleaching predicted for spheroids (a) by the mixed-mechanism model and (b) by a model including only $^1\text{O}_2$ -mediated bleaching. In each case, curves are plotted for high (---) and low (—) oxygen concentrations.

concentration is plotted as a fraction of its initial value. The corresponding curves for purely $^1\text{O}_2$ -mediated bleaching are shown in figure 3.23(b). In both cases, the bleaching is more rapid when oxygen is abundant, indicating that $^1\text{O}_2$ -mediated bleaching dominates even when the triplet-mediated mechanism is available. The determination that Photofrin bleaching in spheroids is mediated by $^1\text{O}_2$ is based on the fact that an oxygen diffusion-with-consumption model incorporating $^1\text{O}_2$ -mediated bleaching provides a better fit to the oxygen concentration data taken at the edge of a spheroid during irradiation than corresponding models for bleaching mediated purely by excited singlet or triplet sensitizer reactions (Georgakoudi *et al.*, 1997). It is possible that the $^1\text{O}_2$ -mediated bleaching model would also provide adequate fits to oxygen measurements made in the presence of bleaching which included a small contribution from triplet sensitizer reactions, in which case the triplet contribution would not be detected. This is plausible given the similarity of the curves shown in figures 3.23(a) and (b).

Our *in vivo* experiments were conducted on the normal skin of rats 24 hours after *i.v.* injection of 10 mg kg^{-1} Photofrin. We have not measured the concentration of Photofrin in the skin under these conditions, however it can be estimated based on values from the literature. Windahl *et al.* (1993) found Photofrin concentrations in the lungs and hearts of rats injected 1 hour previously with 10 mg kg^{-1} Photofrin to be approximately 25 and $15 \mu\text{g g}^{-1}$, respectively, and reported that these concentrations changed little over the 48 hours following injection. The uptake of Photofrin in mouse skin 24 hours after *i.p.* injection is similar to that in the lung and heart, as measured by Gibson *et al.* (1994). Based on these studies, we estimate that the concentration of Photofrin in the skin of our rats is approximately

$20 \mu\text{g g}^{-1}$. Assuming a tissue density of 1 g cm^{-3} , this corresponds to a concentration of $34 \mu\text{M}$, five-fold less than that measured in spheroids under our incubation conditions. The photobleaching of Photofrin and accumulation of photoproduct predicted by the SSTB model for this lower initial sensitizer concentration are plotted in figure 3.24. Both the sensitizer and photoproduct concentrations are plotted as fractions of the initial sensitizer concentration. Unlike the spheroids used in our previous studies, tissues *in vivo* do not have direct access to an air-saturated oxygen supply. The concentration of oxygen which is considered normal for tissues is approximately $67 \mu\text{M}$ (Boag, 1969). The two curves shown in each panel of figure 3.24 represent conditions of normal ($67 \mu\text{M}$) and reduced ($5 \mu\text{M}$) tissue oxygenation, corresponding to low and high irradiance irradiation, respectively. The oxygen dependence in the photobleaching profile is slight enough to be masked by experimental error, while the photoproduct accumulation is significantly greater when oxygen is abundant. The qualitative similarity between these curves and the corresponding measured *in vivo* data (figures 3.19 and 3.20) is clear, although the fluence at which a given fraction of bleaching occurs differs. In highly scattering media such as tissue illuminated by plane-wave irradiation, the irradiance within the superficial 2 mm may be higher than that of the incident beam by a factor of 3 to 4, depending on tissue optical properties and the refractive index mismatch between the tissue and the surrounding air (Jacques, 1992; Star, 1989). Taking into account this irradiance enhancement, the bleaching and photoproduct accumulation observed *in vivo* require approximately 2.5 times less total fluence than the SSTB model predicts. Given the uncertainty in the bleaching parameters measured in spheroids, the simplification of treating living

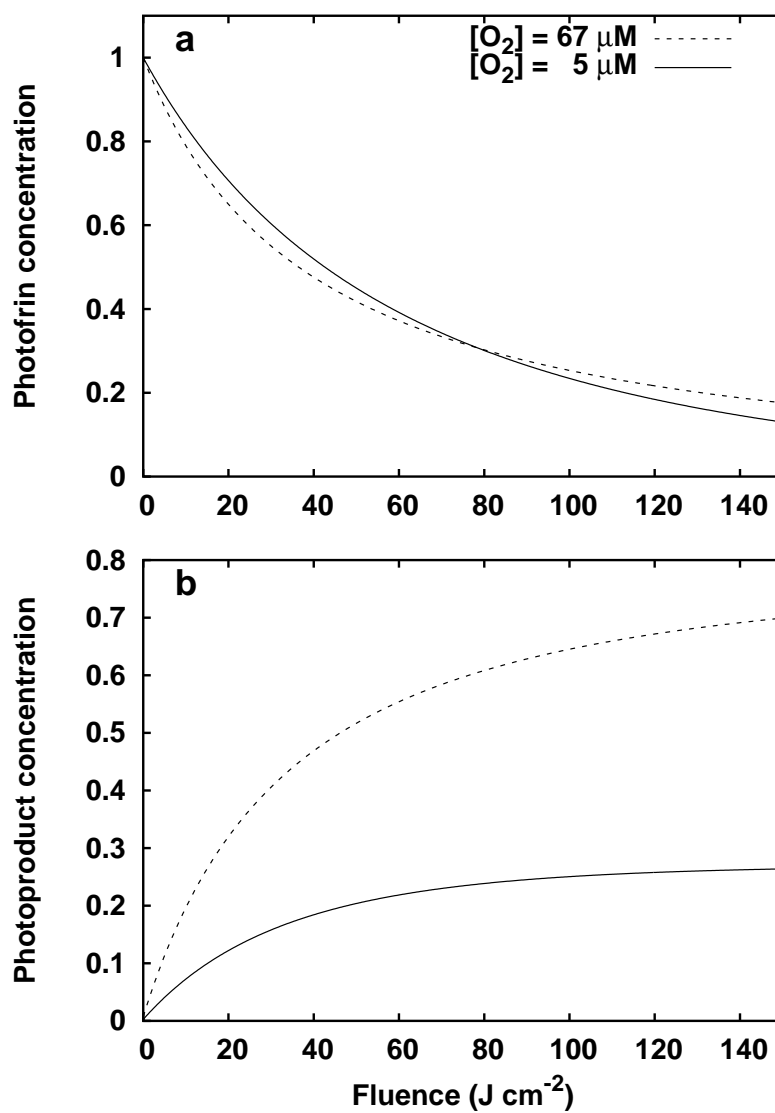


Figure 3.24: Concentrations of (a) ground state sensitizer and (b) photoproduct predicted by kinetic equations for mixed-mechanism bleaching in the case of constant oxygen for well (---) and poorly (—) oxygenated tissue based on estimated *in vivo* conditions. (Reproduced from figure 2.12.)

tissue as a uniformly oxygenated homogeneous medium and the neglect of oxygen consumption and diffusion effects, this discrepancy is a minor one.

Figures 3.23 and 3.24 illustrate that the apparently conflicting observations regarding photobleaching mechanism made in tumor spheroids and in rat skin *in vivo* can be reconciled within the context of a model which incorporates two simultaneous bleaching mechanisms. The only differences between the two systems are the availability of oxygen and the initial concentration of Photofrin. The prediction that the particular sensitizer concentrations present in the two cases lead to such different bleaching profiles is highly dependent on the chosen values of the kinetic parameters described in section 2.6. Among these parameters, only $(k_{ta}[A]/k_{ot})$ has not been measured in spheroids. While we have not measured $(k_{ta}[A]/k_{ot})$ directly, our *in vivo* observations can be used to constrain its value. The bleaching curves shown in figure 3.24(a) assume that $(k_{ta}[A]/k_{ot})$ is equal to $6 \times 10^{-9} \text{ M}^{-1}\text{s}^{-1}$. The effects on the bleaching profile of increasing and decreasing $(k_{ta}[A]/k_{ot})$ by a factor of two are shown in figures 3.25(a) and (b) respectively. When $(k_{ta}[A]/k_{ot})$ is increased, the triplet-mediated bleaching mechanism becomes dominant, and the bleaching is more efficient at low oxygen concentration. Conversely, a two-fold lower value of $(k_{ta}[A]/k_{ot})$ leads to more efficient bleaching in well-oxygenated tissue. The observation of irradiance-independent photobleaching therefore constrains the value of $(k_{ta}[A]/k_{ot})$ to within a factor of 2 of $6 \times 10^{-9} \text{ M}^{-1}\text{s}^{-1}$.

Several possible experiments could test whether multiple simultaneous bleaching mechanisms are in fact involved in the bleaching of Photofrin. The most obvious test would be a measurement of photobleaching, either directly or *via* oxygen

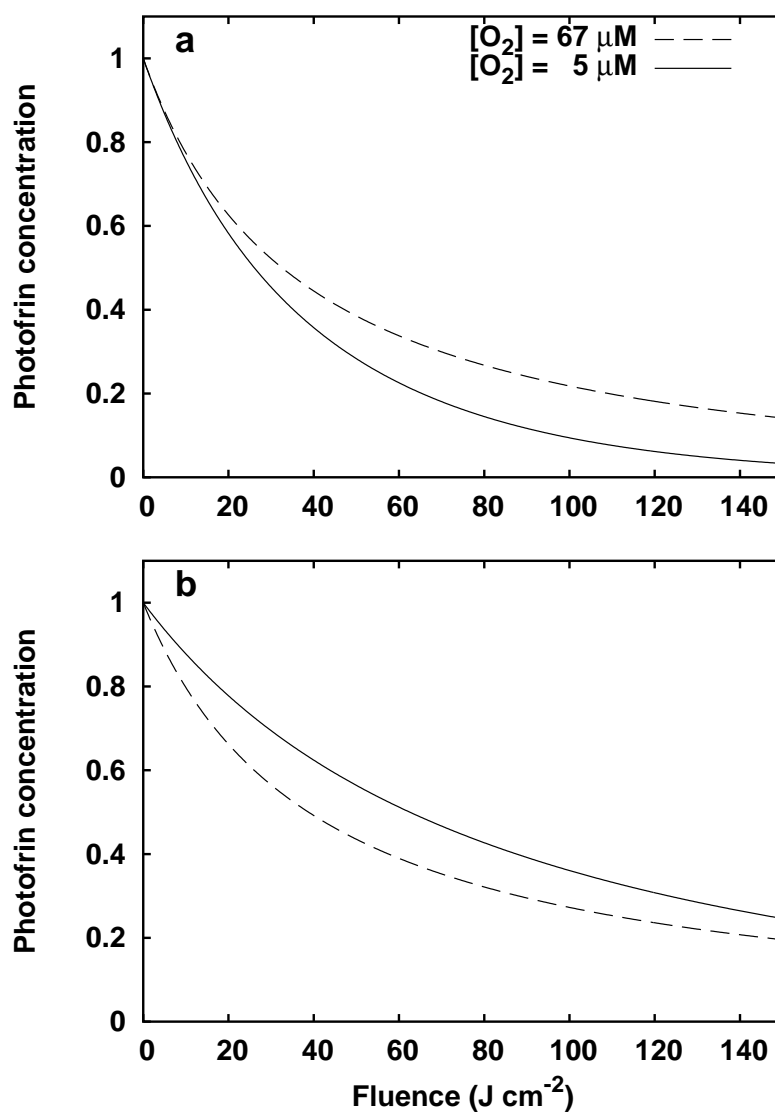


Figure 3.25: Effect on the predicted photobleaching rate of (a) increasing or (b) decreasing the value of the parameter $(k_{ta}[A]/k_{ot})$ by a factor of 2 relative to the conditions shown in figure 3.24(a). All other parameters were unchanged.

concentration, in spheroids incubated with a lower concentration of Photofrin. On-going experiments in our laboratory will use spatially-resolved confocal fluorescence spectroscopy to directly evaluate the photobleaching and photoproduct accumulation in spheroids incubated with a range of Photofrin concentrations. Alternatively, the observation of bleaching in completely deoxygenated tissue would indicate that a non- $^1\text{O}_2$ -mediated mechanism of bleaching is available.

During *in vivo* studies conducted on Photofrin-sensitized mouse mammary tumors irradiated with 630 nm light, Mang *et al.* (1987) observed one case in which the rate of photobleaching in a tumor treated *ex vivo* was increased compared with that observed *in vivo*, an observation which provides at least anecdotal evidence of a triplet-mediated bleaching mechanism. That study did not find evidence for a sensitizer concentration dependence in the photobleaching rate, despite examining a large range (15–60 mg kg⁻¹) of injected sensitizer doses. The SSTB model would predict more rapid bleaching and photoproduct accumulation as the concentration of sensitizer was increased. It is possible that such a concentration dependence was in fact present in the cases observed in the Mang study, but that the method of measurement and data analysis employed did not allow it to be detected. Like the ALA-PpIX bleaching work of Sørensen *et al.* (1998) and Iinuma *et al.* (1999) described in the previous sections, that study did not spectrally resolve the fluorescence emission and thus could not distinguish between the primary sensitizer and its photoproduct. The spectrally integrating measurement is sensitive only to the sum of the emissions of Photofrin and its product over some wavelength range. It is therefore possible in such a measurement for an increase in photobleaching to be offset by an increase in photoproduct accumulation. In that case, the bleaching

observed at low sensitizer concentration (with slow bleaching and slow photoproduct accumulation) and that observed at high concentration (with rapid bleaching and rapid photoproduct accumulation) would be difficult to distinguish.

The consequences of bleaching *via* multiple simultaneous mechanisms for the clinical implementation of fluorescence dosimetry during PDT warrant some attention. The use of fluorescence photobleaching for real-time dosimetry depends on knowledge of the relationship between bleaching and dose. As demonstrated in section 2.6, this relationship is dependent on the initial sensitizer concentration if multiple bleaching mechanisms are present. One potential solution to this difficulty is to use high enough doses of sensitizer to assure that the bleaching is always $^1\text{O}_2$ -dominated. In clinical practice, where skin photosensitivity is already a concern, increasing the drug dose is unlikely to be practical. In cases where triplet-mediated bleaching plays a significant role, our *in vivo* data suggest that the accumulation of photoproduct may be more useful for dosimetry than the photobleaching, a concept borne out by the SSTB model. The results presented here motivate careful attention to the local concentration of sensitizer and to the details of its bleaching mechanism in the formulation of dosimetry and treatment protocols.

3.4.5 Conclusions and future directions

The use of fluorescence spectroscopy as a tool for quantitative dosimetry in PDT is a promising possibility. However, significant development is still required before clinical implementation will be possible. In particular, it is important to realize that each sensitizer is likely to have its own unique spectroscopic behavior.

Photofrin exhibits irradiance dependence only in the accumulation of photoproduct. In contrast, PpIX exhibits irradiance dependence in both the bleaching of the sensitizer and the formation of photoproducts (Finlay *et al.*, 2001; Robinson *et al.*, 1998; 1999). mTHPC, which does not form fluorescent photoproducts, exhibits a two-phase bleaching profile, with only the later stage being irradiance dependent. While each sensitizer has a characteristic spectroscopic signature which is likely related to photodynamic dose, no single metric is generally applicable.

Modelling of oxygen transport and consumption in multicell tumor spheroids has been demonstrated previously (Georgakoudi and Foster, 1998b; Georgakoudi *et al.*, 1997). Extension of this model to a geometry and set of boundary conditions appropriate to capillaries would allow rigorous evaluation of the effects of photodynamic oxygen consumption on local tissue and vascular oxygen tension. The SSTB model used above to describe the photobleaching of Photofrin could be made more accurate by the explicit incorporation of the effects of oxygen consumption and diffusion. Non-invasive measurements of vascular oxygen tension *via* diffuse reflectance spectroscopy will allow monitoring of oxygenation as well as sensitizer concentration during PDT. A new strategy for acquiring such measurements *in vivo* is presented in chapter 4.

The effectiveness of photodynamic treatment is also highly dependent on the distribution of light within the target tissue, which in turn depends on tissue optical properties which are effected by local vascular oxygenation. Methods for evaluating heterogeneity in optical properties and in distribution of sensitizer in tumors and making corresponding adjustments to the irradiation protocol are under investigation by several groups (Lee *et al.*, 2003; Solonenko *et al.*, 2002).

Using the volume-averaged measurements of oxygenation provided by diffuse reflectance spectroscopy and of photobleaching provided by fluorescence spectroscopy and a model which makes reasonable assumptions about capillary spacing and oxygenation of supply vasculature, it may eventually be possible to evaluate in detail the extent of oxygen gradients and microscopic heterogeneity in photobleaching and photodynamic dose deposition in tumors *in vivo*.

References

- Baas, P., Saarnak, A. E., Oppelaar, H., Neering, H., and Stewart, F. A. (2001). Photodynamic therapy with meta-tetrahydroxyphenylchlorin for basal cell carcinoma: A Phase I/II study. *Br. J. Dermatol.* **145**:75–78.
- Bandanas, S., Ma, L., Iani, V., Rotomskis, R., Juzenas, P., and Moan, J. (2000). Phototransformations of 5-aminolevulinic acid-induced protoporphyrin IX *in vitro*: A spectroscopic study. *Photochem. Photobiol.* **72**:186–192.
- Berg, K., Madslien, K., Bommer, J. C., Oftebro, R., Winkelman, J. W., and Moan, J. (1991). Light induced relocation of sulfonated *meso*-tetraphenylporphines in NHIK 3025 cells and effects of dose fractionation. *Photochem. Photobiol.* **53**:203–210.
- Bigelow, C. E., Conover, D. L., and Foster, T. H., (2002). A custom laser scanning confocal fluorescence microscope with simultaneous multi-wavelength imaging, spectroscopy and anisotropy capabilities. American Society for Photobiology 30th Annual Meeting, July 13-17, 2002 Quebec City, Canada, Abstract 248, Book of Abstracts, p 85.
- Blant, S. A., Woodtli, A., Wagnières, G., Fontollet, C., van den Bergh, H., and Monnier, P. (1996). *In vivo* fluence rate effect in photodynamic therapy of early cancers with tetra(m-hydroxyphenyl)chlorin. *Photochem. Photobiol.* **64**:963–968.
- Boag, J. W. (1969), Oxygen diffusion and oxygen depletion problems in radiobiology. In *Current Topics in Radiation Research*, Ebert, M. and Howard, A., editors, volume 5, pages 141–195. North-Holland, Amsterdam/London.
- Boyle, D. G. and Potter, W. R. (1987). Photobleaching of Photofrin II as a means of eliminating skin photosensitivity. *Photochem. Photobiol.* **46**:997–1001.
- Coutier, S., Mitra, S., Bezdetnaya, L. N., Parache, R. M., Georgakoudi, I., Foster, T. H., and Guillemin, F. (2001). Effects of fluence rate on cell survival and photobleaching in *meta*-tetra-(hydroxyphenyl)chlorin-photosensitized Colo 26 multicell tumor spheroids. *Photochem. Photobiol.* **73**:297–303.
- Dietel, W., Bolsen, K., Dickson, E., Fritsch, C., Pottier, R., and Wendenburg, R. (1996). Formation of water-soluble porphyrins and protoporphyrin IX in 5-aminolevulinic-acid-incubated carcinoma cells. *J. Photochem. Photobiol. B.* **33**:225–231.

- Dietel, W., Fritsch, C., Potter, W. R., and Wendenburg, R. (1997). 5-aminioleaeuvulinic-acid-induced formation of different porphyrins and their photomodifications. *Lasers Med. Sci.* **12**:226–236.
- Dougherty, T. J., Gomer, C. J., Henderson, B. W., Jori, G., Kessel, D., Korbelik, M., Moan, J., and Peng, Q. (1998). Photodynamic therapy. *J. Natl. Cancer Inst.* **90**:889–905.
- Farrell, T. J., Hawkes, R. P., Patterson, M. S., and Wilson, B. C. (1998). Modeling of photosensitizer fluorescence emission and photobleaching for photodynamic therapy dosimetry. *Appl. Opt.* **37**:7168–7183.
- Feins, R. H., Hilf, R., Ross, H., and Gibson, S. L. (1990). Photodynamic therapy for human mesothelioma in the nude mouse. *J. Surg. Res.* **49**:311–314.
- Finlay, J. C., Conover, D. L., Hull, E. L., and Foster, T. H. (2001). Porphyrin bleaching and PDT-induced spectral changes are irradiance dependent in ALA-sensitized normal rat skin *in vivo*. *Photochem. Photobiol.* **73**:54–63.
- Finlay, J. C., Mitra, S., and Foster, T. H. (2002). *In vivo* mTHPC photobleaching in normal rat skin exhibits unique irradiance-dependent features. *Photochem. Photobiol.* **75**:282–288.
- Forrer, M., Glanzmann, T., Braichotte, D., Wagnières, G., van den Bergh, H., Savary, J. F., and Monnier, P. (1995). *In vivo* measurement of fluorescence bleaching of meso-tetra hydroxy phenyl chlorin (mTHPC) in the esophagus and the oral cavity. *Proc. SPIE.* **2627**:33–39.
- Foster, T. H., Hartley, D. F., Nichols, M. G., and Hilf, R. (1993). Fluence rate effects in photodynamic therapy of multicell tumor spheroids. *Cancer Res.* **53**:1249–1254.
- Foster, T. H., Murant, R. S., Bryant, R. G., Knox, R. S., Gibson, S. L., and Hilf, R. (1991). Oxygen consumption and diffusion effects in photodynamic therapy. *Rad. Res.* **126**:296–303.
- Gardner, C. M., Jacques, S. L., and Welch, A. J. (1996). Fluorescence spectroscopy of tissue: Recovery of intrinsic fluorescence from measured fluorescence. *Appl. Opt.* **35**:1780–92.
- Georgakoudi, I. and Foster, T. H. (1998a). Effects of the subcellular redistribution of two Nile blue derivatives on photodynamic oxygen consumption. *Photochem. Photobiol.* **68**:115–122.

- Georgakoudi, I. and Foster, T. H. (1998b). Singlet oxygen- *versus* nonsinglet oxygen-mediated mechanisms of sensitizer photobleaching and their effects on photodynamic dosimetry. *Photochem. Photobiol.* **67**:612–625.
- Georgakoudi, I., Nichols, M. G., and Foster, T. H. (1997). The mechanism of Photofrin photobleaching and its consequences for photodynamic dosimetry. *Photochem. Photobiol.* **65**:135–144.
- Gibson, S. L., Foster, T. H., Feins, R. H., Raubertas, R. F., Fallon, M. A., and Hilf, R. (1994). Effects of photodynamic therapy on xenografts of human mesothelioma and rat mammary carcinoma in nude mice. *Br. J. Cancer.* **69**: 473–481.
- Gibson, S. L., VanDerMeid, K. R., Murant, R. S., Raubertas, R. F., and Hilf, R. (1990). Effects of various photoradiation regimens on the antitumor efficacy of photodynamic therapy for R3230AC mammary carcinomas. *Cancer Res.* **50**: 7236–7241.
- Gudgin Dickson, E. F., Holmes, H., Jori, G., Kennedy, J. C., Nadeau, P., Pottier, R. H., Rossi, F., Russell, D. A., and Weagle, G. E. (1995). On the source of the oscillations observed during *in vivo* zinc phthalocyanine fluorescence pharmacokinetic measurements in mice. *Photochem. Photobiol.* **61**:506–509.
- Gudgin Dickson, E. F. and Pottier, R. H. (1995). On the role of protoporphyrin IX photoproducts in photodynamic therapy. *J. Photochem. Photobiol. B.* **29**: 91–93.
- Hadjur, C., Lange, N., Rebstein, J., Monnier, P., van den Bergh, H., and Wagnières, G. (1998). Spectroscopic studies of photobleaching and photoproduct formation of *meta* (tetrahydroxyphenyl) chlorin (*m*-thpc) used in photodynamic therapy. The production of singlet oxygen by *m*-thpc. *J. Photochem. Photobiol. B.* **45**:170–178.
- Heil, P., Stocker, S., Sroka, R., and Baumgartner, R. (1997). *In vivo* fluorescence kinetics of porphyrins following intravesical instillation of 5-aminolaevulinic acid in normal and tumour-bearing rat bladders. *J. Photochem. Photobiol. B.* **38**: 158–163.
- Henderson, B. W., Busch, T. M., Vaughan, L. A., Frawley, N. P., Babich, D., Sosa, T. A., Zollo, J. D., Dee, A. S., Cooper, M. T., Bellnier, D. A., Greco, W. R., and Oseroff, A. R. (2000). Photofrin photodynamic therapy can significantly deplete or preserve oxygenation in human basal cell carcinomas during treatment, depending on fluence rate. *Cancer Res.* **60**:525–529.

- Holmes, H., Kennedy, J. C., Pottier, R., Rossi, R., and Weagle, G. (1995). A recipe for the preparation of a rodent food that eliminates chlorophyll-based tissue fluorescence. *J. Photochem. Photobiol. B.* **29**:199.
- Hua, Z., Gibson, S. L., Foster, T. H., and Hilf, R. (1995). Effectiveness of delta-aminolevulinic acid-induced protoporphyrin as a photosensitizer for photodynamic therapy *in vivo*. *Cancer Res.* **55**:1723–1731.
- Hull, E. L., Conover, D. L., and Foster, T. H. (1999). Carbogen-induced changes in rat mammary tumour oxygenation reported by near infrared spectroscopy. *Br. J. Cancer.* **79**:1709–1716.
- Hull, E. L. and Foster, T. H. (2001). Steady-state reflectance spectroscopy in the P_3 approximation. *JOSA A.* **18**:584–599.
- Iinuma, S., Schomacker, K. T., Wagnières, G., Rajadhyaksha, M., Bamberg, M., Momma, T., and Hasan, T. (1999). *In vivo* fluence rate and fractionation effects on tumor response and photobleaching: Photodynamic therapy with two photosensitizers in an orthotopic rat tumor model. *Cancer Res.* **59**:6164–6170.
- Jacques, S. L. (1992). Simple optical theory for light dosimetry during PDT. *Proc. SPIE.* **1645**:155–165.
- Jacques, S. L., Joseph, R., and Gofstein, G. (1993). How photobleaching effects dosimetry and fluorescence monitoring of PDT in turbid media. *Proc. SPIE.* **1881**:168–179.
- Joep, E. M. (1949), The ultraviolet spectral absorption of haemoglobins inside and outside the red blood cell. In *Haemoglobin*, Roughton, F. J. W. and Kendrew, J. C., editors, pages 205–219. Interscience Publisher, Inc., New York.
- Keijzer, M., Richards-Kortum, R. R., Jacques, S. L., and Feld, M. S. (1989). Fluorescence spectroscopy of turbid media: Autofluorescence of the human aorta. *Appl. Opt.* **28**:4286–4292.
- König, K., Schneckenburger, H., Rück, A., and Steiner, R. (1993). *In vivo* photoproduct formation during PDT with ALA-induced endogenous porphyrins. *J. Photochem. Photobiol. B.* **18**:287–290.
- König, K., Wabnitz, H., and Dietel, W. (1990). Variation in the fluorescence decay properties of haematoporphyrin derivative during its conversion to photoproducts. *J. Photochem. Photobiol. B.* **8**:103–111.

- Krieg, M. and Whitten, D. G. (1984). Self-sensitized photo-oxidation of protoporphyrin IX and related porphyrins in erythrocyte ghosts and microemulsions: A novel photo-oxidation pathway involving singlet oxygen. *J. Photochem.* **25**: 235–252.
- Lee, C. C., Pogue, B. W., O'Hara, J. A., Wilmot, C. M., Strawbridge, R. R., Burke, G. C., and Hoopes, P. J. (2003). Spatial heterogeneity and temporal kinetics of photosensitizer (AlPcS₂) concentration in murine tumors RIF-1 and MTG-B. *Photochem. Photobiol. Sci.* **2**:145–150.
- Ma, L., Moan, J., and Berg, K. (1994a). Evaluation of a new photosensitizer, meso-tetra-hydroxyphenyl-chlorin, for use in photodynamic therapy: A comparison of its photobiological properties with those of two other photosensitizers. *Int. J. Cancer.* **57**:883–888.
- Ma, L. W., Moan, J., and Berg, K. (1994b). Comparison of the photobleaching effect of three photosensitizing agents: Meso-tetra(*m*-hydroxyphenyl)chlorin, meso-tetra(*m*-hydroxyphenyl)porphyrin and Photofrin during photodynamic therapy. *Lasers Med. Sci.* **9**:127–132.
- Mang, T. S., Dougherty, T. J., Potter, W. R., Boyle, D. G., Somer, S., and Moan, J. (1987). Photobleaching of porphyrins used in photodynamic therapy and implications for therapy. *Photochem. Photobiol.* **45**:501–506.
- Melnikova, V. O., Bezdetnaya, L. N., Bour, C., Fester, E., Gramain, M.-P., Merlin, J.-L., Potapenko, A. Y., and Guillemin, F. (1999a). Subcellular localization of meta-tetra (hydroxyphenyl) chlorin in human tumor cells subjected to photodynamic treatment. *J. Photochem. Photobiol. B.* **49**:96–103.
- Melnikova, V. O., Bezdetnaya, L. N., Potapenko, A. Y., and Guillemin, F. (1999b). Photodynamic properties of meta-tetra(hydroxyphenyl)chlorin in human tumor cells. *Radiat. Res.* **152**:428–435.
- Mlkvy, P., Messmann, H., Regula, J., Conio, M., Pauer, M., Millson, C. E., MacRobert, A. J., and Bown, S. G. (1998). Photodynamic therapy for gastrointestinal tumors using three photosensitizers-ALA induced PpIX, Photofrin and mTHPC. A pilot study. *Neoplasma.* **45**:157–161.
- Moan, J. (1986). Effect of bleaching of porphyrin sensitizers during photodynamic therapy. *Cancer Lett.* **33**:45–53.
- Moan, J. and Kessel, D. (1988). Photoproducts formed from Photofrin II in cells. *J. Photochem. Photobiol. B.* **1**:429–436.

- Müller, M., Georgakoudi, I., Zhang, Q., Wu, J., and Feld, M. (2001). Intrinsic fluorescence spectroscopy in turbid media: Disentangling effects of scattering and absorption. *Appl. Opt.* **40**:4633–4646.
- Nichols, M. G. and Foster, T. H. (1994). Oxygen diffusion and reaction kinetics in the photodynamic therapy of multicell tumour spheroids. *Phys. Med. Biol.* **39**:2161–81.
- Peng, Q., Farrants, G. W., Madslien, K., Bommer, J. C., Moan, J., Danielsen, H. E., and Nesland, J. M. (1991). Subcellular localization, redistribution and photobleaching of sulfonated aluminum phthalocyanines in a human melanoma cell line. *Int. J. Cancer.* pages 290–295.
- Peng, Q., Warloe, T., Berg, K., Moan, J., Kongshaug, M., Giercksky, K. E., and Nesland, J. M. (1997). 5-aminolevulinic acid-based photodynamic therapy. Clinical research and future challenges. *Cancer.* **79**:2282–2308.
- Polo, C. F., Frisardi, A. L., Resnik, E. R., Schoua, A. E., and Batlle, A. M. (1988). Factors influencing fluorescence spectra of free porphyrins. *Clin. Chem.* **34**:757–760.
- Potter, W. R., Mang, T. S., and Dougherty, T. J. (1987). The theory of photodynamic therapy dosimetry: Consequences of photo-destruction of sensitizer. *Photochem. Photobiol.* **46**:97–101.
- Ris, H. B., Altermatt, H. J., Inderbitzi, R., Hess, R., Nachbur, B., Stewart, J. C., Wang, Q., Lim, C. K., Bonnett, R., and Berenbaum, M. C. (1991). Photodynamic therapy with chlorins for diffuse malignant mesothelioma: Initial clinical results. *Br. J. Cancer.* **64**:1116–1120.
- Ris, H. B., Altermatt, H. J., Nachbur, B., Stewart, C. M., Wang, Q., Lim, C. K., Bonnett, R., and Althaus, U. (1996). Intraoperative photodynamic therapy with m-tetrahydroxyphenylchlorin for chest malignancies. *Lasers Surg. Med.* **18**:39–45.
- Robinson, D. J., de Bruijn, H. S., van der Veen, N., Stringer, M. R., Brown, S. B., and Star, W. M. (1998). Fluorescence photobleaching of ALA-induced protoporphyrin IX during photodynamic therapy of normal hairless mouse skin: The effect of light dose and irradiance and the resulting biological effect. *Photochem. Photobiol.* **67**:140–149.

- Robinson, D. J., de Bruijn, H. S., van der Veen, N., Stringer, M. R., Brown, S. B., and Star, W. M. (1999). Protoporphyrin IX fluorescence photobleaching during ALA-mediated photodynamic therapy of UVB-induced tumors in hairless mouse skin. *Photochem. Photobiol.* **69**:61–70.
- Savary, J. F., Monnier, P., Fontolliet, C., Mizeret, J., Wagnières, G., Braichotte, D., and van den Bergh, H. (1997). Photodynamic therapy for early squamous cell carcinomas of the esophagus, bronchi, and mouth with m-tetra (hydroxyphenyl) chlorin. *Arch. Otolaryngol. Head Neck Surg.* **123**:162–168.
- Sitnik, T. M. and Henderson, B. W. (1998a). The effect of fluence rate on tumor and normal tissue responses to photodynamic therapy. *Photochem. Photobiol.* **67**:462–466.
- Sitnik, T. M. and Henderson, B. W. (1998b). Reduction of tumor oxygenation during and after photodynamic therapy *in vivo*: Effects of fluence rate. *Br. J. Cancer.* **77**:1386–1394.
- Solonenko, M., Cheung, R., Busch, T. M., Kachur, A., Griffin, G. M., Vulcan, T., Zhu, T., Wang, H.-W., Hahn, S. M., and Yodh, A. G. (2002). *In vivo* reflectance measurements of optical properties, blood oxygenation and motexafin lutetium uptake in canine large bowels, kidneys and prostates. *Phys. Med. Biol.* **47**: 857–873.
- Sørensen, R., Iani, V., and Moan, J. (1998). Kinetics of photobleaching of protoporphyrin IX in the skin of nude mice exposed to different fluence rates of red light. *Photochem. Photobiol.* **68**:835–840.
- Spikes, J. D. (1992). Quantum yields and kinetics of the photobleaching of hematoporphyrin, Photofrin II, tetra(4-sulfonatophenyl)-porphine and uroporphyrin. *Photochem. Photobiol.* **55**:797–808.
- Star, W. M. (1989). Comparing the P_3 -approximation with diffusion theory and with Monte Carlo calculations of light propagation in a slab geometry. *SPIE Institute Series.* **IS5**:46–54.
- Stryer, L. (1988). *Biochemistry*. W.H. Freeman Co., New York, third edition.
- Tromberg, B. J., Orenstein, A., Kimel, S., Barker, S. J., Hyatt, J., Nelson, J. S., and Berns, M. (1990). *In vivo* tumor oxygen tension measurements for the evaluation of the efficiency of photodynamic therapy. *Photochem. Photobiol.* **52**:375–385.

- van Staveren, H. J., Moes, C. J. M., van Marle, J., Prahl, S. A., and van Gemert, M. J. C. (1991). Light scattering in Intralipid-10% in the wavelength range of 400-1100 nm. *Appl. Opt.* **30**:4507–4515.
- Veenhuizen, R. B. and Stewart, F. A. (1995). The importance of fluence rate in photodynamic therapy: Is there a parallel with ionizing radiation dose-rate effects? *Radiother. Oncol.* **37**:131–135.
- Weagle, G., Paterson, P. E., Kennedy, J., and Pottier, R. (1988). The nature of the chromophore responsible for naturally occurring fluorescence in mouse skin. *J. Photochem. Photobiol. B.* **2**:313–320.
- Wessels, J. M., Sroka, R., Heil, P., and Seidlitz, H. K. (1993). Photodegradation of protoporphyrin-dimethylester in solution and in organized environments. *Int. J. Radiat. Biol.* **64**:475–484.
- Wilson, B. C., Patterson, M., and Lilge, L. (1997). Implicit and explicit dosimetry in photodynamic therapy: A new paradigm. *Lasers Med. Sci.* **12**:182–199.
- Windahl, T., Peng, Q., Moan, J., Hellsten, S., Axelsson, B., and Løfgren, L. (1993). Uptake and distribution of intravenously or intravesically administered photosensitizers in the rat. *Cancer. Lett.* **75**:65–70.
- Wu, J., Feld, M. S., and Rava, R. (1993). Analytical model for extracting intrinsic fluorescence in turbid media. *Appl. Opt.* **32**:3583–3595.

Chapter 4

Single-Detector Diffuse Reflectance Spectroscopy

4.1 Introduction

The theory described in chapter 2 models the reflectance and fluorescence captured from tissue for a given set of optical properties and source-detector geometry. In this chapter, these methods are extended to the recovery of optical property information from spectrally resolved reflectance measurements. Previous work in our laboratory has taken the approach of rigorously determining the optical properties at each measured wavelength sequentially using radially-resolved measurements of diffuse reflectance (Hull and Foster, 2001b; Hull *et al.*, 1998; Nichols *et al.*, 1997). The resulting absorption spectra were then fit using an SVD algorithm similar to that described in chapter 2 to determine the concentrations of absorbers. In this chapter, we present an alternative approach requiring spectrally resolved measurements at only one source-detector separation. Rather than fitting the radial reflectance profile at each wavelength, our algorithm uses reasonable assumptions about the shape of the absorption and reduced scattering

spectra of the sample and the P_3 diffuse reflectance theory described in chapter 2 to fit the entire spectrum simultaneously. The algorithm returns the concentrations of known absorbers and information about the reduced scattering spectrum of the sample.

The first part of this chapter introduces the measurement techniques, data analysis procedures and fitting algorithms necessary to extract optical property information from measurements of diffuse reflectance spectra. The remainder of the chapter is devoted to the evaluation of the performance of the fitting algorithms under various conditions. First, we generate synthetic reflectance spectra using Monte Carlo simulation and fit them with our algorithm. Because the absorption and scattering spectra used to generate the data are known exactly, the ability of the fitting algorithm to recover them can be tested rigorously. This method also eliminates the error and artifacts associated with experiments, thereby enabling a test of the method's optimal capabilities. Furthermore, because the absorption and scattering spectra used in the Monte Carlo simulation match the fitting algorithm's basis set exactly, the problems associated with choosing the correct basis spectra can be separated from those associated with modelling the propagation of light.

While simulated data sets are useful from the point of view of algorithm development and initial testing, they represent an idealized case. To evaluate the algorithm under conditions closer to those encountered *in vivo*, we test the ability of the algorithm to recover information about the oxygenation status of hemoglobin in tissue-simulating phantoms containing intact human red blood cells. These phantoms exhibit absorption by hemoglobin in an environment identical to that

encountered *in vivo*; they therefore provide a good test of the ability of the algorithm to recover dynamically changing oxygenation information from optical spectra acquired *in vivo*. Red blood cell phantoms represent the closest possible approximation of the true *in vivo* environment while preserving the simplicity of phantoms.

Finally, we use the algorithm tested and verified in the initial sections of the chapter to assess changes in the hemoglobin concentration and oxygen saturation in rodent tumors *in vivo*. The measurement of tissue oxygenation is of particular interest in the field of PDT because photodynamic treatment depends on the presence of oxygen for the generation of cytotoxicity. Variations in oxygenation during treatment may have significant effects on the biological response to PDT and, as demonstrated in chapter 3, on the photobleaching of the sensitizer. These observations motivate the need for techniques capable of providing noninvasive or minimally invasive measurement of tissue oxygenation during treatment. Our single source-detector spectroscopy technique allows quantitative assessment of the hemoglobin concentration and oxygen saturation of even very small tumors.

A test of the applicability of our spectroscopic methods and a problem of interest in its own right is the response of tumors to changes in the oxygen concentration in breathed gas. Of particular interest is carbogen, a mixture of 95% oxygen and 5% carbon dioxide. The effects of carbogen breathing on tumor tissue specifically have been widely studied. Carbogen inhalation has been shown to increase tumor oxygenation in clinical trials (Kaanders *et al.*, 2002; Rijpkema *et al.*, 2002, and references therein). Much of the quantitative work in this field, however, has been performed in animal models rather than human patients. Tumor oxygenation and

blood flow have been measured *in vivo* using a combination of oxygen-sensitive electrodes and laser Doppler probes (Lanzen *et al.*, 1998), functional magnetic resonance imaging (fMRI) (Howe *et al.*, 1999; Robinson *et al.*, 1995; 1997), electron paramagnetic resonance (EPR) spectroscopy (Ilangovan *et al.*, 2002) and near-infrared spectroscopy (Conover *et al.*, 2000; Hull *et al.*, 1999; Liu *et al.*, 2000). These studies employed a variety of methods and a variety of different tumor models to study the effects of carbogen. While each combination of tumor model and methodology exhibited a detectable increase in the tumor oxygen concentration in response to carbogen breathing, the extent and timecourse of the response varies wildly among different tumor types (Robinson *et al.*, 1997), among animals with the same tumor type (Hull *et al.*, 1999; Ilangovan *et al.*, 2002; Robinson *et al.*, 1995) and even among different locations within a single tumor (Lanzen *et al.*, 1998).

In the context of PDT, heterogeneity in oxygen concentration within a tumor is of particular interest. Even if a tumor's average oxygen concentration is high enough to allow PDT to be effective, local regions of hypoxic tissue may be spared photodynamic damage. An assessment of the importance of such regional inhomogeneities requires a detection method with a resolution greater than that offered by typical near-infrared spectroscopy methods, which derive a single absorption spectrum from a large volume of tissue (Conover *et al.*, 2000). The methods developed in the early sections of this chapter are well-suited to such a study. They require only a single source-detector separation and only a small volume of tissue to measure the concentrations of oxy- and deoxyhemoglobin. The *in vivo* mea-

surements reported in this chapter represent the first direct optical method for determining the heterogeneity of tumor response to carbogen inhalation.

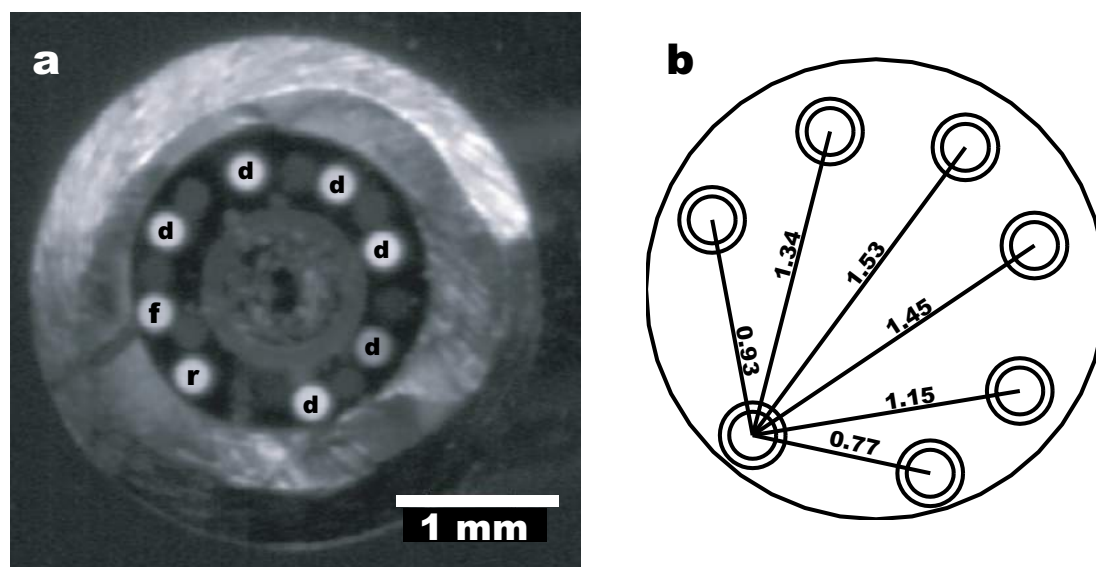


Figure 4.1: (a) Image of the face of the diffuse reflectance/fluorescence probe with the detection (d) and fluorescence (f) and reflectance (r) source fibers illuminated and (b) schematic illustrating the distances (in mm) between detection fibers and the reflectance source fiber.

4.2 Methods

4.2.1 Spectral data acquisition

Diffuse reflectance spectra were acquired using a fiber optic-based probe originally designed for the sequential collection of fluorescence and reflectance data described in chapter 3. The probe consists of a central $400\ \mu\text{m}$ core fiber surrounded by sixteen $200\ \mu\text{m}$ fibers, eight of which are individually terminated in SMA connectors. An end-view of the probe acquired with a digital scanner is shown in figure 4.1(a). In this image, only the eight individually terminated fibers are illuminated. In the experiments described in chapter 3, these eight fibers were used collect diffuse

reflectance and fluorescence signals. In the current implementation, one of these fibers (labelled ‘r’ in the figure) is used as a light source for reflectance measurements. This fiber is illuminated by the output of a 150 W xenon arc lamp. UG-3 and KV-380 colored glass filters (Schott) are used to reduce the intensity of the lamp at short wavelengths and to flatten its spectrum. For the fluorescence spectroscopy experiments described in chapter 5, a second fiber (labelled ‘f’) is used to deliver fluorescence excitation light to the sample. Electronic shutters (Vincent Associates) allow the lamps to be blocked, so that the sample is exposed to light only when spectra are being acquired. The six remaining fibers (labelled ‘d’ in figure 4.1) are used to collect light from the sample. The separations in millimeters between the reflectance source fiber and the detector fibers are illustrated in figure 4.1(b). Light collected by each detection fiber passes through a variable attenuator into one arm of a multi-arm transfer fiber assembly. The output of the transfer assembly is imaged onto a nitrogen-cooled, 512×512 pixel CCD camera *via* an imaging spectrograph. The variable attenuators are adjusted to balance the signal collected by the fibers, minimizing the effects of fiber-to-fiber crosstalk described below. The groove density of the spectrograph grating was chosen to give a wavelength range of approximately 442 nm resolved at 0.86 nm per pixel.

The spectra acquired by this system must be corrected for the effects of detector readout offset, fiber crosstalk, and instrument spectral response. The first effect which must be corrected is the digitization offset applied by the CCD readout electronics. As described in chapter 3, this offset can be subtracted automatically in software during data acquisition. In the experiments described in the following sections, we perform the offset subtraction after data acquisition,

which allows us to average many measurements of the readout offset to obtain a less noisy offset correction. This reduction of noise is helpful in cases where the detected signal is weak.

The second effect that must be corrected is fiber-to-fiber crosstalk within the imaging optics, spectrograph and CCD. Because of imperfect imaging of the transfer fibers onto the face of the CCD, the signal detected on the region of the CCD dedicated to one fiber may include contributions from light that originated in other fibers. The crosstalk may be characterized by a matrix C such that

$$I_{meas} = C \times I_0, \quad (4.1)$$

where I_{meas} and I_0 are the measured signal and that measured by a perfect (crosstalk-free) detector, respectively (Hull, 1999). I_{meas} and I_0 are each column vectors whose length, n_d , is equal to the number of channels being used, six in this case. C is an $n_d \times n_d$ square matrix.

The matrix C can be evaluated by illuminating one fiber at a time. In this case, I_0 has only one non-zero element. For example, if only fiber two is illuminated, equation 4.1 becomes

$$\begin{pmatrix} I_{meas\,1} \\ I_{meas\,2} \\ \vdots \\ I_{meas\,n_d} \end{pmatrix} = \begin{pmatrix} C_{11} & C_{21} & \cdots & C_{n_d1} \\ C_{12} & C_{22} & \cdots & C_{n_d2} \\ \vdots & \vdots & \ddots & \vdots \\ C_{1n_d} & C_{2n_d} & \cdots & C_{n_dn_d} \end{pmatrix} \times \begin{pmatrix} 0 \\ I_{02} \\ \vdots \\ 0 \end{pmatrix} = \begin{pmatrix} I_{02}C_{21} \\ I_{02}C_{22} \\ \vdots \\ I_{02}C_{2n_d} \end{pmatrix}. \quad (4.2)$$

Because the true signal in the non-illuminated fibers is zero, the signal in these

channels is due purely to crosstalk from fiber 2. The elements C_{ij} are given by

$$C_{ij} = \frac{I_{meas\ i}}{I_{meas\ j}}, \quad (4.3)$$

where it is assumed that only fiber j is illuminated. The true signal I_0 is found by inverting equation 4.1, and is given by

$$I_0 = C^{-1} \times I_{meas}. \quad (4.4)$$

In the case of spectroscopy, the crosstalk is known to be wavelength-dependent, so a different crosstalk matrix is needed for each wavelength (Hull, 1999). To apply the crosstalk correction, we apply equation 4.4 at each wavelength sequentially. If only a single detection fiber illuminates the CCD no crosstalk correction is necessary. However, all the data presented in the following sections were acquired using multiple source-detector separations simultaneously. Even when only one detector's signal is used in the final analysis, the presence of other fibers in the original measurement requires that crosstalk correction be implemented.

The final correction accounts for the spectral response of the CCD, the transmission of the fibers, spectrograph, and imaging optics, and, in the case of reflectance measurements, the spectral intensity of the light source. We obtain the true reflectance spectrum of a sample by dividing the measured reflectance spectrum by that of an integrating sphere coated with white reflecting paint (CAT 849 1656, Scientific Imaging Systems, Eastman Kodak Company, Rochester, NY). This accounts for the throughput of the probe, the spectrum of the source, and the

spectral response of the CCD. The use of an integrating sphere ensures uniform illumination of the probe, which corrects for differences in transmission between fibers and for differences in the settings of the variable attenuators.

4.2.2 Nonlinear fitting of spectral data

The processed data are fit to obtain the optical properties of the medium using the nonlinear fitting algorithm described in section 2.5.2. Prior to fitting, the data are normalized to 1 at 650 nm. This allows us to fit the shape of the reflectance spectrum rather than the absolute reflectance intensity. The goal of the fitting algorithm is to extract a vector \mathbf{a} of parameters that characterize the sample. In the examples presented here, the elements of \mathbf{a} are the concentrations of known absorbers and parameters describing the scattering spectrum, as described below. Prior to fitting, an initial \mathbf{a} is chosen. The choice of the initial vector is not critical, however the closer it is to the correct value, the faster the convergence of the fit will be. At each iteration, the fitting algorithm must convert the vector \mathbf{a} into a diffuse reflectance spectrum. Three steps are involved. First, the μ_a and μ'_s spectra are calculated based on the absorber concentrations and scattering parameters that constitute \mathbf{a} , as described in the following sections. Second, the diffuse reflectance at each wavelength is calculated using the P_3 model and these values of μ_a and μ'_s , yielding a theoretical reflectance spectrum. Finally, the theoretical spectrum is normalized to 1 at 650 nm and compared with the normalized measured spectrum. The iterative procedure continues until the theoretical spectrum derived from the current value of \mathbf{a} and the normalized measured spectrum agree to within a predetermined precision. The details of the models

used to construct the absorption and reduced scattering spectra are described in the following sections.

4.2.2.1 Absorption components

It is assumed that the absorption spectrum of the sample being measured is dominated by a linear combination of absorption spectra of known absorbers. The spectral data considered here span the wavelength range from 380 to 770 nm. In this spectral region, the absorption in tissues and erythrocyte-containing phantoms is predominantly due to hemoglobin in its oxygenated and deoxygenated forms. The absorption coefficient can therefore be expressed as a function of wavelength λ by

$$\mu_a(\lambda) = \mathbf{a}_1\mu_{aHbO_2}(\lambda) + \mathbf{a}_2\mu_{aHb}(\lambda), \quad (4.5)$$

where $\mu_{aHbO_2}(\lambda)$ and $\mu_{aHb}(\lambda)$ are the millimolar absorption coefficients of oxy- and deoxyhemoglobin at wavelength λ , and the parameters \mathbf{a}_1 and \mathbf{a}_2 are equal to their concentrations. The absorption spectra are taken from published sources and interpolated to obtain absorption coefficients at the wavelengths at which our spectral data were taken. Previous experiments in our laboratory (Hull and Foster, 2001a; Hull *et al.*, 1998) have verified the accuracy of the spectra provided by Wray *et al.* (1988) in the near infrared and those of Zijlstra *et al.* (1991) in the visible wavelengths. We have scaled the Wray data to match that of Zijlstra at 750 nm. For the near UV wavelengths, where neither of these authors report measurements, we have adopted the spectra provided by Prahl (1999). Guided by the quality of fits to reflectance spectra taken from erythrocyte phantoms,

Wavelength range	Source of hemoglobin absorption spectra
250 – 450 nm	Prahl (1999)
400 – 440 nm (Deoxy only)	Van Assendelft (1970)
450 – 750 nm	Zijlstra <i>et al.</i> (1991)
490 – 545 nm	Takatani and Graham (1987)
750 – 1000 nm	Wray <i>et al.</i> (1988)

Table 4.1: Published sources of hemoglobin absorption spectra and the wavelength range over which each was used.

we have used the data provided by Van Assendelft (1970) for deoxyhemoglobin’s Soret absorption band and that provided by Takatani and Graham (1987) for both forms between 490 and 545 nm. Table 4.1 lists the references from which the hemoglobin absorption data are taken for each wavelength range.

All of the published spectra listed in table 4.1 were derived from measurements of extracted hemoglobin in homogeneous solution. In our tissue-simulating phantoms and in living tissue, the hemoglobin is packaged in cells that constitute a small fraction of the total sample volume. As described in section 2.4, this confinement to the intact erythrocyte has the effect of flattening the peaks in the hemoglobin absorption spectra. This effect is evident in the reflectance measured from erythrocyte phantoms. In figure 4.2, we plot a typical reflectance spectrum obtained from one such phantom at a source-detector separation of 0.77 mm along with the best fits obtained using the absorption spectra of oxy- and deoxyhemoglobin in homogeneous solution (---) and the corresponding flattened spectra expected in intact erythrocytes (—). The fit using the homogeneous solution spectra catastrophically underestimates the reflectance in regions where

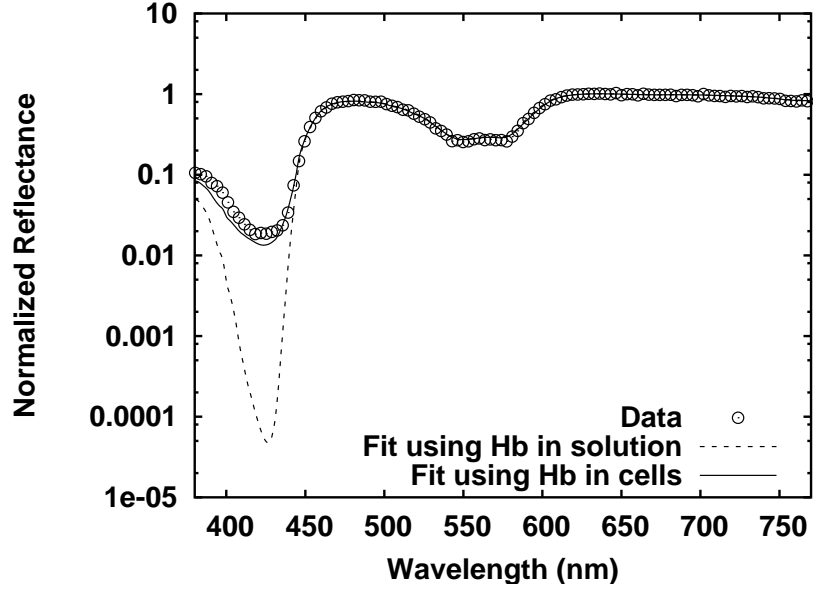


Figure 4.2: Diffuse reflectance spectrum obtained from a partially deoxygenated erythrocyte phantom (\circ) and best fit of the P_3 -based fitting algorithm using basis spectra of hemoglobin in homogeneous solution (---) and corrected for the effects of pigment packaging (—).

hemoglobin is highly absorbing. In the region of the visible absorption peaks, this effect is relatively small, and the fitting algorithm can compensate by adjusting the fitted hemoglobin concentration. In the Soret band, however, the packaging of hemoglobin into erythrocytes causes a reduction in the absorption coefficient by a factor of approximately 3. This effect must be taken into account if a reasonable fit in this spectral region is to be obtained. In this example, the goodness of fit as determined by the value of χ^2 is improved by a factor of 5 when the spectral flattening is considered.

As shown in equations 2.68 and 2.69, the extent of flattening depends on the product of the particle radius and its internal absorption coefficient. In section

2.4, we made reasonable estimates of these parameters for the purposes of illustration. To construct the basis spectra used in the following sections, we adjusted the extent of flattening to minimize the differences between the best fit and measured data. The resulting flattening effect corresponds to erythrocytes of radius $5.5 \mu\text{m}$ with an internal hemoglobin concentration of 3.125 mM . These optimized flattening parameters give good fits to the reflectance spectra collected by all of the fibers in our probe. While it is unlikely that the measurements presented here are sensitive enough to provide reliable information concerning the size or hemoglobin content of human erythrocytes, it is encouraging that the values that optimize the fit are physically reasonable.

4.2.2.2 Hemoglobin oxygen saturation and the Hill equation

In many cases, the concentrations of oxy- and deoxyhemoglobin are more useful if expressed in terms of the total hemoglobin concentration and the oxygen saturation. The total hemoglobin concentration $[Hb]_t$ is the sum of $[Hb]$ and $[HbO_2]$. Each hemoglobin molecule contains four heme binding sites and is therefore capable of binding four oxygen molecules. The hemoglobin oxygen saturation SO_2 is equal to the fraction of heme units which are bound to oxygen, defined by

$$SO_2 = \frac{[HbO_2]}{[HbO_2] + [Hb]}. \quad (4.6)$$

We have expressed the oxy- and deoxyhemoglobin concentrations in terms of hemoglobin molecules rather than heme units. Implicit in this convention is the interpretation that $[HbO_2]$ and $[Hb]$ are one-fourth the concentrations of bound

and unbound heme units, respectively. The dependence of SO_2 on the local oxygen concentration is described by the Hill equation (Hill, 1910),

$$SO_2 = \frac{(pO_2)^n}{(pO_2)^n + (p_{50})^n}, \quad (4.7)$$

where pO_2 is the partial pressure of oxygen, p_{50} is the oxygen partial pressure at which half of the available heme units are bound to oxygen, and n is the Hill parameter, which is a measure of the cooperativity of binding. Typical values of p_{50} and n are 26 Torr and 2.8, respectively (Stryer, 1988). In a study comparing nine different mathematical models of blood oxygen equilibrium, O’Riordan *et al.* (1985) found that the Hill model accurately describes the oxygen-hemoglobin equilibrium curve, but caution that it is valid only in the range of saturations between 20 and 98%. Therefore, data points at saturations outside this range should not be included in fits used to determine the Hill parameters.

The saturation values we recover by fitting the reflectance or fluorescence spectra are fitted with a Hill curve in order to extract the parameters p_{50} and n . The same nonlinear fitting algorithm used to extract the concentrations of oxy- and deoxyhemoglobin from the measured reflectance is used here to extract the Hill parameters from the fitted hemoglobin saturations. Because only two free parameters are needed to characterize the Hill curve and because the Hill equation is computationally simple, this fitting converges extremely rapidly. Previous studies of the oxygen-hemoglobin equilibrium curve have accomplished an equivalent fitting using a linear regression between $\ln(pO_2)$ and $\ln(SO_2/(1 - SO_2))$ (Hull *et al.*, 1999; Zwart *et al.*, 1984). The Hill parameter n is given by the slope of this line.

Only the data points at saturations between 20% and 80% are included in the fit. We have fit our data using this method for the purpose of comparison with the results obtained by these researchers.

4.2.2.3 Scattering components

Scattering in tissue is caused by a variety of scatterers, ranging in size from organelle membranes to whole cells (Mourant *et al.*, 1998). Their shapes vary from spheres (cells) to ellipsoids (mitochondria) to extended cylinders (collagen fibers) (Saidi *et al.*, 1995). Single scattering spectra and phase functions for each of these shapes can be calculated using Mie theory and each contains distinct wavelength-dependent structure. This wavelength dependence can be observed in reflectance measurements from solutions containing only a single size and shape of scatterer (Nichols *et al.*, 1997) or in measurements of singly-scattered light from thin tissue layers (Backman *et al.*, 1999). However, tissue contains a continuous range of scatterer shapes and sizes. The result is that any wavelength dependent structures are ‘smeared out’; the true *in vivo* scattering spectrum is nearly featureless and monotonically decreasing throughout the visible wavelengths. Mourant *et al.* (1998) found that a wide variety of scatter distributions led to reduced scattering spectra of the form

$$\mu'_s = A\lambda^{-b}, \quad (4.8)$$

where λ is the wavelength, and the parameter A depends on the scatterer number density. b is determined by the specific distribution of scatterers and varies from 0.37 for particles much larger than λ to 4.0 for particles much smaller than λ ,

in agreement with Rayleigh limit. Suspensions of cells exhibit a distribution of scatter sizes such that b is approximately 1.0 (Mourant *et al.*, 1998). Jacques (1996) found that the scattering spectra of a variety of intact tissues could be fit using $b = 1.5$ and A ranging from 2×10^4 to $2 \times 10^5 \text{ mm}^{-1}$.

The same model can be applied to our tissue simulating phantoms. In a detailed study, van Staveren *et al.* (1991) have investigated the scattering properties of Intralipid, a lipid emulsion similar to Liposyn II, and have found that the scattering coefficient and anisotropy over the wavelength range from 400 to 1100 nm are given approximately by

$$\mu_s = 0.016 \times \lambda^{-2.4} \quad (4.9a)$$

and

$$g = 1.1 - 0.58 \times \lambda, \quad (4.9b)$$

respectively, where λ is the wavelength in microns. For the range of scattering coefficients relevant to tissue biology, the scattering coefficient is proportional to the concentration of Liposyn II in the phantom. In the experiments described here, we have used a dilution of 1 part Liposyn II in 11 parts total phantom volume. Figure 4.3 shows the reduced scattering spectrum calculated for this concentration using equations 4.9a and 4.9b, as well as the reduced scattering spectrum calculated from equation 4.8 which best approximates this spectrum over the wavelength range from 400 to 800 nm. The best fit is achieved when $A = 488 \text{ mm}^{-1}$ and $b = 0.937$. In our Liposyn phantoms, we have found better agreement with a value of b between 1.5 and 2. This agrees with the work of Mourant *et al.*

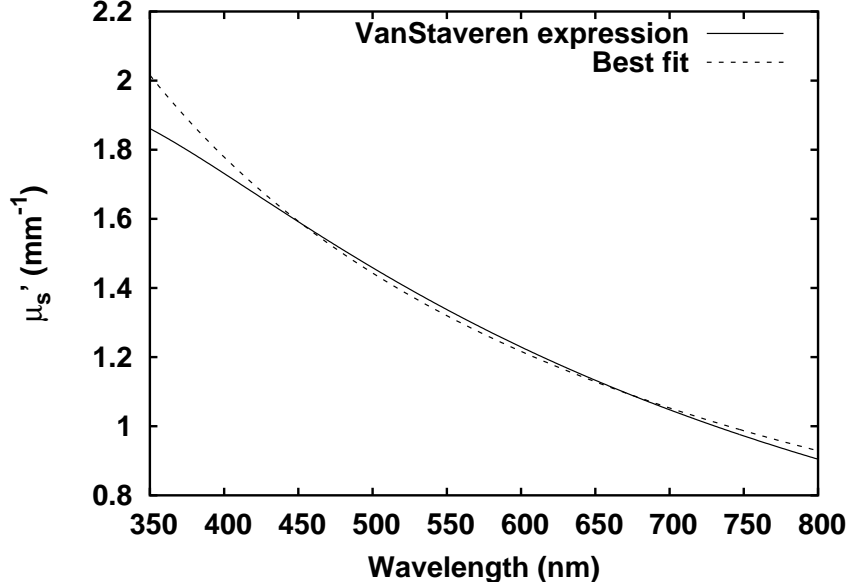


Figure 4.3: Reduced scattering coefficient μ'_s of Liposyn II solution with 0.9% lipid content, as approximated by van Staveren *et al.* (1991) (solid line) and the best fit spectrum of the form $\mu'_s = A\lambda^{-b}$ (dotted line).

(1997b), who found good matches to the reduced scattering spectrum of Intralipid in the range from 450 to 600 nm using $b = 2.0$.

For the purposes of fitting, we have adopted the equivalent model

$$\mu'_s = \mathbf{a}_3 \left(\frac{\lambda}{\lambda_0} \right)^{-\mathbf{a}_4}. \quad (4.10)$$

In this model, \mathbf{a}_3 is the value of μ'_s at λ_0 , and \mathbf{a}_4 is identical to b in equation 4.8. While the exact value of λ_0 is not critical, values within the range of the data being fit tend to decrease the crosstalk between \mathbf{a}_3 and \mathbf{a}_4 . For the fits described here, λ_0 was set to 630 nm. This model does not account for such effects as Rayleigh scattering (Saidi *et al.*, 1995) or provide characterization of scatterers,

however it does allow the entire reduced scattering spectrum to be represented by two parameters, one of which (a_3) has intuitive physical meaning.

4.2.3 Phantom preparation

Tissue-simulating phantoms were fluid emulsions consisting of 1 part 10% Liposyn II (Abbott Labs, North Chicago, IL) in 11 parts total phantom volume. The resulting lipid content of 0.9% gave a scattering coefficient similar to that of tissue. The solvent was Hank's Balanced Salt Solution (HBSS) buffered with 50 μ M phosphate and adjusted to pH 7.40 at 37° C. This solution, which has phosphate buffer concentration equivalent to that of phosphate buffered saline (PBS) and concentrations of glucose and potassium similar to those found in blood, will be referred to as phosphate-buffered HBSS (PBHBSS). The phantoms were continuously stirred using a microprocessor-controlled heated stirplate (Model 460, Corning, Inc., Corning, NY) to prevent settling and ensure optical homogeneity. Optical absorption was provided by intact human erythrocytes at a volume fraction of 1.6%.

To prepare erythrocytes, we obtained whole blood from healthy, nonsmoking volunteers who had given informed consent. The blood was drawn into containers prefilled with sodium heparin to prevent clotting. The blood samples were mixed with an approximately equal volume of PBHBSS, agitated gently to mix, and centrifuged at 2500 rpm for 5 minutes. The supernatant, including a small pellet of non-erythrocyte solids, was aspirated off. The washing process was repeated two more times or until the supernatant was clear. The remaining pellet of erythrocytes was refrigerated until use.

Because the oxygen dissociation curve is highly dependent on temperature (Zwart *et al.*, 1984), it was necessary to maintain the erythrocyte phantoms at constant temperature throughout the course of measurements. This was accomplished using the stirplate's heater controller, which continuously monitored the phantom temperature *via* a digital thermometer accessory. To verify adequate thermal control the temperature was also monitored by an electronic thermometer. Throughout the course of measurements on each phantom, the temperature varied by less than 1° C.

The oxygen tension in the phantom was monitored by a teflon-tipped oxygen sensitive electrode (Microelectrodes, Inc, Londonderry, NH). The electrode reading was converted to oxygen tension *via* a linear two-point calibration. The air-saturated calibration point was acquired by allowing the electrode to come to equilibrium in the phantom prior to addition of erythrocytes. The zero oxygen-tension calibration value was taken from the electrode reading after complete deoxygenation of a sample of the phantom by sodium dithionite. The oxygen tension and electrode output were assumed to be linearly related between these values.

The outputs of the oxygen electrode and the electronic thermometer were digitized and recorded by a computer equipped with a data acquisition board, which also recorded the state of the CCD shutter for purposes of co-registering the spectral data with the temperature and oxygen tension values. The data were digitized at a rate of 10 Hz, providing approximately 100 samples of the thermometer and electrode output for each spectrum obtained. The average of

the temperature and oxygen data taken during each spectrum acquisition was assigned to that spectrum.

In order to simulate the fluorescence emission of tissue, we added reduced nicotinamide adenine dinucleotide (NADH) to the phantoms. The analysis of fluorescence spectra acquired from the phantoms is presented in chapter 5. The absorption due to NADH is negligible compared with that of hemoglobin over the wavelength range of the reflectance measurements presented here.

4.2.4 *In vivo* tumor model

The tumor model we have chosen for our spectroscopy work is an EMT-6 mammary carcinoma grown subcutaneously in female BALB/c mice. The induction of EMT-6 tumors has been described previously by Lee *et al.* (1998). EMT-6 cells were grown in culture media under 5% CO₂, 37° C incubation. While still subconfluent, the cells were detached from the substrate using trypsin. The cells were washed once in serum-containing Eagle's Basal Medium (BME) and twice in Hank's Balanced Salt Solution (HBSS) to remove any remaining culture media and trypsin. The concentration of viable cells was assessed with a Trypan blue exclusion assay and a hemocytometer. The cells were resuspended at a concentration of 10⁶ cells per ml and stored on ice until injection.

8 to 12 week old BALB/cJy mice (Jackson Labs, Bar Harbor, ME) weighing approximately 25 g were maintained on a chlorophyll-free diet prepared according to the recipe of Holmes *et al.* (1995). Tumors were initiated in the subcutaneous space on the upper back by injection of a 0.1 ml bolus of HBSS containing 10⁵ EMT-6 cells. The large subcutaneous space between the shoulders allows

unrestricted tumor growth. Tumors were allowed to grow to a diameter of approximately 5 mm, which required 10 to 14 days.

Measurements of diffuse reflectance and the fluorescence measurements described in chapter 5 were made on each mouse. Five randomly selected mice were given 200 mg kg⁻¹ aminolevulinic acid (ALA) *via* tail vein injection 3 hours before measurements for the purpose of inducing protoporphyn IX (PpIX) fluorescence. Immediately prior to reflectance measurement, each animal was anesthetized with 66 mg kg⁻¹ Ketamine and 6.6 mg kg⁻¹ Xylazine. The skin over the tumor was resected, and the animal was restrained with tape. The tumor was irrigated with PBS to prevent drying. Anesthesia was maintained with sodium pentobarbital as needed throughout the duration of measurements. Barbiturate anesthetics such as sodium pentobarbital can interfere with an animal's ability to regulate its body temperature, especially in small mammals such as mice. To prevent hypothermia, we surrounded the animal with a flexible container filled with 37° C water.

The probe described above was placed in contact with the tumor surface. After an initial set of measurements were made, a plastic cone was placed over the nose of each animal. Carbogen was delivered through the cone at a rate of 3 L min⁻¹. Spectra were acquired continuously over a period of several minutes, after which no further changes in the measured spectra were observed. The nose cone was removed and the animal was allowed to breathe room air for several minutes. Again, the measured spectra stabilized after this period. Finally, the nose cone was replaced and dry nitrogen was delivered at 3 L min⁻¹ until the animal asphyxiated. Data acquisition was interrupted to place and remove the nose

cone and to periodically verify the animal's breathing but otherwise proceeded continuously.

4.3 Validation of the diffuse reflectance fitting algorithm

4.3.1 Simulated spectral data

In order to test the ability of the reflectance fitting algorithm described above to accurately recover the optical properties of a turbid sample, we have generated a series of test spectra using Monte Carlo simulation. Generating a reflectance spectrum one wavelength at a time would be very time-consuming. As an alternative, we have adopted a scaled Monte Carlo algorithm based on that described by Kienle and Patterson (1996). First, we conducted Monte Carlo simulations using the geometry of our diffuse reflectance probe and a refractive index mismatch at the air-sample boundary of 1.4. Simulations were performed for values of μ'_s ranging from 0.5 to 2.25 mm⁻¹ in 0.25 mm⁻¹ steps, each with μ_a held constant at 0.0005 mm⁻¹. The distribution of photon pathlengths collected by each detector was recorded. The signal collected by each detector from a medium with arbitrary μ_a is then given by

$$R = \int_0^{\infty} e^{-(\mu_a - \mu_{a\ MC})l} p(l) dl, \quad (4.11)$$

where $p(l)$ is the probability of a photon being detected after travelling a distance l and $\mu_{a\ MC}$ is the value of μ_a used to perform the original simulations. The integral is approximated by dividing the continuous pathlength distribution into bins and replacing the integration with summation. Equation 4.11 assumes that the values of μ'_s in the medium and that used to generate the original simulation are equal. For media whose μ'_s does not correspond to those included in the original

simulation set, linear interpolation is used to calculate the diffuse reflectance. We have added normally distributed random noise to the Monte Carlo simulated spectra corresponding to the relative uncertainty expected from our experimental measurements.

The first set of simulated data was designed to evaluate the ability of our fitting algorithm to recover the concentration and oxygen saturation of hemoglobin from reflectance spectra. We varied $[Hb]_t$ from 20 to 200 μM in 20 μM increments and SO_2 from 0 to 1 in increments of 0.25. A total of 50 simulated reflectance spectra were generated for each source-detector separation, each spanning the range from 380 to 750 nm. The reduced scattering coefficient at 630 nm and the scattering exponent were held constant at 1.0 mm^{-1} and -1.5 , respectively. In figure 4.4(a), the fitted concentration of hemoglobin is plotted as a function of the hemoglobin concentration used to generate each simulated data set. Each data point represents the mean of fits at five different oxygen saturations, and the errorbars depict the standard deviation within each group. The solid line indicates perfect agreement between the fit and the parameters used to create the data sets. For the signal-to-noise ratio typical of our experimental measurements, the fitted and true values of $[Hb]_t$ differ by as much as 20%, especially at short source-detector separations. This can be explained by the fact that at low albedos and short source-detector separations, the diffusion- P_3 hybrid reflectance expression systematically overestimates the reflectance for a given μ_a , as shown in figure 2.2, or, equivalently, systematically underestimates μ_a for a given reflectance. This effect is greater at higher μ_a and hence at higher $[Hb]_t$, leading to greater error in the fitted $[Hb]_t$ as the real $[Hb]_t$ is increased. Because the systematic error in the

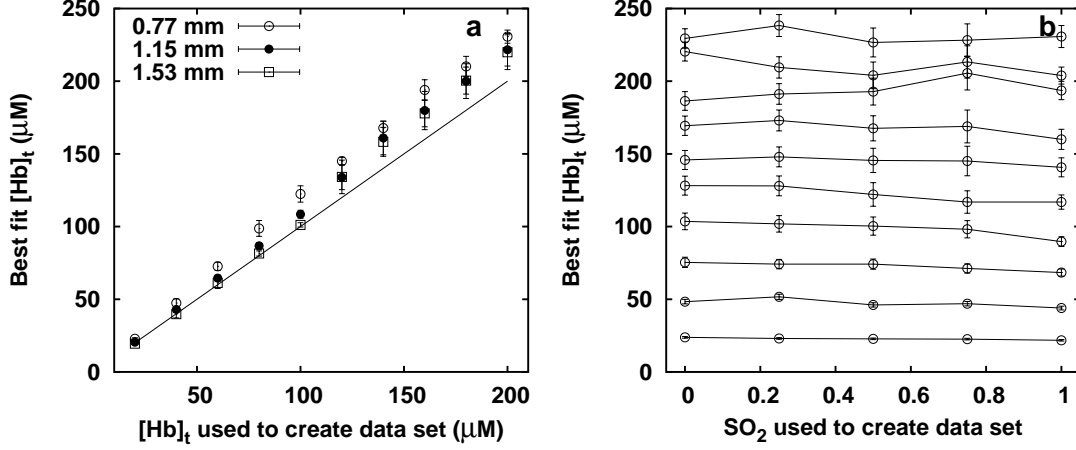


Figure 4.4: Best fit hemoglobin concentration extracted from a synthetic data set as a function of (a) the hemoglobin concentration used to create the simulated data and (b) the hemoglobin oxygen saturation used to create the data set. Only the results for the detector at 0.77 mm are shown in panel (b).

P_3 expression is a smooth function of μ_a , relative changes in $[Hb]_t$ are recovered more accurately than the absolute concentration.

In the context of *in vivo* measurements, it is desirable to separate the changes in $[Hb]_t$ from changes in SO_2 . The best fit values of $[Hb]_t$ obtained from the detector at 0.77 mm from the source are plotted as a function of the true SO_2 in figure 4.4(b). There does not appear to be a correlation between the true values of SO_2 and the recovered values of $[Hb]_t$. It is therefore unlikely that the fitting algorithm will incorrectly interpret changes in SO_2 as changes in $[Hb]_t$. Similar results are obtained for all the source-detector separations studied.

In figure 4.5(a), the same data points are plotted as a function of the hemoglobin saturation used to generate the simulated data set. Each data point

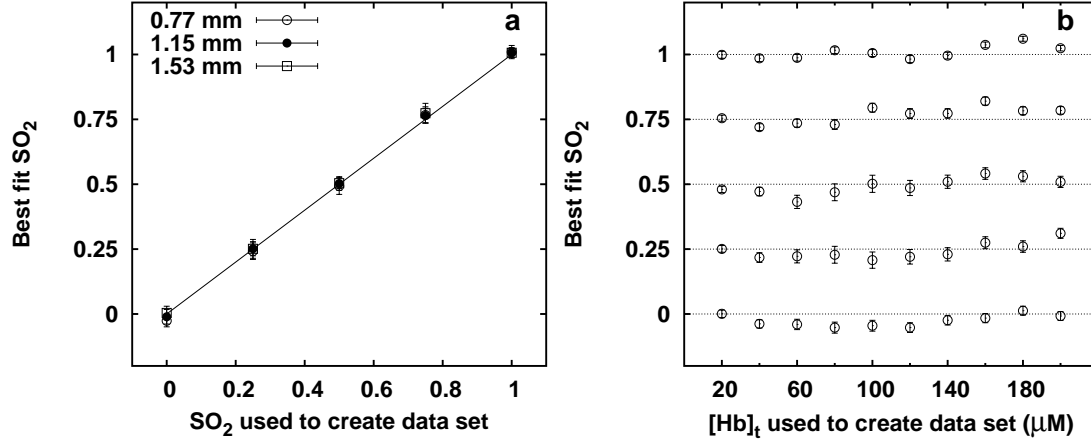


Figure 4.5: Best fit hemoglobin saturation extracted from the synthetic data set used to generate figure 4.4 plotted as a function of (a) the hemoglobin saturation used to create the simulated data and (b) the total hemoglobin concentration used to create the data set. In panel (b), only results for the source-detector separation of 0.77 mm are shown.

represents the mean results of ten simulations with $[Hb]_t$ ranging from 20 to 200 μM . The hemoglobin saturation is recovered within an uncertainty of 0.07 over the full range of values from zero to one. The effect of changes in $[Hb]_t$ on the recovered SO_2 is illustrated in figure 4.5(b) for the fits to simulated reflectance at 0.77 mm, although similar results are obtained at all source-detector separations studied. Each data point represents a single fit, and the dashed lines show the correct values. The variations in the best fit SO_2 are on the order of the uncertainty in the measurement, and do not show any systematic dependence on $[Hb]_t$. It is therefore unlikely that a change in $[Hb]_t$ will be misdiagnosed as a change in SO_2 .

A second set of synthetic spectra was designed to assess the sensitivity of

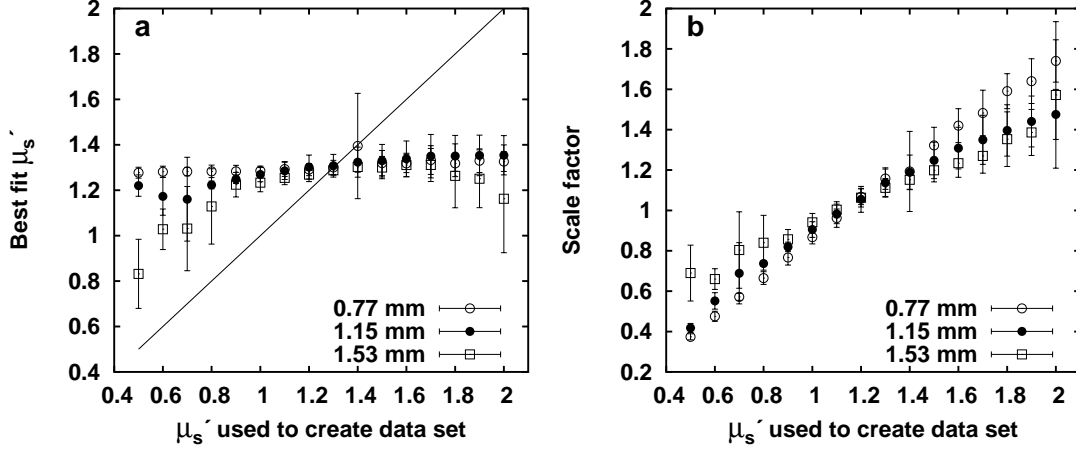


Figure 4.6: (a) Best fit μ'_s extracted from a synthetic data set plotted as a function of the μ'_s used to create the simulated data. The solid line indicates perfect agreement. The algorithm is relatively insensitive to variations in the reduced scattering coefficient. (b) Ratio of the normalization factors for the simulated and best-fit spectra. The value of this scale factor is approximately proportional to μ'_s .

our diffuse reflectance measurements to changes in μ'_s . The concentration of hemoglobin was held constant at 100 μM , while the value of μ'_s at 630 nm was varied from 0.5 to 2 mm^{-1} and SO_2 was varied from 0 to 1. As shown in figure 4.6, diffuse reflectance measurements made at short source-detector separations do not differentiate well between spectra with different scattering coefficients. This is a result of the fact that the spectra are normalized prior to fitting. The algorithm is therefore sensitive only to the shape of the diffuse reflectance spectrum. The shape of the spectrum depends on the value of μ'_s via its effect on the effective pathlength of the collected photons. However, it has been shown that for the range of source-detector separations employed in our probe, the mean pathlength travelled by photons that reach the detector is nearly independent of μ'_s (Mourant

et al., 1997a). It is therefore not surprising that our measurements are incapable of distinguishing changes in μ'_s .

Although the pathlength of detected photons is insensitive to μ'_s , the amplitude of the reflectance signal is not. It is therefore reasonable to expect that the scattering coefficient may be determined more sensitively by a measurement of absolute rather than normalized reflectance. In fact, when the data is not normalized prior to fitting, μ'_s can be recovered more accurately (data not shown).

This improved sensitivity to μ'_s comes at the price of the experimental difficulty of making absolutely calibrated measurements. In addition, the recovery of hemoglobin concentration and saturation are compromised. As an alternative, we can perform the fitting on normalized data and still take advantage of the absolute amplitude of the reflectance. After fitting, we calculate a scale factor equal to the ratio of the factors by which the measured (or simulated) and calculated spectra are scaled during normalization. This ratio, shown in figure 4.6(b), is sensitive to variations in the amplitude of the reflectance. It therefore provides a means of identifying changes in scattering coefficient. Under conditions similar to those we expect to encounter *in vivo*, the scale factor is approximately proportional to μ'_s . Multiplying the recovered μ'_s by the scale factor yields a significant improvement for short source-detector separations, as shown in figure 4.7. At large source-detector separations, the relationship between μ'_s and the measured reflectance becomes increasingly nonlinear as μ'_s increases, and the correction becomes less effective. The corrected values are sensitive to changes in μ'_s , but at large source-detector separations, we can expect the magnitude of these changes to be underreported.

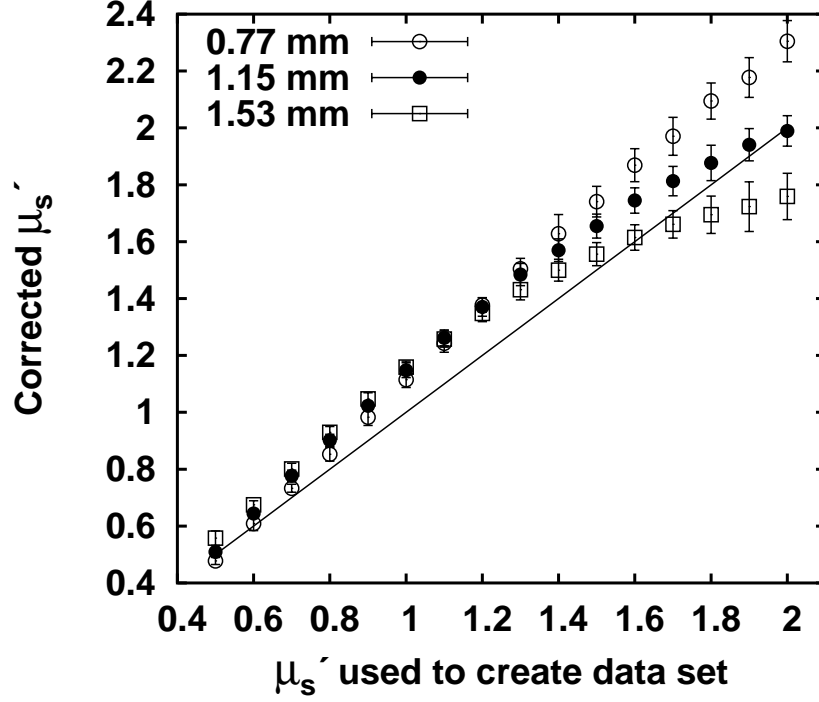


Figure 4.7: Best fit values of μ'_s shown in figure 4.6 after correction for changes in scale factor, as described in the text.

The lack of accuracy in the recovery of μ'_s in the uncorrected fits motivates investigation of the impact of changes in μ'_s on the algorithm's ability to recover $[Hb]_t$ and SO_2 . Figure 4.8 demonstrates the effect of changing μ'_s on the recovered values of $[Hb]_t$ and SO_2 . As shown in figure 4.8(a), $[Hb]_t$ suffers the previously observed systematic overestimation over a wide range of μ'_s . The extent of this systematic error, however, is nearly independent of μ'_s . The error in the recovered hemoglobin saturation exhibits a slight correlation with μ'_s , however a large change

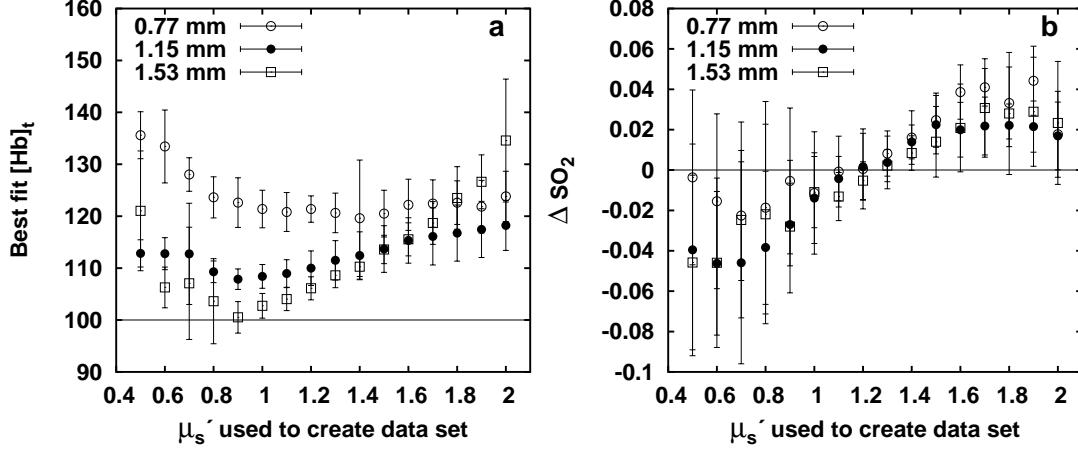


Figure 4.8: Effect of changing μ'_s on (a) the recovered value of $[Hb]_t$ and (b) the error in SO_2 . Each data point represents the mean value from a group of fits to five simulated spectra generated with SO_2 ranging from 0 to 1. The solid line in each panel indicates a perfect fit.

in μ'_s is required to cause a small error in SO_2 . We can therefore expect $[Hb]_t$ and SO_2 to be recovered accurately, even when μ'_s is not.

The model presented in equation 4.10 makes the approximation that μ'_s is proportional to λ^{-a_4} . Like the reduced scattering coefficient at 630 nm, the scattering exponent a_4 is poorly constrained by normalized data taken at short source-detector separations. When the basis spectra used in the fitting algorithm match those used to create the data set, a_4 can be recovered accurately, however it is very sensitive to inaccuracies in the basis spectra or to the presence of absorbers not included in the basis set. It is useful to include a_4 as a free parameter in the fits, however it would be a mistake to ascribe any importance to small changes in its value. Even large changes in a_4 are probably better taken as indicators of

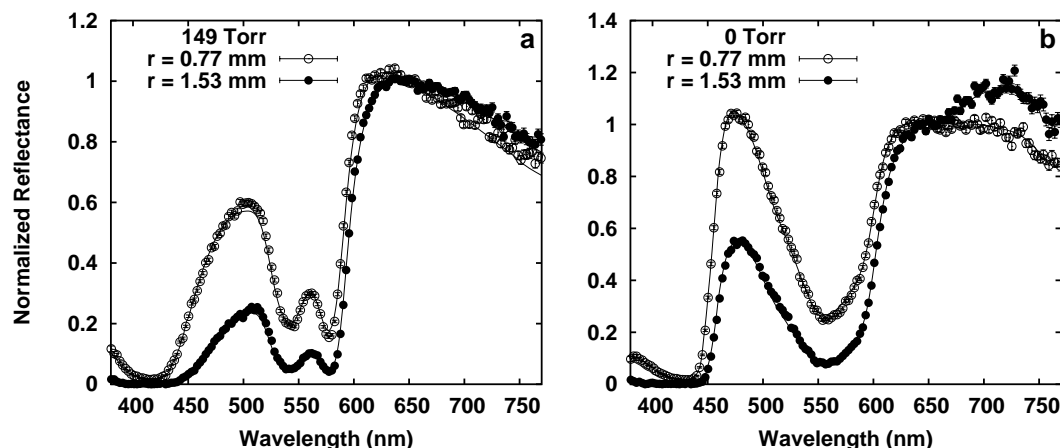


Figure 4.9: Typical normalized diffuse reflectance spectra acquired from an erythrocyte phantom at oxygen tensions of (a) 149 and (b) 0 Torr with detection fibers 0.77 mm and 1.53 mm from the source fiber. For clarity, only every third data point is plotted. The solid lines represent the best fits of the diffusion- P_3 hybrid expression for diffuse reflectance to each spectrum.

mismatches in the basis set than of real changes in the shape of the scattering spectrum.

4.3.2 Phantoms containing erythrocytes

We have measured the diffuse reflectance from the surface of a phantom containing intact erythrocytes throughout the course of deoxygenation with yeast. The first spectra were obtained when the phantom oxygenation was 149 Torr. Data were taken at regular intervals until the oxygen partial pressure reached zero. The diffuse reflectance spectra acquired from an erythrocyte phantom at the initial and final oxygen concentrations are plotted in figures 4.9(a) and (b), respectively. The data, indicated by the symbols and errorbars, are well-matched by the best fit of

the P_3 expression for diffuse reflectance (solid lines). The data are normalized to 1 at 650 nm prior to fitting. Data were acquired at six source detector separations ranging from 0.77 to 1.53 mm. Only the two extreme values are plotted here, however the intermediate results are similar in terms of quality of fit and prominence of spectral features attributable to hemoglobin.

Fits such as those depicted in figure 4.9 yield the concentrations of oxy- and deoxyhemoglobin and the sample scattering parameters. Figure 4.10 shows the fitted concentrations of oxy- and deoxyhemoglobin and $[Hb]_t$ recovered from diffuse reflectance measurements made at source-detector separations of 0.77, 0.93 and 1.53 mm over the full range of oxygen concentrations during the deoxygenation of the phantom. The corresponding fitted values of μ'_s at 630 nm are shown in figure 4.11. As described above, the values of μ'_s were corrected by multiplying by a scale factor that accounts for changes in absolute intensity. The scale factor was normalized to that of a phantom without absorber. The resulting corrected μ'_s deviates from its initial value by approximately 10%. This deviation is likely a result of coupling between the scattering and absorption parameters in the fitting algorithm. Consistent with this hypothesis, the variation in $[Hb]_t$ between data sets taken at different source-detector separations and the variation within each data set are each approximately 10% as well. The coupling is especially evident in figures 4.10(b) and 4.11(b). While it is difficult to identify uniquely the causes of parameter crosstalk in our model, the fact that it is not evident to this extent in our Monte Carlo studies indicates that it is not fundamental to the fitting algorithm. In the simulated data sets, the absorption basis spectra and scattering model used in the fitting are exact matches to those used to generate the data. In

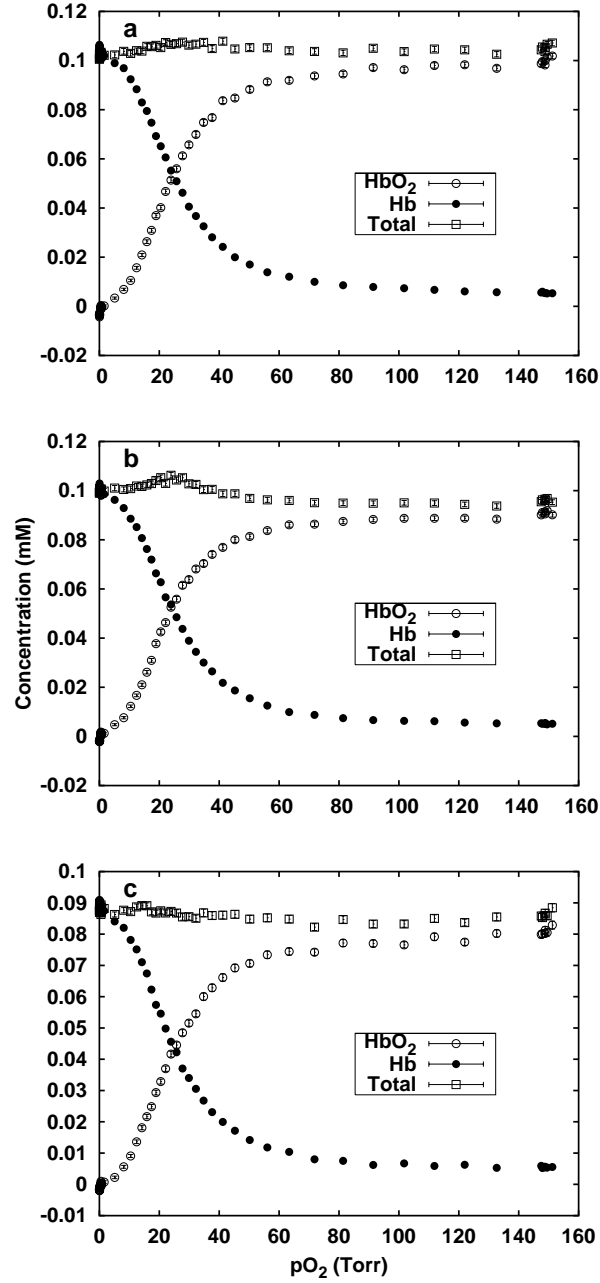


Figure 4.10: Fitted concentrations of oxy- and deoxyhemoglobin based on reflectance spectra acquired from an erythrocyte phantom with detection fibers (a) 0.77, (b) 0.93 and (c) 1.53 mm from the source fiber.

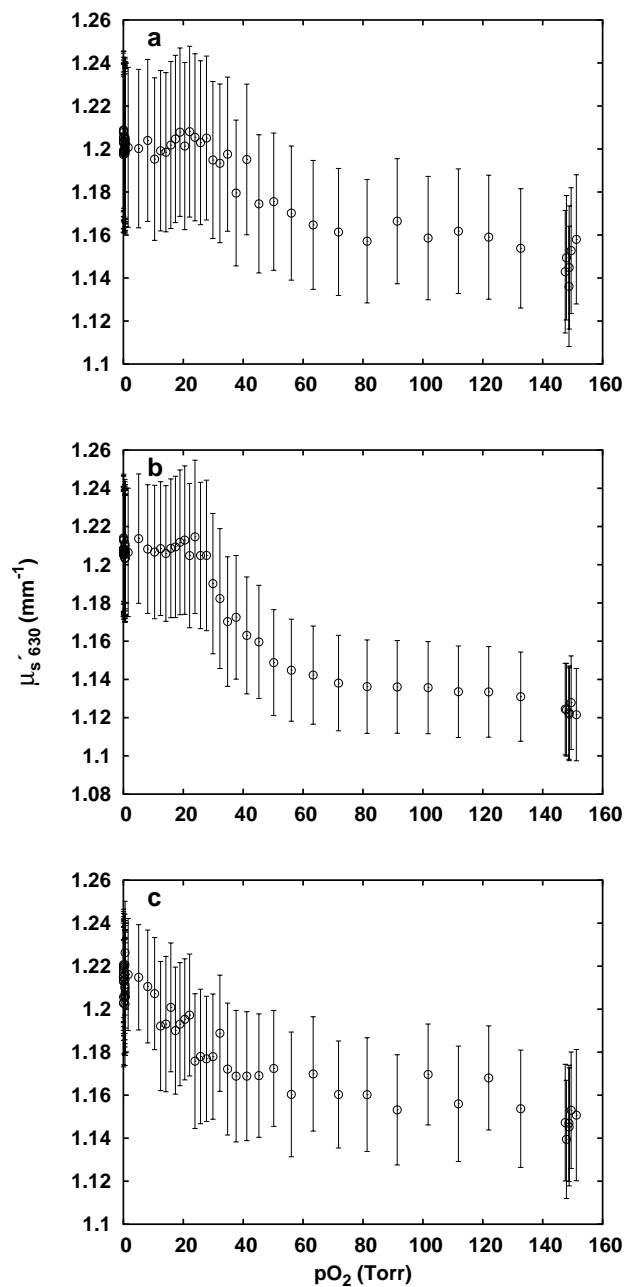


Figure 4.11: Fitted value of μ'_s at 630 nm extracted from the fits used to generate figure 4.10. The values plotted are corrected for changes in intensity as described in section 4.3.1.

the phantom data, both the basis spectra and the scattering model are approximate. The parameter crosstalk's presence in the phantom data and absence in the simulated data suggests that it arises from mismatches between our basis spectra and the true hemoglobin spectra or between our scattering model and the true scattering spectrum. Improvements in both these areas are possible but beyond the scope of this work.

Figure 4.12 shows the hemoglobin dissociation curves obtained from the fits used to generate figure 4.10. The data points with errorbars depict the values of SO_2 derived from fitting the measured reflectance. The solid line is the Hill curve calculated using the parameters which provide the best fit to the data at saturations between 20 and 90%, as determined by a nonlinear fit. For comparison with previous researchers, we have also performed a linear regression on the $\ln(SO_2/(1 - SO_2))$ vs. $\ln(p_{O_2})$ curve. The slope of this curve is equal to n , and the intercept can be used to calculate p_{50} . The Hill curve generated by the parameters derived from the linear fit is plotted with a dashed line in each panel of figure 4.12. In each case, the two fits are almost indistinguishable and yield parameters which agree within their uncertainties. The fitted values of the Hill parameters p_{50} and n extracted from the SO_2 vs p_{O_2} curves found at each source-detector separation are listed in table 4.2. The values obtained from the six different source-detector separations agree within their uncertainties and are in agreement with the literature values. The agreement in the parameters taken from different fibers illustrates the importance of accounting for pigment packaging. We have performed the same fitting procedure using hemoglobin basis spectra uncorrected for this effect. While

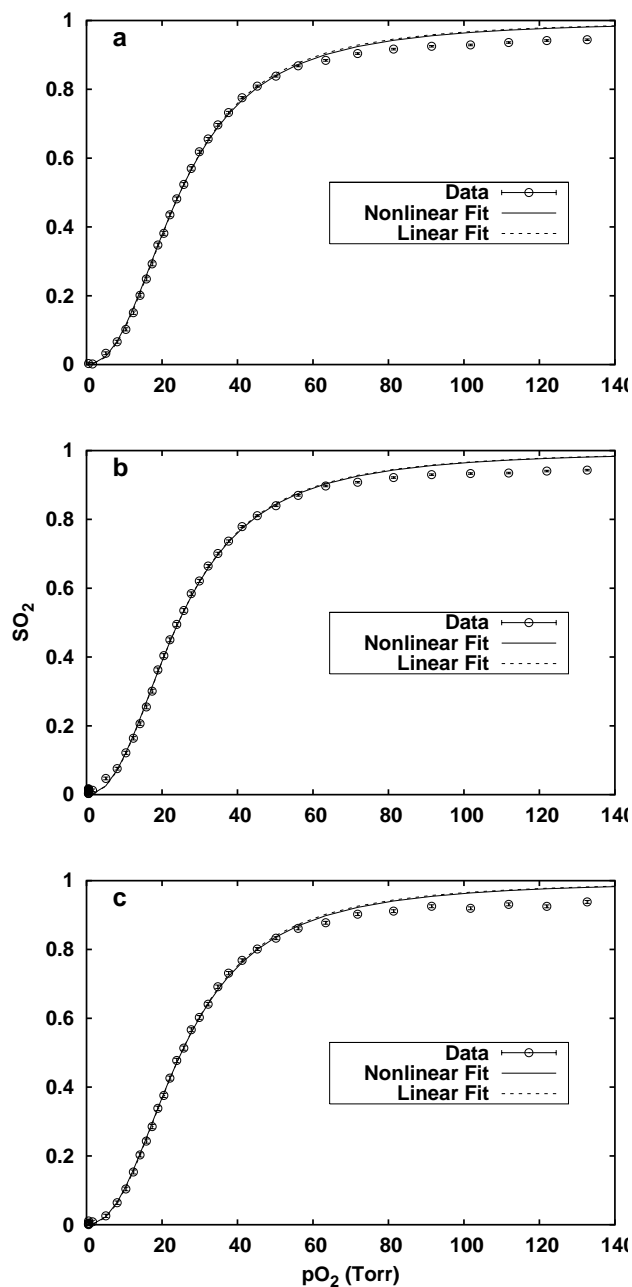


Figure 4.12: Fits of the Hill equation to phantom reflectance data. Oxygen saturation values corresponding to the concentrations depicted in 4.10 are plotted as a function of pO_2 . The solid and dashed lines, which are nearly indistinguishable, depict the Hill curves calculated based on the values of p_{50} and n found by fitting the data points at saturations between 20 and 90% with a nonlinear fitting algorithm and with a linear fitting algorithm after linearization of the Hill equation, respectively.

Fiber	S-D (mm)	n	p50 (Torr)
1	0.77	2.35 ± 0.11	24.7 ± 0.5
2	0.93	2.33 ± 0.08	24.3 ± 0.4
3	1.15	2.34 ± 0.13	24.4 ± 0.5
4	1.34	2.30 ± 0.11	24.5 ± 0.5
5	1.45	2.33 ± 0.14	25.3 ± 0.6
6	1.53	2.32 ± 0.14	25.2 ± 0.6

Table 4.2: Hill parameters extracted from erythrocyte phantom reflectance. The values listed are the best fit values obtained from fits of the Hill equation to the hemoglobin oxygen saturations recovered from a phantom containing intact human erythrocytes.

the resulting fits appeared accurate except in the regions of highest absorption, the Hill parameters they returned varied wildly with source-detector separation.

4.4 *In vivo* diffuse reflectance measurements

We have used the spectroscopy apparatus and analysis methods tested in the previous sections to investigate the hemodynamics of EMT-6 tumors grown subcutaneously in female BALB/c mice. Typical reflectance spectra obtained *in vivo* from the exposed surface of one such tumor are shown in figure 4.13. The spectra shown in panel (a) were acquired while the animal breathed room air using detection fibers 0.93 and 1.45 mm from the source fiber. Corresponding spectra taken after 11 minutes of carbogen inhalation are shown in panel (b). This particular tumor exhibited a distinct dark vein visible to the naked eye corresponding to the position of the detection fiber 0.93 mm from the source. As expected, the spectra acquired with this fiber exhibit more attenuation due to hemoglobin than those acquired with the fibers remote from the heavily pigmented region. The P_3 -diffusion hybrid algorithm provides excellent fits to the measured spectra at both concentrations, as indicated by the solid lines.

The best fit lines shown in figure 4.13 exhibit a systematic deviation from the data in the spectral region around 730 nm, especially in the data taken at 1.45 mm. 730 nm corresponds to a peak in the absorption spectrum of water, which is not included in our basis set. The absorption due to water is less evident in the spectra acquired from the pigmented region where it is masked by absorption due to hemoglobin. Because water does not exhibit significant absorption in between 380 and 700 nm, it has little effect on the quality of the fits in this region of the spectrum. We have found that adding a water absorption to our basis set makes no significant improvement to the fits and does not reliably recover the concentration

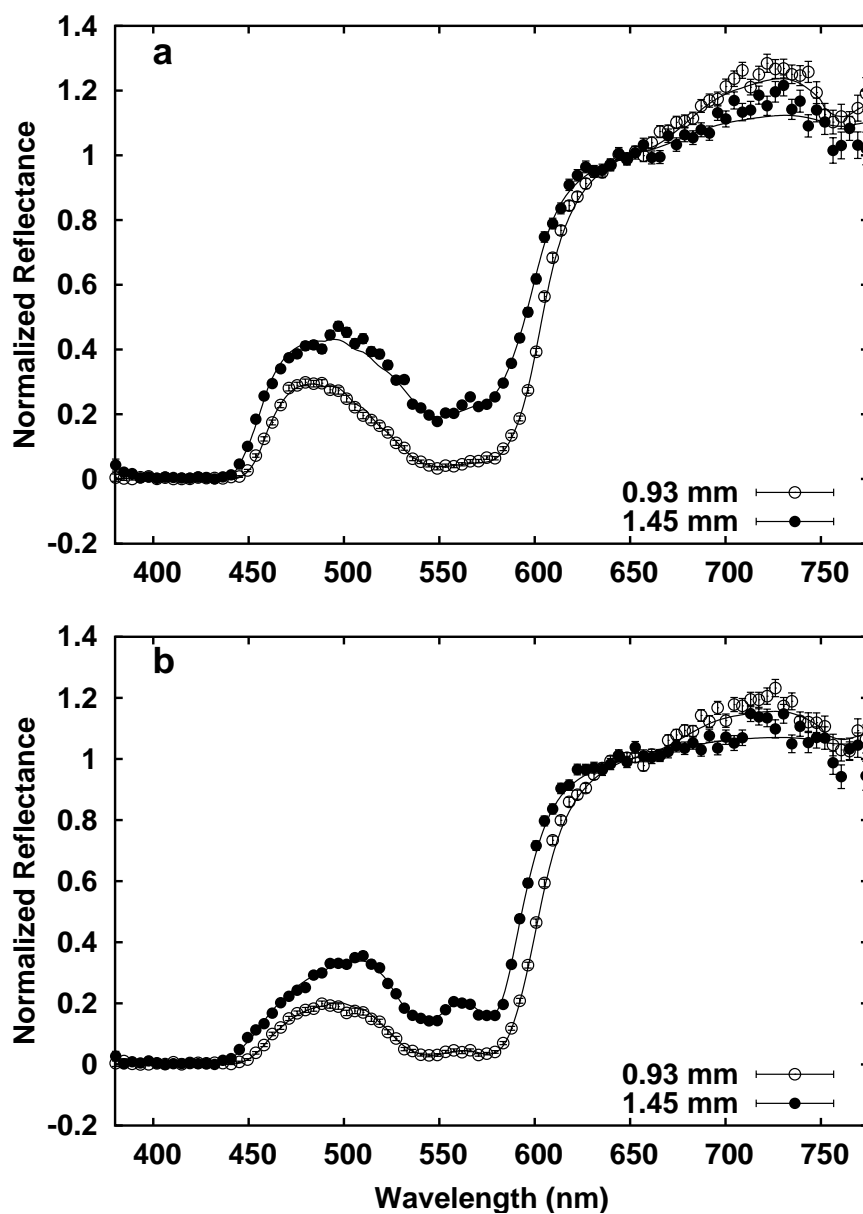


Figure 4.13: Normalized diffuse reflectance spectra acquired *in vivo* from an EMT-6 tumor grown subcutaneously in a female BALB/c mouse. Spectra were acquired (a) while the mouse breathed room air and (b) after 12 minutes of carbogen inhalation. The source-detector separations are indicated in the legend. For clarity, only every fifth data point is shown. The solid lines indicate the best fits obtained from the P_3 diffuse reflectance algorithm.

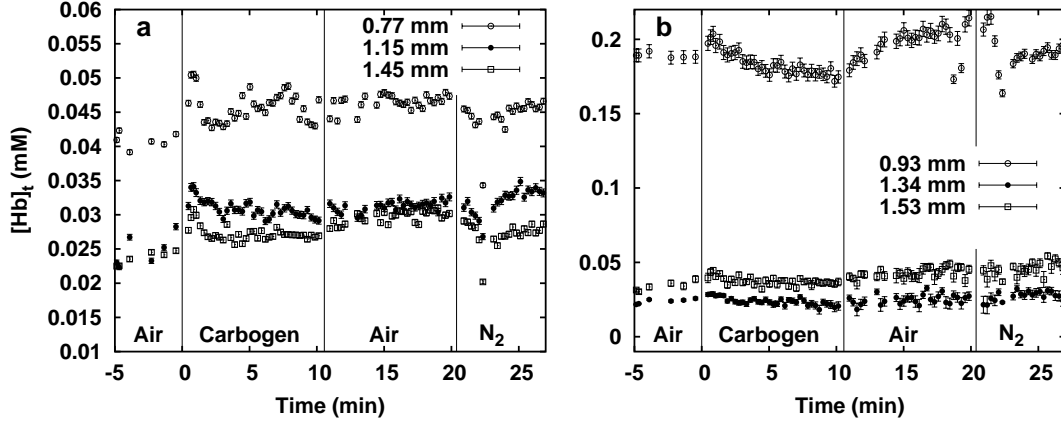


Figure 4.14: Total hemoglobin concentration obtained from fits to spectra such as those shown in figure 4.13 obtained *in vivo* from murine tumors. Each line on the plot represents one source-detector separation. Fibers on the (a) left and (b) right halves of the probe are plotted separately. Source-detector separations are given in the legend. Vertical lines indicate changes in the inhaled gas, as indicated by the labels.

of water. For the analysis presented in this chapter, we have therefore used a basis set which does not include water.

In figure 4.14, the total tissue hemoglobin concentration measured by each detection fiber is plotted as a function of time after the onset of carbogen inhalation. The solid vertical lines at 0, 11, and 20 minutes indicate the onset of carbogen breathing, the cessation of carbogen breathing, and the onset of nitrogen asphyxiation, respectively. The curves obtained from fibers on the right and left halves of the probe (see figure 4.1) are shown in panels (a) and (b), respectively. An increased hemoglobin concentration is evident at the position of the visible dark area on the tumor surface sampled by the fiber 0.93 mm from the source. The local concentration of hemoglobin varied by nearly an order of magnitude between

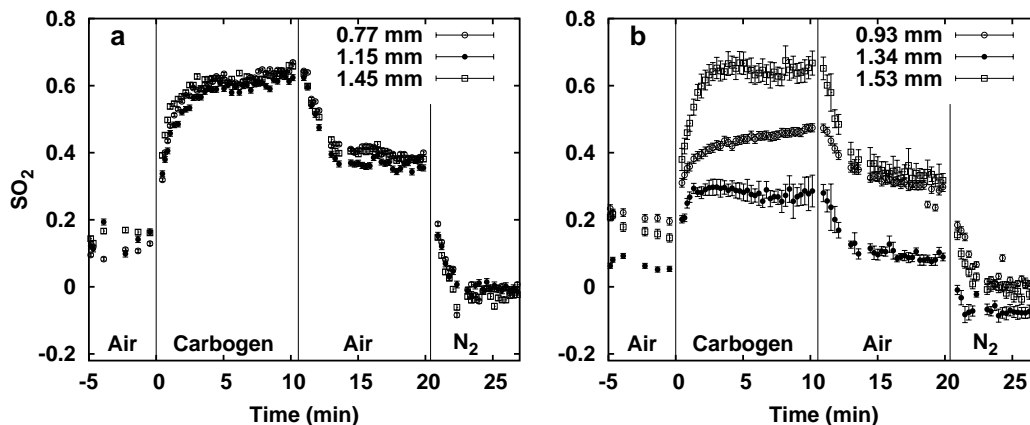


Figure 4.15: Hemoglobin oxygen saturation corresponding to the total concentrations shown in figure 4.14. Fibers on the (a) left and (b) right halves of the probe are plotted separately. Source-detector separations are given in the legend. Vertical lines indicate changes in the inhaled gas, as indicated by the labels.

this fiber and the other fibers in the probe, despite the fact that the greatest separation between any two fibers is less than 2 mm.

Figures 4.15(a) and (b) show the corresponding best fit values of the hemoglobin oxygen saturation. The saturation detected by each fiber exhibits an increase of 0.1 to 0.5 during the period when the animal breathed carbogen, corresponding to the emergence of the oxyhemoglobin absorption features around 550 nm in the spectra shown in figure 4.13(b). After a few minutes of carbogen breathing, the measured SO_2 stabilizes at an elevated level. The timecourse of the elevation and stabilization of SO_2 are in qualitative agreement with the results of previous optical studies (Hull *et al.*, 1999; Liu *et al.*, 2000) and consistent with observed changes in MRI signal (Ilangovan *et al.*, 2002; Robinson *et al.*, 1995; 1997), although it should be noted that MRI measurements do not directly mea-

sure SO_2 . After carbogen administration is stopped, the tumor oxygen saturation decreases, but remains elevated relative to its pre-carbogen level, as observed previously (Hull *et al.*, 1999). As expected, the saturation level drops to zero with nitrogen asphyxiation.

The responses to carbogen breathing illustrated in figures 4.13, 4.14 and 4.15 are not exceptional, however it is interesting to note that each animal's response is different. In figure 4.16, we have plotted the change in hemoglobin saturation induced by carbogen inhalation as a function of the initial saturation.

The initial oxygen saturation was determined by averaging the values obtained from several spectra taken immediately before the administration of carbogen. The final values were found from a similar average of several measurements made after 10 minutes of carbogen breathing. In each case, we have confined SO_2 to be positive. Each data point represents the median of the six measurements made with different detector fibers on a single tumor. Errorbars span the range from the minimum of the six measurements to the maximum. They therefore indicate the variations within each tumor, not the uncertainties in the measurement. The solid line indicates a final carbogen-induced SO_2 of 100%. The filled data points indicate measurements made on mice that received ALA prior to measurement.

Several features of tumor oxygenation dynamics in response to carbogen are evident in figure 4.16. First, the initial oxygen saturations measured from murine tumors in this study span the range from 0 to 70% saturation. A similar range of initial saturations was observed previously in experiments in our laboratory in which rats bearing R3230 tumors were exposed to inhaled carbogen (Hull *et al.*, 1999). In those experiments, oxygen saturation was determined by radially-resolved re-

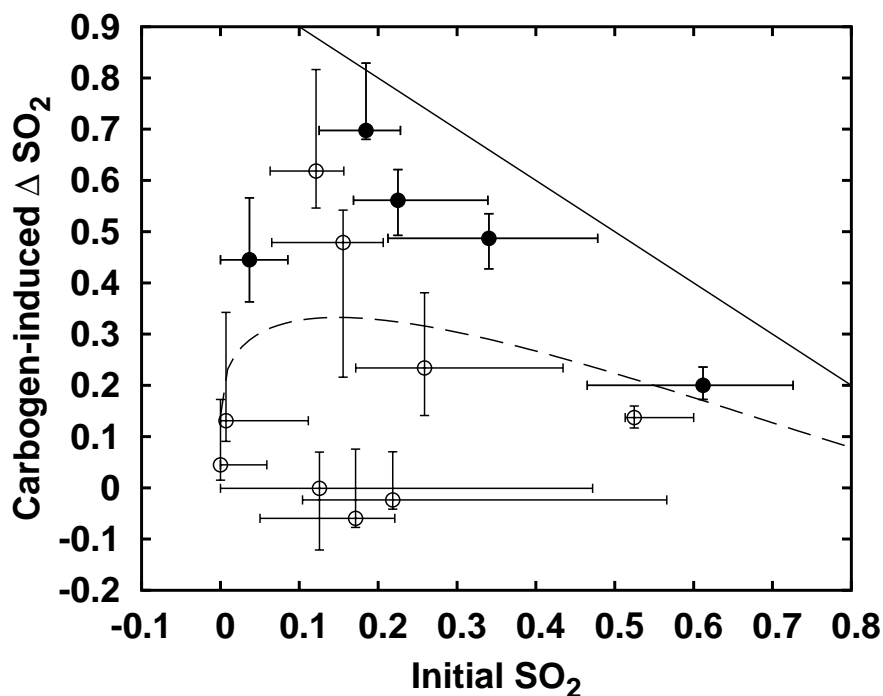


Figure 4.16: Change in SO_2 induced by carbogen as a function of initial SO_2 . Each data point represents the median of six measurements made with six detector fibers on the same tumor. The errorbars span the range of the six measurements. The solid line indicates a carbogen-induced saturation of 100%. Mice that received ALA injection are indicated by filled data points. The dashed line represents a change in pO_2 of 16.1 Torr, a value determined by a best fit to these data.

flectance spectroscopy, yielding a measurement of the average saturation over a large portion of the tumor volume. In contrast, the measurements depicted in figure 4.16 require only one detection fiber each. Each detection fiber samples a small, distinct volume of the tumor, as shown in appendix B.1. This allows an assessment of the variation in tissue oxygenation and response to carbogen not only among tumors, but within a single tumor as well. As illustrated in figures 4.14

and 4.15, the oxygenation and total hemoglobin concentration may vary considerably within a single tumor. This is reflected in the errorbars in figure 4.16, which represent the range of measurements within each tumor. In extreme cases, the intra-tumoral variation in initial SO_2 is nearly as large as the differences between animals.

The change in tumor oxygen saturation induced by carbogen inhalation (ΔSO_2) also varies significantly among animals. This nonuniformity of response has been observed previously in a number of tumor model systems (Hull *et al.*, 1999; Ilangoan *et al.*, 2002; Lanzen *et al.*, 1998; Robinson *et al.*, 1995). The initial value of SO_2 is not predictive of the carbogen-induced change in SO_2 . Some tumors with initial tissue oxygen saturations of 20% exhibit increases in SO_2 of nearly 80%, while others with the same initial saturation show no change or a slight decrease.

The response to carbogen within individual tumors exhibits some heterogeneity, as shown in figure 4.15 and by the vertical errorbars in figure 4.16. In the cases presented here, it was rare to see a large response to carbogen in one part of a tumor and no response in another. Of the 14 animals involved in this study, 11 exhibited increases in SO_2 in all six detection fibers with the onset of carbogen. In the remaining three animals, SO_2 increased in some fibers and decreased in others. In these cases, the carbogen-induced changes in SO_2 were not significantly greater than the uncertainty in the measurement.

In their analysis of carbogen-induced saturation changes in rat tumors, Hull *et al.* (1999) determined a global best fit value of the carbogen-induced change in

pO_2 of 29.7 ± 6.6 Torr by fitting the equation

$$\Delta SO_2 = \frac{\left[\left(\frac{SO_2 p_{50}^n}{1 - SO_{2init}} \right)^{\frac{1}{n}} + \Delta pO_2 \right]^n}{\left[\left(\frac{SO_{2init} p_{50}^n}{1 - SO_{2init}} \right)^{\frac{1}{n}} + \Delta pO_2 \right]^n + p_{50}^n} - SO_{2init} \quad (4.12)$$

to the measured ΔSO_2 , where SO_{2init} is the tumor's initial SO_2 . We have performed the same analysis on our murine tumor data using the same values of n (2.46) and p_{50} (33.7 Torr), and found a best fit value for ΔpO_2 of 16.1 ± 3.8 Torr. The corresponding line of constant ΔpO_2 is shown in figure 4.16. Like those of Hull *et al.* (1999), our results are suggestive of two subpopulations of tumors with different degrees of response to carbogen. Three of the tumors we have examined exhibited negligible response to carbogen inhalation. The remainder, including the two tumors with the lowest initial SO_2 , exhibited a median increase in pO_2 of at least 8 Torr.

Those mice that received ALA injection before measurement, indicated by the filled symbols in figure 4.16, did not exhibit significantly different initial blood hemoglobin saturations from those that did not. The increase in SO_2 induced by carbogen breathing, however, was significantly greater in the ALA-sensitized mice, with a Student's T-test p value of 0.03. All five of these mice exhibited increases in pO_2 greater than the best fit value of 16.1 Torr, a characteristic shared by only two of the nine non-ALA mice.

Measurements of $[Hb]_t$ during carbogen inhalation can provide some insight into the mechanism of the carbogen-mediated increase in tissue oxygenation. In a tumor with partially closed or blocked vessels, an increase in blood flow could

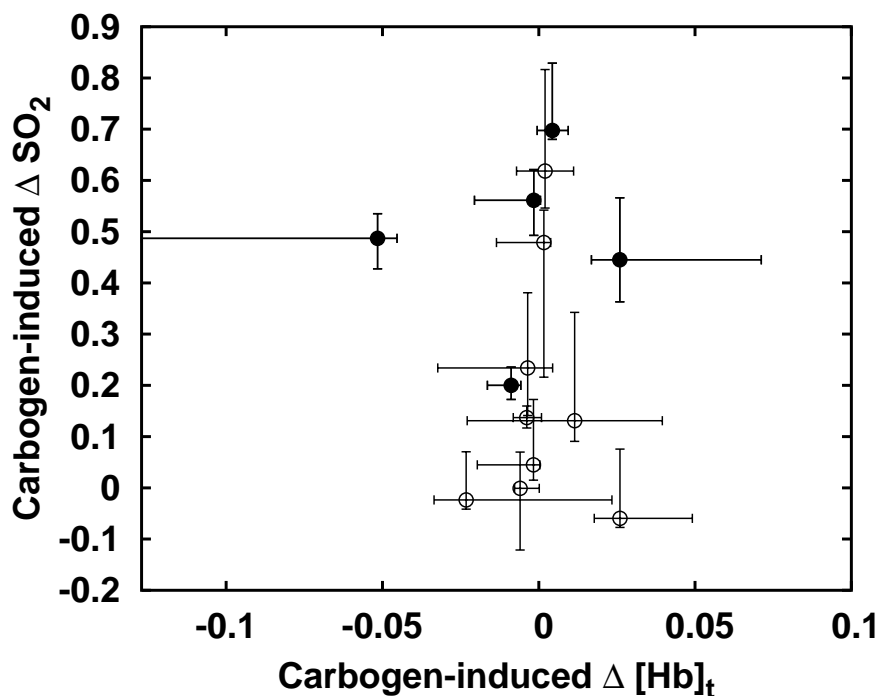


Figure 4.17: Change in SO_2 induced by carbogen breathing as a function of the corresponding change in $[Hb]_t$. Each data point represents the median of six measurements made with six detector fibers on the same tumor. The errorbars span the range of the six measurements. Mice that received ALA injection are indicated by filled data points.

lead to an opening of vessels and an increase in local blood volume and oxygen saturation. We find no correlation between the change in SO_2 induced by carbogen and the accompanying change in $[Hb]_t$, as shown in figure 4.17.

These results, which agree with those of Hull *et al.* (1999), suggest that the primary mechanism leading to the increase in tumor SO_2 is not related to the opening of closed blood vessels. In 8 of the 14 animals studied, the median $[Hb]_t$ decreased with carbogen breathing. 9 of the 14, however, exhibited increases in

one region of the tumor and decreases in another. It may be that the changes in $[Hb]_t$ we observe are correlated with changes in local blood flow rate within already open blood vessels. In a study of R3230 tumors in rats, Lanzen *et al.* (1998) found tumors in which the blood flow, as measured by laser Doppler probes, increased in one region and decreased in another. It is possible that the two measurements are detecting the same physiological phenomenon, however the lack of simultaneous flow and blood volume measurements in both studies makes a direct correlation impossible.

4.5 Discussion

In this chapter, we have demonstrated the ability of spectrally resolved measurement of diffuse reflectance at a single source-detector separation to yield quantitative information about the concentration and identity of absorbers in turbid media. This development represents a significant step toward the implementation of diffuse reflectance spectroscopy in clinical settings. Previously developed radially-resolved methods require relatively large probes (Hull and Foster, 2001b; Nichols *et al.*, 1997). This limits their applicability to skin and other easily accessible tissues or to invasive measurements. In contrast, the source-detector separations used in the measurements presented here are small enough to allow construction of probes compatible with endoscopy. The probe we have used is ideal for testing purposes because it allows simultaneous measurement at many source-detector separations. The spectral analysis, however, requires only a single source-detector pair. It can therefore be applied to data acquired by much simpler probes.

We have demonstrated the ability of this apparatus and method of analysis to extract relevant physical information from spectra measured *in vivo* in a murine tumor model. Our P_3 -based fitting algorithm provides accurate analysis of data obtained at source-detector separations much smaller than those required for radially-resolved diffuse reflectance spectroscopy. The inclusion of data at wavelengths where hemoglobin is highly absorbing makes it possible to quantify the effects of absorption using these small source-detector separations, allowing us to measure much smaller tumors. Unlike previous studies in our laboratory (Hull *et al.*, 1999), no special tumor geometry is required to match the dimensions of

the probe or the geometrical requirements of the fitting model. This allows us to conduct quantitative *in vivo* experiments on tumors of a size and shape that could reasonably be treated clinically using PDT. In addition to extending the work done previously in our laboratory to a new tumor model and a much smaller probe, our results allow a measure of the heterogeneity in hemodynamics within a single tumor. Heterogeneity in oxygenation is especially relevant to PDT. If even a small fraction of the tumor volume is rendered hypoxic and thus protected from photodynamic damage, the surviving cells can initiate tumor regrowth, leading to a failure of treatment. Given a rigorous model of oxygen transport in tissue, the methods developed in this chapter provide a means of assessing the likelihood of local PDT-induced hypoxia, which could prove valuable for treatment planning.

The observation that variations in $[Hb]_t$ and SO_2 on millimeter distance scales can be resolved by our probe and quantified using the P_3 fitting algorithm suggests that a properly designed probe could be used to generate low-resolution images of tissue. A probe consisting of a source fiber surrounded by concentric rings of detection fibers, for example, could sample a circular region of tissue 3 mm in diameter without exceeding the range of source-detector separations over which our methods have been tested. While the volume of data generated by such a probe would be significant, the analysis of the data would be fundamentally identical to that demonstrated here. Further studies would be required to determine the actual resolution of such a device, however the preliminary results shown here are promising.

Finally, the increased carbogen sensitivity of mice given ALA prior to measurement is a potentially interesting result. While our small sample size and lack

of rigorous controls make a definitive evaluation of the causes of this effect impossible, two possible explanations present themselves. First, ALA has been observed to increase heart rate and reduce blood pressure in patients with previous cardiovascular disease (Waidelich *et al.*, 2001). It is possible that the increased SO_2 response in ALA-sensitized mice is due to a systemic cardiovascular response. Second, the region of the tumor being measured is exposed to light from our fiber-optic probe. While the total power delivered to the tumor is much lower than that which would be given during a PDT treatment, the fluence rate immediately under the source fiber may be large enough to cause some photodynamic damage. It is possible that the increased SO_2 we observe is due to a physiological response to photodynamic insult. While the results we have obtained here are preliminary, the possibility that ALA could both sensitize tumors and make them more responsive to carbogen warrants further investigation.

The results presented here demonstrate the basic methods of single-point reflectance spectroscopy and hint at its potential. We anticipate that the accuracy and efficiency of the algorithm can be further improved by the implementation of a more accurate set of absorption basis spectra. An independent characterization of the absorption spectrum of hemoglobin in its native environment would allow the spectral flattening effect resulting from pigment packaging to be accounted for directly, rather than approximated as it is here. Our results in phantoms and *in vivo* indicate that even with partially flawed basis spectra and an approximate model of the reduced scattering spectrum, the reflectance fitting algorithm can extract a wealth of information from a simple set of measurements in a variety of model systems.

References

- Backman, V., Gurjar, R., Badizadegan, K., Itzkan, I., Dasari, R. R., Perelman, L. T., and Feld, M. S. (1999). Polarized light scattering spectroscopy for quantitative measurement of epithelial cellular structures *in situ*. *IEEE Journal of Selected Topics in Quantum Electronics*. **5**:1019–1026.
- Conover, D. L., Fenton, B. M., Foster, T. H., and Hull, E. L. (2000). An evaluation of near infrared spectroscopy and cryospectrophotometry estimates of haemoglobin oxygen saturation in a rodent mammary tumour model. *Phys. Med. Biol.* **45**:2685–2700.
- Hill, A. V. (1910). The possible effects of the aggregation of the molecules of hemoglobin on its dissociation curves. *J. Physiol. (Proc.)*. **40**:iv–vii.
- Holmes, H., Kennedy, J. C., Pottier, R., Rossi, R., and Weagle, G. (1995). A recipe for the preparation of a rodent food that eliminates chlorophyll-based tissue fluorescence. *J. Photochem. Photobiol. B*. **29**:199.
- Howe, F. A., Robinson, S. P., Rodrigues, L. M., and Griffiths, J. R. (1999). Flow and oxygenation dependent (FLOOD) contrast MR imaging to monitor the response of rat tumors to carbogen breathing. *Magnetic Resonance Imaging*. **17**:1307–1318.
- Hull, E. L., Conover, D. L., and Foster, T. H. (1999). Carbogen-induced changes in rat mammary tumour oxygenation reported by near infrared spectroscopy. *Br. J. Cancer*. **79**:1709–1716.
- Hull, E. L. and Foster, T. H. (2001a). Cytochrome spectroscopy in scattering suspensions containing mitochondria and red blood cells. *Appl. Spectr.* **55**:149–154.
- Hull, E. L. and Foster, T. H. (2001b). Steady-state reflectance spectroscopy in the P_3 approximation. *JOSA A*. **18**:584–599.
- Hull, E. L., Nichols, M. G., and Foster, T. H. (1998). Quantitative broadband near-infrared spectroscopy of tissue-simulating phantoms containing erythrocytes. *Phys. Med. Biol.* **43**:3381–3404.
- Hull, E. L., (1999). *Spectroscopy and characterization of turbid media within the diffusion and P_3 approximations*. PhD thesis, University of Rochester, Rochester, NY.

- Ilangovan, G., Li, H., Zweier, J. L., Krishna, M. C., Mitchell, J. B., and Kuppusamy, P. (2002). *In vivo* measurement of regional oxygenation and imaging of redox status in RIF-1 murine tumor: Effect of carbogen-breathing. *Mag. Res. Med.* **48**:723–730.
- Jacques, S. L. (1996). Origins of optical properties in the UVA, visible, and NIR regions. *OSA Trends in Optics and Photonics on Advances in Optical Imaging and Photon Migration*. **2**:364–371.
- Kaanders, J. H. A. M., Bussink, J., and van der Kogel, A. J. (2002). ARCON: a novel biology-based approach in radiotherapy. *Lancet Oncology*. **3**:728–737.
- Kienle, A. and Patterson, M. (1996). Determination of the optical properties of turbid media from a single Monte Carlo simulation. *Phys. Med. Biol.* **41**: 2221–2227.
- Lanzen, J. L., Braun, R. D., Ong, A. L., and Dewhirst, M. W. (1998). Variability in blood flow and pO_2 in tumors in response to carbogen breathing. *Int. J. Radiation Oncology Biol. Phys.* **42**:855–859.
- Lee, J., Fenton, B. M., Koch, C. J., Frelinger, J. G., and Lord, E. M. (1998). Interleukin 2 expression by tumor cells alters both the immune response and the tumor microenvironment. *Cancer Res.* **58**:1478–1485.
- Liu, H., Song, Y., Worden, K. L., Jiang, X., Constantinescu, A., and Mason, R. P. (2000). Noninvasive investigation of blood oxygenation dynamics of tumors by near-infrared spectroscopy. *Appl. Opt.* **39**:5231–5243.
- Mourant, J. R., Bigio, I. J., Jack, D. A., Johnson, T. M., and Miller, H. D. (1997a). Measuring absorption coefficients in small volumes of highly scattering media: Source-detector separations for which path lengths do not depend on scattering properties. *Appl. Opt.* **36**:5655–5661.
- Mourant, J. R., Freyer, J. P., Hielscher, A. H., Eick, A. A., Shen, D., and Johnson, T. M. (1998). Mechanisms of light scattering from biological cells relevant to noninvasive optical-tissue diagnosis. *Appl. Opt.* **37**:3586–3593.
- Mourant, J. R., Fusilier, T., Boyer, J., Johnson, T. M., and Bigio, I. J. (1997b). Predictions and measurements of scattering and absorption over broad wavelength ranges in tissue phantoms. *Appl. Opt.* **36**:949–957.
- Nichols, M. G., Hull, E. L., and Foster, T. H. (1997). Design and testing of a white-light, steady-state diffuse reflectance spectrometer for determination of optical properties of highly scattering systems. *Appl. Opt.* **36**:93–104.

- O’Riordan, J. F., Goldstick, T. K., Vida, L. N., Honig, G. R., and Ernest, J. T. (1985). Modelling whole blood oxygen equilibrium: Comparison of nine different models fitted to normal human data. In *Oxygen Transport to Tissue VII*, Kreuzer, F., Cain, S. M., Turek, Z., and Goldstick, T. K., editors, volume 191 of *Adv. Exp. Med. Biol.*, pages 505–522. Plenum Press, New York.
- Prahl, S. A., (1999). Optical properties of hemoglobin. Available from the website omlc.ogi.edu.
- Rijkema, M., Kaanders, J. H. A. M., Joosten, F. B. M., van der Kogel, A. J., and Heerschap, A. (2002). Effects of breathing a hyperoxic hypercapnic gas mixture on blood oxygenation and vascularity of head-and -neck tumors as measured by magnetic resonance imaging. *Int. J. Radiation Oncology Biol. Phys.* **53**: 1185–1191.
- Robinson, S. P., Howe, F. A., and Griffiths, J. R. (1995). Noninvasive monitoring of carbogen-induced changes in tumor blood flow and oxygenation by functional magnetic resonance imaging. *Int. J. Radiation Oncology Biol. Phys.* **33**:855–859.
- Robinson, S. P., Rodrigues, L. M., Ojugo, A. S. E., McSheehy, P. M. J., Howe, F. A., and Griffiths, J. R. (1997). The response to carbogen breathing in experimental tumour models monitored by gradient-recalled echo magnetic resonance imaging. *Brit. J. Cancer.* **75**:1000–1006.
- Saidi, I. S., Jacques, S. L., and Tittle, F. K. (1995). Mie and Rayleigh modeling of visible-light scattering in neonatal skin. *Appl. Opt.* **34**:7410–7418.
- Stryer, L. (1988). *Biochemistry*. W.H. Freeman Co., New York, third edition.
- Takatani, S. and Graham, M. D. (1987). Theoretical analysis of diffuse reflectance from a two-layer tissue model. *IEEE Trans. Biomed. Eng.* **BME-26**:656–664.
- Van Assendelft, O. W. (1970). *Spectrophotometry of Haemoglobin Derivatives*. Charles C. Thomas, Springfield, IL.
- van Staveren, H. J., Moes, C. J. M., van Marle, J., Prahl, S. A., and van Gemert, M. J. C. (1991). Light scattering in Intralipid-10% in the wavelength range of 400–1100 nm. *Appl. Opt.* **30**:4507–4515.
- Waidelich, R., Stepp, H., Baumgartner, R., Weninger, E., Hofstetter, A., and Kriegmair, M. (2001). Clinical experience with 5-aminolevulinic acid and photodynamic therapy for refractory superficial bladder cancer. *J. Urol.* **165**: 1904–1907.

- Wray, S., Cope, M., Delpy, D. T., Wyatt, J. S., and Reynolds, E. O. R. (1988). Characterization of the near-infrared absorption spectra of cytochrome aa₃ and hemoglobin for the noninvasive monitoring of cerebral oxygenation. *Biochim. Biophys. Acta.* **933**:184–192.
- Zijlstra, W. G., Bursma, A., and Meeuwssen-van der Roest, W. P. (1991). Absorption spectra of human fetal and adult oxyhemoglobin, de-oxyhemoglobin, carboxyhemoglobin, and methemoglobin. *Clin. Chem.* **37**:1633–1638.
- Zwart, A., Kwant, G., Oeseburg, B., and Zijlstra, W. (1984). Human whole blood oxygen affinity: Effect of temperature. *J. Appl. Physio.* **57**:429–434.

Chapter 5

Forward-adjoint Fluorescence Spectroscopy

5.1 Introduction

In the experiments described in chapter 3, we made use of *in vivo* fluorescence spectroscopy to quantify the extent of sensitizer photobleaching during PDT. In addition to its applications in photodynamic dosimetry, sensitizer fluorescence has been used to identify cancerous tissue, which takes up or retains sensitizer more efficiently than surrounding normal tissue, a technique known as photodynamic diagnosis (PDD) (Chaudhury *et al.*, 2001; Marcus *et al.*, 1996, and references therein). In the absence of exogenous fluorophores, many tissues exhibit inherent fluorescence, known as autofluorescence. The shape and intensity of the autofluorescence spectrum depend on the identity and relative concentrations of naturally occurring fluorophores in the tissue. Variations in tissue autofluorescence have

been used to distinguish diseased from normal tissue (Andersson-Engels *et al.*, 1991; Richards-Kortum and Sevick-Muraca, 1996). For example, fluorescence emitted by naturally occurring and induced porphyrins has been observed at elevated levels in oral cancers (Inaguma and Hashimoto, 1999) and psoriatic plaques (Bissonnette *et al.*, 2001; 1998).

Another fluorophore of particular interest in PDT is reduced nicotinamide adenine dinucleotide (NADH). NADH and its nonfluorescent, oxidized counterpart NAD form a redox pair which play a vital role in electron transport in living cells. A decrease in cellular oxygenation can lead to the reduction of NAD into NADH, resulting in an increase in NADH fluorescence. This effect has been observed *ex vivo* in skin samples (Pappajohn *et al.*, 1972) and *in vivo* in pig and rat muscle tissue (Cordeiro *et al.*, 1995; van der Laan *et al.*, 1998). In addition, Pogue *et al.* (2001) have observed decreases in the NADH fluorescence of normal muscle in response to damage induced by PDT, potentially allowing it to be used as a surrogate measure of photodynamic dose.

The quantitative evaluation of *in vivo* fluorescence is complicated by the fact that any measurement of the fluorescence of intact tissue is subject to distortion by the effects of absorption and scattering. For fluorescence to be used for quantitative determination of fluorophore concentration, this distortion must be removed, leaving only the intrinsic fluorescence spectrum of the sample. We define the intrinsic fluorescence spectrum of a sample as the spectrum that would be measured from the same sample in the absence of absorption and scattering.

The recovery of intrinsic fluorescence has been investigated by several researchers. The methods and algorithms they have developed fall into three general

categories. The first comprises those methods that depend on an approximate relation between the measured fluorescence and the reflectance at one or more wavelengths to correct distortions in the fluorescence. The empirical method employed in chapter 3, in which the fluorescence is divided by the reflectance at the emission wavelength and by the reflectance at the excitation wavelength raised to the 0.8 power, is one example. Weersink *et al.* (2001) developed a similar method in which the fluorescence measured at one source-detector separation is corrected for absorption and scattering by dividing by the excitation-wavelength reflectance acquired at a different separation. The optimal source-detector separations for the measurement of reflectance and fluorescence were determined by analyzing the results of Monte Carlo simulations. Fluorescence correction algorithms of this type do not depend on knowledge of the sample's optical properties, but do not provide a measure of the optical properties either. They are useful in cases such as the measurement of photosensitizer bleaching presented in chapter 3 where the sample optical properties do not vary greatly. Because these methods rely on approximate relations between fluorescence and reflectance, they generally are effective only over a limited range of absorption and scattering and only for a specific source-detector geometry.

The second category of fluorescence correction schemes includes those which require quantitative knowledge of the sample optical properties to perform the correction. The known values of μ_a and μ'_s inform a model of fluorescence generation and propagation that is used to extract the intrinsic fluorescence. To be useful, these methods must be coupled with algorithms or measurements capable of determining the sample optical properties. Several researchers have proposed

various correction algorithms based on one-dimensional models of light propagation, each including a means of determining the sample μ_a and μ'_s (Durkin *et al.*, 1994; Gardner *et al.*, 1996; Zhadin and Alfano, 1998). These models necessarily impose limitations on the geometry of the fluorescence measurement, requiring wide collimated excitation beams and model-specific detector configurations. In order to correct fluorescence measurements made with small fiber optic probes of arbitrary geometry, a three-dimensional model of fluorescence propagation is needed. One such algorithm, developed by Wu *et al.* (1993) and later refined by Müller *et al.* (2001), uses an analytic function of the reflectance at the excitation and emission wavelengths to correct the fluorescence emission. The analytic function requires knowledge of μ'_s at both the excitation and emission wavelengths. A separate analysis of the reflectance spectrum is required to determine these values.

In the discussion so far, we have presented the distortion in the fluorescence resulting from absorption and scattering within tissue as a hindrance to the extraction of quantitative fluorescence from measurements. The distortion itself, however, carries potentially useful information about the optical properties of the tissue. A third category of methods for determination of intrinsic fluorescence makes use of the fluorescence distortion to determine the sample's optical properties, which are then used to remove the fluorescence distortion. In an early investigation of this concept, Vari *et al.* (1993) measured the autofluorescence spectra of rabbit kidneys during blood vessel occlusion and found that the ratio of measured emission intensities at two wavelengths was correlated with the level of blood perfusion. In a subsequent study, Shehada *et al.* (2000) used the ratio of autofluorescence emission measured at two different radial positions to obtain an

‘attenuation spectrum’ of rabbit kidney and myocardium tissue. They obtained a measure of the hemoglobin oxygen saturation by fitting the attenuation spectrum as a linear combination of attenuation spectra measured in tissues with varying degrees of hypoxia. While these studies demonstrated that absorption information could be extracted from the fluorescence distortion, both used empirical methods to relate the measured data to physiologically relevant quantities, and neither proceeded to the final step of correcting distortions in the measured fluorescence.

In this chapter we present two sets of fluorescence correction algorithms. Both are based on the forward-adjoint model of fluorescence in turbid media developed in chapter 2. The details of the forward-adjoint model used in each algorithm depend on the geometry of the measurement. The simplest geometry is one in which both the source and the detector are isotropic and both are embedded in an infinite scattering medium. This infinite-medium case is of particular interest here because the forward-adjoint P_3 approximation has an analytic solution in infinite media, as shown in section 2.3.1. In the more complicated case of a semi-infinite scattering medium interrogated by an optical fiber-based probe, we use the forward-adjoint scaled Monte Carlo algorithm described in section 2.3.2 to evaluate the fluorescence.

The first set of algorithms we have developed corrects the fluorescence using prior knowledge of the sample optical properties, which is obtained *via* the reflectance fitting algorithm described in chapter 4. Our method has the advantage that it is applicable to arbitrary optical properties and source-detector geometry and, unlike the model of Müller *et al.* (2001), requires no instrument-dependent correction factors. The second set of algorithms allows quantitative extraction of

the sample optical properties and recovery of the intrinsic fluorescence from a single fluorescence emission spectrum. In this case, the forward-adjoint fluorescence model is fit to the fluorescence spectrum by a nonlinear fitting algorithm analogous to that used for the analysis of reflectance in chapter 4. The free parameters in the fit are the concentrations of known absorbers, the amplitude and shape of the reduced scattering spectrum and the concentrations of known fluorophores.

To test these algorithms' ability to obtain accurate intrinsic fluorescence spectra, we start with the simplest case, that of simulated fluorescence in an infinite medium. We then move on to measurements made in a semi-infinite geometry in tissue-simulating phantoms containing human erythrocytes. Finally, we present preliminary results on the fitting of fluorescence acquired *in vivo* from murine tumors.

5.2 Methods

5.2.1 Definition of intrinsic fluorescence

Before we develop the algorithms and experimental methods for correcting the distortions that absorption and scattering impose on the measured fluorescence spectrum, we must define what is meant by the undistorted or ‘intrinsic’ spectrum. In section 2.3, we described a forward-adjoint model of fluorescence propagation in which the fluorescence signal detected from a sample with uniformly distributed fluorophores is given by

$$R_{det} = (\lambda_x/\lambda_m)\mu_{af}\phi_f \int_V \Phi_x(\mathbf{r})\tilde{\Phi}_m(\mathbf{r}) d^3r, \quad (5.1)$$

where Φ_x is the excitation fluence rate, $\tilde{\Phi}_m$ is the emission-wavelength positional importance, μ_{af} is the fluorophore absorption coefficient at the excitation wavelength, ϕ_f is the fluorescence quantum yield, the wavelength ratio (λ_x/λ_m) accounts for differences in photon energy at the excitation and emission wavelengths, and the integral is over the volume of the sample. Φ_x and $\tilde{\Phi}_m$ depend on the sample optical properties. The remaining terms, however, do not; they are intrinsic characteristics of the fluorophore or fluorophores that make up the sample. We therefore define the intrinsic fluorescence F_0 as the product $(\lambda_x/\lambda_m)\mu_{af}\phi_f$. This definition makes intuitive sense: F_0 is independent of optical properties except for μ_{af} , and because of its dependence on μ_{af} , it is proportional to fluorophore concentration. Equation 5.1 is dimensionally consistent. The product $(F_0\Phi_x)$ gives the effective source distribution, with dimensions of power per unit volume.

Because Φ_x has dimensions of power per unit area, F_0 must have dimensions of inverse length.

F_0 as we have defined it is an experimentally obtainable quantity. To illustrate this, we consider a small sample of fluorophore dissolved in a non-scattering, non-absorbing solvent. The sample is illuminated by an excitation source of unit fluence rate that provides uniform irradiation of the sample. Emitted fluorescence is collected by a detector, such as an integrating sphere, that is capable of capturing all of the light emitted by the sample. In this case, both Φ_x and $\tilde{\Phi}_m$ are unity over the sample volume, so R_{det} takes the form

$$R_{det} = (\lambda_x/\lambda_m)\mu_{af}\phi_f \int_V (1 \cdot 1) d^3r = F_0V. \quad (5.2)$$

F_0 can therefore be understood as the rate of fluorescence emission per unit volume per unit excitation fluence rate. When multiple fluorophores are considered, the F_0 of the mixture is equal to the sum of the F_0 's of the individual fluorophores.

5.2.2 Generation of simulated fluorescence spectra

To evaluate the ability of the forward-adjoint fluorescence model to correct fluorescence distortion and to extract information about tissue optical properties, we have created several data sets using Monte Carlo simulation. The details of the Monte Carlo algorithm used depend on the geometry of the measurement we wish to simulate, as detailed below.

5.2.2.1 Simulation of fluorescence in infinite media

First, we consider the case of an isotropic source of excitation light and an isotropic detector embedded in an infinite homogeneous medium with a uniform distribution of absorbers, scatterers and fluorophores. We have created a simulated data set appropriate to this geometry using a variant of the scaled Monte Carlo method described in chapter 2. The infinite geometry does not require attention to boundaries. Furthermore, the spherical symmetry of the problem allows us to count every absorption event within the spherical shell containing the detector as a detection event. The result is an efficient, fully forward Monte Carlo routine. Although the forward-adjoint formalism is not employed here, the end result is the same as that of the routine described in section 2.3.2: a joint probability distribution $p(l_x, l_m)$ that is equal to the signal contributed by fluorescence photons that have travelled a distance l_m in the tissue after being excited by excitation photons that have travelled a distance l_x prior to absorption.

The total signal collected in a medium with arbitrary absorption coefficients is then given by

$$F(\mu_{ax}, \mu_{am}) = \int_0^\infty \int_0^\infty p(l_x, l_m) e^{-(\mu_{ax} - \mu_{ax MC})l_x} e^{-(\mu_{am} - \mu_{am MC})l_m} dl_m dl_x, \quad (5.3)$$

where the subscripts x and m indicate optical properties at the excitation and emission wavelengths, respectively, and the subscript MC indicates the value of μ_a used in the original Monte Carlo simulation. In practice, the integrals in equation 5.3 are approximated by summation. A separate simulation is run for each set of scattering coefficients for which simulated data is needed.

Cases where the desired scattering coefficient is not among those for which a simulation has been run can be handled by linear interpolation. To generate a simulated spectrum, equation 5.3 is applied using the value of μ_{am} at each wavelength where emission is detected. The simulations described above assume a uniformly distributed fluorophore with a flat emission spectrum. The actual detected fluorescence spectrum can be obtained by multiplying the Monte Carlo-derived signal by the fluorophore's intrinsic emission spectrum. Random noise is then added to the calculated spectrum to simulate the noise in a real measurement.

5.2.2.2 Simulation of fluorescence in semi-infinite media

In the case of semi-infinite media, the algorithm we wish to test is based on a scaled Monte Carlo algorithm. In the spirit of using an independent model to test the algorithm, we use a non-scaled Monte Carlo routine to generate the simulated semi-infinite data set. This algorithm traces excitation photons, fluorescence photons and emission-wavelength reflectance photons independently, allowing the simulation of the fluorescence and reflectance spectra one would obtain from a real measurement. In order to construct these spectra, a separate simulation was run at each wavelength of interest. Because the errors at different wavelengths are uncorrelated, random noise was not added to this data set. Instead, the simulation was terminated when the error in each signal reached the levels expected from experiments. The design of the Monte Carlo algorithm and the matching of the error in the reflectance and fluorescence signals is detailed in appendix A.

5.2.3 Fluorescence phantom preparation

Tissue-simulating phantoms were prepared as described in section 4.2.3. In order to simulate the fluorescence emission of tissue, we added reduced nicotinamide adenine dinucleotide (NADH) to the phantoms. NADH, one of the major components of tissue autofluorescence, is excited efficiently by 365 nm light and has a broad emission peak centered around 455 nm. We expect fluorescence acquired *in vivo* to include contributions from other fluorophores as well. A reasonable test of the fitting algorithm should therefore include multiple fluorophores. In the phantom case, non-NADH fluorescence was provided by the inherent fluorescence emission of the Liposyn emulsion, which has an emission peak at a shorter wavelength than that of NADH. At the concentrations used in our phantoms, the emission intensity of NADH was approximately 4 times that of the Liposyn.

5.2.4 Animal tumor model

EMT-6 tumors were grown subcutaneously in BALB/c mice as described in chapter 4. These tumors exhibit fluorescence due to naturally occurring NADH. To provide fluorescence typical of sensitized tissue, several randomly selected animals were given *i.v.* injections of aminolevulinic acid (ALA) at a dose of 200 mg kg⁻¹, leading to the production of protoporphyrin IX (PpIX) in the tumor and surrounding tissue. As described in chapter 4, the animals were anesthetized and the tumors exposed surgically prior to spectroscopic measurements. Measurements were made while the animals breathed room air, carbogen, and nitrogen sequentially.

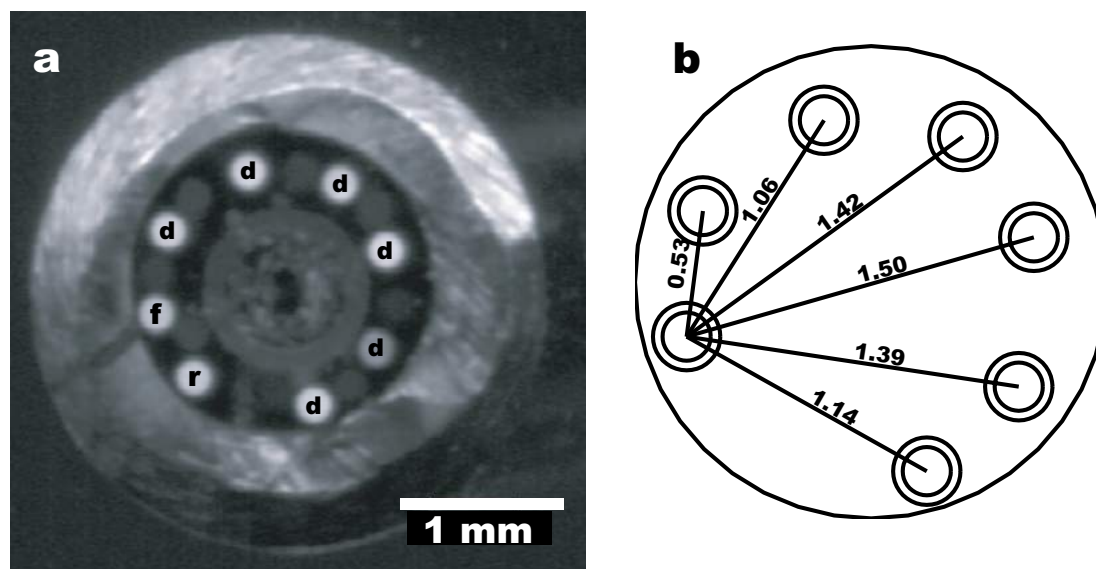


Figure 5.1: (a) Image of the face of the diffuse reflectance/fluorescence probe with the detection and source fibers illuminated and (b) schematic illustrating the distances in millimeters between detection fibers and the fluorescence excitation source fiber.

5.2.5 Spectral data acquisition

Fluorescence spectra were acquired using the fiber-optic probe described in chapter 4. The end view of the probe shown in figure 4.1 is reproduced in figure 5.1, along with a schematic illustrating the source-detector geometry used for fluorescence measurements. The fiber labelled 'r' in figure 5.1(a) was used to deliver white light for the reflectance measurements described in chapter 4. For fluorescence measurements, a second fiber (labelled 'f') was used to deliver fluorescence excitation light to the sample. 365 nm excitation light was provided by a 100 W mercury arc lamp and double monochromator. Electronic shutters (Vincent Associates) allowed the lamps to be blocked, so that each sample was exposed to

light only when spectra were being acquired. The six remaining fibers (labelled 'd') were used to collect light from the sample.

The signal from each fiber was captured and digitized by the spectrograph and CCD system described in section 4.2.1. The spectra acquired by the CCD were corrected for digitization offset and fiber-to-fiber crosstalk using the methods presented in that section. In the case of fluorescence measurements, the throughput of the probe and the response of the CCD were characterized by comparing the known and measured spectra of a calibrated light source (Ocean Optics LS-1-CAL). This process yielded a wavelength-dependent calibration factor, which was multiplied by each measured fluorescence spectrum to correct its shape for fiber absorption and spectral variations in instrument response.

The wavelength range of the spectrograph and CCD combination was such that a fraction of the reflected excitation light was collected by the detector. This signal was integrated over the bandpass of the excitation monochromator to provide a relative measure of the reflectance at the excitation wavelength.

5.2.6 Correction of fluorescence spectral distortion

In cases where the optical properties of a turbid sample are known, the forward-adjoint theory described in chapter 2 predicts the distortion imposed by absorption and scattering on the fluorescence spectrum recovered from the sample. The distortion spectrum is found by evaluating equation 2.51 or 2.61 at each emission wavelength of interest with the fluorophore absorption coefficient μ_{af} and quantum yield ϕ_f set equal to one. The intrinsic fluorescence is then found by dividing the measured fluorescence emission spectrum by the distortion spectrum.

The distortion spectrum calculation is informed by the absorption and scattering properties of the medium at both the excitation and emission wavelengths. It therefore corrects distortions in the shape of the emission spectrum, which are caused primarily by absorption of emitted fluorescence, as well as distortions in fluorescence amplitude, which may result from absorption of the excitation light, the emitted fluorescence or both.

5.2.7 Fluorescence fitting algorithm

The algorithm we use to extract optical property information from fluorescence emission spectra acquired in turbid media is similar to that used to fit diffuse reflectance spectra in chapter 4. As with reflectance, the goal of the fitting is to determine the best fit value of a vector \mathbf{a} that characterizes the medium. The first four elements of \mathbf{a} have the same meaning as they did in the reflectance case. \mathbf{a}_1 and \mathbf{a}_2 are the concentrations of oxy- and deoxyhemoglobin, respectively, and the reduced scattering spectrum is given by the equation

$$\mu'_s(\lambda) = \mathbf{a}_3(\lambda/\lambda_0)^{-\mathbf{a}_4}, \quad (5.4)$$

as described in section 4.2.2.3.

The fitting of fluorescence spectra also requires a model of the intrinsic fluorescence emission spectrum defined in section 5.2.1. We model this spectrum as a superposition of spectra of known fluorophores, as we did in chapter 3, however in this case we omit the Fourier series in the interest of limiting the number of fitting parameters. According to this model, the intrinsic fluorescence is given by

$$F_0(\lambda) = F_1(\lambda) + \mathbf{a}_5 F_2(\lambda) + \mathbf{a}_6 F_3(\lambda) + \cdots, \quad (5.5)$$

where the $F_n(\lambda)$ is the fluorescence emission intensity of the n^{th} fluorophore at wavelength λ . For purposes of fitting, the algorithm normalizes both the measured and best fit spectra to 1 at a predetermined wavelength λ_N , in this case 650 nm. The algorithm assumes that the amplitude of the first fluorophore is equal to 1.0, and uses the shape of the fluorescence spectrum to determine the relative contributions of the other fluorophores, \mathbf{a}_5 , \mathbf{a}_6 and so on. When the fit is complete, the amplitudes of all the fluorophores are scaled by a common factor to obtain their true values. This factor accounts for the fact that the measured spectrum and the best fit spectrum are multiplied by different numbers to achieve normalization and is given by the ratio of the absolute measured fluorescence to the best fit fluorescence at the normalization wavelength.

Each iteration of the fluorescence fitting algorithm consists of four steps. First, a trial vector \mathbf{a} is chosen. Second, the corresponding fluorophore concentrations \mathbf{a}_5 , \mathbf{a}_6 , and so on are used to generate a trial intrinsic fluorescence spectrum. Third, the P_3 forward adjoint expression derived in section 2.3.1 or the scaled Monte Carlo forward-adjoint algorithm described section 2.3.2, informed by the optical properties specified by \mathbf{a}_1 through \mathbf{a}_4 , is used to generate a trial distorted fluorescence spectrum. Finally, this trial distorted spectrum is normalized to 1 at λ_N and compared with the normalized measured spectrum. The process is repeated, with a new \mathbf{a} chosen after each iteration, until the two match to within predefined criteria. Our fitting algorithm returns the concentrations of

known absorbers, parameters describing the scattering, and amplitudes of known fluorophores. These parameters allow us to reconstruct the optical properties of the medium, and we can use this knowledge to determine the intrinsic fluorescence spectrum as described in section 5.2.6.

Fluorescence fitting, because it admits more free parameters than reflectance fitting, is more sensitive to parameter crosstalk. In our phantom data, we find that this crosstalk is especially troublesome in the fitting of the scattering exponent \mathbf{a}_4 in equation 5.4. The fitting algorithm has a tendency to find local minima of χ^2 where the value of \mathbf{a}_4 is very low or even negative. We have found no reports in the literature to support values of the scattering exponent less than 1 or greater than 2 over the wavelength range of our measurements. We therefore restrict the fitting algorithm to this range during fluorescence fitting.

Fluorescence fitting generally requires more computer time than reflectance fitting because the larger number of free parameters increases the size of the parameter space that must be searched and therefore the number of iterations required to reach convergence. In the infinite medium case, the analytic solution to the forward-adjoint problem can be used. In this case, the fitting takes only slightly longer than the corresponding reflectance fitting. When fitting fluorescence from semi-infinite media, however, we generate the forward-adjoint solution using scaled Monte Carlo simulations. This process is extremely computationally intensive. To reduce the time required for fitting, we decrease the number of wavelengths involved in each fit by a factor of 5. This degrades the resolution of the fluorescence spectra from 0.8 nm to 4 nm, however this is sufficient to resolve the narrowest spectral features we expect to encounter. Resampling

has the added advantage that the spectrum's signal-to-noise ratio is improved by approximately $\sqrt{5}$.

In cases of high absorption and large source-detector separation, the fluorescence spectra we obtain have weak signal and therefore low signal-to-noise ratio. To further reduce the effects of random noise, we filter each spectrum with the Savitzky-Golay smoothing algorithm described by Press *et al.* (1992) prior to resampling. The Savitzky-Golay filter reduces high-frequency noise while maintaining the shape of true spectral features.

In the reflectance fitting described in chapter 4, we found that fitting of normalized data led to ambiguity in the determination of μ'_s . In that case, the fitted value of μ'_s was shown to be determined poorly by the fitting algorithm, a shortcoming that was easily corrected by multiplying by the ratio of the factors by which the measured and constructed reflectance spectra were scaled. This correction was based on the observation that the absolute magnitude of the reflectance and the value of μ'_s share an approximately linear relationship over the source-detector separations of our measurements. In the case of fluorescence fitting, the situation is slightly more complicated. As described above, the ratio of scaling factors in this case is used to determine the concentration of fluorophore present in the sample. Some ambiguity remains however; an increase in the measured fluorescence intensity resulting from an increase in scattering coefficient could be misinterpreted as an increase in fluorophore concentration. A separate measurement of μ'_s or of fluorophore concentration is required to resolve this ambiguity.

Our measured data includes a relative measurement of the reflectance at the excitation wavelength, R_x . Using the values of μ_a and μ'_s obtained by fitting the

fluorescence spectrum, we can calculate a ‘best fit’ R_x . Comparing the theoretical and measured values of R_x can serve as a check on the accuracy with which μ'_s has been determined. We cannot, however, use the ratio of the best fit R_x to the measured value to correct errors in the determination of μ'_s . Over the range of source-detector separations and optical properties we expect to encounter in the studies presented here, R_x is not a monotonic function of μ'_s . An overestimate of R_x is as likely to result from an underestimate of μ'_s as from an overestimate.

5.2.8 Choice of fluorescence basis spectra

Our fluorescence phantoms contain two separate fluorophores. The majority of the fluorescence emission arises from NADH, which we have added for the specific purpose of generating fluorescence. A smaller component arises from Liposyn, whose primary purpose is to scatter light within the phantom. Because Liposyn is highly scattering, its fluorescence emission spectrum cannot be measured in nonscattering solution. In addition, we have observed that some fluorophores exhibit altered absorption spectra in the presence of Liposyn. To avoid these complications, we have generated basis spectra derived from measurements of the fluorophores of interest in Liposyn phantoms that did not include any other absorbers. These spectra may still be distorted by wavelength-dependent scattering. We have corrected these effects using the scaled Monte Carlo forward-adjoint algorithm. For the purposes of this correction, we have assumed that the Liposyn phantom, which contained 0.9% lipids by volume, had a reduced scattering coefficient proportional to $\lambda^{-1.5}$ and equal to 1.0 mm^{-1} at 630 nm and produced negligible absorption over

the wavelength range we measured. These assumptions are in agreement with the work of van Staveren *et al.* (1991).

For the fitting of fluorescence spectra acquired *in vivo*, we have adopted the NADH spectrum described above as one of our basis spectra. The animals also exhibit fluorescence at wavelengths shorter than those at which NADH emits strongly. Similar fluorescence has been observed in colonic tissue by Schomacker *et al.* (1992), who attributed it to naturally occurring collagen, although other pigments, such as elastin, may contribute to the emission in this wavelength range as well (Wagnières *et al.*, 1998). To account for these fluorophores and others at shorter wavelengths, we have added a basis spectrum consisting of a Lorentzian centered at 350 nm. This spectrum does not correspond to any particular fluorophore, however it approximates the short-wavelength non-NADH fluorescence of tissue.

5.3 Correction of fluorescence distortion using algorithms informed by reflectance measurement

In this section, we present several examples in which the distortions imposed on measured fluorescence spectra by absorption and scattering are corrected using a forward-adjoint fluorescence model informed by reflectance measurements acquired from the same sample with the same source-detector geometry. The optical properties of the sample are obtained solely from the reflectance measurement; the only information gained from the fluorescence measurement is the intrinsic fluorescence emission spectrum of the sample. The particular fluorescence model used to correct the distortions in the fluorescence is determined by the geometry of the measurement. In the case of isotropic sources and detectors in an infinite medium, we use the analytic forward-adjoint P_3 expression derived in section 2.3.1. For semi-infinite media interrogated by our optical fiber probe, we use the scaled Monte Carlo forward-adjoint model developed in section 2.3.2.

5.3.1 Correction of simulated fluorescence in infinite media using the forward-adjoint P_3 model

Using the method described in section 5.2.2, we have created a synthetic data set which simulates the fluorescence spectra expected in infinite media. In each case, the intrinsic fluorescence spectrum is composed of two Lorentzian lineshapes centered at 455 and 350 nm, representing contributions from NADH and from

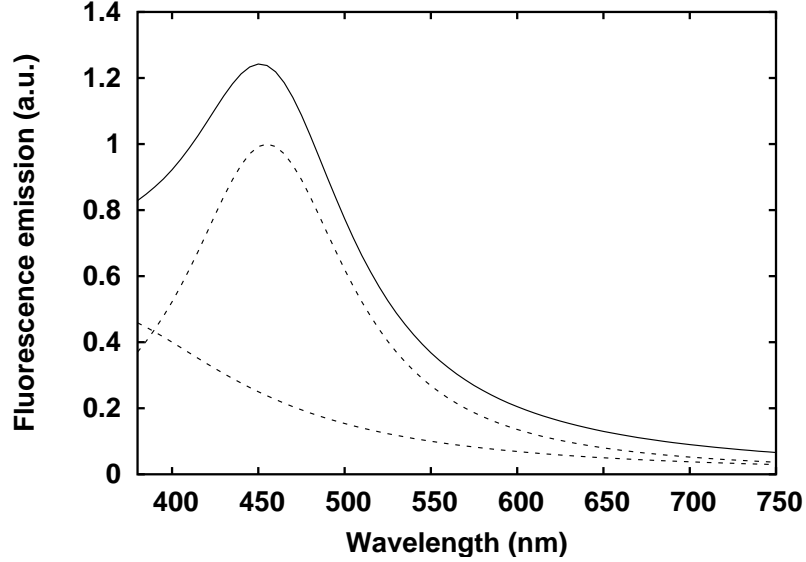


Figure 5.2: Synthetic intrinsic fluorescence spectrum used in Monte Carlo simulation (—) and the two Lorentzian components of which it is composed (- - -).

other fluorophores with shorter wavelength emission, respectively, as shown in figure 5.2. We will refer to the second contribution as ‘background’ fluorescence. This intrinsic spectrum multiplied by the Monte Carlo-derived distortion yields the distorted fluorescence emission spectrum. Several examples of the calculated distorted fluorescence spectrum are shown in figure 5.3. The hemoglobin oxygen saturation, SO_2 , is 0.75 for each of the spectra shown. The total hemoglobin concentration, $[Hb]_t$, varies from 40 to 140 μM , as indicated in the legend. The scattering coefficient at 630 nm and the scattering exponent are 1.0 mm^{-1} and -1.5, respectively, and the distances from the source to the detector are 0.55 and 1.05 mm in panels (a) and (b), respectively. The distortions caused by the Soret band and visible absorption bands of hemoglobin are clearly evident.

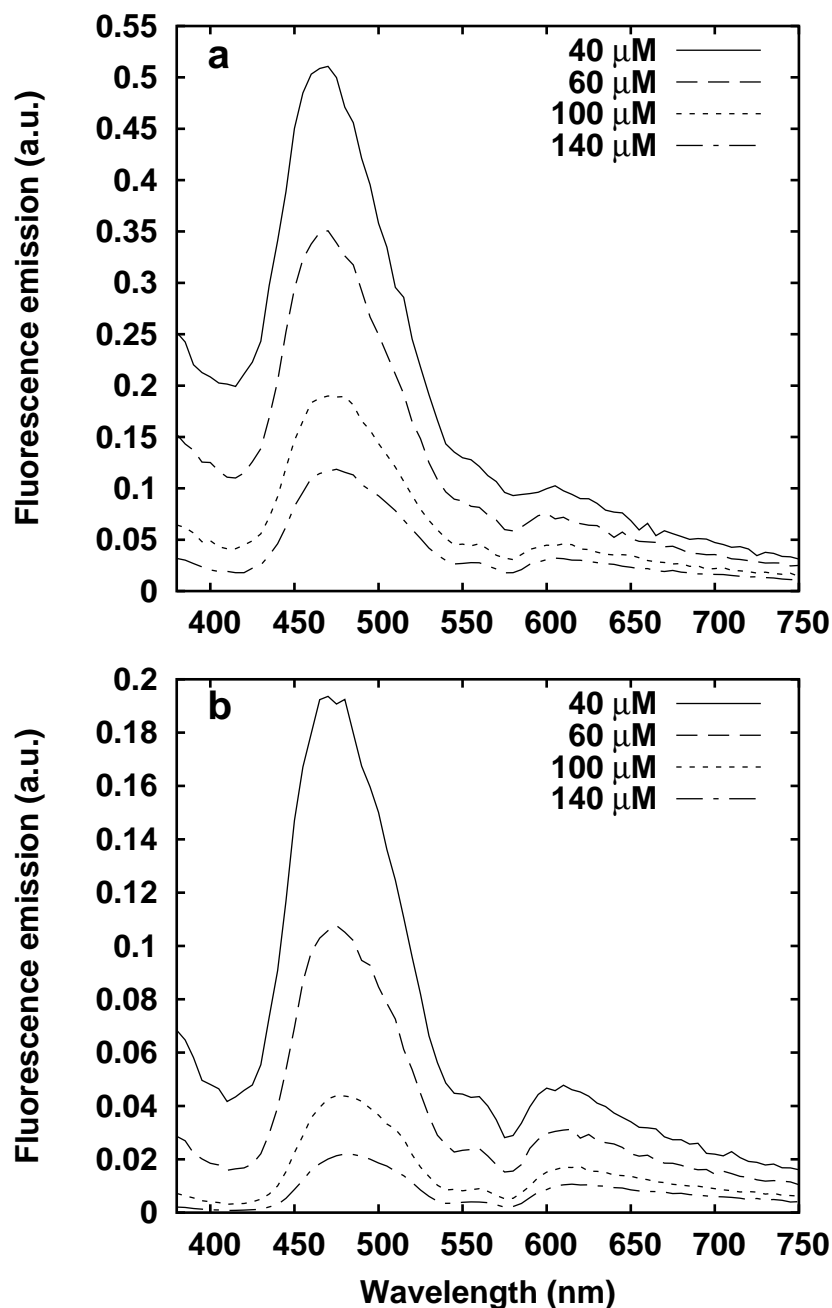


Figure 5.3: Simulated fluorescence spectra detected at source-detector separations of (a) 0.55 and (b) 1.05 mm in turbid media containing various concentrations of hemoglobin, as indicated in the legend. The intrinsic fluorescence spectrum is that shown in figure 5.2. The distortion is calculated by a scaled Monte Carlo method, as described in the text. Calculations were performed for tissue with a μ'_s of 1 mm^{-1} at 630 nm, a scattering exponent of -1.5, and SO_2 of 0.75.

For each fluorescence spectrum we generated, we have also created a simulated diffuse reflectance spectrum. We have used the P_3 fluence expression given in equation 2.18 to fit each simulated reflectance spectrum and extract the hemoglobin concentration, reduced scattering coefficient at 630 nm and the scattering exponent a_4 . We then used the P_3 forward-adjoint algorithm, informed by these values, to recover the intrinsic fluorescence spectra.

The resulting intrinsic spectra are shown in figure 5.4. Each spectrum shown corresponds to one spectrum in figure 5.3. At a source-detector separation of 0.55 mm (panel (a)), the intrinsic fluorescence spectra recovered by the P_3 algorithm and the true intrinsic spectrum, indicated by the thick solid line, are in close agreement over the range of total hemoglobin concentrations investigated. As the detector is moved to a distance of 1.05 mm from the source (panel (b)), the corrected spectra begin to deviate from the intrinsic spectrum. This deviation results primarily from the decreased ability of the reflectance fitting algorithm to recover the tissue optical properties accurately; in cases where the optical properties are recovered correctly, the intrinsic fluorescence is as well. Even when the algorithm begins to fail, as in the high- $[Hb]_t$ cases shown in figure 5.4(b), the errors in the recovered intrinsic spectra are small compared with the dramatic distortions being corrected, shown in figure 5.3(b).

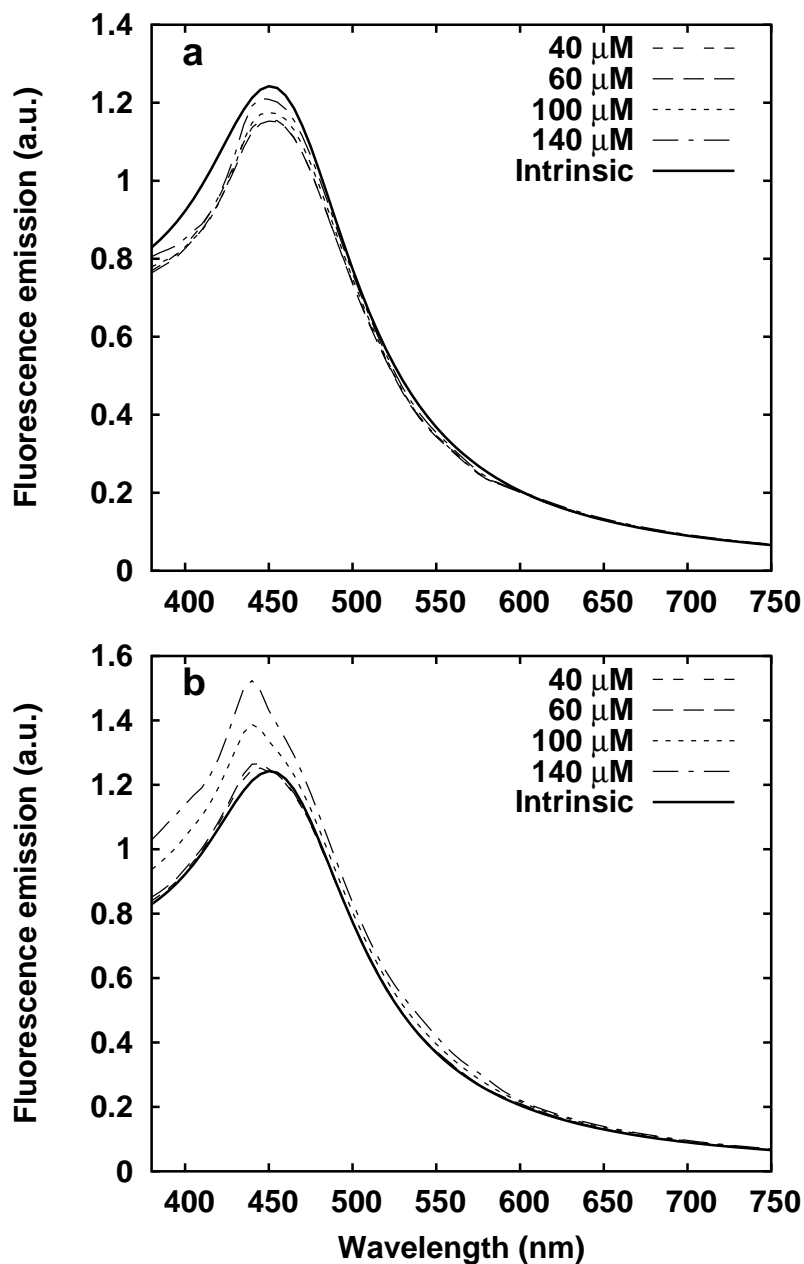


Figure 5.4: Simulated fluorescence spectra at source-detector separations of (a) 0.55 and (b) 1.05 mm in infinite media corrected for the effects of absorption and scattering using a forward-adjoint P_3 algorithm informed by the optical properties obtained by fitting reflectance spectra. Total hemoglobin concentrations are indicated in the legend. The solid line in each panel depicts the intrinsic fluorescence emission spectrum.

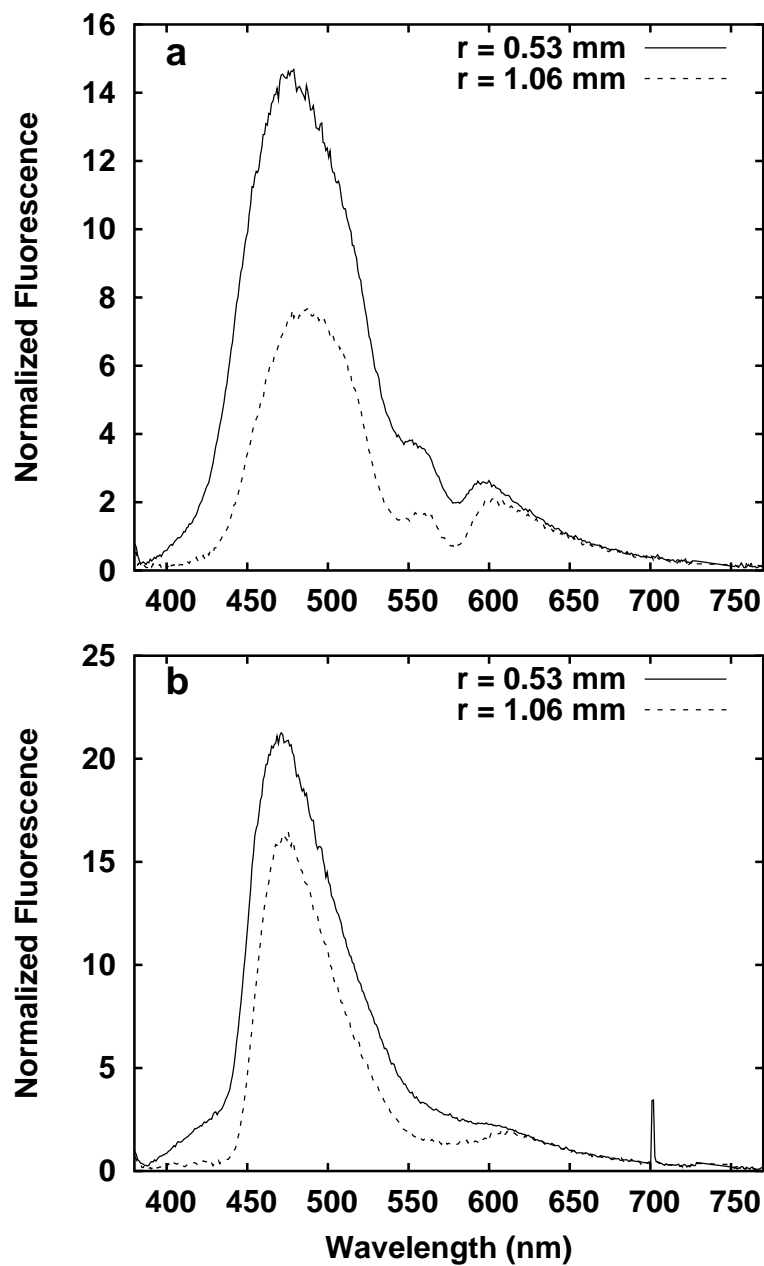


Figure 5.5: Typical normalized fluorescence spectra acquired from an erythrocyte phantom containing NADH at oxygen tensions of (a) 149 and (b) 0 Torr with detection fibers 0.53 and 1.06 mm from the source fiber. Each spectrum is the average of several spectra obtained at the same oxygen tension. Errorbars are omitted for clarity.

5.3.2 Correction of fluorescence in erythrocyte phantoms using the scaled Monte Carlo forward-adjoint algorithm

To test the scaled Monte Carlo forward-adjoint algorithm in semi-infinite media, we turn to fluorescence spectra acquired from the surface of tissue-simulating phantoms containing NADH and human erythrocytes. In these experiments, reflectance and fluorescence spectra were obtained sequentially as the phantom was deoxygenated, allowing continuous monitoring of the phantom optical properties. Typical fluorescence spectra obtained from the phantom at oxygen tensions of 149 and 0 Torr are shown in figure 5.5(a) and (b), respectively. Each spectrum is the average of several spectra, normalized to 1 at 650 nm. Errorbars are omitted for clarity. The fluorescence spectra exhibit obvious distortions due to hemoglobin absorption.

We have corrected each spectrum for the effects of absorption and scattering using the forward-adjoint algorithm and the optical properties determined by fits to the corresponding reflectance spectra. The results are shown in figure 5.6. The corrected spectra are normalized to one at their peak wavelength. The intrinsic fluorescence spectrum of the phantom, similarly normalized, is indicated by the solid line accompanying each curve. The errorbars are found by propagation of errors based on the calculated noise in the CCD signal. When the phantom is well-oxygenated (panel (a)), the shape of the intrinsic fluorescence is recovered reasonably accurately, although the spectrum acquired with the fiber 1.06 mm from the source exhibits slight overcorrection in the wavelength range corresponding to

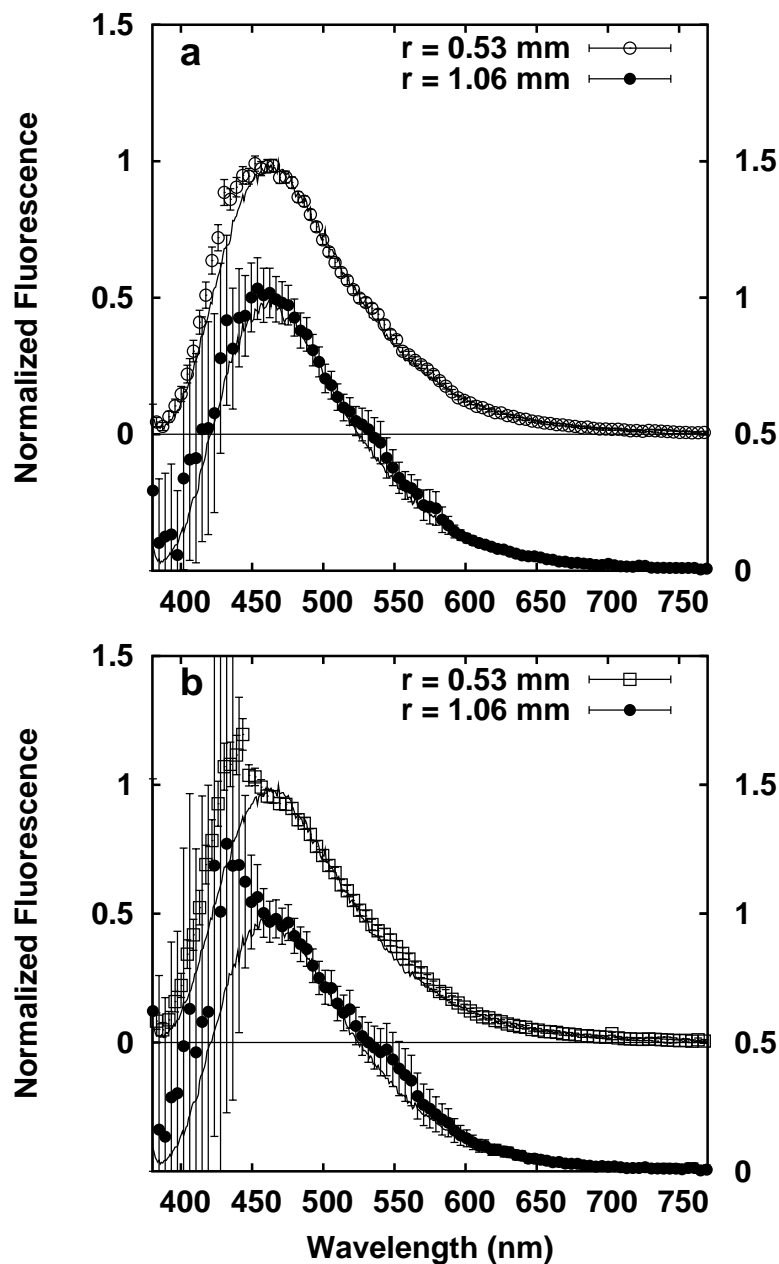


Figure 5.6: Normalized fluorescence emission spectra obtained from phantoms containing NADH and human erythrocytes, corrected for the effects of absorption and scattering using the scaled Monte Carlo forward- adjoint algorithm informed by optical properties obtained by reflectance fitting. The spectra obtained at oxygen tensions of (a) 149 and (b) 0 Torr correspond to those shown in figure 5.5(a) and (b), respectively. For clarity, only every 5th point is shown. The solid lines indicate the normalized intrinsic fluorescence of the phantom.

the visible absorption bands of oxyhemoglobin. In such regions of high absorption, the relatively weak signal and the large distortion imposed by absorption conspire to give large uncertainty in the corrected spectrum, as indicated by the errorbars.

In the deoxygenated phantom (figure 5.6(b)), the spectrum is recovered accurately as well, with the exception of the region around 430 nm, corresponding to deoxyhemoglobin's Soret absorption band. The systematic overcorrection in this region is likely the result of inaccuracies in the basis spectrum. Because the distortion imposed on the fluorescence by the Soret band is the most severe encountered anywhere in the visible spectrum, the correction required to recover the intrinsic fluorescence, and hence the sensitivity to inaccuracies in the absorption basis spectra, is the greatest in this wavelength range. This region is also the most sensitive to the absorber packaging effect described in section 2.4 and to errors in the packaging parameters. The fact that the spectral shape is recovered accurately in the face of similarly intense absorption when the absorber is oxyhemoglobin provides evidence that the overcorrection is a feature of our choice of basis spectrum and not of the correction algorithm itself.

To verify that the errors evident in figure 5.6(b) are indeed the result of a mismatch between our absorption basis spectra and the true hemoglobin absorption, we have generated simulated fluorescence data sets as described in section 5.2.2. The simulations were designed to match the conditions under which the fluorescence spectra we obtained from erythrocyte phantoms were measured. Each simulated fluorescence spectrum was corrected for the effects of absorption and scattering using optical properties obtained by fitting a corresponding simulated reflectance spectrum. The results are shown in figure 5.7. The simulated spectra

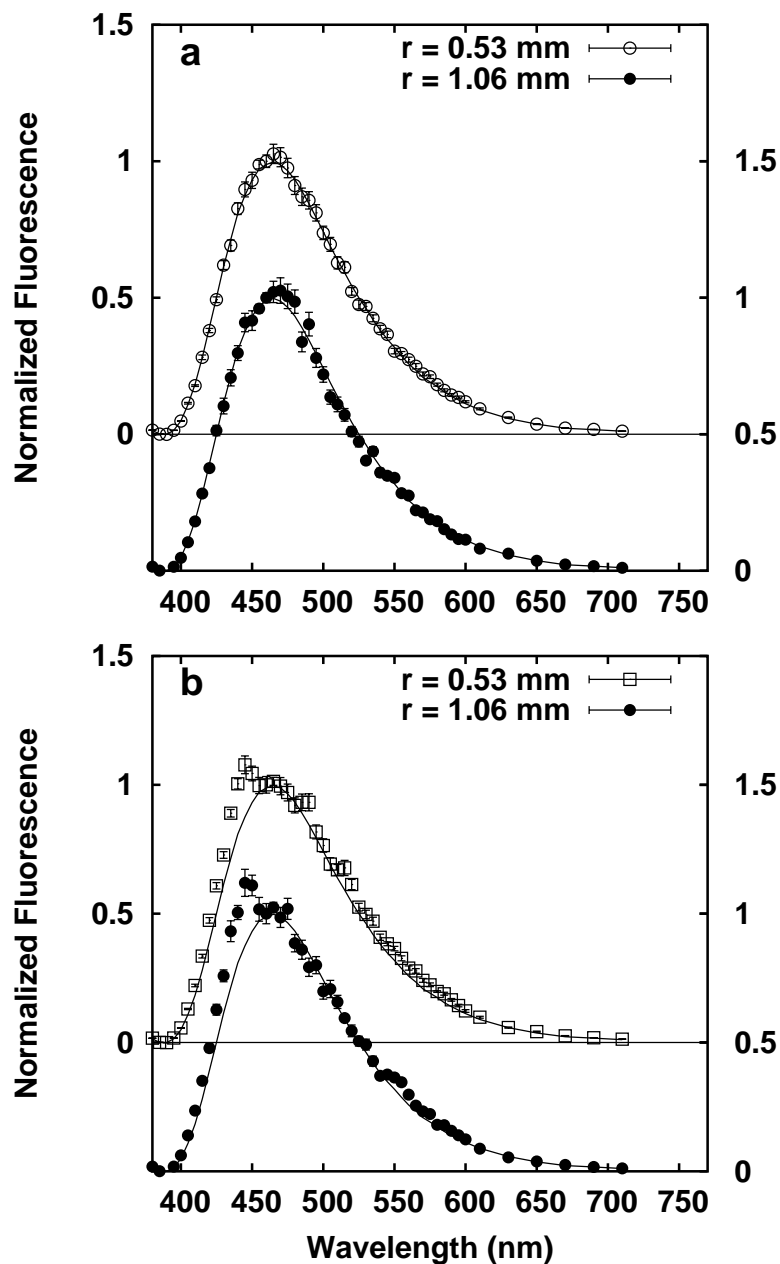


Figure 5.7: Fluorescence emission spectra obtained from Monte Carlo simulation, corrected for the effects of absorption and scattering using the scaled Monte Carlo forward-adjoint algorithm described in section 2.3.2. The spectra were simulated using oxygen saturations of (a) 1 and (b) 0. The spectra were normalized at their peak. The solid lines indicate the true intrinsic fluorescence used in the simulations.

were generated using a total hemoglobin concentration of $100\ \mu\text{M}$. The simulated hemoglobin oxygen saturations were 1 and 0 in panels (a) and (b), respectively. Figure 5.7 and figure 5.6 were generated using the same algorithms. The primary differences between the two are the higher signal-to-noise ratio in the simulated data and the fact that the absorption basis spectra exactly match the absorbers in the sample in the case shown in figure 5.7. The observation that the errors in the recovered intrinsic fluorescence are much greater in the experimental case indicates that they do in fact originate largely from errors in the basis spectra. Even in the case of simulated data, the recovery of intrinsic fluorescence is imperfect, due to small errors in the determination of the sample's optical properties by the reflectance fitting routine. In the cases shown, the reflectance fits overestimate both μ'_s and $[Hb]_t$. The overcorrection is more obvious in the deoxygenated case for three reasons. First, for this particular set of simulated data, the overestimate of $[Hb]_t$ is greater in the deoxygenated case. This is coincidental; it was shown in chapter 4 that the overestimate of $[Hb]_t$ by reflectance fitting bears no systematic relation to SO_2 . Second, the peak μ_a of deoxyhemoglobin is greater than that of oxyhemoglobin. A larger correction is therefore required to obtain the intrinsic fluorescence in the deoxygenated case. As a result, the deoxygenated case is more sensitive to errors in the determination of the tissue optical properties. Finally, the Soret absorption band of deoxyhemoglobin has its peak around 430 nm, compared to 415 nm for oxyhemoglobin. Errors in the recovery of intrinsic fluorescence in the deoxygenated case are therefore magnified by the fact that they occur close to the fluorescence emission peak.

5.4 Determination of optical properties and fluorophore concentrations by fitting of fluorescence spectra

Section 5.3 focussed on the correction of fluorescence distortion using algorithms informed by reflectance measurements. In this section, we investigate the correction of fluorescence using only information contained in the fluorescence spectrum itself. We return to the sample systems described in section 5.3, simulated fluorescence in infinite media and fluorescence measured from erythrocyte phantoms, but now we fit the fluorescence spectra using the appropriate forward-adjoint algorithm to extract both the fluorophore concentrations and the sample optical properties simultaneously. Again, the choice between the forward-adjoint P_3 model and the scaled Monte Carlo forward-adjoint model is based on the geometry of the measurement.

5.4.1 Fitting of simulated fluorescence in infinite media using the forward-adjoint P_3 model

In section 5.3.1, we demonstrated the ability of the analytic forward-adjoint P_3 model to correct distortions in simulated fluorescence in infinite media. In this section, we fit the same simulated data set to obtain optical property information directly. The simulated fluorescence spectra originally shown in figure 5.3 are reproduced in figure 5.8. The solid lines in the figure indicate the best fits to the data returned by the P_3 forward-adjoint fitting algorithm. At all concentrations

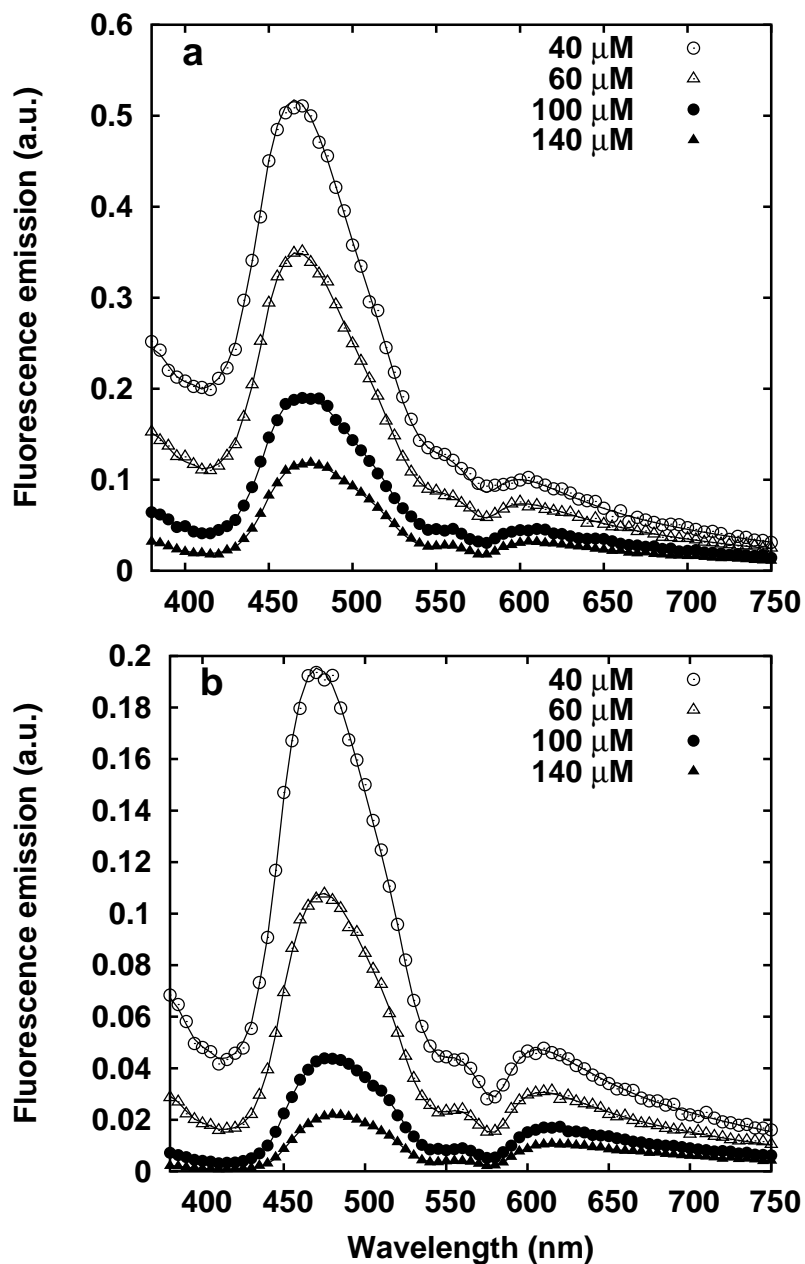


Figure 5.8: Simulated fluorescence spectra distorted by propagation through (a) 0.55 and (b) 1.05 mm of turbid media (symbols) and best fits using the forward-adjoint P_3 model (lines). Calculations were performed for samples with a μ'_s of 1 mm^{-1} at 630 nm, a scattering exponent of -1.5, and SO_2 of 0.75. The value of $[Hb]_t$ for each curve is listed in the legend. The solid lines indicate the best fit to each curve using the forward-adjoint P_3 expression.

investigated, the fits agree with the simulated data.

Using the optical properties obtained from fits to each of these fluorescence spectra, we have extracted the corresponding intrinsic fluorescence spectra. These are shown in figure 5.9, along with the intrinsic fluorescence emission spectrum used to create the simulated data set. The spectral shape of the fluorescence emission is recovered accurately, despite the significant distortions evident in figure 5.8. The amplitude of the fluorescence, however, is systematically underestimated, especially in the case of spectra acquired 1.05 mm from the source. This underestimation is due primarily to a systematic underestimation of the total hemoglobin concentration of the sample and hence of the distortion imposed on the fluorescence, as described below.

The fitting algorithm we have used assumes that the sample's intrinsic fluorescence consists entirely of emission from the two fluorophores shown in figure 5.2 and returns the best fit amplitudes of each fluorophore. One of the corrected fluorescence spectra shown in figure 5.9 is reproduced in figure 5.10 along with the two components of the intrinsic fluorescence spectrum assigned by the fitting algorithm. As expected, the total intrinsic fluorescence spectrum found by summing the two components matches the corrected spectrum.

In figure 5.11, the fitted amplitudes of the two fluorophores used in the simulated data set are shown for spectra obtained under a variety of simulated hemoglobin concentrations and values of SO_2 . The systematic underestimation of the fluorescence observed in figure 5.9 is reflected in the fitted amplitudes of NADH and the background, whose correct amplitudes are 1.0 of 0.5, respectively. At a source-detector separation of 0.55 mm (panel (a)), the amplitudes of both com-

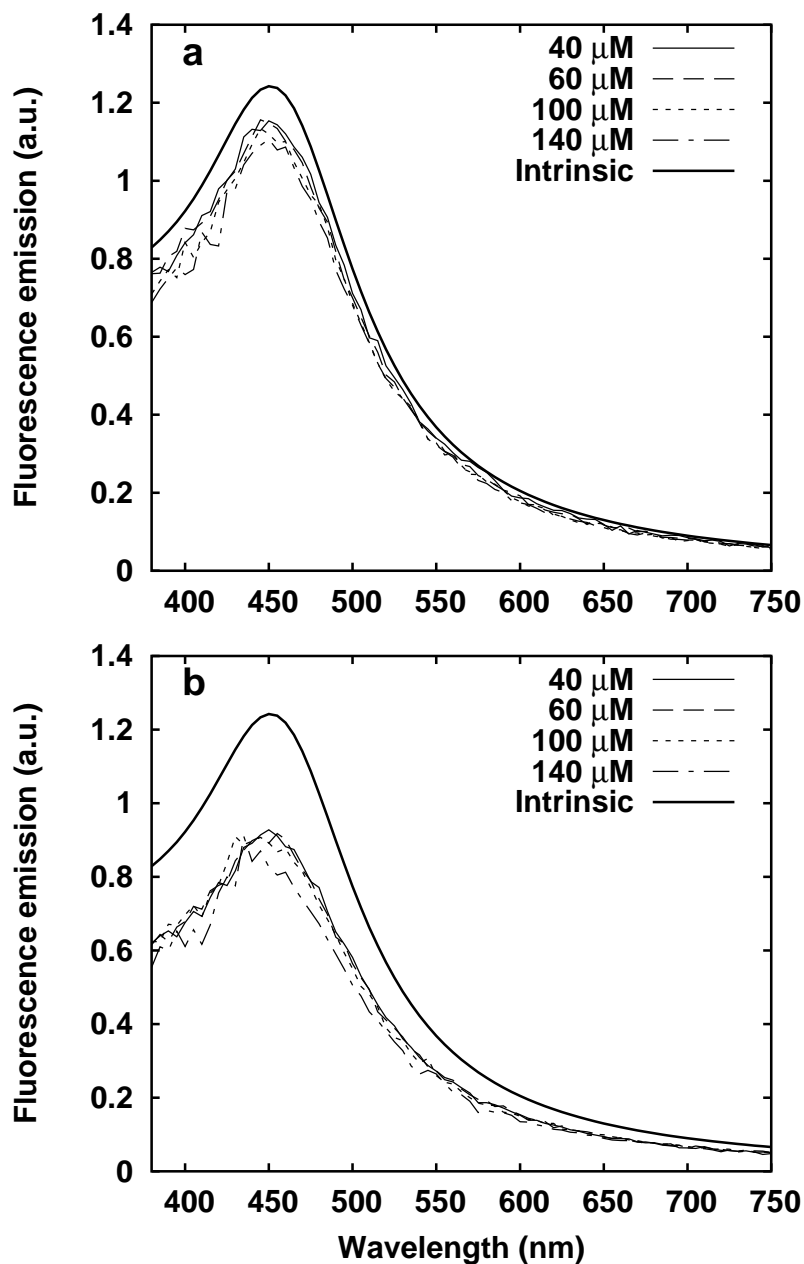


Figure 5.9: Simulated fluorescence spectrum corrected for the effects of absorption and scattering by the forward-adjoint fitting algorithm. The corrected spectra are derived from the spectra shown in figure 5.3 generated at source-detector separations of (a) 0.55 and (b) 1.05 mm. The solid line in each plot indicates the intrinsic fluorescence emission spectrum used to generate the data set.

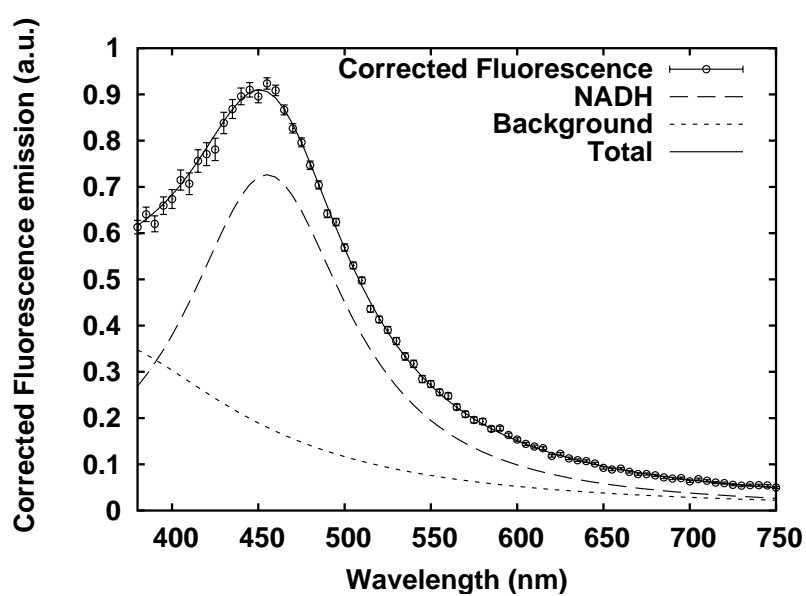


Figure 5.10: A typical corrected fluorescence spectrum (symbols) along with the spectral components assigned by the forward-adjoint fitting algorithm (dashed lines). The sum of the two components (solid line) agrees with the corrected spectrum. The spectrum shown represents fluorescence acquired at a source-detector separation of 1.05 mm, with SO_2 and $[Hb]_t$ equal to 0.75 and 60 μM , respectively.

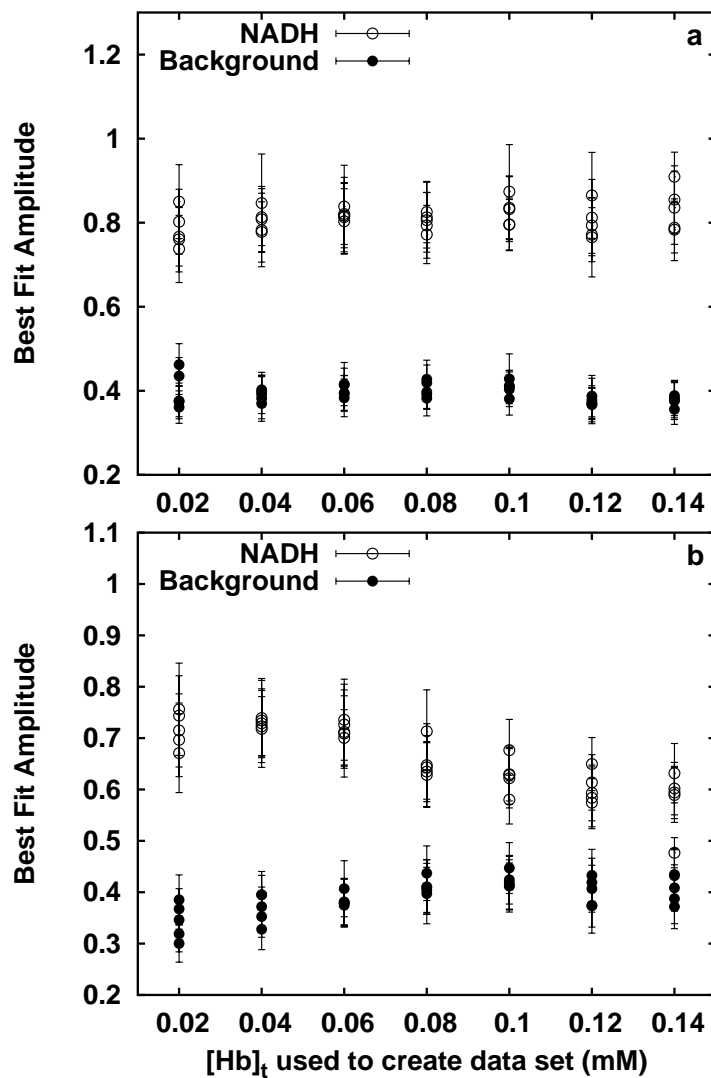


Figure 5.11: Fluorescence amplitudes of the NADH and background components recovered from fits to the simulated data sets with source-detector separations of (a) 0.55 and (b) 1.05 mm. At each $[Hb]_t$, the results of five fits at different values of SO_2 are plotted. Errorbars indicate the uncertainties in the fitted values.

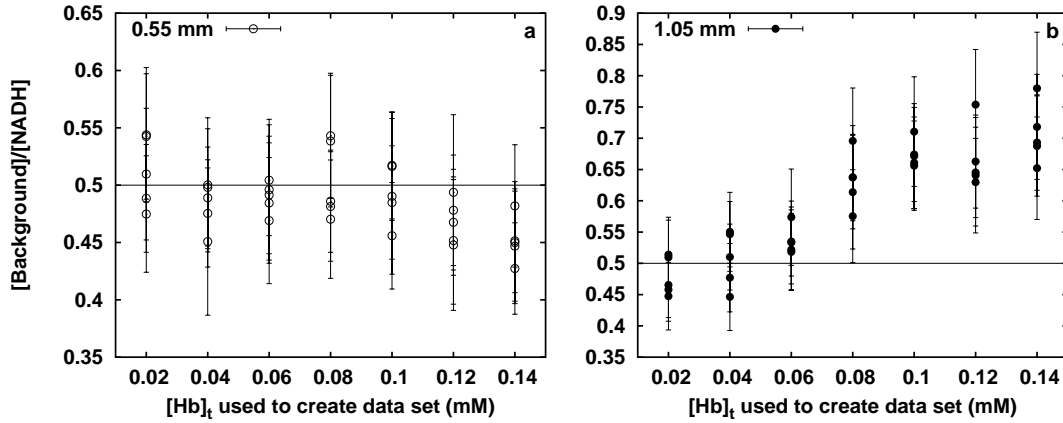


Figure 5.12: Ratio of the best fit amplitudes of background fluorophores to NADH obtained from simulated data at source-detector separations of (a) 0.55 and (b) 1.05 mm. For all the fits shown, the correct ratio was 0.5, as indicated by the solid line. Errorbars indicate the uncertainties in the fitted values.

ponents are correctly reported as constant, and their ratio is reported correctly, although both are slightly underestimated. As the source-detector separation is increased to 1.05 mm (figure 5.11(b)), the algorithm's ability to recover the correct amplitudes is degraded, as is the accuracy of the ratio of the two amplitudes. This ratio is plotted as a function of $[Hb]_t$ in figure 5.12. The synthetic data set was generated using a ratio of 0.5. At a source-detector separation of 0.55 mm, the best fit ratio is approximately correct over the range of hemoglobin concentrations and saturations investigated. At 1.05 mm, the NADH fluorescence is increasingly underestimated as the total hemoglobin concentration is increased. The underestimation of the NADH amplitude is mirrored by an overestimation of the background fluorescence amplitude. The total fluorescence intensity, however, remains approximately constant. The difficulty in assigning fluorescence

amplitude to one or the other fluorophore is a result of the dramatic fluorescence distortion in the region where the two fluorophores being considered emit most strongly. Over the range of hemoglobin concentrations we have investigated, the fluorescence intensity near 403 nm measured 1.05 mm from the source varies by a factor of more than 300. Over the same range, the intrinsic fluorescence amplitude recovered by the fluorescence fitting algorithm varies by less than 30%, as shown in figures 5.9 and 5.11.

Although the recovery of intrinsic fluorescence is the main goal of the fitting algorithm described above, extracting information about the medium's optical properties is useful as well. We have tested this ability over a wide range of $[Hb]_t$ and SO_2 . With source-detector separations of 0.55, 1.05 and 2.05 mm, the algorithm is able to determine the hemoglobin saturation with an accuracy of $\pm 9\%$, as shown in figure 5.13(a). Each point in figure 5.13(a) represents the average of 10 fits at the same SO_2 , but with different values of $[Hb]_t$. Figure 5.13(b) shows the corresponding plot for the recovered value of $[Hb]_t$. In both panels, the errorbars represent the maximum deviation from the true value within each data set. Over the full range of $[Hb]_t$ and at all values of SO_2 , the best fit $[Hb]_t$ systematically underestimates the true value. Because the shape of the distortion is largely dependent on SO_2 , this has little effect on the shape of the recovered intrinsic fluorescence spectrum. The recovered fluorescence amplitude, however, is decreased by the underestimates of μ_a at both the excitation and emission wavelengths, contributing to the systematic underestimate of amplitude seen in figures 5.9 and 5.11.

The difficulty in obtaining accurate amplitudes and the lack of fluorescence

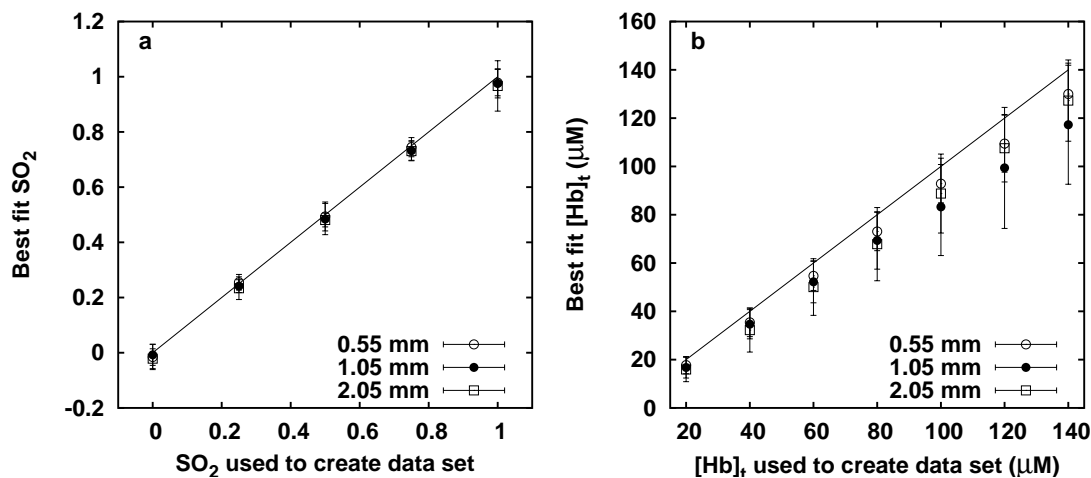


Figure 5.13: Best fit values of (a) SO_2 and (b) $[Hb]_t$ extracted from a synthetic fluorescence data set by the forward-adjoint P_3 fitting routine, plotted as functions of the true values.

intensity far from the source both place a practical upper limit on the source-detector separation at which our measurement scheme is effective. The exact value of this limit will depend on the source and detector employed, the sample optical properties and the accuracy required. In the relatively highly absorbing samples we have investigated here, it is on the order of 1 mm. In less absorbing media, the algorithm may be applicable over a wider range.

5.4.2 Fitting of fluorescence acquired from erythrocyte phantoms using the scaled Monte Carlo forward-adjoint model

Typical fluorescence emission spectra obtained from the surface of a tissue simulating phantom at source-detector separations of 0.53 and 1.06 mm are shown in figure 5.14, along with the best fits returned by the scaled Monte Carlo forward-adjoint fitting algorithm. The spectra and fits are normalized to 1 at 650 nm. The basis spectra used by the fitting algorithm were those of Liposyn and NADH, both measured in a phantom free of other absorbers and corrected for the effects of scattering. The fits provided by the scaled Monte Carlo forward-adjoint algorithm match the data accurately.

In figure 5.15, we show the corresponding intrinsic fluorescence spectra returned by the fitting algorithm, along with the intrinsic fluorescence emission spectrum of the phantom. The recovered intrinsic fluorescence spectra are normalized to 1 at their maxima. In each spectrum shown in figure 5.15, the shape of the undistorted spectrum is recovered accurately, although some overcorrection near the visible hemoglobin absorption peaks is evident, especially in the well-oxygenated case. The correction is remarkably good in the region near the hemoglobin Soret band, despite the fact that this spectral region exhibited the greatest errors when the intrinsic fluorescence was extracted using optical properties obtained from fits to reflectance spectra.

One of the spectra shown in figure 5.15, acquired at a source-detector separation of 0.53 mm in the fully oxygenated phantom, is shown in figure 5.16. The

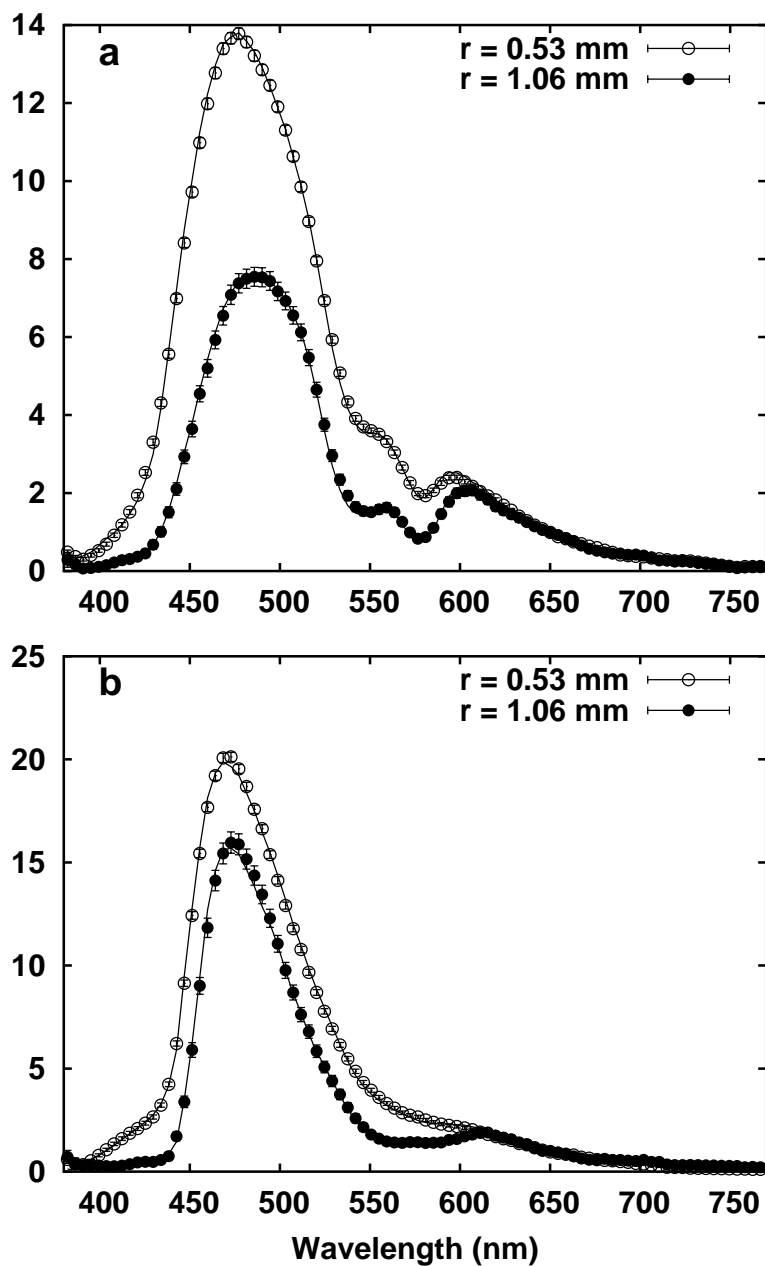


Figure 5.14: Typical normalized fluorescence spectra acquired from an erythrocyte phantom at oxygen tensions of (a) 149 and (b) 0 Torr with detection fibers 0.53 and 1.06 mm from the source fiber. The solid lines represent the best fit to each spectrum using the scaled Monte Carlo forward-adjoint algorithm.

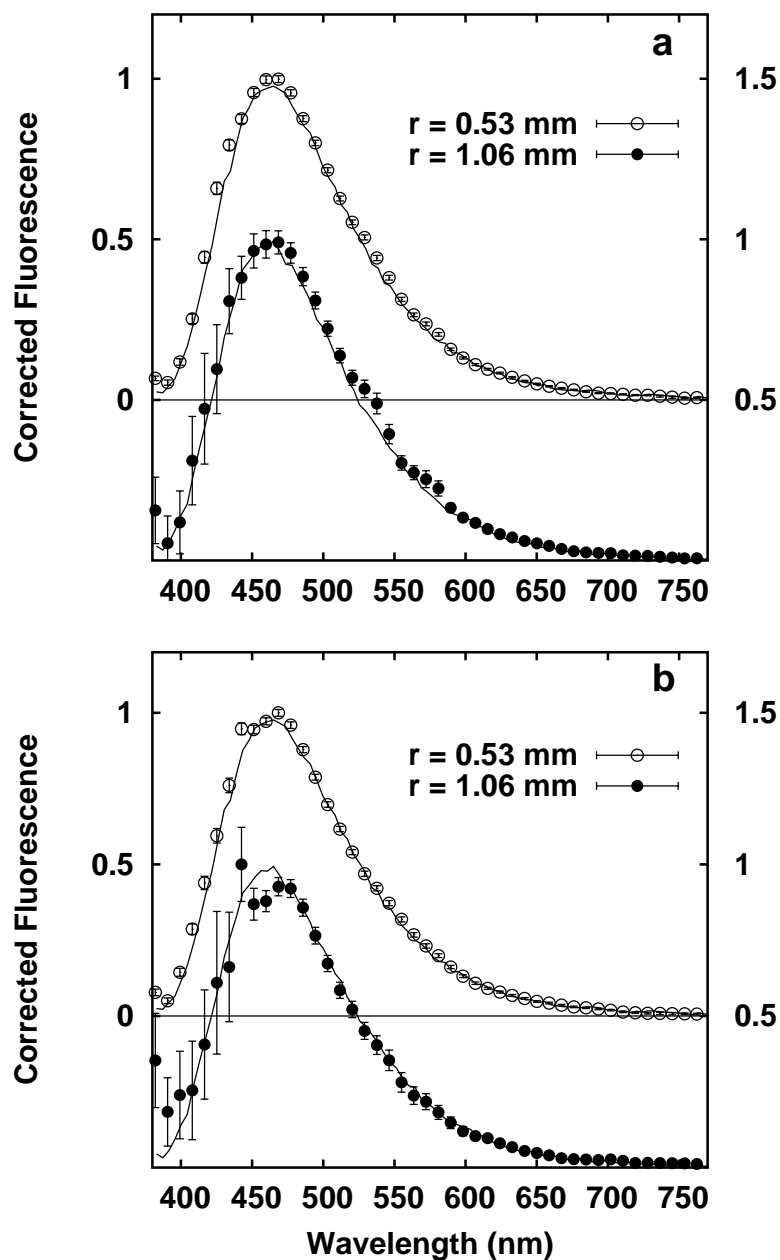


Figure 5.15: Fluorescence emission spectra obtained from an erythrocyte phantom after correction for the effects of absorption and scattering, normalized to 1.0 at the peak. Data were obtained at oxygen concentrations of (a) 149 and (b) 0 Torr and correspond to those shown in figure 5.14. The solid line corresponds to the phantom's intrinsic fluorescence emission spectrum.

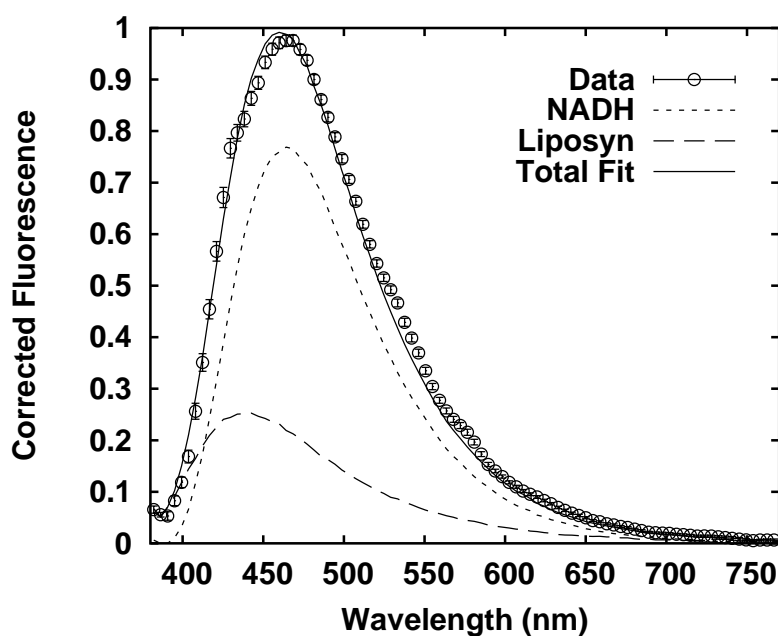


Figure 5.16: Typical erythrocyte phantom fluorescence spectrum (symbols) corrected for the effects of absorption and scattering, along with the contributions of spectral components assigned by the forward-adjoint fitting algorithm (dashed lines) and their sum (solid line).

dashed lines indicate the best fit contributions of NADH and Liposyn to the intrinsic fluorescence. The agreement between the total of these two components (solid line) and the calculated intrinsic fluorescence spectrum (data points) indicate that the phantom's fluorescence is adequately modelled by the sum of NADH and Liposyn emission. The small differences between the total fit and the calculated intrinsic fluorescence could result from errors in the calculated absorption and scattering spectra or from the presence of fluorophores not accounted for in our basis set.

The best fit amplitudes of the two fluorescence components are plotted in figure 5.17. The amplitudes are normalized such that the initial total amplitude is equal to one. At the shortest source-detector separation, the NADH and Liposyn amplitudes are both reported as constant, and their relative amplitudes are reported in agreement with the values observed prior to the addition of erythrocytes of 0.8 and 0.2, respectively. The amplitudes of both fluorophores exhibit an artifactual decrease at low oxygen tension due to crosstalk between the fluorescence amplitudes and the scattering coefficient in the fitting algorithm, as described below. As the source-detector separation is increased, the uncertainty in the assignment of the fluorescence amplitudes increases. This reflects the dramatic increase in the fluorescence distortion, especially at the shorter wavelengths where the two fluorophores are most easily distinguished.

The corresponding best fit values of μ'_s at 630 nm obtained from each fluorescence spectrum are plotted in figure 5.18. As expected, the value of μ'_s is not affected by changes in the phantom's oxygenation status. This indicates that crosstalk between μ'_s and the other free parameters in the fitting algorithm

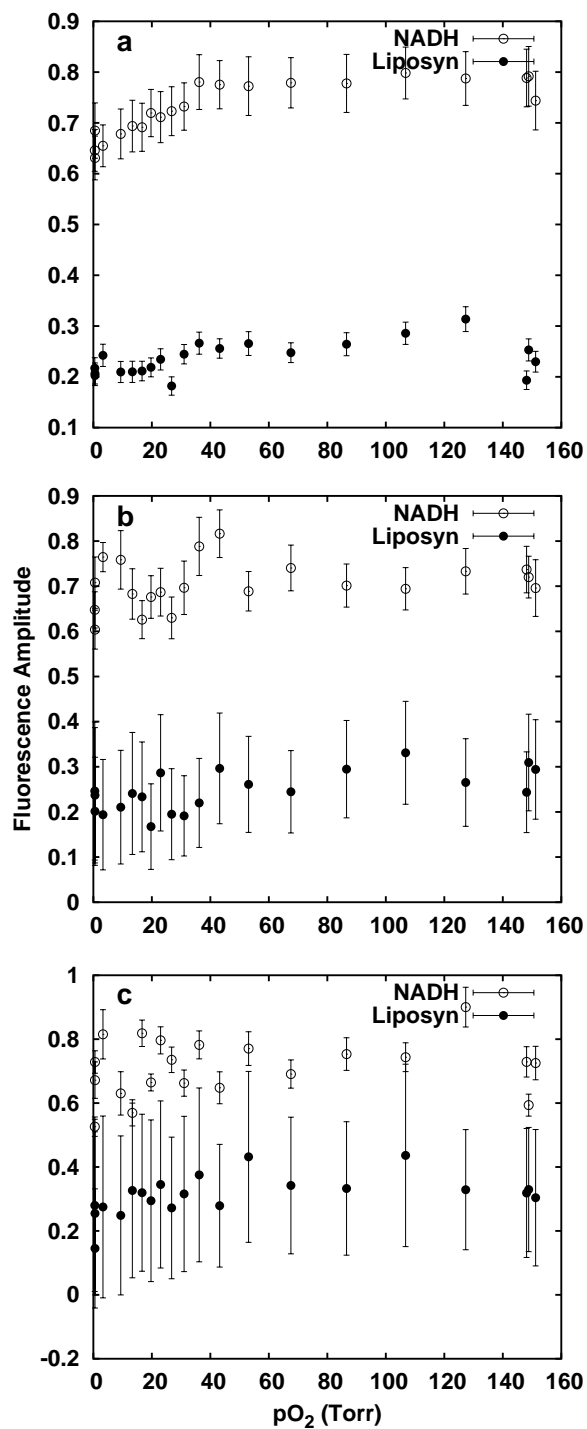


Figure 5.17: Best fit values of the fluorescence amplitudes of NADH and Liposyn in a phantom containing erythrocytes as functions of phantom oxygen concentration. Fits are shown for source-detector separations of (a) 0.53 (b) 1.06 and (c) 1.50 mm.

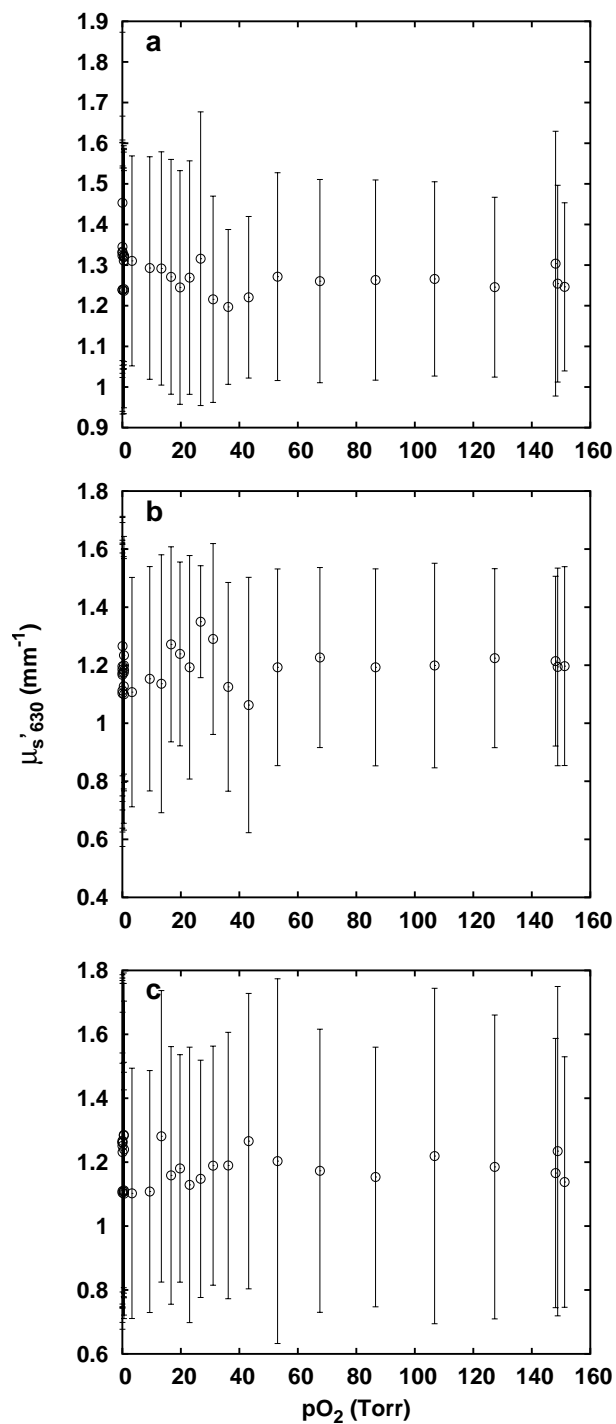


Figure 5.18: Fitted value of μ'_s at 630 nm extracted from the fits used to generate figure 5.19.

is minimal. An exception is the artifactual increase in μ'_s and decrease in the recovered fluorescence amplitude at low oxygen tension in the fits to data acquired at 0.53 mm from the source. The large errorbars on the best fit μ'_s at all source-detector separations indicate that the fluorescence fitting algorithm is not extremely sensitive to μ'_s and will reliably detect only very large scattering changes.

The oxy- and deoxyhemoglobin concentrations recovered from fitting to these fluorescence spectra are shown in figure 5.19. At each source-detector separation, the total hemoglobin concentration is correctly reported as constant, although the value of $[Hb]_t$ recovered from these fits to fluorescence spectra is approximately 20% lower than that reported by the fits to the corresponding reflectance spectra presented in chapter 4. At all the source-detector separations investigated, the turnover from oxy- to deoxyhemoglobin as the phantom deoxygenates is clearly evident. The crosstalk between the fluorescence amplitude and μ'_s at the shortest source-detector separation has no apparent effect on the determination of the total hemoglobin concentration or saturation, indicating that the sample optical properties may be determined accurately even when such crosstalk is present.

In figure 5.20, we plot the hemoglobin saturation determined by fitting to fluorescence spectra as a function of the phantom oxygen tension. As described in section 4.2.2.2, the theoretical relation between these two variables is given by the Hill equation. The solid lines in each plot represent the Hill curve which provides the best fit to the data. To restrict our fitting to the range of validity of the Hill equation, we exclude from the fit any data points whose SO_2 is less than 0.2 or greater than 0.9, as in chapter 4. The dashed line in each panel indicates the best

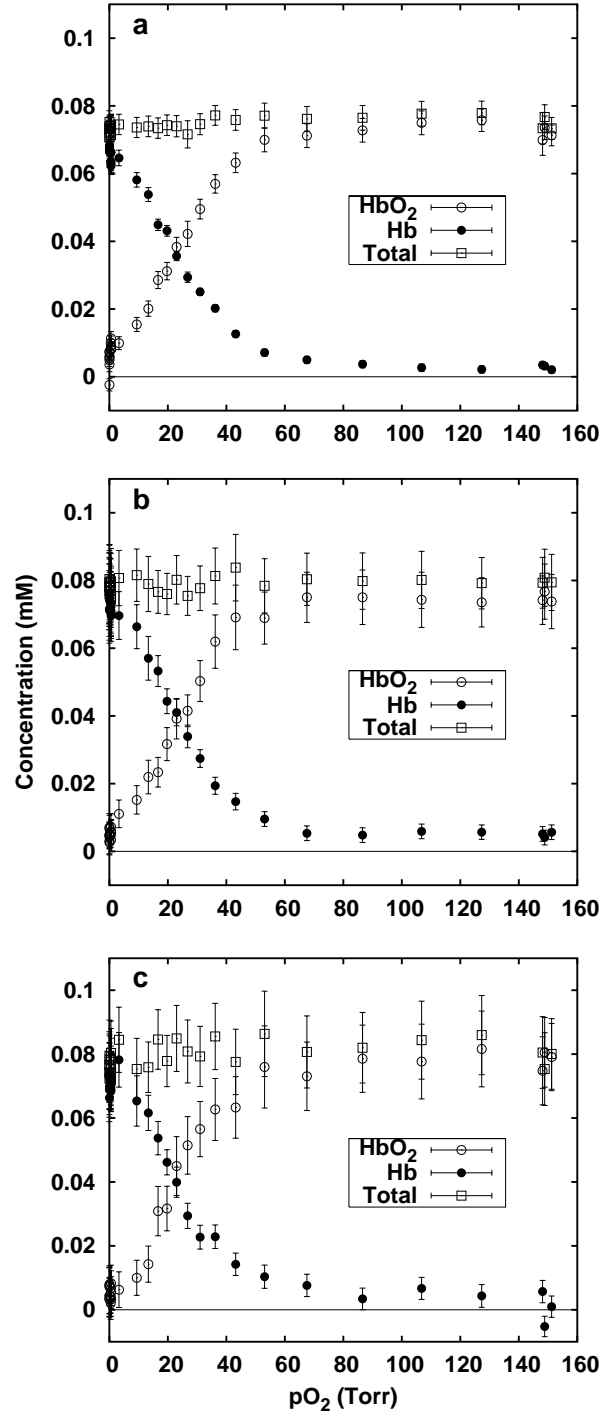


Figure 5.19: Fitted concentrations of oxy- and deoxyhemoglobin based on fluorescence spectra acquired from an erythrocyte phantom with detection fibers (a) 0.53, (b) 1.06 and (c) 1.50 mm from the source fiber.

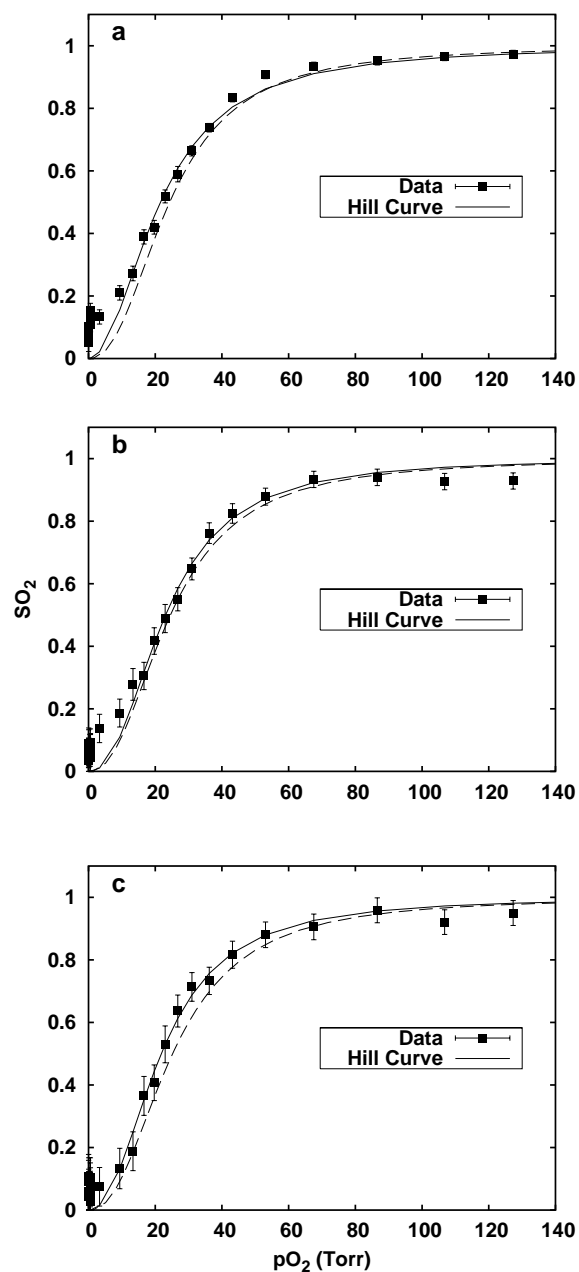


Figure 5.20: Fits of the Hill equation (—) to phantom SO_2 determined *via* fluorescence fitting (symbols) measured at source-detector separations of (a) 0.53, (b) 1.06 and (c) 1.50 mm. Dashed lines (- - -) indicate the Hill curves derived from fits to reflectance spectra acquired by each fiber.

Fiber	S-D (mm)	n	p50 (Torr)
1	0.53	2.04 ± 0.37	21.5 ± 1.7
2	1.06	2.01 ± 0.31	21.0 ± 1.5
3	1.14	2.32 ± 0.85	23.1 ± 3.3
4	1.40	2.24 ± 1.18	21.8 ± 4.5
5	1.50	2.34 ± 0.28	21.6 ± 5.2

Table 5.1: Hill parameters extracted from erythrocyte phantom fluorescence. The values listed were returned by nonlinear fits of the Hill equation to the hemoglobin oxygen saturations recovered from a fluorescence measured in a phantom containing intact human erythrocytes.

fit Hill curve constructed by fitting reflectance spectra obtained with the same detection fiber. The values of p_{50} and n determined for each fiber by the fluorescence fitting are given in table 5.1. These values agree with those obtained from reflectance spectroscopy in chapter 4 within their uncertainties, and are consistent with values reported by other researchers. The agreement between the reflectance and fluorescence fitting algorithms indicates that the fitting of fluorescence can give information equivalent to that obtained from reflectance fitting, and also provide a quantitative measure of fluorophore concentration without the need for an independent reflectance spectrum.

5.5 Analysis of fluorescence spectra acquired *in vivo* from tumor-bearing mice

In chapter 4, we investigated the changes in the hemoglobin oxygenation status of tumors in mice exposed to different mixtures of gasses, as reported by reflectance spectroscopy. For each reflectance spectrum acquired for that study, we also recorded a fluorescence emission spectrum. The goal of the fluorescence measurements was to determine the changes, if any, in intrinsic fluorescence induced by the breathing of carbogen and nitrogen. Fluorescence emission spectra acquired *in vivo* at source-detector separations of 1.14 mm and 1.34 from one EMT-6 tumor are shown in figures 5.21(a) and (b), respectively. In each panel, we show the spectra obtained while the animal breathed room air, carbogen and nitrogen. These spectra include only contributions from naturally occurring fluorophores. The most prominent of these over the range of wavelengths shown is expected to be NADH, with an emission peak near 450 nm. The apparent shift of the emission maximum to 470 nm is caused by the preferential absorption of light at short wavelengths by hemoglobin. The hemoglobin absorption maxima around 550 nm lead to a narrowing of the red side of the emission peak. The best fit, which includes the effects of absorption and scattering as well as fluorescence contributions from NADH and a Lorentzian representing collagen and other fluorophores, agrees with the measured data. The distortion of the spectrum by oxyhemoglobin, indicated by the minima around 540 and 575 nm, is clearly visible in the cases where the animal breathed room air or carbogen, and switches over

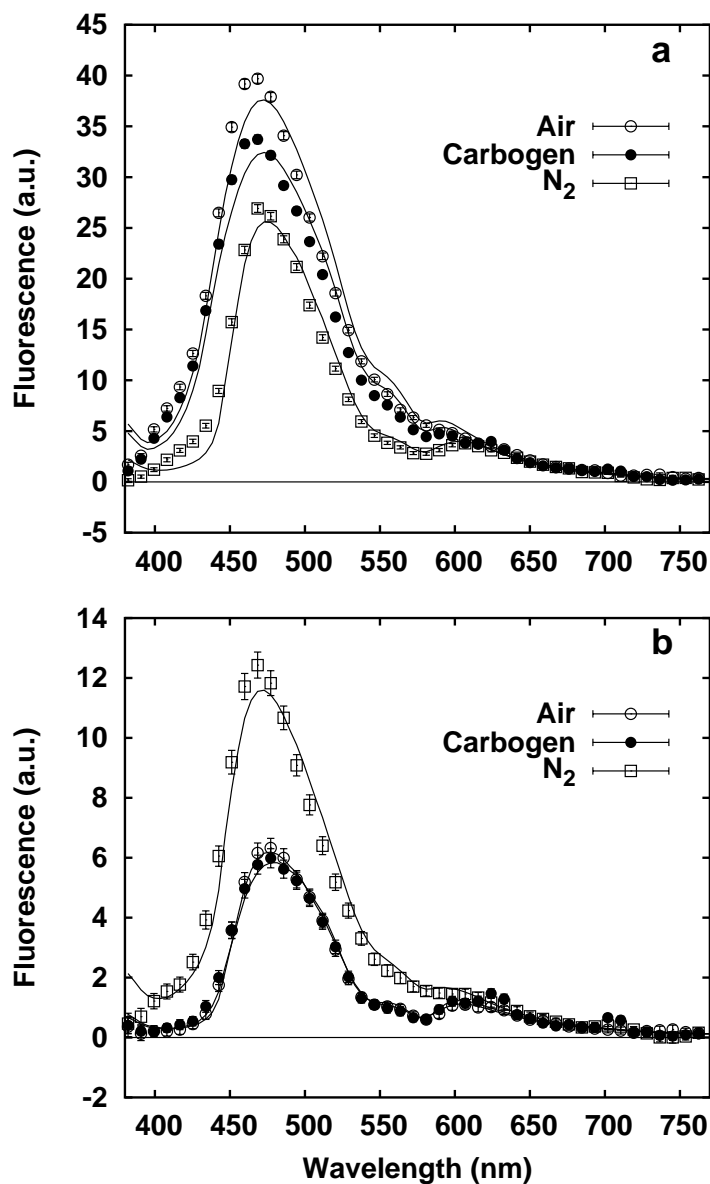


Figure 5.21: Fluorescence emission spectra obtained *in vivo* at source-detector separations of (a) 1.14 and (b) 1.34 mm on the surface of an EMT-6 tumor in an unsensitized mouse. Spectra were taken while the animal breathed room air, carbogen and nitrogen.

during nitrogen inhalation to deoxyhemoglobin, with a single absorption peak around 555 nm.

We first extract the intrinsic fluorescence spectra from these data using the optical properties obtained by fitting the corresponding reflectance spectra. The resulting intrinsic fluorescence spectra are shown in figure 5.22. In the case of the data acquired at 1.14 mm source-detector separation shown in panel (a), the algorithm overcorrects the distortion of fluorescence, resulting in artificial peaks in the regions of maximal hemoglobin absorption. At the greater source-detector separation shown in panel (b), the correction is more effective, and a qualitatively reasonable intrinsic fluorescence spectrum is recovered.

The better performance of the algorithm at greater source-detector separation is coincidental and results from optical heterogeneities in the tissue being sampled. As demonstrated in chapter 4, the optical properties of the EMT-6 tumors we investigated can vary dramatically over distance scales on the order of our probe's source-detector separations. As shown in appendix B, the volume of tissue that contributes to our reflectance and fluorescence measurements, especially at wavelengths where μ_a is large, is small enough that each detection fiber samples a distinct region of the tumor. The same holds true for sources; the reflectance and fluorescence measurements use separate source fibers and therefore interrogate slightly different regions of the sample. The result is that the reflectance spectrum recorded by any given fiber may sample a different set of optical properties than those that distort the fluorescence spectrum measured by the same fiber. This is an effect of the particular design of our probe. A fiber-based probe which used the same source fiber for both reflectance and fluorescence measurements would

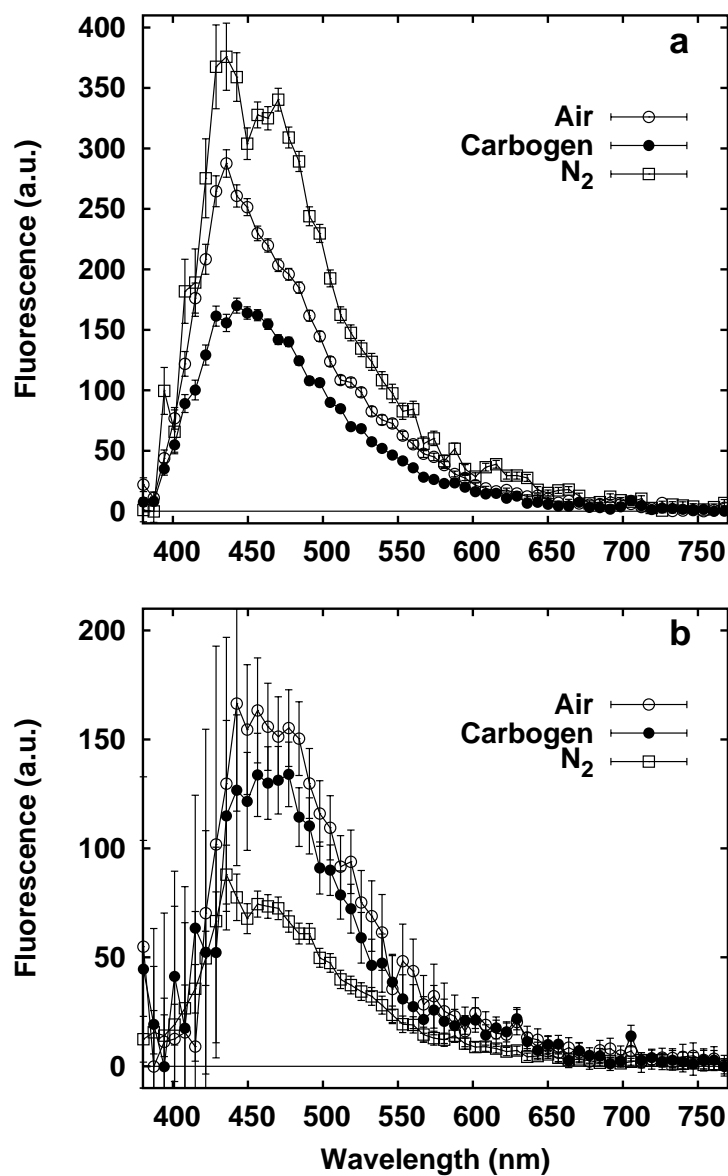


Figure 5.22: Intrinsic fluorescence emission spectra extracted from murine tumors using optical properties determined by reflectance fitting. Spectra were acquired at source-detector separations of (a) 1.14 and (b) 1.34 mm. The corresponding uncorrected fluorescence spectra are shown in figure 5.21.

sample nearly identical volumes of tissue with the two measurements. In the case of our measurements, however, the differences in sampled volume complicate the already challenging problem of fluorescence recovery. For this reason, we will not analyze the reflectance-based correction of these spectra in detail.

The fitting of fluorescence spectra to obtain both optical property information and intrinsic fluorescence spectra has no such limitations. Since only the fluorescence is being fit, the volume of tissue contributing to the optical characterization of tissue and that contributing to the fluorescence emission spectrum are necessarily identical. In the following section, we will consider the fitting of fluorescence spectra to obtain intrinsic fluorescence without incorporating reflectance information. The best fits to the measured spectra given by this algorithm are indicated by the solid lines in figure 5.21. The corresponding calculated intrinsic fluorescence spectra are shown in figure 5.23. The solid lines in each panel indicate the best fit sum of the fluorophore basis spectra used in the fit. In both cases, the broad emission peak of NADH is recovered, and the obvious distortions due to hemoglobin absorption are removed or reduced. While there are significant mismatches between the recovered intrinsic data and the best fit sum of basis fluorophores, the recovery of reasonable intrinsic fluorescence spectra is much better than that attained with reflectance-derived optical properties.

In the case of the data obtained at a source-detector separation of 1.14 mm (panel (a)), the fluorescence due to NADH decreases slightly with carbogen breathing and increases dramatically after several minutes of nitrogen breathing. This is likely caused by a shift of NADH from its oxidized to its reduced state and reflects the expected shift in the redox state of the tumor tissue. In contrast, the NADH

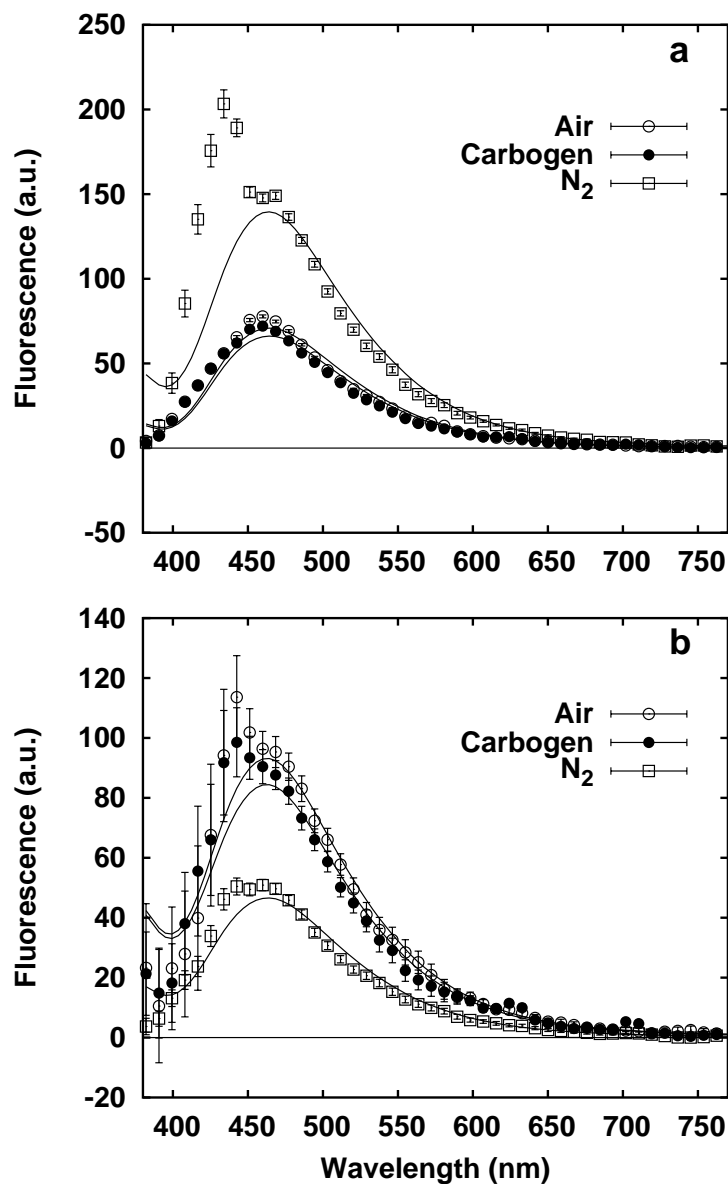


Figure 5.23: Intrinsic fluorescence emission spectra extracted from murine tumors using optical properties determined by fluorescence fitting. Spectra were acquired at source-detector separations of (a) 0.77 and (b) 1.34 mm. The corresponding distorted fluorescence spectra and best fit lines are shown in figure 5.21.

fluorescence in the data taken at a source-detector separation of 1.34 mm (panel (b)) decreases with nitrogen inhalation. Possible explanations for this discrepancy include variations in cellular oxygenation among different regions in the tumor or a slight shift in probe position during the measurement. Whatever the cause, the lack of agreement between measurements made at two different positions on the same tumor at the same time indicates that care must be taken in analyzing *in vivo* fluorescence data.

The recovery of reasonable intrinsic fluorescence from these badly distorted spectra is encouraging, however the fits here are clearly not as good as those shown for the Monte Carlo and phantom data. Significant improvements to the fluorescence and absorption basis sets are required before any quantitative analysis of *in vivo* optical properties or fluorophore concentrations is possible.

5.6 Discussion

In this chapter, we have demonstrated a set of methods for interpreting fluorescence spectra measured in turbid media. These algorithms are capable of recovering the intrinsic fluorescence spectrum accurately over a wide range of optical properties. They are based on a sound theoretical foundation and account for the source-detector geometry of the measurement explicitly without the need for empirical corrections. The algorithms that fit the fluorescence spectrum directly are able to correctly determine the optical properties of the sample and the intrinsic fluorescence spectrum simultaneously. Although a number of algorithms for extracting intrinsic fluorescence have been developed by previous researchers, none of these have determined the sample's optical properties from the fluorescence spectrum directly. We have demonstrated our methods in infinite and semi-infinite geometries using computer simulations and experiments with tissue-simulating phantoms. These numerical and experimental tests confirm that our algorithms are applicable over a range of absorption and scattering coefficients that includes all but the most highly absorbing tissues. Because our algorithms require only a single source-detector pair with a separation on the order of 1 mm or less, they can be implemented using fiber-optic probes compatible with endoscopes, providing the potential for quantitative, minimally invasive fluorescence spectroscopy of the lungs and gastrointestinal tract.

We have developed two general classes of algorithms, one which fits the reflectance spectrum to get the sample's optical properties and another which obtains them by fitting the fluorescence directly. Each method has its strengths and

weaknesses. When the fluorescence is fit directly to determine optical properties and intrinsic fluorescence, only one measurement is required. This simplifies the experimental design and, in the case of measurements made during PDT, reduces the interruption of treatment required for measurement. In addition, the use of a single measurement eliminates concern about sample heterogeneity. When the reflectance spectrum is used to determine optical properties, there is the potential for the volume of tissue that contributes to the absorption and scattering characterization to be different from that which generates the measured fluorescence. This potential problem would be reduced in a system which used the same source fiber for fluorescence excitation and reflectance measurements, however the differences in the depth sampled by the two measurements could still be problematic, as described in appendix B.

Perhaps a more fundamental difference between the reflectance-based algorithms and the fluorescence fitting methods is the way in which the free parameters are coupled in the two systems. The reflectance fitting approach decouples the determination of optical properties from the extraction of intrinsic fluorescence. This has the advantage that errors in the absorption basis spectra can be identified in the reflectance fitting step, before the fluorescence enters the analysis. It also allows extraction of intrinsic fluorescence without a fluorescence basis spectrum, an advantage when the identities of fluorophores that make up the sample are unknown. When the fluorescence is fit directly, it is difficult to determine whether a poor fit results from errors in the absorption basis set, the fluorescence basis set or the scattering model. The coupling of variables also makes the determination of optical properties sensitive to errors in the fluorescence basis spectrum

and crosstalk with the fluorescence amplitudes, a problem not encountered in the reflectance fitting.

There is however an advantage to the fluorescence fitting algorithm's coupling of intrinsic fluorescence to the optical properties. Because this algorithm optimizes the modelled absorption, scattering and fluorescence spectra simultaneously, it necessarily finds a set of optical properties which lead to a reasonable shape in the recovered intrinsic fluorescence. When the absorption and fluorescence basis sets are complete, the result is more accurate recovery of the intrinsic fluorescence spectrum than can be achieved by fitting reflectance. This improved fluorescence recovery can be seen by comparing figures 5.6 and 5.15, for instance. If a complete set of fluorescence and absorption basis spectra are available, the experimental simplicity and accurate fluorescence recovery of the fluorescence fitting algorithm make it an attractive alternative to methods that depend on reflectance fitting to determine optical properties.

In both the infinite and semi-infinite geometries, the accuracy of forward-adjoint fluorescence model is sufficiently good that the limiting factor in the recovery of intrinsic fluorescence is the ability of the reflectance fitting algorithm to determine the sample optical properties. The most obvious route toward improving the recovery of intrinsic fluorescence is therefore to develop more accurate methods for the determination of the sample's optical properties. Potential areas of improvement of our single source-detector reflectance fitting algorithms have been discussed in chapter 4. As more accurate reflectance fitting algorithms are developed, they can be used to inform our fluorescence correction algorithms, resulting in more accurate determination of the intrinsic fluorescence spectra.

Given a sufficiently accurate determination of optical properties, the recovery of intrinsic fluorescence will be limited by the signal to noise ratio (SNR) of the fluorescence measurement. The correction of fluorescence for absorption effects often requires the multiplication of a small measured signal by a large correction factor. This has the effect of magnifying the uncertainty in spectral regions of high absorption. In the data presented here, the uncertainties in the recovered intrinsic fluorescence become unacceptably large for source-detector separations greater than 1 mm, especially in the hemoglobin Soret band. This limitation can be overcome by (a) limiting the source-detector separation of the probe to a range where the SNR is acceptable, (b) implementing a probe with a larger detection fiber or more efficient spectrometer or (c) increasing the power of the excitation light. A probe designed for the specific purpose of single-detector fluorescence spectroscopy could improve the SNR of our measurements dramatically.

We have implemented the extraction of intrinsic fluorescence with and without the use of information obtained *via* reflectance fitting in both infinite and semi-infinite geometries. In the case of infinite media, the P_3 reflectance theory and the forward-adjoint P_3 fluorescence theory both give closed-form analytic solutions, allowing efficient calculation and rapid iterative fitting. The infinite geometry is ideal for modelling and for the testing of fitting algorithms, however it also has a practical application. Because the penetration of light into tissue is limited to a few centimeters at most, photodynamic treatment of large solid tumors or of tumors embedded in internal organs requires the insertion of optical fibers for interstitial delivery of the treatment light. In such cases, the addition of fibers for the measurement of fluorescence will not significantly increase the invasiveness

of the procedure. Fluorescence collected deep in a solid tumor samples an effectively infinite medium, and can therefore be analyzed using the analytic methods presented in this chapter. Such a measurement strategy increases the number of organs that can be considered optically accessible for the purposes of fluorescence spectroscopy.

The imposition of a physical boundary in the semi-infinite geometry requires a more complex model, and does not lend itself to a straightforward analytic solution. We have therefore adopted the scaled Monte Carlo forward-adjoint method to perform these calculations. The efficacy of this algorithm is demonstrated by the recovery of the intrinsic fluorescence spectra and oxygen saturation curves from fits to fluorescence emitted by tissue simulating phantoms containing erythrocytes and NADH. For the full range of optical properties investigated, the Hill parameters obtained from fluorescence fitting agree with those determined by fitting the corresponding reflectance data and with previously published values. The accurate determination of SO_2 persists even at large source-detector separations where the magnitude of the fluorescence distortion makes recovery of intrinsic fluorescence difficult. It appears that the fitting of fluorescence spectra can characterize the absorption spectrum of the medium more robustly than it can the intrinsic fluorescence emission spectrum. This is likely a result of the fact that the absorption spectra of oxy- and deoxyhemoglobin contain many well-defined features while the fluorescence emission spectra of NADH and Liposyn are relatively featureless and therefore more subject to crosstalk with one another and with the scattering spectrum.

Once a library of Monte Carlo simulations is established, the scaled Monte

Carlo forward-adjoint routine can model the propagation of fluorescence with an accuracy comparable to that obtained by running individual Monte Carlo simulations for each data point, but with far less computation time. The iterative fitting routine based on this model is still computationally intensive and time-consuming, requiring as much as 30 minutes to fit a single fluorescence spectrum. The ever-increasing speed of available computers and the potential for improvement in the efficiency of the non-linear fitting algorithm make the time required for fluorescence fitting a minor concern.

Our preliminary analysis of the fluorescence recovered from EMT-6 tumors in BALB/c mice indicates that more work will be required before the fluorescence fitting algorithm can be implemented for routine analysis of *in vivo* fluorescence spectra. There are several areas of potential improvement. First, the reflectance fitting results described in chapter 4 show that the hemoglobin basis spectra used in the current analysis are imperfect, especially in the case of deoxyhemoglobin. Errors in the absorption basis set are expected to reduce the accuracy of the *in vivo* fluorescence fitting, however the quality of the fits to phantom fluorescence spectra described here and of the fits to *in vivo* reflectance spectra shown in chapter 4 indicate that reasonable fits can be obtained despite these errors. It is likely that the more significant source of error lies in the fluorescence basis set. In our current implementation, we have grouped all of the non-NADH fluorophores together in a single Lorentzian component. In reality, the non-NADH fluorescence of tissue arises from a variety of fluorophores. A complete fluorescence basis set would necessarily include the individual fluorescence emission spectra of each of these. The accurate determination of the identity and intrinsic fluorescence

of these spectra would enable a more accurate fitting algorithm and one which would provide more useful information about changes in individual fluorophore concentrations. The development of such a basis set, however, is beyond the scope of this work.

The methods we have presented here significantly extend the range of optical properties and therefore of wavelengths over which intrinsic fluorescence can be determined. There are, however, several areas of potential improvement which require attention. First, we have used a limited set of absorbers in our basis spectrum and a relatively simple model of the scattering spectrum. As described in chapter 4, improvements in the hemoglobin basis spectra are certainly possible. In addition, it is possible that a more sophisticated model of tissue scattering could prove useful. For example, Saidi *et al.* (1995) have characterized the scattering spectrum of human skin tissue using a model that includes a Mie theory component and a Rayleigh scattering component. The $A\lambda^{-b}$ model we have employed here can model Rayleigh scattering using b equal to 4 or Mie scattering with a different value of b . Incorporating both components with a single value of b over the full wavelength range of our measurements is impossible. The Rayleigh component was observed to be most important at short wavelengths, corresponding to the region of the spectrum where our fits to mouse data exhibit the most obvious errors. An improved scattering model may improve the fits to *in vivo* data, especially when coupled with more accurate absorption basis spectra.

Second, none of the algorithms described here make use of the reflectance at the excitation wavelength. This makes them vulnerable to one particular source of error. Consider an absorber with a large μ_a at the excitation wavelength but a

very low μ_a over the wavelength range sampled by the reflectance and fluorescence measurements. Because it absorbs little of the reflectance or emission light, this absorber cannot be quantified by either fitting algorithm. It can, however, have a significant impact on the amplitude of the measured fluorescence. One such example is provided by the tissue-simulating phantom experiments described in this chapter. Both Liposyn and NADH exhibit negligible absorption over the wavelength range of our measurements, and both absorb 365 nm light to some extent as evidenced by their fluorescence. The 365-nm μ_a of NADH and Liposyn combined is much smaller than that of hemoglobin, so their absorption has little effect on our erythrocyte phantoms. In the phantoms without erythrocytes, which we used to calculate the true intrinsic fluorescence of Liposyn and NADH, however, the effect of the unaccounted absorption due to Liposyn and NADH leads to an underestimation of the fluorescence amplitude by as much as a factor of two. Absorption at 365 nm has negligible effect on the shape of the calculated fluorescence spectrum, so the basis spectra, which are normalized for fitting purposes, are unaffected. In general, care should be exercised when interpreting results from samples in which hemoglobin may not be the dominant absorber at the excitation wavelength.

This source of error could be eliminated by a fitting algorithm which explicitly takes into account the reflectance at the excitation wavelength R_x . In the case of reflectance fitting, this would require extending the wavelength range of the measurement to include the excitation wavelength. In the fluorescence case, a calibrated, absolute measurement of R_x would be required. While this adds a level of complexity to the measurement, it is technically feasible, and may lead to

an improvement in the accuracy of the algorithm. Another potential benefit of the explicit characterization of the optical properties at the excitation wavelength is the potential to reduce crosstalk between the scattering amplitude and the fluorescence amplitude. In the current implementation, crosstalk between these two parameters can be detected by comparing changes in the measured and calculated values of R_x . Without a calibrated absolute measurement, such a comparison can detect errors, but not provide guidance on how they might be corrected. In the data presented here, the relative changes in the measured R_x match those expected from the best fit optical properties.

In conclusion, we have demonstrated that the extraction of intrinsic fluorescence from single source-detector separation, steady state measurements in turbid media is possible, and evaluated two distinct algorithms to accomplish the task. These methods are based on rigorous physical models, are quantitatively accurate, and can be extended to arbitrary sets of absorbers and fluorophores. They require only a single source-detector separation and only relatively simple and inexpensive CW light sources. While any iterative algorithm would benefit from increased computing resources, the demands of the algorithms we present here are satisfied by the current generation of personal computers. Given a sufficiently complete basis set and an appropriately designed optical probe, it should be possible to measure optical properties and fluorophore concentrations simultaneously at multiple locations in living tissue. The implementation of such a system during photodynamic treatment has the potential to generate a spatial map of tissue oxygenation, autofluorescence, and sensitizer photobleaching simultaneously.

References

- Andersson-Engels, S., Johansson, J., and Svanberg, K. (1991). Fluorescence imaging and point measurements of tissue: Applications to the demarcation of malignant tumors and atherosclerotic lesions from normal tissue. *Photochem. Photobiol.* **53**:807–814.
- Bissonnette, R., Zeng, H., McLean, D. I., Korbely, M., and Lui, H. (2001). Oral aminolevulinic acid induces protoporphyrin IX fluorescence in psoriatic plaques and peripheral blood cells. *Photochem. Photobiol.* **74**:339–345.
- Bissonnette, R., Zeng, H., McLean, D. I., Schreiber, W. E., Roscoe, D. L., and Lui, H. (1998). Psoriatic plaques exhibit red autofluorescence that is due to protoporphyrin IX. *J. Invest. Dermatol.* **111**:586–591.
- Chaudhury, N. K., Chandra, S., and Mathew, T. L. (2001). Oncologic applications of biophotonics: prospects and problems. *Appl. Biochem. Biotechnol.* **96**:183–204.
- Cordeiro, P. G., Kirschner, R. E., Hu, Q.-Y., Chiao, J. J. C., Savage, H., Alfano, R. R., Hoffman, L. A., and Hidalgo, D. A. (1995). Ultraviolet excitation fluorescence spectroscopy: A noninvasive method for the measurement of redox changes in ischemic myocutaneous flaps. *Plast. Reconstr. Surg.* **96**:673–80.
- Durkin, A., Jaikumar, S., Ramanujam, N., and Richards-Kortum, R. (1994). Relation between fluorescence spectra of dilute and turbid samples. *Appl. Opt.* **33**:414–23.
- Gardner, C. M., Jacques, S. L., and Welch, A. J. (1996). Fluorescence spectroscopy of tissue: Recovery of intrinsic fluorescence from measured fluorescence. *Appl. Opt.* **35**:1780–92.
- Inaguma, M. and Hashimoto, K. (1999). Porphyrin-like fluorescence in oral cancer. *Cancer.* **86**:2201–2211.
- Marcus, S. L., Sobel, R. S., Golub, A. L., Carroll, R. L., Lundahl, S., and Shulman, D. (1996). Photodynamic therapy (PDT) and photodiagnosis (PD) using endogenous photosensitization induced by 5-aminolevulinic acid (ALA): current clinical and development status. *J. Clin. Laser Med. Surg.* **14**:59–66.
- Müller, M., Georgakoudi, I., Zhang, Q., Wu, J., and Feld, M. (2001). Intrinsic fluorescence spectroscopy in turbid media: Disentangling effects of scattering and absorption. *Appl. Opt.* **40**:4633–4646.

- Pappajohn, D. J., Pennys, R., and Chance, B. (1972). NADH spectrofluorometry of rat skin. *J. Appl. Physio.* **33**:684–687.
- Pogue, B. W., Pitts, J. D., Mycek, M. A., Sloboda, R. D., Wilmot, C. M., Brandsema, J., and O'Hara, J. A. (2001). *In vivo* NADH fluorescence monitoring as an assay for cellular damage in photodynamic therapy. *Photochem. Photobiol.* **74**:817–824.
- Press, W. H., Teukolsky, S. A., Vetterling, W. T., and Flannery, B. P. (1992). *Numerical Recipes in C: The Art of Scientific Computing*. Cambridge University Press, New York, second edition.
- Richards-Kortum, R. and Sevick-Muraca, E. (1996). Quantitative optical spectroscopy for tissue diagnosis. *Annu. Rev. Phys. Chem.* **47**:555–606.
- Saidi, I. S., Jacques, S. L., and Tittle, F. K. (1995). Mie and Rayleigh modeling of visible-light scattering in neonatal skin. *Appl. Opt.* **34**:7410–7418.
- Schomacker, K. T., Frisoli, J. K., Compton, C. C., Flotte, T. J., Richter, J. M., Nishioka, N. S., and Deutsch, T. F. (1992). Ultraviolet laser-induced fluorescence of colonic tissue: Basic biology and diagnostic potential. *Lasers Surg. Med.* **12**:63–78.
- Shehada, R. E. N., Marmarelis, V. Z., Mansour, H. N., and Grundfest, W. S. (2000). Laser induced fluorescence attenuation spectroscopy: Detection of hypoxia. *IEEE Trans. Biomed. Eng.* **47**:301–312.
- van der Laan, L., Coremans, A., Inde, C., and Bruining, H. A. (1998). NADH videofluorimetry to monitor the energy state of skeletal muscle *in vivo*. *J. Surg. Res.* **74**:155–160.
- van Staveren, H. J., Moes, C. J. M., van Marle, J., Prahl, S. A., and van Gemert, M. J. C. (1991). Light scattering in Intralipid-10% in the wavelength range of 400–1100 nm. *Appl. Opt.* **30**:4507–4515.
- Vari, S. G., Papazoglou, T. G., Pergadia, V. R., Stavridi, M., Snyder, W. J., Papaioannou, T., Duffy, J. T., Weiss, A. B., Thomas, R., and Grundfest, W. S. (1993). Blood perfusion and pH monitoring in organs by laser induced fluorescence spectroscopy. *Proc. SPIE.* **2081**:117–128.
- Wagnières, G. A., Star, W., and Wilson, B. C. (1998). *In vivo* fluorescence spectroscopy and imaging for oncological applications. *Photochem. Photobiol.* **68**:603–632.

-
- Weersink, R. W., Patterson, M. S., Diamond, K., Silver, S., and Padgett, N. (2001). Noninvasive measurement of fluorophore concentration in turbid media with a simple fluorescence/reflectance ratio technique. *Appl. Opt.* **40**:6389–6395.
- Wu, J., Feld, M. S., and Rava, R. (1993). Analytical model for extracting intrinsic fluorescence in turbid media. *Appl. Opt.* **32**:3583–3595.
- Zhadin, N. and Alfano, R. (1998). Correction of the internal absorption effect in fluorescence emission and excitation spectra from absorbing and highly scattering media: Theory and experiment. *J. Biomed. Opt.* **3**:171–86.

Appendix A

Variance-matching Fluorescence

Monte Carlo

A.1 Introduction

Monte Carlo simulation has become the gold standard for generating theoretical fluence distributions and reflectance profiles for comparison with analytic solutions to radiative transport. Although they are applicable to arbitrary geometry and optical properties, Monte Carlo algorithms are computationally intensive, requiring many orders of magnitude more time than corresponding analytic approximations. A set of techniques known collectively as variance reduction has been developed in an attempt to increase the precision of Monte Carlo routines while decreasing the computation time. Many of these techniques were originally developed in the context of the analogous problems of neutron transport (Kahn and Harris, 1951) and dose modelling in radiation therapy (Kawrakow and Fippel,

2000). The implicit capture method (Prahl *et al.*, 1989) is particularly appropriate to simulations of *in vivo* reflectance and fluorescence measurements, where the detected signal often depends strongly on contributions from photons which have been scattered many times. Variance reduction becomes more complicated when fluorescence and reflected excitation light are modelled simultaneously. A simulation may give acceptable variance for fluorescence, but not for reflectance or *vice-versa*. To address this problem, we have developed an algorithm in which the variances in the fluorescence and reflectance are matched independently to the variances expected from experiment.

A.2 Methods

The structure of the variance-matched Monte Carlo routine is illustrated in Figure A.1. The routine makes use of the implicit capture variance reduction technique described by Prahl *et al.* (1989) and implemented in the widely used MCML code (Wang *et al.*, 1995). Under this method, a photon packet is launched with a weight of 1.0. At each scattering/absorption event, the packet's direction is changed by an angle selected from the Henyey-Greenstein distribution, and its weight is decremented by a factor of the albedo a . The distance between scattering events is selected randomly from an exponential distribution whose scale length is determined by the mean free path in the tissue. This process continues until the packet's weight is below a threshold value w_t , at which point it undergoes roulette. Roulette consists of random sampling such that a packet has a one in ten chance of survival. Those packets which survive have their weights incremented by a

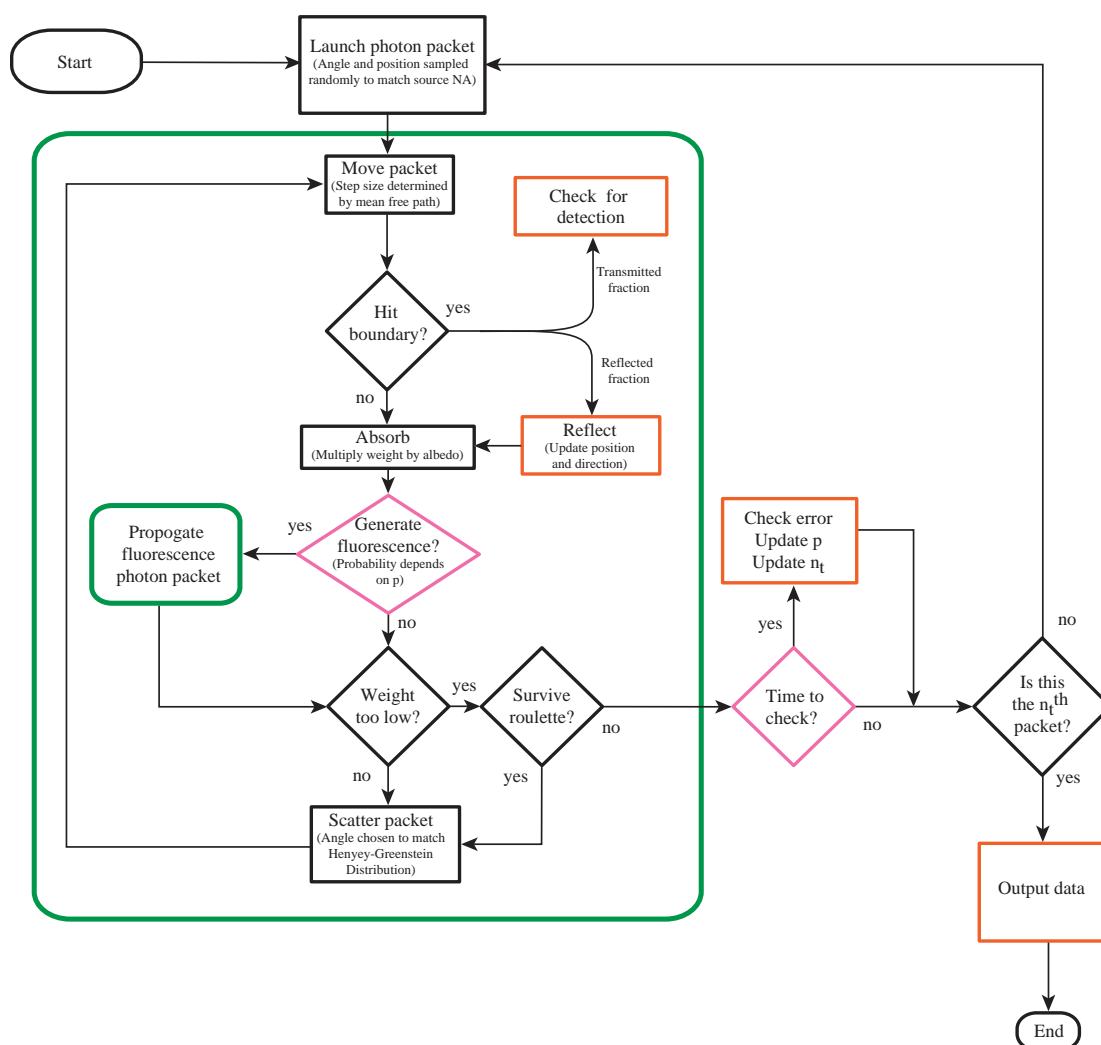


Figure A.1: Flowchart of the variance matching fluorescence Monte Carlo routine. Fluorescence packets are propagated in the same manner as excitation packets, with the exception that they do not generate fluorescence.

factor of 10 while those that do not are terminated. Each absorption event has a probability p (discussed below) of generating a fluorescence packet, which is traced in the same manner. Fluorescence generated by absorption of fluorescence packets is not traced. When a fluorescence packet is launched, it is traced until termination before the excitation photon packet takes another step. Reflectance at the emission wavelength can be evaluated separately.

For the variance to be matched to a desired value, it must first be evaluated. A Monte Carlo simulation can be treated as a series of experiments, each consisting of the launching and tracing of a single photon packet. The mean reflectance signal $E(k)$ collected by the detector after k packets have been traced can be written,

$$E(k) = \frac{1}{k} \sum_{i=1}^k r_i, \quad (\text{A.1})$$

where r_i is the reflectance signal contributed by the i^{th} photon packet. The best estimate of the statistical uncertainty in $E(k)$ is given by the standard error of the mean (SEM). We define the standard variance of the mean (V) as the square of the SEM, given by

$$V(k) = \frac{k \sum r_i^2 - (\sum r_i)^2}{k^2(k-1)}. \quad (\text{A.2})$$

A consequence of the Central Limit Theorem is that for sufficiently large k ,

$$V(k) = \frac{\sigma^2(r)}{k}, \quad (\text{A.3})$$

where $\sigma^2(r)$ is the standard deviation in r_i over the population of all possible photon packets.

Variance matching is accomplished by tracing a number packets n_t such that $V(n_t)$ is equal to the predetermined desired variance V_0 . During the simulation the value of n_t can be predicted using equation A.3, and is given by

$$n_t = \frac{V(k)}{V_0}. \quad (\text{A.4})$$

In simulations that track only reflectance, determining n_t is sufficient to match V to any given value of V_0 .

In the case of simultaneous simulation of reflectance and fluorescence, variance matching is more complicated. Consider a simple implementation in which each excitation absorption event launches a fluorescence photon packet. Because each excitation packet undergoes many absorption events, many fluorescence packets will be launched for each excitation packet. As a result, the variance in the simulated fluorescence signal will generally be much less than that in the reflectance signal, and no single choice of n_t will match both variances to the desired values.

In order to match the variances in the reflectance and fluorescence signals independently, we allow absorption events to generate fluorescence with a probability p less than or equal to 1. The weight of each packet is divided by p prior to launch, so packet weight is conserved. This method is equivalent to the Russian Roulette technique described by Kawrakow and Fippel (2000). For every k excitation packets launched, a total of kp fluorescence photon packets are generated. The standard variance in the mean fluorescence signal $V_F(k)$ after k excitation

packets have been traced is given by

$$V_f(k) = \frac{\sigma_f^2}{kp}, \quad (\text{A.5})$$

where σ_f^2 is the variance in the signal over the population of possible fluorescence packets. At the conclusion of the simulation, when n_t excitation packets have been traced, the standard variance in the fluorescence signal is given by

$$V_f(n_t) = \frac{\sigma_f^2}{n_t p}. \quad (\text{A.6})$$

The optimal value of n_t is determined by the desired variance in the excitation wavelength reflectance using equation A.4. We seek an optimal fluorescence probability p_0 which matches $V_f(n_t)$ to the desired standard variance in the fluorescence V_{0f} . This optimal value is given by

$$p_0 = \frac{\sigma_f^2}{n_t V_{0f}}. \quad (\text{A.7})$$

The value of σ_f^2 is not known *a priori*, however it can be estimated at any point in the simulation by

$$\sigma_f^2 \approx (kp_k)V_f(k), \quad (\text{A.8})$$

where p_k is the value of p used in tracing the first k packets. $V_f(k)$ can be determined statistically by applying equation A.2 to the fluorescence signal. Sub-

stituting equation A.8 into equation A.7 gives

$$p_0 = \frac{kV_f(k)}{n_t V_{0f}} p_k. \quad (\text{A.9})$$

In practice, p is updated many times during each simulation. The value of p_k used in equation A.9 is therefore the mean value of p used for the first k packets, \bar{p}_k . Further, the most appropriate choice of p for the remaining packets is that which makes the mean of p for the entire simulation (\bar{p}_t) equal to p_0 . This is found by manipulating the equation

$$\bar{p}_t = \frac{(n_t - k)p + n\bar{p}_n}{n_t} = p_0, \quad (\text{A.10})$$

giving

$$p = \frac{n_t p_0 - k\bar{p}_n}{(n_t - k)}. \quad (\text{A.11})$$

The derivation above allows the routine to independently match the variances in the reflectance and fluorescence signal to those expected from experiment.

A.3 Results

A.3.1 Uncertainty estimation

To test the accuracy with which our routine is able to match a given desired variance, we have simulated fluorescence detection using a set of tissue optical properties typical of near UV excitation and visible emission, as listed in table A.1. For simplicity, the detector consisted of a single fiber in contact with the

	Optical Properties			Target	Mean	Standard
	$\mu_a(mm^{-1})$	$\mu_s(mm^{-1})$	g	σ	σ	Deviation
R_x	1.0	16.0	0.88	2%	1.98%	2.23%
R_m	7.0	12.0	0.86	2%	2.00%	1.88%
F	—	—	—	2%	2.00%	1.88%

Table A.1: achieved by the variance-matching Monte Carlo routine. The optical properties under which the algorithm was tested are listed. Each of 100 runs attempted to reach the target standard deviation. The mean calculated standard deviation of all 100 runs is listed, along with the standard deviation found by comparing the 100 runs.

tissue surface used as both an excitation source and a detector. The fiber was modelled with a diameter of 0.5 mm and a numerical aperture of 0.22. The simulation was run 100 times using a different set of random numbers for each run. The target uncertainty was set to 2%. Within each run, the values of n_t and p were adjusted by the routine according to equations A.4 and A.9. At the end of each run, the variance was determined according to equation A.2. The square root of this quantity divided by the simulated signal was taken as the estimated relative uncertainty. The true relative uncertainty was found by dividing the standard deviation in the signal from all 100 runs by the mean signal from all 100 runs.

As shown in table A.1, the desired uncertainty was obtained for the fluorescence signal and for the reflectance at the excitation and emission wavelengths. Further, the difference between the estimated and the true uncertainties was less than 10% for each quantity measured. The accuracy with which the desired un-

certainty is achieved does not depend upon the specific source-detector geometry or the optical properties being modelled. The target uncertainties for the 3 signals may be set to different values without effecting the accuracy with which they are achieved.

A.3.2 Evaluation of efficiency

The gain in computational efficiency using variance matching depends on the optical properties being studied but can be significant. As an example, we have simulated generation of fluorescence in homogeneous turbid samples in which the optical properties at the excitation and emission wavelengths are identical (run 1), and in two cases in which the optical properties are typical of situations encountered *in vivo*. Runs 2 and 3 simulate *in vivo* fluorescence generation by NADH and porphyrins, respectively. The quantity being monitored is the signal collected by a single 1 mm diameter fiber on the surface. The source is a pencil beam incident 1 mm from the center of the fiber. The time required to reach a relative uncertainty of 10% or less in both the fluorescence and excitation reflectance signals was recorded for the variance-matched Monte Carlo routine and for the naive Monte Carlo approach (in which p is set to 1.0, so that every absorption event launches a fluorescence packet). At the end of the simulations in which p was set to 1.0, the optimal value of p was calculated according to equation A.7. The results are presented in Table A.2. Because the emission-wavelength reflectance is calculated separately, its computational efficiency is not affected by the parameter p . Hence, it is not listed in table 2. The times given are the total computation time on a 2.4 GHz personal computer. Allowing p to vary improves the efficiency

run	Excitation			Emission			Time	Time	p_0
	μ_a	μ_s	g	μ_a	μ_s	g	$p = 1.0$	p varied	
1	0.2	10.0	0.90	0.2	10.0	0.90	261.8	7.3	0.022
2	1.0	17.0	0.88	7.0	12.0	0.86	8.4	2.8	0.237
3	2.7	14.0	0.87	0.05	5.0	0.73	113.5	2.9	0.016

Table A.2: Total simulation times for various optical parameters. For each simulation the time is reported for the case where p is set to 1.0 and for the case where p is varied optimally by the Monte Carlo code. μ_a and μ_s are given in mm^{-1} and times are in minutes.

of the simulation by a factor ranging from 3 to 40. The fact that the optimal value of p differs by an order of magnitude among the cases shown here indicates that no single value of p can be chosen which will optimize simulations with arbitrary optical properties.

References

- Kahn, H. and Harris, T. E. (1951), Estimation of particle transmission by random sampling. In *Monte Carlo Method*, volume 12 of *Applied Mathematics Series*, pages 27–30. U.S. Government Printing Office, Washington.
- Kawrakow, I. and Fippel, M. (2000). Investigation of variance reduction techniques for Monte Carlo photon dose calculation using XVMC. *Phys. Med. Biol.* **45**:2163–83.
- Prahl, S. A., Keijzer, M., Jacques, S. L., and Welch, A. J. (1989). A Monte Carlo model of light propagation in tissue. *SPIE Institute Series*. **IS5**:102–111.
- Wang, L., Jacques, S. L., and Zheng, L. (1995). MCML- Monte Carlo modeling of light transport in multi-layered tissues. *Comput. Methods Programs Biomed.* **47**:131–146.

Appendix B

Volume Probed by Spectroscopic Measurements

In chapters 4 and 5, we presented the results of reflectance and fluorescence spectroscopy measurements made with a probe in contact with the sample surface. One advantage of this method over those using an off-surface geometry is that an optical fiber-based probe with multiple detectors can be used to assess the heterogeneity of optical properties in a sample. To make use of this feature, however, one must know the volume of the sample that contributes to each measurement. In this appendix, we investigate the volume sampled by reflectance and fluorescence measurements, especially with respect to its dependence on the optical properties of the sample being measured and the distance between the source and detector fibers.

B.1 Reflectance spectroscopy

In order to assess the volume of the phantom or tissue which is sampled by reflectance measurements at each source-detector separation, we have utilized the Monte Carlo method described by Hull *et al.* (1999). In this scheme, the tissue is divided into annular rings concentric with the source fiber. The rings have thickness equal to the diameter of the detection fibers. Photons which exit the upper boundary of the tissue at angles within the acceptance cone of the detection fibers have their paths scored. The result is a two-dimensional array for each detection fiber which records the distribution in radius and depth of photons contributing to signal collected by that fiber. The simulations are performed using a modified version of the MCML routine (Wang *et al.*, 1995).

In figures B.1(a) and (b), the median depth sampled by a diffuse reflectance measurement is plotted as a function of source-detector separation for optical properties typical of tissue in the hemoglobin Soret band and at 630 nm, respectively. The errorbars in each panel indicate the depth interval containing the median 50% of the detected photon paths. In the case of low μ_a (figure B.1(b)), the median depth sampled by diffuse reflectance increases with increasing source detector separation. Any photon that has travelled far enough to reach a distant detector has sampled a range of depths, and photons that remain near the sample surface are likely to be scattered out of the sample before reaching a detector. The low μ_a ensures that even photons which take long paths through the tissue have a low probability of being absorbed.

In contrast, in wavelengths where μ_a is large (figure B.1(a)), the depth sampled

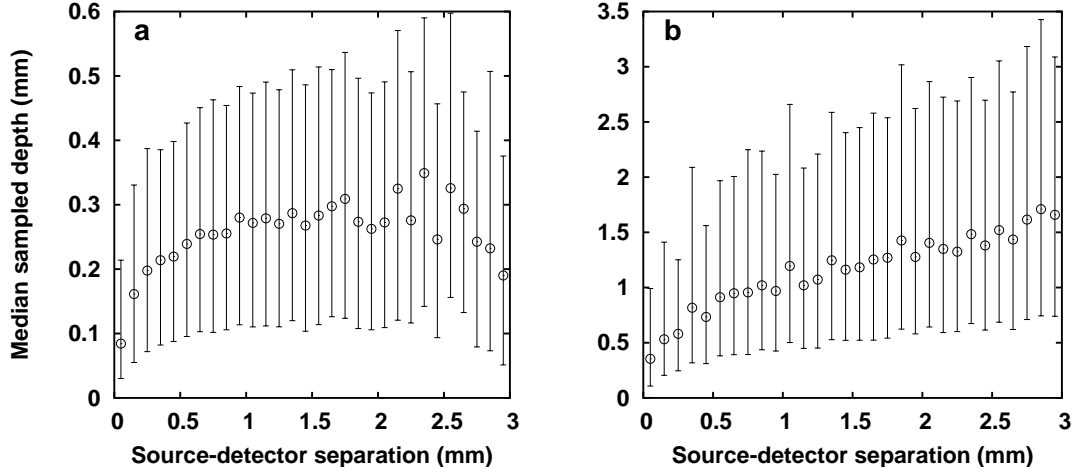


Figure B.1: Median depth probed by diffuse reflectance measurement as a function of source-detector separation for scattering media with optical properties typical of tissue (a) in the hemoglobin Soret band ($\mu'_s = 1.8 \text{ mm}^{-1}$, $\mu_a = 2.0 \text{ mm}^{-1}$) and (b) at 630 nm ($\mu'_s = 1.0 \text{ mm}^{-1}$, $\mu_a = 0.05 \text{ mm}^{-1}$) in the case of poorly oxygenated tissue. The errorbars in each plot correspond to the depth interval containing the median 50% of the detected photon paths.

is nearly independent of source detector separation. This can be understood in terms of the distribution of photon path lengths. When μ_a is large, only those photons that take short paths from the source to the detector avoid absorption. The shortest possible path is constrained by the requirement that the photons must be scattered sufficiently many times to reverse their direction. In the case of a pencil beam incident on a semi-infinite tissue, the mean depth travelled by photons before their direction is randomized is given by $1/\mu'_t$, as shown in section 2.1.4. In the case plotted here, this distance is 0.26 mm. Even at a source-detector separation of 3 mm, the photons collected by the detector have penetrated only far enough to reverse their direction.

Our diffuse reflectance measurements sample volumes with dimensions of the order of the separation between different detection fibers in our probe. Each detection fiber therefore samples a distinct volume of the sample. In the phantom studies described in chapter 4, we have taken care to ensure that the absorbers and scatterers are uniformly distributed within the sample. The volume sampled by the measurement is therefore irrelevant. Measurements made in real tissue, such as those described in section 4.4, present a more complicated situation. Tissue is often optically heterogeneous. Hemoglobin is confined to the vasculature, presenting inhomogeneities in absorption ranging in scale from vessels a few millimeters in diameter to capillaries with diameters of tens of microns. Many optically accessible tissues such as skin and encapsulated tumors exhibit layered structures where the optical properties close to the surface may differ from those at depth. In these cases, measurements made with different detector fibers can provide a measure of the heterogeneity of the sample. In such a situation, the reflectance measured at different wavelengths may sample regions of the tissue with different optical properties. The ability of the fitting routine described in chapter 4 to match the measured data indicate that this is unlikely to be problematic except in extreme cases.

B.2 Fluorescence spectroscopy

A corresponding analysis of the volume sampled by fluorescence measurement is possible. In this case, we are interested in the volume from which the measured fluorescence originates. This distribution will depend on the optical properties at the excitation and emission wavelengths and on the distribution of fluorophore within the sample. We have performed simulations of fluorescence using the Monte Carlo routine described in appendix A, which assumes a uniform distribution of fluorophore molecules. Each time a fluorescence photon packet is captured by a detector, its point of origin within the sample is scored. The result is a map of the relative contributions to the measurement of fluorophore molecules at various depths. The fluorescence origin distributions corresponding to the optical properties of tissue in the hemoglobin Soret band and in regions of low hemoglobin absorption are shown in figure B.2(a) and (b), respectively. In both cases, the optical properties at the excitation wavelength were chosen to match those encountered in tissue at 365 nm. The depth of origin of the recovered fluorescence is nearly insensitive to the emission wavelength optical properties, and is less than 0.5 mm for the range of optical properties we have investigated. This is due to the fact that μ_a at the excitation wavelength is relatively large, confining the volume illuminated by the excitation light to a small, superficial region.

After they are emitted, fluorescence photons propagate according to the same mechanism as reflectance photons at the same wavelength and hence sample similar volumes of tissue. The depths sampled by emitted photons can therefore be

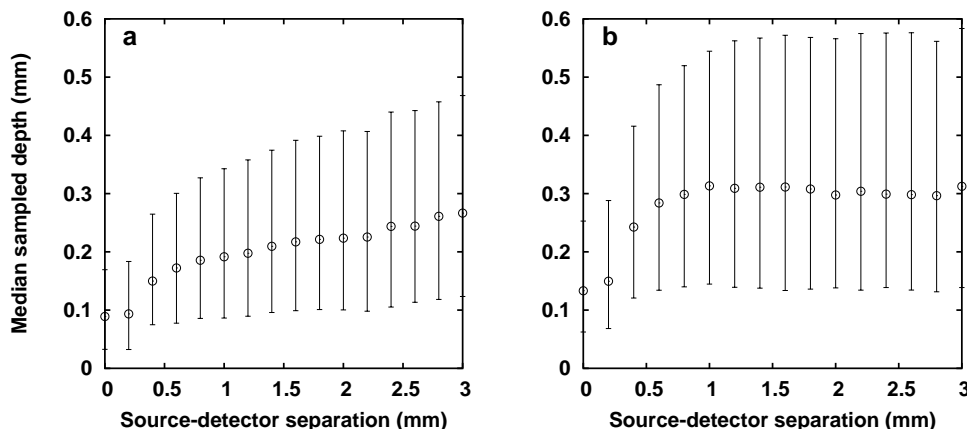


Figure B.2: Median depth of origin of detected fluorescence measurement as a function of source-detector separation for scattering media with emission wavelength optical properties typical of tissue (a) in the hemoglobin Soret band ($\mu'_s = 1.8 \text{ mm}^{-1}$, $\mu_a = 2.0 \text{ mm}^{-1}$) and (b) at 630 nm ($\mu'_s = 1.0 \text{ mm}^{-1}$, $\mu_a = 0.05 \text{ mm}^{-1}$) in the case of poorly oxygenated tissue. The excitation wavelength optical properties ($\mu'_s = 2.3 \text{ mm}^{-1}$, $\mu_a = 0.9 \text{ mm}^{-1}$) were chosen to approximate those of tissue at 365 nm. The errorbars in each plot correspond to the depth interval containing the median 50% of the points of origin of detected photons.

expected to vary considerably with wavelength (see figure B.1). Fluorescence photons will be emitted from a small volume of excited tissue, but may pass through a much larger volume of absorbers and scatterers on the way to the detector.

Like the reflectance measurements described in chapter 4, the fluorescence measurements presented in chapter 5 sample volumes with dimensions of the order of the separation between different detection fibers in our probe. Measurements made with a multifiber probe such as the one employed in these studies can therefore give a measure of the heterogeneity of optical properties within the sample. The emission of fluorescence is confined to a relatively small volume near the excitation source, however, so the signal in all of the detection fibers arises mostly

from fluorescence emitted within that volume. The small volume of tissue sampled renders our fluorescence measurements insensitive to fluorophores located farther than 0.5 mm from the tissue surface. This can be an advantage in studies such as those presented in chapter 3, where it is desirable to restrict the volume measured to a superficial structure such as the skin. Obtaining fluorescence information from deeper tissues, however, requires the use of an excitation wavelength where the absorption is less severe.

References

- Hull, E. L., Conover, D. L., and Foster, T. H. (1999). Carbogen-induced changes in rat mammary tumour oxygenation reported by near infrared spectroscopy. *Br. J. Cancer*. **79**:1709–1716.
- Wang, L., Jacques, S. L., and Zheng, L. (1995). MCML- Monte Carlo modeling of light transport in multi-layered tissues. *Comput. Methods Programs Biomed.* **47**:131–146.

Appendix C

Errata (Corrected)

1. Reference to Lee *et al.* (1998) omitted one author
2. p. 104: In the sentence '*...the deposited $^1\text{O}_2$ dose is measured is on the order of 4 mM...*', the phrase '*is measured*' should be omitted.
3. p. 185: In the sentence '*The qualitative similarity... ...although the irradiance at which a given fraction of bleaching occurs differs.*', the word '*irradiance*' should be changed to '*fluence*'.

References

- Lee, J., Fenton, B. M., Koch, C. J., Frelinger, J. G., and Lord, E. M. (1998). Interleukin 2 expression by tumor cells alters both the immune response and the tumor microenvironment. *Cancer Res.* **58**:1478–1485.